TECHNISCHE UNIVERSITÄT MÜNCHEN

TUM School of Natural Sciences

Development of Novel Chiral Hybrid Metal Halide Perovskites for Efficient Chiroptical Applications

Shangpu Liu

Vollständiger Abdruck der von der TUM School of Natural Sciences
der Technischen Universität München zur Erlangung des akademischen Grades eines

Doktors der Naturwissenschaften

genehmigten Dissertation.

Vorsitz:		Prof. Dr. David Egger
Prüfende der Dissertation:	1.	TUM Junior Fellow Dr. Felix Deschler
	2.	Apl. Prof. Dr. Hristo Iglev

Die Dissertation wurde am 30.07.2024 bei der Technischen Universität München eingereicht und durch die TUM School of Natural Sciences am 13.09.2024 angenommen

Abstract

Hybrid metal-halide perovskites offer special advantages for optoelectronic applications, such as high energy-transfer efficiency, ease of fabrication, cost efficiency, bandgap tuneability, excellent defect tolerance, and high charge carrier mobility. These properties make them highly attractive for solar cells, light-emitting diodes (LEDs), lasers, or photodetector applications. Further, metal-halide perovskites hold promise for spintronic applications, e.g., strong spin-orbit coupling, large Rashba splitting, long spin lifetimes, and efficient spin injection and transport. These characteristics enable optical spin injection and manipulation, potentially leading to advanced spintronic devices with enhanced performance and lower energy consumption, such as, spin LEDs or spin valve device. This work mainly focuses on ultrafast carrier polarization dynamics and chiroptical applications using chiral perovskite materials. High-quality chiral perovskite single crystals and thin films are fabricated by solution-processed methods, including hydrothermal crystal growth and spin-coating approaches. Single-crystal X-ray diffraction is used to identify the detailed crystal structure of as-obtained crystal samples. We report on a series of novel chiral perovskite materials ranging from zero-dimensional lead-free (R/S)-$CHEA_4Bi_2Br_xI_{10-x}$ (x = 0 - 10) with disconnected octahedral dimers through one-dimensional (R/S)-$EAPbI_3$ with helical face-sharing octahedral chains to two-dimensional layered structure (R/S)-$3BrMBA_2PbI_4$ with corner-sharing octahedra. Importantly, all of them show interesting chiroptical properties.

Lead-free (R/S)-$CHEA_4Bi_2Br_xI_{10-x}$ samples exhibit color-tunable circular dichroism signals due to variable halide compositions. By combining the advantages of lead-free perovskite and chirality transfer from chiral organic groups, we observe long-lived polarized photocarriers in chiral (R/S)-$CHEA_4Bi_2Br_xI_{10-x}$ samples at room temperature, with depolarization lifetime of ~1 μs. But due to the disconnected octahedron, chiral lead-free perovskites did not show any PL features at room temperature, which is hard for us to transfer such high exciton polarization to chiroptical readout, like circularly polarized photoluminescence (CPL). Thus, we move our focus to chiral lead-based perovskites, which would offer us strong PL signals at room temperature.

In chiral (R/S)-$EAPbI_3$ thin film samples, we find efficient chirality transfer from chiral perovskite phases to nonchiral PbI_2 heterostructure, resulting in the bright CPL from PbI_2 heterostructures at cryogenic temperatures. Our findings reveal fast carrier transfer (a few ps)

from chiral perovskite phases to PbI_2 nanostructures which supports achieving high PL intensities and large degrees of circular polarization.

It is challenging to achieve both strong chirality and high PLQE in chiral perovskite materials. There is a competition between them. If chiral organic molecules are introduced into the perovskite structures, in some cases, the PL features of the perovskite may be hindered due to distortion, which causes the transfer from direct bandgap to indirect bandgap. Also, increasing the layers of perovskites will dilute the chirality due to the addition of 3D phase perovskites. Here, by cation engineering, we carefully design the structure of chiral organic groups and change the position of the Br atom on the aromatic rings from para to meta-position. We obtain bright CPL in chiral (R/S)-3BrMBA$_2$PbI$_4$ at room temperature, which offers us suitable starting materials for circularly polarized LED fabrication.

However, pure 2D layered perovskites have poor electric conductivity, which strongly hinders their optoelectronic applications. Thus, by directly embedding chiral organic group (R/S)-3BrMBA into $(FA_{0.7}MA_{0.1}GA_{0.2})_{0.87}Cs_{0.13}PbBr_3$ perovskite precursors, we successfully develop a nanoscale chiral perovskite heterostructure of quasi-2D domains and bulk-3D hybrid metal-halide perovskites, which form by self-assembly during spin-coating process. Our circularly polarized LEDs using chiral perovskite heterostructure emitters show a very high degree of electroluminescence polarization (~0.2) and an exceptionally high brightness of 220,000 cd m^{-2} with a high EQE value of ~9%. Our study provides detailed insights into the working mechanisms of our chiral emitter, which provides clear guidelines for exploiting our findings in a wide range of future chiroptical technologies.

Zusammenfassung

Hybride Metall-Halogenid-Perowskite bieten spezielle Vorteile für optoelektronische Anwendungen, wie hohe Energieübertragungseffizienz, einfache Herstellung, Kosteneffizienz, Bandlücken-Tunbarkeit, ausgezeichnete Defekttoleranz und hohe Ladungsträgermobilität. Diese Eigenschaften machen sie äußerst attraktiv für Solarzellen, Leuchtdioden (LEDs), Laser oder Photodetektor-Anwendungen. Darüber hinaus halten Metall-Halogenid-Perowskite vielversprechende Möglichkeiten für spintronische Anwendungen bereit, z. B. starke Spin-Bahn-Kopplung, große Rashba-Spaltung, lange Spin-Lebensdauern und effiziente Spin-Injektion und -Transport. Diese Eigenschaften ermöglichen optische Spin-Injektion und -Manipulation, was potenziell zu fortschrittlichen spintronischen Geräten mit verbesserter Leistung und geringerem Energieverbrauch führen könnte, wie Spin-LEDs oder Spin-Ventil-Geräte. Diese Arbeit konzentriert sich hauptsächlich auf ultraschnelle Trägerpolarisation-Dynamiken und chiroptische Anwendungen unter Verwendung chiraler Perowskitmaterialien. Hochwertige chirale Perowskit-Einkristalle und Dünnfilme werden durch lösungsbasierte Methoden, einschließlich hydrothermalem Kristallwachstum und Spin-Beschichtungsverfahren, hergestellt. Röntgen-Einkristalldiffraktion wird verwendet, um die detaillierte Kristallstruktur der erhaltenen Kristallproben zu identifizieren. Wir berichten über eine Reihe neuartiger chiraler Perowskitmaterialien, die von null-dimensionalen bleifreien (R/S)-$CHEA_4Bi_2Br_xI_{10-x}$ (x = 0 - 10) mit nicht verbundenen oktaedrischen Dimeren über eindimensionale (R/S)-$EAPbI_3$ mit helikalen, flächenverknüpften oktaedrischen Ketten bis hin zu zweidimensionalen geschichteten Strukturen (R/S)-$3BrMBA_2PbI_4$ mit eckenverknüpften Oktaedern reichen. Wichtig ist, dass alle interessante chiroptische Eigenschaften zeigen.

Bleifreie (R/S)-$CHEA_4Bi_2Br_xI_{10-x}$ Proben zeigen farbabstimmbare Signale des zirkularen Dichroismus aufgrund variabler Halogenidzusammensetzungen. Durch die Kombination der Vorteile von bleifreien Perowskiten und der Chiralitätsübertragung von chiralen organischen Gruppen beobachten wir langlebige polarisierte Phototräger in chiralen (R/S)-$CHEA_4Bi_2Br_xI_{10-x}$ Proben bei Raumtemperatur, mit einer Depolarisationslebensdauer von ~1 µs. Aufgrund der nicht verbundenen Oktaeder zeigten chirale bleifreie Perowskite jedoch keine PL-Merkmale bei Raumtemperatur, was es uns erschwert, eine so hohe Exzitonpolarisation in ein chiroptisches Auslesen wie zirkular polarisierte Photolumineszenz

(CPL) zu übertragen. Daher verlagern wir unseren Fokus auf chirale bleihaltige Perowskite, die uns starke PL-Signale bei Raumtemperatur bieten würden.

In chiralen (R/S)-EAPbI_3 Dünnschichtproben finden wir eine effiziente Chiralitätsübertragung von chiralen Perowskitphasen zu nicht-chiralen PbI2-Heterostrukturen, was zu einer starken zirkular polarisierten Photolumineszenz (CPL) von PbI_2-Heterostrukturen bei kryogenen Temperaturen führt. Unsere Ergebnisse zeigen einen schnellen Trägertransfer (einige ps) von chiralen Perowskitphasen zu PbI_2-Nanostrukturen, was hohe PL-Intensitäten und große Grade der zirkularen Polarisation unterstützt.

Es ist herausfordernd, sowohl starke Chiralität als auch eine hohe PLQE in chiralen Perowskitmaterialien zu erreichen. Es gibt einen Wettbewerb zwischen diesen beiden Eigenschaften. Wenn chirale organische Moleküle in die Perowskitstrukturen eingeführt werden, können in einigen Fällen die PL-Eigenschaften des Perowskits aufgrund von Verzerrungen beeinträchtigt werden, was zu einem Übergang von einem direkten Bandabstand zu einem indirekten Bandabstand führt. Außerdem führt das Erhöhen der Perowskitschichten zur Verdünnung der Chiralität durch die Hinzufügung von 3D-Phasen-Perowskiten. Hier haben wir durch Kationen-Engineering die Struktur der chiralen organischen Gruppen sorgfältig entworfen und die Position des Br-Atoms an den aromatischen Ringen von der Para- zur Meta-Position verändert. Wir erzielen eine starke CPL in chiralen (R/S)-3BrMBA_2PbI_4 bei Raumtemperatur, was uns geeignete Ausgangsmaterialien für die Herstellung von zirkular polarisierten LEDs bietet.

Reine zweidimensionale (2D) geschichtete Perowskite haben jedoch eine schlechte elektrische Leitfähigkeit, was ihre optoelektronischen Anwendungen stark behindert. Daher haben wir durch das direkte Einbetten der chiralen organischen Gruppe (R/S)-3BrMBA in $(FA_{0.7}MA_{0.1}GA_{0.2})_{0.87}Cs_{0.13}PbBr_3$ Perowskitvorstufen erfolgreich eine nanoskalige chirale Perowskit-Heterostruktur aus quasi-2D-Domänen und bulk-3D-Hybrid-Metallhalogenid-Perowskiten entwickelt, die sich während des Spin-Coating-Prozesses selbst zusammensetzen. Unsere zirkular polarisierten LEDs mit Emittern aus chiraler Perowskit-Heterostruktur zeigen einen sehr hohen Grad an Elektrolumineszenzpolarisation (~0,2) und eine außergewöhnlich hohe Helligkeit von 220.000 cd m^{-2} mit einem hohen EQE-Wert von ~9 %. Unsere Studie liefert detaillierte Einblicke in die Arbeitsmechanismen unseres chiralen Emitters, was klare

Richtlinien für die Nutzung unserer Ergebnisse in einer Vielzahl zukünftiger chiroptischer Technologien bietet.

Contents

List of Common Abbreviations

R	Right-handed
S	Left-handed
HMHP	Hybrid metal-halide perovskite
CHEA	Cyclohexylethylamine
CD	Circular dichroism
CISS	Chiral-induced spin selectivity
CPL	Circularly polarized photoluminescence
SOC	Spin-orbit coupling
SCXRD	Single-crystal X-ray diffraction
CTA	circularly polarized transient absorption
TA	transient absorption
DMF	N, N´-dimethylformamide
VBM	Valence band minima
CBM	Conduction band minima
DFT	Density-functional theory
PL	Photoluminescence
PIA	Photo-induced absorption
GSB	Ground state bleaching
TCSPC	Time-correlated single photon counting
PLQE	Photoluminescence quantum efficiency
3BrMBA	1-(3-Bromphenyl)-ethylamine
4BrMBA	1-(4-Bromphenyl)-ethylamine
Rac	Racemic
LED	Light-emitting diode
2D	Two-dimensional
GIWAXS	Grazing incident wide-angle X-ray scattering
EA	α-Ethylbenzylamine
HI	Hydroiodic acid
DMSO	Dimethyl sulfoxide
CPeLED	Circularly-polarized perovskite light-emitting diode

EL	Electro-luminescence
CEL	Circularly polarized electro-luminescence
EQE	External quantum efficiency
TRPL	Time-resolved photoluminescence
FWHM	Full width at half maximum

List of Tables and Figures

Chapter 1: Introduction

1.1 Challenges in Optoelectronic Applications

Light is the primary energy source for most living organisms on our planet. Since ancient times, mankind's life is strongly bonded to light. Light is not only an important symbol in the spiritual world of human beings but is also closely related to our daily lives. People start to pursue light, understand light, and then use light. There are many types of light, and each of them has unique properties, e.g., different wavelengths, frequencies, and directions, and can be considered for wide-range applications, e.g., display, sensing, information, communication, medical, and energy areas. The energy problem is the main problem in society. The primary energy consumption in modern life still strongly relies on fossil fuels. For investigating renewable energy, transferring light into electricity offers us a good opportunity to solve such problems. A solar cell is an important green energy technology that converts available solar energy into useful electric energy. Due to their high stability and availability in the earth's crust, silicon (Si) materials are currently the most widely used solar cell materials. Si solar cells show a typical efficiency of ~20%. Even in 2024, the per unit cost of electricity generated using solar cells is more expensive than electricity generated using hydro/thermal/nuclear power. Although we have improved the efficiency of solar cells over time to meet the cost of the ways mentioned above of making electricity, the efficiency of Si solar cells is reaching saturation limits. Thus, there is a need to look for new, affordable materials for solar electricity production.

In search of new materials that can replace Si, a new type of material called perovskite has emerged recently. Hybrid metal-halide perovskites (HMHPs) are solution-processed materials with tuneable compositions and band structures, which are promising versatile materials for optoelectronic applications. According to the best research-cell efficiencies chart from the National Renewable Energy Laboratory, the highest tandem solar cell (perovskite/Si) efficiency nowadays has reached 33.9% by LONGi solar technology company (*1*), which represents a big step in solar electricity production. HMHPs are famous materials for optoelectronic applications because of their excellent emission quantum efficiencies, strong defect tolerance, and low-cost solution-processed fabrication. However, the stability of perovskite materials is still a big issue (*2*). Besides solar electricity generation, the efficient consumption of electricity is also important. Over 20% of the total electricity produced

worldwide is used for lighting and display applications. In the 21st century, a new kind of efficient lighting solution that emerged over incandescent bulbs is called light-emitting diodes (LEDs). Recently, it has been reported that LEDs using HMHPs can achieve a high external quantum efficiency (EQE) of 30.84% (*3*). All these results have proved that HMHPs are efficient optoelectronic materials showing exceptional tolerance in their electronic states to defects and crystal strain.

Nevertheless, efficient generation and control of light is still a challenging problem. It is common knowledge that light is an electromagnetic wave. Among many properties of light, polarization is one crucial property used in many applications, such as virtual reality, liquid crystal displays, quantum computing and information, and optical sensing. Generating polarized light usually requires additional optical structures, e.g., linear polarizers or quarter-wave plates, which are inherently inefficient because more than 50% of light is filtered out. Linearly polarized light emission by HMHP nanostructures has been recently reported (*4*), while many works still focus on the generation of circularly polarized light. Circularly polarized light is a particular type of electromagnetic wave where the electric field vector rotates in a circle as the wave propagates. Traditional spintronic devices using GaAs can reach 100% degree of emission circular polarization, which requires low cryogenic temperature and strong magnetic fields (*5*). Besides, the efficiency of corresponding devices remains low. Several recent works reported using chiral layered perovskites as spin filters to produce circularly polarized light at room temperature. However, most of the reported work only shows low values of emission polarization (< 0.2) or even low device efficiency. Thus, finding suitable solutions for generating circularly polarized light is an active area of research in the scientific community.

1.2 The Scope of Our Work

The main purpose of the current work is to find novel perovskite materials for efficient and highly circularly polarized light generation. In Chapter 2, we explain the physical background of semiconductor materials. We further introduce the concept of chirality and HMHPs and the connections between them. Chapter 3 details the fabrication methods of all related materials in the current work and their characterization methods.

In Chapter 4, we present a pioneering study on the fabrication of novel chiral zero-dimensional (0D) bismuth-based semiconductors ((R/S)-$CHEA_4Bi_2Br_xI_{10-x}$). By adjusting halide ratios, these materials exhibit color-tuneable circular dichroism from 300 to 500 nm. Single crystal XRD measurements confirm the formation of a unique chiral structure with disconnection bismuth octahedral dimers. DFT calculation proves the difference in chirality (R/S) results in opposite spin textures at band edge structures. More importantly, circularly polarized transient absorption spectroscopy indicates the existence of long-lived polarized excitons in chiral bismuth-based samples, which show a polarization lifetime of a few microseconds.

In Chapter 5, we report the synthesis of chiral one-dimensional (1D) lead halide perovskite single crystal and thin films ((R/S)-$EAPbI_3$). In-situ XRD and GIWAXS measurements indicate the importance of spin-coating solvents, which can control the crystallized orientation of as-obtain thin films. Using transient absorption and PL spectra, we find the 500 nm signals in both TA and PL positions attributed to chiral perovskite/PbI_2 heterostructure formation. By efficient and fast chirality transfer from chiral perovskite to PbI_2 heterostructure, our chiral perovskite thin films show bright and polarized emission at low temperatures.

In Chapter 6, we report the growth of the chiral two-dimensional (2D) lead halide perovskite single crystals ((R/S)-$3BrMBA_2PbI_4$), which show a bright circularly polarized emission at room temperature with a PLQE value of ~39% and degree of polarization of ~30%. Transient absorption spectroscopy and time-resolved PL measurements confirm the high PLQE values derived from the fast and dominant radiative decay channel in chiral 2D perovskites. DFT calculations proved the existence of large Rashba splitting in the conduction band due to highly distorted octahedra structures. Besides, circularly polarized TA measurements demonstrate our chiral 2D perovskite has long-lived excitons with a polarization lifetime of ~2 μs, which explains their intense circular polarization.

In Chapter 7, we report on the fabrication of circularly polarized perovskite LEDs based on chiral perovskite emitters. These exhibit a large degree of electroluminescence polarization of ~20%, high external quantum efficiency of ~9%, and an exceptionally large brightness of ~220000 cd/m^2. Confocal PL mapping and time-resolved PL spectroscopy prove the formation of chiral perovskite heterostructures of quasi-2D nanodomains and 3D bulk phases.

Chiral quasi-2D domains serve as efficient chirality injections to produce polarized excitons, which are then transferred to 3D bulk phases. 3D bulk phases work as efficient charge transfer layers, emitting bright and highly polarized luminescence. Circularly polarized transient spectroscopy and microscopy measurements further confirm that the bright and highly polarized luminescence derives from efficient carrier transfer from chiral quasi-2D domains.

Finally, we conclude all the results we found in the current work and propose improved plans for chiral perovskite circularly polarized LEDs.

The current work is based on two publications (*6*, *7*), and other works are still under review processes.

S. Liu, M. W. Heindl, N. Fehn, S. Caicedo-Dávila, L. Eyre, S. M. Kronawitter, J. Zerhoch, S. Bodnar, A. Shcherbakov, A. Stadlbauer, G. Kieslich, I. D. Sharp, D. A. Egger, A. Kartouzian, F. Deschler. Optically Induced Long-Lived Chirality Memory in the Color-Tunable Chiral Lead-Free Semiconductor (*R*)/(*S*)-$CHEA_4Bi_2Br_xI_{10-x}$ (x = 0–10). *J. Am. Chem. Soc.* ***144****, 14079–14089 (2022)*}. Copyright {2022} American Chemical Society.

S. Liu, M. Kepenekian, S. Bodnar, S. Feldmann, M. W. Heindl, N. Fehn, J. Zerhoch, A. Shcherbakov, A. Pöthig, Y. Li, U. W. Paetzold, A. Kartouzian, I. D. Sharp, C. Katan, J. Even, F. Deschler. Bright circularly polarized photoluminescence in chiral layered hybrid lead-halide perovskites. *Science Advances, **9**, eadh5083 (2023)*. Copyright © 2023 Distributed under a Creative Commons Attribution NonCommercial License 4.0 (CC BY-NC).

S. Liu, Y. Li, S. Bodnar, J. Zerhoch, J. A. Gessner, P. Kollenz, A. Shcherbakov, G. May, N. Solhtalab, M. W. Heindl, U. W. Paetzold, F. Deschler. Bright Circularly Polarized Light-Emitting Diodes Using Chiral Lead-Halide Perovskite Heterostructure Emitters. (under review)

S. Liu, J. Zerhoch, M. W. Heindl, C. Zhang, T. Kodalle, K. Sun, A. Shcherbakov, S. Bodnar, C. Jandl, A. Pöthig, I. D. Sharp, P. Müller-Buschbaum, C. M. Sutter-Fella, F. Deschler.

Chirality Funnels in Low-Dimensional Hybrid Perovskite Heterostructures for Circularly Polarized Photoluminescence. (to be submitted)

Chapter 2: Theoretical Background

In this chapter, we introduce the fundamental concepts and theory behind the experiments and analysis that are being used in the thesis. The main parts of our work are focused on finding novel chiral perovskite materials for superior chiroptical properties. Hybrid metal halide perovskites are novel semiconductor materials with exceptional optical electronic features. Thus, it is essential to understand the fundamental semiconductor physics that lies behind the material's properties.

2.1 Semiconductor Physics

2.1.1 Crystal structure

Solid-state material contains countless atoms or molecules, e.g., there are usually ~10^{23} atoms in 1 cm^3 volume space. How to arrange these numerous atoms determines the structure of matter, which is one of the most fundamental features of materials. There are two main types of solid-state materials, crystalline materials and amorphous materials, depending on whether there is periodical distribution of atoms. For an ideal crystal, the alignment of atoms is highly ordered with periodical repeatability in the whole structure, while amorphous materials wouldn't show long-term repeatability in their structures.

In 1912, German theoretical physicist Max Laue, together with his colleagues Walter Friedrich and Paul Knipping, performed the first successful X-ray diffraction experiment. Laue and coworkers directed X-rays at a ZnS crystal and observed the diffraction pattern (*8*, *9*). Later, Laue was awarded the Nobel Prize in Physics in 1914. Such a result first relates the X-ray diffraction and crystal structures, confirming that crystals have a periodic structure that can diffract X-rays. Then, in the following year (1913), William Lawrence Bragg and his father, William Henry Bragg, formulated Bragg's Law (*10*), which describes the relationship between the X-ray incident angles, lattice distance, and wavelength. This result provides us with a general approach to determining crystal structures. The Braggs were then awarded the Nobel Prize in Physics in 1915 for their X-ray diffraction and crystal structure determination work. Nowadays, X-ray diffraction is a standard and essential technique in materials science, chemistry, and physics area for determining the atomic and molecular structure of crystals, which helps us to understand the fundamental part of matters and correlate the structure

properties with material functionalities for discovering novel materials with better performance.

There are several important parameters to describe the structure of a crystal. For instance, crystal lattice, which represents the arrangement of atoms or molecules in a crystal structure, is defined as the three-dimensional pattern of atoms or groups of atoms that extend throughout the entire material. Such a pattern is composed of the intersections of three parallel planes and repeats at regular intervals while maintaining the same orientation to each other. The smallest repeated unit in a crystal is denoted as a crystal unit cell. All crystal lattices are composed of unit cells. The important lattice parameters are the edge distance (a, b, c) of a unit cell and their mutual angles (α, β, γ). These parameters describe the size and shape of the unit cell and are crucial for determining the crystal's overall structure and symmetry, as well as for further understanding their properties. There are 14 fundamental lattices (Bravais lattices) in three-dimensional structures (Table 2.1). Depending on the shapes and symmetries of the unit cells, they can be separated into seven types of crystal lattices, e.g., cubic, monoclinic, trigonal, orthorhombic, hexagonal, tetragonal, and triclinic. The cubic structure usually shows complete symmetry with equal unit distances and angles, while the triclinic structure exhibits the least symmetry with all different lattice parameters.

Table 2. 1. Crystal lattice of three-dimensional crystals

Crystal lattice	Lattice Parameter	Primitive	Base-Centered	Body-Centered	Face-Centered
Triclinic	$a\neq b\neq c$, $\alpha\neq\beta\neq\gamma$	√			
Monoclinic	$a\neq b\neq c$, $\alpha=\beta=90°\neq\gamma$	√	√		
Orthorhombic	$a\neq b\neq c$, $\alpha=\beta=\gamma=90°$	√	√	√	√
Tetragonal	$a=b\neq c$, $\alpha=\beta=\gamma=90°$	√		√	
Cubic	$a=b=c$, $\alpha=\beta=\gamma=90°$	√		√	√
Trigonal	$a=b=c$, $\alpha=\beta=\gamma<120°\neq90°$	√			
Hexagonal	$a=b\neq c$, $\alpha=\beta=90°$, $\gamma=120°$	√			

Similar to crystal lattice, symmetry is another essential feature of a crystal. Symmetry means the repetition of objects in space or in time. In the crystal structure, symmetry happens all through a fixed point, and such a point remains unchanged when a symmetry operation is applied, which is called point symmetry. There are four types of symmetry operations in crystal structures, including rotations, reflections, inversions, and rotary inversions. Due to the requirements of periodic repetition in the crystal structure, only two- (180°), three- (120°), four- (90°), or six-fold (60°) rotation axes are allowed for space filling of three-dimensional structures. Thus, by combining various allowed rotation axes, mirror planes, and inversions, there are 32 unique crystallographic point groups. In addition, inside such 32-point groups, only 11 of them show centrosymmetric structures, which are also named Laue groups. To describe the symmetry in crystals, space group is another important way. Unlike the point group, which only describes the symmetry of isolated objects, space groups indicate both the point symmetry and translational symmetry inside the whole structures, which is absent in the diffraction patterns. Therefore, the types of space groups increase to 320. 73 of them are the symmorphic space groups. 22 of them are the enantiomorphic pairs with chiral space groups. 65 of them belong to Sohncke space groups, which only contain first-kind symmetry operations, such as rotations, translations, and roto-translations (*11*, *12*).

Further, orientation is an essential factor for crystal structures and material features. The orientation of single crystals refers to the alignment of the crystal lattice concerning a reference coordinate system. This orientation is significant because the properties of a crystal can vary depending on the direction due to the anisotropic nature of crystalline materials. Miller indices (hkl) are usually used to specify the orientations of the crystal lattices by indexing the reciprocals of where the plane intersects with the axes. There are many methods to determine the crystal orientations in single crystal samples, e.g., X-ray diffractions, optical goniometry, and the Laue method. In general, the orientation of single crystals is a fundamental aspect that influences their physical properties and behaviors. Understanding and controlling crystal orientation with desired properties is essential in various scientific and industrial applications.

2.1.2 Band theory

Band theory is the dominant cornerstone for describing electron mobility in solid-state physics. After the establishment of quantum mechanics, band theory eventually became popular, boosting semiconductor-based applications.

Band theory is a theoretical model which describes the electronic structure of solids. In an isolated atom, electrons in each orbit have specific energy levels. However, in a solid made of a large number of atoms, electrons in the outer shell of each atom are strongly influenced by their neighboring atoms. The energy level of such a complicated system is usually described using Band theory. Describing such complicated systems with numerous electrons is a big challenge. There are two complementary models for electron motions in condensed matter. One is nearly free electron model, in which the motion of each electron is considered as independent and moving within an effective potential field. Based on this, the second model assumes that, as atoms come together to form a solid, their outermost electron orbitals start to overlap due to their close proximity. This overlap causes shifts in electron energy levels to either higher or lower than their original levels. Electrons in the same orbit display different energy levels. Such variable energy levels with finite energy width are referred to as energy bands. Besides, the inner electrons, which are close to the nucleus, are not obviously affected by neighboring atoms, which would result in little-to-no energy splits in inner electron orbitals.

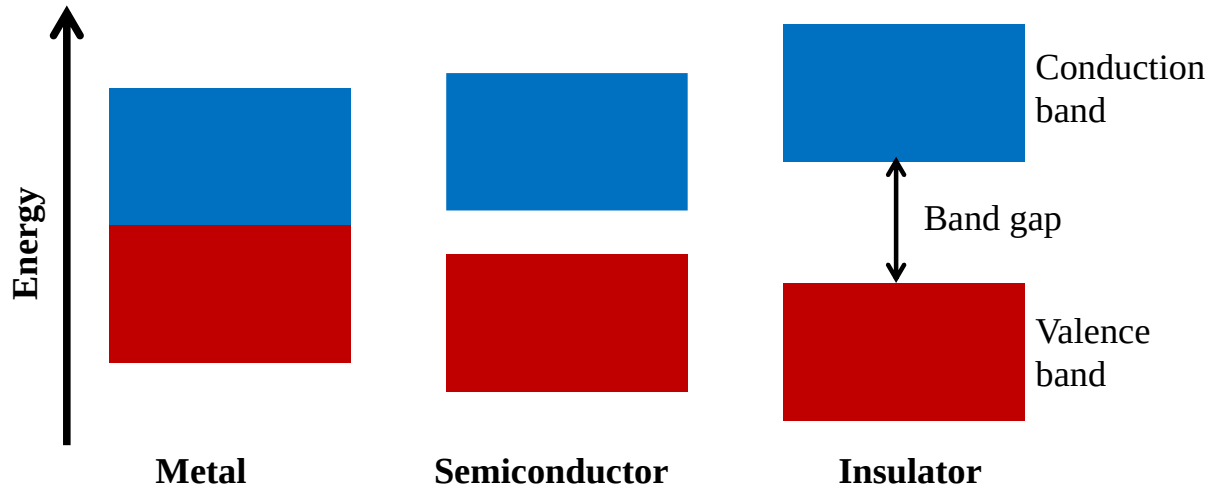

Fig. 2. 1. Schematic illustration of bandgap structures for conductor, semiconductor, and insulator.

The electrons in the outermost orbitals are also referred to as valence electrons. The energy band occupied by these valence electrons is called the valence band. The highest energy level in the valence band is represented as the valence band maximum (VBM). In the outermost orbitals, the empty band, which contains no occupied electrons, is the conduction band. The smallest energy level in the conduction band is called the conduction band minimum (CBM). The valence and conduction bands are separated by a forbidden band of energy (Eg), also called bandgap energy. If there is no forbidden bandgap between the valence band and the conduction band, such solid-state material can be considered as a (semi-)metal (Fig. 2.1). A very small amount of energy would allow electrons to move freely in the conduction band, which would further result in an effective electric current inside metals. In insulators, the band gap is large enough to avoid electrons jumping from the valence band to the conduction band. As a result, the electrons are mostly fixed at certain positions with low conductivities. However, the energy gap in semiconductors is sufficient to drive electrons between valence and conduction bands using electric or optical pumps.

In semiconductor photovoltaic materials, the Parabolic band approximation simplifies the description of the electronic states near the bandgap. The energy E(**K**) near the VBM or CBM (**K** = $\mathbf{K_0}$) can be approximated using a Taylor expansion:

$$E(\boldsymbol{K}) \approx E(\boldsymbol{K_0}) \pm \frac{\hbar^2(\boldsymbol{K}-\boldsymbol{K_0})^2}{2m^*} \quad (1)$$

Where E($\mathbf{K_0}$) represents the conduction or valence band edge energy; the positive and negative signs represent the case of conduction or valence band, representatively; $\hbar$ is the reduced Planck's constant; m^* is the effective mass of the electron (hole) in the conduction (valence) band, which is defined by the following equation:

$$\frac{1}{m^*} = \pm\frac{1}{\hbar}\frac{\partial^2 E}{\partial k^2} \quad (2)$$

The effective mass of the electron (or hole) defines how the electron (or hole) responds to external forces, such as electric fields, within the crystal. Thus, effective mass is important for determining the carrier mobility, recombination rate, and optical and electronic properties of semiconductors, such as absorption coefficients and bandgap energies.

2.1.3 Optical properties of materials

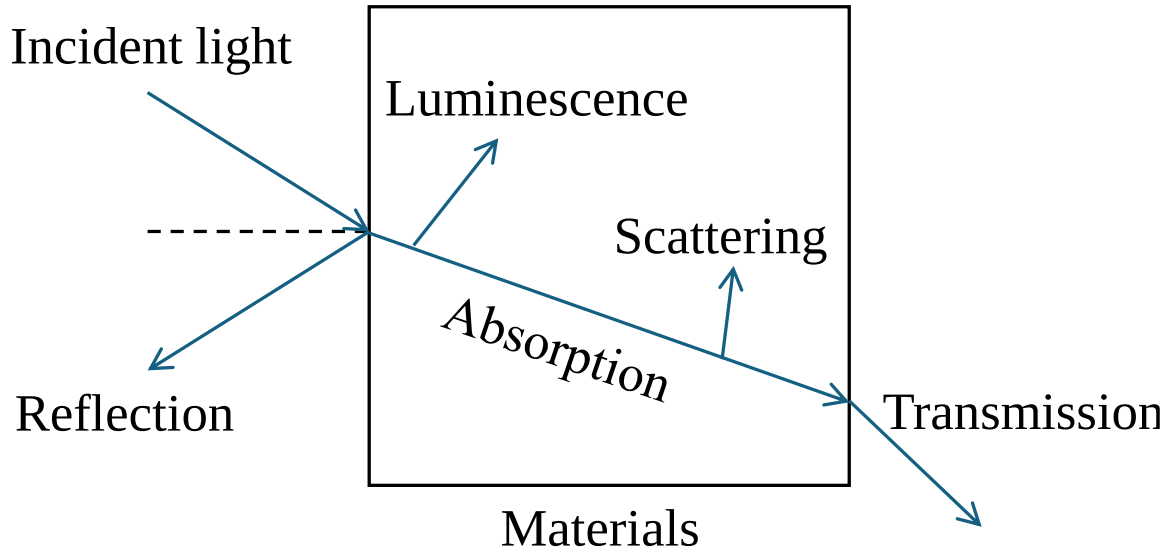

Fig. 2. 2. Fundamental process during light-matter interactions.

Understanding the optical properties of solid-state materials is paramount for their technological applications. When the light interacts with a solid (Fig. 2.2), part of it is reflected from the surface. Due to the interaction with the electrons and atoms inside materials, light can also be absorbed by the materials, which would further excite electrons from VB to CB. During the relaxation process, the excited electrons fall back to the CB, releasing the excess energy. The relaxation process can be radiative and non-radiative. The radiative part is also known as photoluminescence (PL). During the light propagation process inside materials, the direction and/or frequency of light would also be changed due to the interaction with the medium, which corresponds to light scattering. The rest of the light would pass through the medium as transmitted light. In general, the amount of incident light should be equal to the total amount of reflection light, absorption, and transmitted light.

2.1.4 Exciton

When a material is excited optically or electrically, the electrons in the valence band will make a transition to the conduction band to form free electrons with a negative charge, which would leave a positive hole in the valence band. Due to the Coulomb force, the free electron may be coupled with a hole to form a bonded exciton. The exciton can be viewed conceptually as similar to a hydrogen atom, which is an electrically neutral system. The

energy levels of excitons are usually slightly below conduction bands, which can be described using a modified version of the hydrogenic model. In this model, the binding energy of the exciton is analogous to the Rydberg energy of a hydrogen atom. Still, it is adjusted for the material's dielectric constant and the effective masses of the electron and hole. Thus, the excitonic energy levels E_n in a semiconductor can be expressed as:

$$E_n = -\frac{R_H}{\epsilon_r^2}\frac{\mu}{m_e}\frac{1}{n^2} \quad (3)$$

Where R_H is the Rydberg constant for hydrogen ($R_H \approx 13.6$ eV), $\in_r$ is the dielectric constant, m_e is the free electron mass, and μ is the reduced mass of the electron-hole pair, which is defined as,

$$\mu = \frac{m_h^* m_e^*}{m_h^* + m_e^*} \quad (4)$$

where m_e^* and m_h^* are the effective masses of the electron and hole, respectively.

When excitons travel through the lattice, they interact with phonons, defects, or other entities hosted by the lattice. These interactions can lead to either recombination or dissociation of excitons. During recombination, the excited excitons would directly decay to the ground states, releasing the energy to the lattice or emitting it as light. In the case of dissociation, excitons are separated into free carriers (electrons and holes), which would further contribute to photoconductivity.

Exciton binding energy, referring to the energy required to decompose an exciton to a free electron and hole, is an important parameter in understanding the formation of excitons. For nearly free carriers, the value of exciton binding energy would be just a few meV. There are two types of excitons, depending on the bonding strength. When the binding energy between electron and hole (~10 meV) is smaller, the distance between electron and hole is much larger than the distance between neighboring atoms. Such weakly bound excitons are also called Wannier-Mott excitons, which are common in inorganic semiconductors, e.g. GaAs. In the opposition case, when the binding energy is much larger (~0.1 - 1 eV), these excitons are strongly bound, also known as Frenkel excitons, and typically observed in insulators or molecular crystals.

2.1.5 Charge Carrier Recombination

Charge carrier recombination refers to the process by which free electrons and holes (excitons) in a semiconductor material recombine (decay). This recombination process can occur through various mechanisms, such as radiative recombination, Shockley-Read-Hall recombination, and Auger recombination (Fig. 2.3).

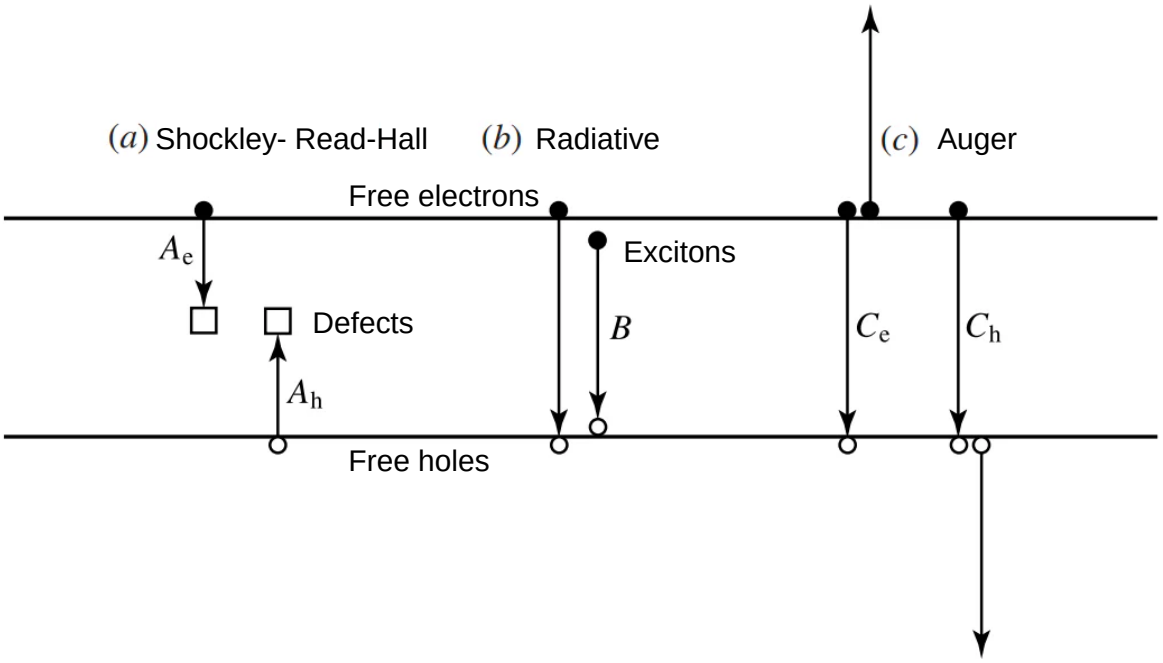

Fig. 2. 3. Carrier recombination processes in a semiconductor. a, Shockley-Read-Hall recombination. **b,** Radiative recombination. **c,** Auger recombination.

The Shockley-Read-Hall recombination mechanism refers to the recombination that occurs through defect or trap states within the band gap. These defect states act as intermediates, capturing and releasing carriers, which leads to non-radiative recombination. The following equation gives the Shockley-Read-Hall recombination rate:

$$R_{SRH} = \frac{np - n_i^2}{\tau_e(n + n_{trap}) + \tau_h(p + p_{trap})} \quad (5)$$

where n and p represent electron and hole concentration, respectively; n_i is the intrinsic carrier concentration; τ_e and τ_h are the electron and hole lifetime, respectively; n_{trap} or p_{trap} is the electron or hole concentration when the trap energy level E_t is equal to the intrinsic Fermi level E_i, which is calculated by the following equations.

$$n_{trap} = N_c e^{-\frac{E_t - E_c}{kT}} \quad (6)$$

$$p_{trap} = N_v e^{+\frac{E_t - E_v}{kT}} \quad (7)$$

Here, N_c and N_v represent the effective density of states in the conduction and valence band, respectively. E_c and E_v CBM and VBM energy. k is the Boltzmann constant, while T is the absolute temperature. For a high carrier density regime, where ($\Delta n = \Delta p = n \gg n_i$). The Shockley-Read-Hall recombination rate can be simplified as,

$$R_{SRH} = k_{SRH} n \tag{8}$$

$$k_{SRH} = \frac{1}{\tau_e + \tau_h} \tag{9}$$

According to the above equations, the Shockley-Read-Hall recombination rate strongly depends on the trap density and carrier lifetime.

In radiative recombination, also known as band-to-band recombination (exciton recombination), an electron in the conduction band recombines with a hole in the valence band, emitting a photon. The radiative recombination rate R_{rad} is given by:

$$R_{rad} = k_{rad}(np - n_0 p_0) \tag{10}$$

where n_0 and p_0 represent the electron and hole density in the darkness (without any excitations). K_{rad} is the radiative recombination coefficient, which relates to the intrinsic properties of the semiconductor material, such as the band gap and the electronic structure. When a semiconductor is excited optically (by light) or electrically (by an applied voltage), additional electron-hole pairs are generated, increasing the carrier concentrations. The radiative recombination rate under these conditions would be given by,

$$\begin{aligned} R_{rad} &= k_{rad}\big((n_0 + \Delta n)(p_0 + \Delta p) - n_0 p_0\big) \\ &= k_{rad}(n_0 \Delta p + p_0 \Delta n + \Delta n \Delta p) \end{aligned} \tag{11}$$

The excess carrier concentrations are equal in many practical cases, especially in direct bandgap semiconductors under steady-state conditions ($\Delta n = \Delta p = n$). Besides, the excited carrier population (n) is much larger than the dark carrier (n_0 and p_0). Thus, the radiative recombination rate can be simplified to:

$$R_{rad} = k_{rad} n^2 \tag{12}$$

In Auger recombination, an electron-hole pair recombines without emitting a photon. The energy is transferred to another electron or hole, which is then excited to a higher energy state. Auger recombination is a three-body process that usually happens at high carrier concentrations, which leads to the loss of energy as heat. The Auger recombination rate can be expressed as,

$$R_{Auger} = C_e n^2 p + C_h p^2 n \tag{13}$$

where C_e and C_h are the Auger recombination coefficients for electrons and holes, respectively. At a high carrier density ($\Delta n = \Delta p = n \gg n_i$). The recombination rate, therefore, becomes,

$$R_{Auger} = k_{Auger} n^3 \tag{14}$$

Considering all three recombination rates, the total recombination rate in a semiconductor can be expressed by simply adding up all the individual recombination rates:

$$-\frac{dn}{dt} = k_{SRH} n + k_{radiative} n^2 + k_{Auger} n^3 \tag{15}$$

This total rate provides a comprehensive understanding of how quickly carriers recombine through all available mechanisms in semiconductors. It is an important method for analyzing and optimizing the performance of semiconductor devices, including solar cells, LEDs, and lasers.

2.2 Chirality and Spin

Chirality is a property of asymmetry. An object or a system is chiral if it is distinguishable from its mirror image. That means it cannot be superimposed onto its mirror image. It is a general feature in the whole natural world, from simple molecules to DNA, proteins, or even spiral galaxies.

2.2.1 Chiroptical features

Chirality is most commonly observed in molecules. For example, one carbon atom substituted with four different bound substituents would result in two chiral enantiomers in opposite directions: right-handed (R) and left-handed (S) (Fig. 2.4). Because of their unique asymmetry structures, chiral materials typically exhibit chiroptical features, such as circular dichroism (CD) and circularly polarized photoluminescence (CPL). The CD is a phenomenon where chiral materials absorb right-handed and left-handed circularly polarized light to different extents. The differential absorption occurs because the unique chiral environment within the chiral materials creates distinct energy levels or states that interact more favourably with one type of circular polarization over the other. Besides, except for the differential absorption in the VB, upon excitation, chiral materials can also emit CPL at CB. This means that the emitted light has a preferred handedness (either right-handed or left-handed circular polarization).

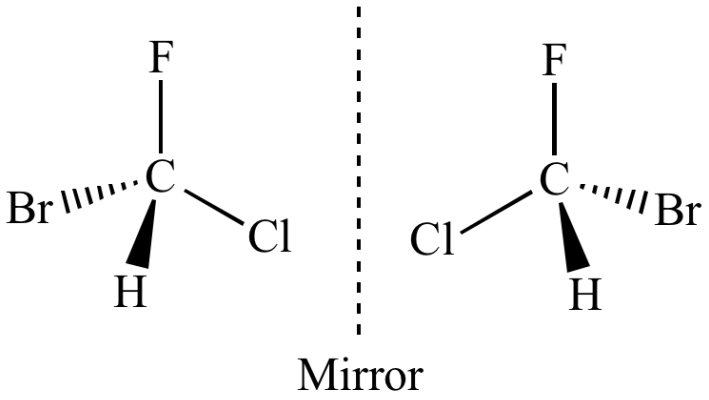

Fig. 2. 4. Mirror structures of chiral (R)-bromochlorofluoromethane and (S)-bromochlorofluoromethane.

There are lots of applications based on chiroptical features. Both CD and CPL features have already been essential parts of the biomedical area for drug development, quality control, and efficient delivery. Further, chiral materials can be used in optoelectronic applications. Strong CD signals of chiral materials are ideal for circularly polarized photodetector applications (*13*, *14*), while large CPL signals in chiral materials can be employed in bright, circularly polarized light-emitting diodes (*7*, *15*). Detailed CD and CPL calculations and measurements will be discussed further in Sections 3.3.2 and 3.4.2.

2.2.2 Spin in semiconductors

Electrons (holes) have an intrinsic angular momentum known as spin, which can be oriented in various directions. In semiconductors, electron spin can be either "up" or "down", which can be utilized for spintronic applications, such as information storage and processing. Compared to traditional charge-based technologies, semiconductor spintronic applications offer unique advantages. These include increased data processing speed and reduced power consumption due to efficient spin injections and manipulations. Effective spin injection is fundamental for any spintronic device because it generates spin-polarized currents or spin accumulations in the semiconductor. There are two main methods of spin injection. One is using ferromagnetic materials as spin injection layers, which introduce spin-polarized carriers into a non-magnetic semiconductor. However, this approach may require additional magnetic fields or cryogenic temperatures. Another way is optical spin injection by circularly polarized light, which excites electrons to create spin-polarized carriers due to the selection rules in

optical transitions. The most common method for manipulating spins is applying external magnetic fields, which allow control over the alignment of spins. Besides, optical spin injection can occur on very short timescales, in the femtosecond to picosecond range, allowing for rapid modulation of spin states.

Spin-orbit coupling (SOC) plays a crucial role in determining the electronic properties of materials and is a fundamental part of many spintronic applications, from memory devices to quantum computing. SOC arises from the interaction between an electron spin and the effective magnetic field created by its motion around the nucleus. This interaction occurs due to the relativistic effect, where the electron, moving in the electric field of the nucleus, experiences a magnetic field. The Rashba effect, which occurs in systems with structural inversion asymmetry, is one of the most important phenomena based on strong SOC. In the presence of the Rashba effect, the electronic energy bands are split into two branches with opposite spin orientations (Fig. 2.5). This splitting can be visualized as follows:

$$E_{\pm}(k) = \frac{\hbar^2 k^2}{2m^*} \pm a_R|k| \tag{16}$$

where $E_{\pm}(k)$ represents the energy of the spin-split bands; m^* is the effective mass of the electron (hole); a_R is the Rashba effect constant; $|k|$ is the magnitude of the wavevector.

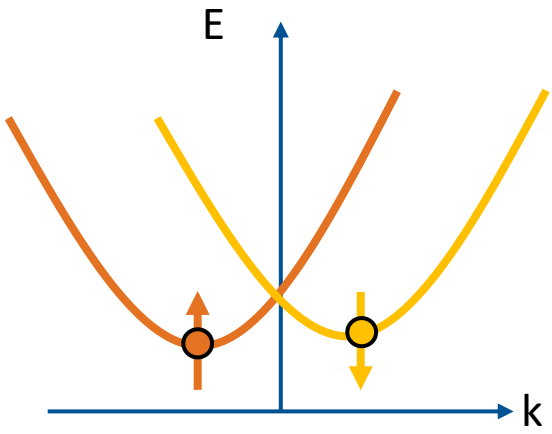

Fig. 2. 5. Splitting of the band structures due to Rashba effect.

2.3 Hybrid Organic-Inorganic Lead-Halide Perovskites

Hybrid organic-inorganic metal-halide materials are famous optoelectronic semiconductors, which have a general formula of ABX_3, where A represents small monovalent cations, such as cesium (Cs), Methylammonium (MA), or formamidinium (FA); B site is a divalent metal cation, e.g. lead (Pb) or tin (Sn); X site represents negative halide anion, like chloride (Cl), bromide (Br), or iodide (I) (Fig. 2.3).

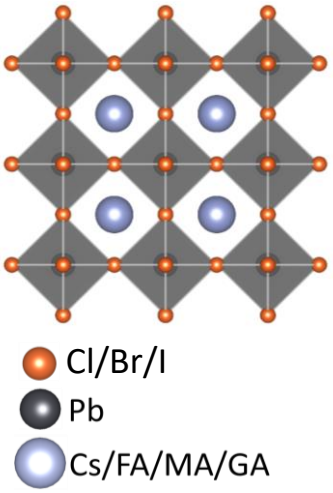

Fig. 2. 6. Schematic illustration of three-dimensional perovskite structures.

Perovskites with different dimensions

Perovskite materials have several promising features, such as high defect tolerance, easy fabrications, tuneable bandgaps, and long carrier diffusion lengths. All these features have made metal halide perovskite promising materials for many optoelectronic applications, such as solar cells, LEDs, lasers, photodetectors (*16–21*). Three-dimensional perovskite typically contains corner-sharing connected metal-halide BX_6 octahedra with A cation site sitting between them. The formation of perovskite structures follows the geometric tolerance factor (t) (*22*),

$$t = \frac{r_A + r_X}{\sqrt{2(r_B + r_X)}} \tag{17}$$

where r_A, r_B, and r_X represent the ionic radii of ions A, B, and X, respectively. The tolerance factor t should be 1 for an ideal cubic perovskite structure. The distortion of octahedra would result in the decrease of t to the value below 1, with decreased crystal symmetry.

Besides, metal halide perovskites can be engineered in different dimensionalities, ranging from three-dimensional (3D) bulk structures to lower-dimensional forms such as two-

dimensional (2D) layered structures, one-dimensional (1D) chain structures, and zero-dimensional (0D) molecular-like structures. The important factors in controlling the dimension of perovskite materials are the sizes and types of A-site cations, which may involve new functionalities inside perovskite structures, such as chiral perovskites. Each dimensional form exhibits unique properties and offers specific advantages for various applications in optoelectronics, photovoltaics, and light-emitting devices. For instance, 3D perovskites are famous for their good electric conductivity, potentially enabling efficient solar cells and LED materials (*23–26*). 2D perovskites offer much broader options for large A site cations, which can be used as good quantum well materials due to their layered structures (*27, 28*). By involving chiral organic molecules inside 1D perovskites, chirality transfer from organic molecules would cause a highly distorted helical chain octahedron, which shows strong circular dichroism signals and could be used as good circularly polarized photodetectors (*16*). 0D perovskites usually exhibit bright white light emission due to the formation of self-trapped excitons, which makes them good alternative materials for white light LEDs (*29*).

Chapter 3: Materials and Methods

3.1 Materials Fabrication

3.1.1 Materials

All the materials were used directly without further purification. Methylammonium bromide (MABr), formamidinium bromide (FABr), and guanidinium bromide (GABr) were purchased from Greatcell Solar Materials. Caesium bromide (CsBr), Chiral (R), (S), racemic-1-(3-Bromphenyl)-ethylamine (3BrMBA), chlorobenzene (CB), (R)/(S)/(Rac)-1-cyclohexylethylamine (CHEA), bismuth Oxide (Bi_2O_3), hydrobromic acid (HBr), hydroiodic acid (HI), (R)-(+)-α-ethylbenzylamine, (S)-(-)-α-ethylbenzylamine ((R/S)-EA), lead oxide (PbO), N,N-dimethylformamide (DMF), and dimethyl sulfoxide (DMSO) were ordered from Sigma-Adrich. 2,2',2''-(1,3,5-Benzenetriyl)-tris(1-phenyl-1H-benzimidazole) (TPBi) and lead bromide ($PbBr_2$) were purchased from TCI.

3.1.2 Single Crystals Growth

Preparation of (R)/(S)-$CHEA_4Bi_2Br_xI_{10-x}$ crystals

The single crystal chiral lead-free perovskite derivatives were grown using a hydrothermal approach. In a typical synthesis process, Bi_2O_3 (0.25 mmol) and excess (R)/(S)-CHEA (2.0 mmol) precursors were successively dissolved in an HBr/HI mixture (6 mL). The *x* value in color-tunable (R)/(S)-$CHEA_4Bi_2Br_xI_{10-x}$ (x = 0 to 10) was determined by the ratios between HBr and HI. After continuously stirring at 120 °C for ~30 min, the mixture was transferred into a 20 mL autoclave and reacted at 120 °C for 12 h. Finally, large single crystals emerged after slowly cooling down (1 °C/h) the reaction solution to room temperature, while powder samples were formed after natural cooling to room temperature. All as-synthesized samples were cleaned and then stored in a glovebox for further usage.

Fabrication of chiral 1D perovskite single crystals

The chiral 1D perovskite single crystals were also prepared by a hydrothermal synthesis. For a general process, 200 mg PbO and 200 μL (R/S)-EA were separately dissolved in 6 mL HI solutions at 95 °C. The resulting solutions were transferred to 25 mL autoclaves and kept at the same temperature (95 °C) inside the oven for 24 h. After slowly decreasing the temperature to room temperature at a rate of 1 ℃/h, large needle-shaped single crystals appeared at the bottom of autoclaves. Diethyl ether was used to clean the obtained crystals

three times, which were then dried under vacuum conditions. The crystals were stored inside a N_2-filled glovebox before usage.

Synthesis of 2D (R/S/Racemic)-3BrMBA$_2$PbI$_4$ single crystals

Chemicals, such as PbI_2, HI, DMF, Racemic, and (S)-3BrMBA, were purchased from Sigma-Aldrich, and (R)-3BrMBA was ordered from Alfa Aesar. All chemicals were used without further purification. As a general synthesis procedure of 2D perovskite single crystals, 0.231 g PbI_2 and 151 µL (R), (S), or racemic-3BrMBA were separately dissolved in 6 mL HI by heating at 90 °C for 30 min. After adding 1 mL H_2O into the solution, the mixture was further transferred into a 25 mL autoclave and allowed to react at 95 °C for 24 h. On cooling the solution slowly to room temperature with a cooling rate of 0.5 °C/h, orange plate-like single crystals formed gradually. In contrast, a relatively fast cooling rate resulted in needle-like single crystals or powder samples.

3.1.3 Thin Films Fabrication

Fabrication of chiral perovskite thin films using as-prepared single-crystal samples

The perovskite thin-film fabrication was performed in a nitrogen-filled glovebox using glass coverslips that had been previously treated with oxygen plasma for 5 min as substrates. For transferring the as-prepared single crystal to perovskite thin films. First, we dissolve 200 mg of as-synthesized perovskite crystals or powders in 1 mL DMF to prepare precursor solutions. After that, the precursor solution was spin-coated on the glass substrates with a rotation speed of 4000 rpm for 35 s, after which they were annealed at 90 °C for 10 min. The obtained perovskite thin films were stored inside the glovebox for further characterization.

Fabrication of chiral perovskite heterostructure thin films

All the fabrication process was performed inside a N_2-filled glovebox. The stock solution was prepared by mixing MABr (27.2 mg), GABr (67.2 mg), CsBr (78.8 mg), FABr (212.0 mg), and $PbBr_2$ (881.0 mg) in 3 mL DMSO. After fully dissolving the whole solution at 80 °C, different amounts of chiral 3BrMBABr additives (from 1% to 50% relative to $PbBr_2$ molar concentration) were added into the above stock solutions. Chiral perovskite films were prepared by spin-coating the final precursor solutions on glass substrates (4000 rpm, 35 s). 150 µL CB (or 0.1wt% TPBi-dissolved CB) was dropped onto the substrate 10 s before the end of spin coating. After that, the prepared thin films were stored inside the glovebox with a

room-temperature casting process for one hour.

3.1.4 Device Fabrication

Fabrication and characterization of CPeLED

The commercial ITO (135 nm) was first ultrasonically cleaned with detergent, acetone, and isopropanol in turn for 10 min. Then, NiO (5 nm) was sputtered reactively using a Kurt J. Lesker PVD-75 thin-film deposition system. Followed by 3 min O_2 plasma treatment, PEDOT:PSS (Al4083, 1/1, v/v, diluted with deionized water) was spin-coated at 4000 rpm for 20 s (ramp rate 800 rpm s^{-1}), and annealed at 150 ^oC for 15 min in air. After cooling down to room temperature, the substrates were transferred into a N_2-filled glovebox to deposit perovskite layers as mentioned above. Afterward, PMMA (2mg ml^{-1} in CB) was dynamically spin-coated onto perovskite layers at 4000 rpm. Finally, TPBi (40 nm), LiF (1 nm), and Al (100 nm) were sequentially evaporated under the vacuum of 1.0×10^{-6} mbar. The active area (3.5 mm × 3 mm) of the LED was defined by the overlapping area of ITO and Al contacts.

The electroluminescence characteristics of the LED were measured inside a N_2 filled glovebox. A Keithley SMU 2400 was used to drive the LED, and the forward emission was collected by an integrating sphere coupled into an Instrument Systems CAS140 spectrometer with an optical fiber. Luminance was determined by assuming a Lambertian emission profile.

3.2 X-Ray Diffraction (XRD) Measurements

X-ray diffraction pattern measurement is an important technique to determine the crystal structure of materials, providing information on the distribution of atoms within crystals. When the X-ray was introduced on well-crystallized materials that have periodical arrangements of their atoms, the scattered X-rays with certain wavelengths would interact with each other either constructively or destructively. The constructive interference happens following the Bragg equation

$$n\lambda = 2dsin\theta \tag{18}$$

where n is an integer (1, 2, 3, …); λ represents X-ray wavelength; θ is X-ray incident angle; d represents lattice distance. Thus, the suitable incident X-ray directions and the arrangements of the crystal structure are important factors in getting stronger X-ray diffraction intensities. Besides, by detailed analysis of the relationship between incident angle of X-ray and X-ray

intensities, we can derive the lattice distances between each crystal plane, which can help us understand the crystal structure of materials.

3.2.1 Single Crystals XRD

Single crystal XRD (SCXRD) measurements fully resolve the crystal structure of measured materials and determine the distribution of each atom. The measured samples have to be well-crystallized single crystals with clear crystal directions rather than polycrystalline samples, e.g., powders or thin films. The SCXRD data for as-synthesized chiral perovskite single crystals were measured at 100 K on a Bruker D8 Venture Duo IMS system equipped with a Helios optic monochromator and a Mo IMS microsource (λ= 0.71073 Å). Detailed information regarding data collection and structure refinement can be found in Table B1, B3, B5 and their corresponding cif documents.

3.2.2 Thin Films and Powders XRD

For thin film and powder samples, their XRD patterns were collected by an X-ray diffractometer (Rigaku SmartLab) with Cu Kα irradiation. The resulting patterns were further compared with simulated results from SCXRD to confirm the formation of correct crystal structures.

3.2.3 In-situ XRD

In-situ XRD measurements were performed at beamline 12.3.2 at the Advanced Light Source at Lawrence Berkeley National Laboratory utilizing a customized spin-coating setup. For this, the sample was placed at an angle of 1° in the X-ray beam, and the signal was recorded utilizing a DECTRIS Pilatus 1 M X-ray detector placed at 35° relative to the sample. Images were recorded with an exposure time of 1s. The sample chamber was constantly purged with nitrogen to avoid oxidation effects during the measurement. The experiments were conducted at a beam energy of 10 keV and a wavelength of 1.2398 Å. However, to allow for easy comparison with steady-state XRD data, the reflexes displayed in this work were re-calculated to match the wavelength of Cu Kα radiation.

3.2.4 Grazing Incident Wide Angle X-Ray Scattering (GIWAXS)

The GIWAXS measurement was performed at Beamline PO3 at Deutsches Elektronen-

Synchrotron (DESY, Hamburg) under an incidence angle of 0.4° with an X-ray beam energy of 11.87 keV. The data was recorded with an exposure time of 1 s on a Lambda 9M detector (X-Spectrum). The reshaped GIWAXS, index, and line cuts of scattering data were done with the Python tool INSIGHT (*30*).

3.3 Absorption Spectroscopy

3.3.1 UV-vis Absorption Spectroscopy

The absorption spectroscopy is a general characterization tool, which is widely used in the material science area to detect the absorption of radiation interacting with materials. When light passes through a medium, due to the interaction of electromagnetic radiation with matter, the atoms or molecules inside the medium absorb the radiation energy to reach a higher-energy state. Depending on the types of atoms, molecules, or materials, they would absorb the different radiations with certain wavelengths.

In the current work, the absorption and CD spectroscopy data were collected by CD spectrometers JASCO J-815 and JASCO J-1700.

3.3.2 Circular Dichroism Spectroscopy

Circular Dichroism (CD) spectroscopy is an important measurement for analysing the chirality in chiral materials. Chiral materials usually can differentially absorb left-handed and right-handed light. Due to the unique chiral asymmetry structures, chiral materials would exhibit circular birefringence or optical rotations. Left-handed and right-handed light would have different propagation speeds across the chiral materials, which results in different amounts of absorption.

The difference between left-handed ($\sigma-$) and right-handed ($\sigma+$) absorbance (ΔA) can be expressed by,

$$\Delta A = A_{\sigma-} - A_{\sigma+} \tag{19}$$

which can be also defined as the Beer–Lambert law,

$$\Delta A = (\varepsilon_{\sigma-} - \varepsilon_{\sigma+})bC \tag{20}$$

where ε is the absorption coefficient, b is the optical path length, and C represents the sample molar concentration.

The signals of the CD spectrum are usually indicated in degrees of ellipticity (θ), which relates to unequal contributions of left-handed and right-handed light. The ellipticity of light polarization can be defined as following,

$$\tan\theta = \frac{E_{\sigma+} - E_{\sigma-}}{E_{\sigma+} + E_{\sigma-}} \tag{21}$$

Here $E_{\sigma+}$ and $E_{\sigma-}$ represent the magnitude of right-handed and left-handed electric field vectors, respectively. By several equations transfer, ellipticity (θ) can be related to ΔA as,

$$\theta = \left(\frac{ln10}{4}\right)\left(\frac{180}{\pi}\right)\Delta A = 32.98\Delta A \tag{22}$$

To avoid the influence of sample concentration and optical path length, the CD anisotropy factor (g_{abs}) can be calculated using the following equations,

$$g_{abs} = \frac{2\times(A_{\sigma-} - A_{\sigma+})}{A_{\sigma-} + A_{\sigma+}} \tag{23}$$

Importantly, during CD measurements, we find that strong linear dichroism (LD) and linear birefringence (LB) may also contribute to the CD signals for thin film samples. The detailed analysis of CD signals is based on the Muller Matrix model. According to previously reported work (*31*), the measured CD signals can be expressed by the following equation,

$$CD_{total} \approx CD_{intrinsic} + 0.5(LD' \cdot LB - LD \cdot LB') + (LD'\sin2\theta - LD\cos2\theta)\sin\alpha + \left(P_x^2 - P_y^2\right)\sin2a(LB'\sin2\theta - LB\cos2\theta) \tag{24}$$

where the first term of the equation represents the intrinsic CD signals; the second term indicates the contribution from LDLB, which would flip their sign by sample flipping during measurements; the third term and fourth term are highly related to instrument artifacts, e.g., photoelastic modulator (PEM). Rotating the sample would reveal such artifacts.

It is important to get intrinsic CD signals, which describe the chiroptical features of chiral materials, independent of measurement artifacts. Thus, we always flip and rotate thin film samples during CD measurements to avoid additional contributions.

3.3.3 Transient Absorption (TA) Measurements

Transient absorption spectroscopy is a pump-probe technique to detect the photo-excited states of materials and their recombination kinetics. For the general TA measurement process (Fig. 3.1), a single-color high energy laser would be used as a pump beam to excite the

samples, while a broad-band white light can be used as a probe beam to detect the TA signals $\frac{\Delta T}{T} = \frac{T_{pumped} - T_{unpumped}}{T_{unpumped}}$, where T_{pumped} and $T_{unpumped}$ represent the transmission signals after and before pump happens.

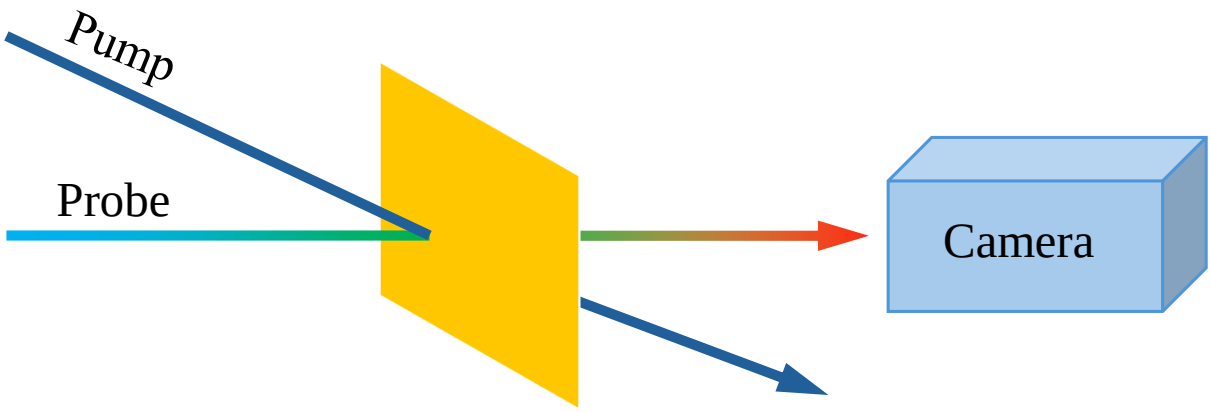

Fig. 3. 1. Schematic illustration of transient absorption spectroscopy.

For short-term TA and circularly polarized TA measurements (below 2 ns), a home-built TA setup was used. A Yb:YAG laser system (LightConversion Pharos) with an external harmonic generator (Light Conversion Hiro) produces both pump (515 nm, 5 KHz) and probe (white light continuum) lasers. The pump beam further went through a delay stage (Newport DLS325), and a chopper to block alternating pump pulses. The pump and probe were then overlapped on the sample films. The transmitted probe beam was recorded by a spectrometer (Andor Kymera 193i) with an sCMOS camera (Andor Zyla 5.5). Linear polarizer and quarter waveplate were further placed in front of the samples to control the polarization of the probe beam for circularly polarized TA measurements. Long-term TA measurements were performed by a commercial TA setup (Ultrafast Systems, HELIOS, and EOS).

In the current work, we additionally study the spatio-temporal carrier dynamics in the chiral perovskite by Ultrafast Holographic Transient microscopy (UHT) in a wide-field configuration (*32*, *33*). Our technique gives us access to the dynamic carrier population promoted by diffusion mechanisms within different domains. This is realized with multiplexed off-axis holography, which allows for recording the pumped (photoexcited) T_{pumped} and unpumed $T_{unpumped}$ optical transmission signal through the studied material in a single camera exposure, enabling a balanced detection scheme with a significantly reduced

signal-to-noise ratio (~0.1%). Thus, the spatial distribution of the transient absorption signal $\frac{\Delta T}{T} = \frac{T_{pumped} - T_{unpumped}}{T_{unpumped}}$ can also be recorded with long exposures of the camera, without typical read-out limitations in the signal repetition rate due to the camera frame rate. The 400 nm pump is generated via second harmonic generation (SHG) of 35 fs-laser pulses centred at 800 nm with 1 kHz repetition rate (Astrella, Coherent). The probe source is a home-built NOPA (Noncollinear Optical Parametric Amplifier) set at 530 nm. The probe beam transmitted through the sample is collected by an objective lens (Zeiss Neofluar, x40, $NA = 0.75$, glass correction 0.17 mm) and contains all the information for the sample image. A 10% fraction of the probe light is used as a reference in order to create the holographic pattern (interference with the probe image) on the camera (Basler a2A2448-75umPRO). The creation of interference between the reference and the signal allows us to access both the amplitude and the phase changes of the probe electric field induced by the material under analysis. A full image reconstruction is hence possible. Due to the off-axis geometry, the reference beams will interfere with the signal under different angles of incidence. Thus, the two interference terms are located in two different positions in k-space. With a spatial fast Fourier transform, we retrieve both the pumped and unpumped images from one single raw image. In the current setting, the sample is pumped from the back. This geometry allows us to control the pump and the probe spot size, separately.

3.4 Photoluminescence (PL) Spectroscopy

3.4.1 Room-Temperature and Time-Resolved PL Spectroscopy

When the materials absorb light, the energy state of the materials can jump from the ground state to a higher-energy excited state, which is an unstable state, and prefer to release their energy to go back to the ground state. When the photons are released during such a recombination process, the materials will exhibit radiative light emissions, which is noted as photoluminescence (PL). PL spectroscopy is used to detect such photogenerated emission, which is an important factor in evaluating the performance of optical materials. When the photo-excited carriers gradually decay back to the ground state, time-resolved PL spectroscopy is used to determine the decay rate of such radiative decay channel and calculate the PL lifetime of corresponding materials.

In the current work, PL and time-resolved PL measurements were performed using a Yb:YAG laser system (Light Conversion). A part of the fundamental output was seeded into PHAROS (Light conversion) to generate 405 nm pulsed excitation. The generated emission signals were collected by an ICCD camera (Andor iStar). For the temperature-dependent PL measurements, the sample was placed inside a temperature cryostation (Montana Instrument) and a 50x long working distance objective (Mitutoyo) was used to focus the excitation beam and collect PL signals.

3.4.2 Circularly Polarized PL Spectroscopy

Circularly polarized PL (CPL) spectroscopy measurement is an important technique for evaluating the chiroptical features in chiral materials. The easiest way to measure the CPL is by rotating a quarter waveplate, which can separate circularly polarized left-handed and right-handed emissions from linear polarized emissions. With a 45-degree linear polarizer, we can then collect the PL intensity difference from left-handed and right-handed emission contributions. However, CPL is a very sensitive measurement. It is difficult to get reliable CPL results due to many factors, e.g., sample degradation, laser stability, and instrument artifacts contributions.

To get more reliable CPL results, in our current work, we explored two additional CPL measurement configurations. The first one uses a Wollaston prism, which can help us measure left-handed and right-handed emissions at the same time. In detail, we use the same 405 nm linear excitation mentioned above to excite the samples. Then, the generated emission was collected by a 50x long working distance objective (Mitutoyo) and passed through a quarter waveplate to transfer the CPL signals to linearly polarized signals. After that, a Wollaston prism followed by a 45-degree linear polarizer was used to separate the right- and left-handed circularly polarized PL. Both right-handed and left-handed PL polarizations were collected from two regions of interest on the ICCD camera at the same time to get rid of the influence of sample degradation or excitations.

Another configuration uses PEM, which can modulate the right-handed and left-handed emission with a certain frequency. After photo-exciting or electro-exciting the samples, the generated luminescence was passed through a PEM (Hinds Instruments PEM-200) with a frequency of 84 KHz. A linear polarizer set to 45 degrees was placed after the PEM with

respect to the fast axis of the PEM to cut periodically the one-handedness of the light. Subsequently, a chopper running at 980 Hz was placed to provide modulation for detecting the total emission. Then, a monochromator (Princeton Instruments Acton SP2300) and APD detector (Laser Components) were used to collect the resulting signals. Two lock-in amplifiers (Stanford Research Systems SR830) were connected to PEM and a chopper to measure the circularly polarized luminescence and the total luminescence at the same time.

Chapter 4: Excitation Populations with Microsecond Chirality Memory in the Color Tunable Chiral Lead-Free Semiconductor (R)/(S)-$CHEA_4Bi_2Br_xI_{10-x}$ (x = 0 - 10)

In this chapter, we introduce chiral organic molecules (R)/(S)/(Rac)-cyclohexathylethylamine (CHEA) into bismuth halide structures and successfully synthesize the chiral bismuth-based perovskites (R)/(S)-$CHEA_4Bi_2Br_xI_{10-x}$ (x = 0 - 10) as single crystals, powders, and solution-processed films. We use SCXRD to determine the crystal structure. And we find both chiral bismuth iodide and bromide samples crystallize in a monoclinic P 1 2_1 1 space group, which belongs to Sohncke space groups (*11*), and possess a highly distorted chiral crystal structure. DFT calculations on chiral bismuth-based crystals confirm that chiral lead-free perovskites synthesized in this work show little dispersion in both valence and conduction band edges due to their zero-dimension structure with separated octahedral dimers. More importantly, the difference in the chirality of (R)- and (S)-$CHEA_4Bi_2Br_{10}$ compound induces opposite spin textures at the band edge position, which gives them strong chiroptical properties. We then investigate their optical properties and find circular-dichroism (CD) signals in the optical absorption, which can be tuned over a wider wavelength range from 300 nm to 500 nm by changing the ratios of bromide and iodide anions. Finally, we use transient absorption (TA) and time-resolved PL spectra to investigate charge-carrier dynamics on chiral bismuth-based perovskite samples, which show long-lived microsecond optically induced chirality.

The work in this chapter is based on a recent publication (6). Reprinted and adapted with permission from {*Shangpu Liu, et al.* Optically Induced Long-Lived Chirality Memory in the Color-Tunable Chiral Lead-Free Semiconductor (*R*)/(*S*)-$CHEA_4Bi_2Br_xI_{10-x}$ (*x* = 0–10). *J. Am. Chem. Soc.* ***144****, 14079–14089 (2022)*}. Copyright {2022} American Chemical Society.

4.1 Background

HMHPs are famous for their promising optoelectronic properties, such as high charge-carrier mobility, long carrier lifetime, color-tunable bandgap, and superior photoluminescence quantum efficiency (PLQE) (*34–36*). All these properties render HMHPs as a good platform for next-generation optoelectronic applications moving from basic research to industrial applications. HMHPs also possess attractive properties for spintronics, e.g. large spin-orbit coupling, large Rashba splitting, and strong magneto-optical effects. Although the optoelectronic properties of perovskite material are comparable to traditional spintronic materials, such as GaAs, the spin relaxation time of most perovskite materials is far shorter, only reaching a few picosecond ranges at room temperature (*37–41*). Thus, our main interest is fabricating novel perovskite materials with longer spin lifetimes for future real spintronic devices and applications.

Recently, it has been reported that the chirality of organic molecules can be introduced into perovskites to get chiral perovskite materials, which usually exhibit strong CPL or high CD signals. Embedding chiral organic molecules into the perovskite crystal structure results in the distortion of the octahedral arrangement of atoms. According to the Rashba effect (*37*, *42–44*), the highly asymmetric perovskite structure would further cause spin-polarized band edges, which would, in turn, show interesting chiroptical features. Furthermore, the chiral-induced spin selectivity effect has enabled the chiral materials' intrinsic spin injection by selectively spin filtering, which is totally different from other traditional spintronic materials and would thus result in more intriguing spintronic devices with novel functionalities, such as organic spin-valve devices, spin-LEDs, and CPL detectors (*13*, *45–48*).

As follows from prior works, chiral 2D lead-halide perovskite single crystals usually show strong circularly polarized photoluminescence (*7*), while strong circular dichroism was observed in chiral 1D lead halide perovskites (*14*). There are fewer reports investigating chiral lead-free perovskites. However, lead-free perovskites usually show much longer carrier lifetime (*49–52*), compared to lead halide perovskite. Thus, the chiral lead-free perovskites would likely be a good starting point for long spin polarization lifetime material due to the combination of the advantages of both chirality and lead-free perovskites.

4.2 Result and Discussion

4.2.1 Single crystal structure of chiral lead-free perovskites

We use hydrothermal synthesis approaches to grow chiral lead-free perovskite single crystal (see details in the Method section). After slowly cooling down the reaction solutions, which contain chiral organic molecules and bismuth halide precursors, to room temperature, we obtain large perovskite single crystals with different colors (Fig. 4.1).

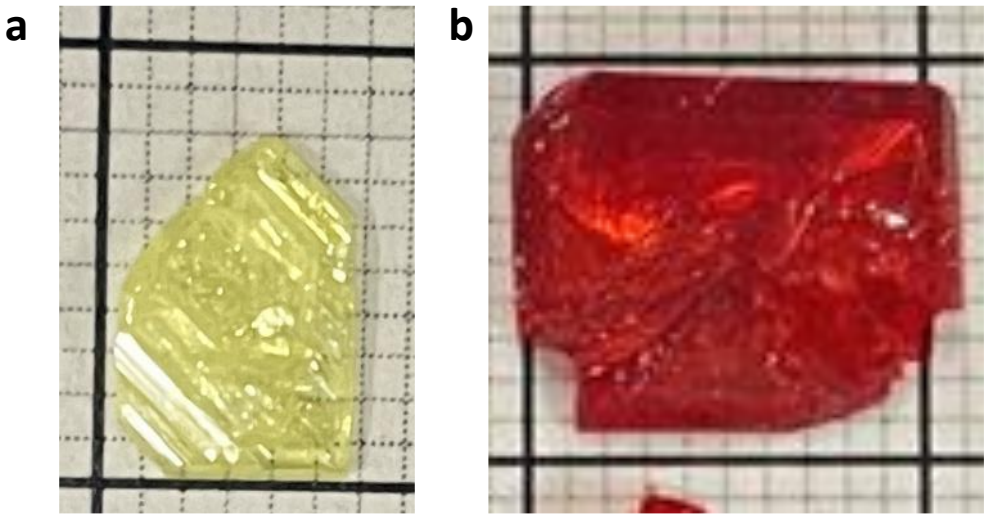

Fig. 4. 1. Pictures of (R)-CHEA$_4$Bi$_2$Br$_{10}$ (a) and (R)-CHEA$_4$Bi$_2$I$_{10}$ (b) single crystals on millimeter paper. The size of crystals strongly depends on the cooling rates and reaction solution concentrations.

We then use single crystals x-ray diffraction (SCXRD) measurements to identify the crystal structure of as-obtained crystal samples. The measurements were performed at 100 K. Detailed measurement conditions, and crystal data are shown in Table B1. As expected, chiral (R)- and (S)-CHEA$_4$Bi$_2$Br$_{10}$ crystals show the same crystal structure except for opposite chirality. As shown in Fig. 4.2, both (R)-CHEA$_4$Bi$_2$Br$_{10}$ and (R)-CHEA$_4$Bi$_2$I$_{10}$ single crystals crystallize in a monoclinic P 1 2_1 1 space group, which is one of Sohncke space groups (*11*). We consider this as direct evidence for the successful chirality transfer from chiral organic groups to bismuth halide structures, resulting in a chiral crystal structure. Our bismuth-based samples show a zero-dimension (0D) molecular-like structure, which consists of edge-sharing bismuth-halide dimers, which are surrounded by isolated chiral organic molecules.

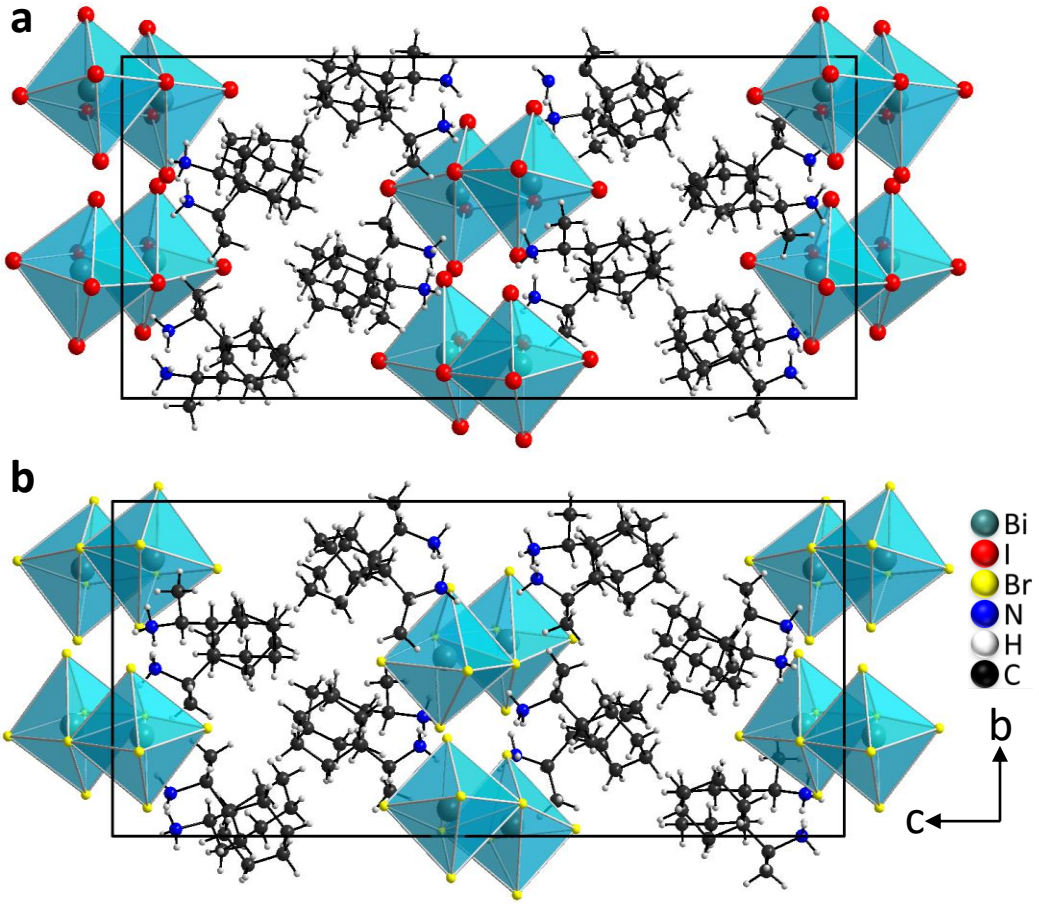

Fig. 4. 2. Single-crystal structure characterization of chiral lead-free bismuth-based perovskite derivatives. a, b, Single-crystal X-ray structure of (R)-$CHEA_4Bi_2I_{10}$ (a) and (R)-$CHEA_4Bi_2Br_{10}$ enantiomers (b). Both of them acquire a similar chiral structure, which belongs to the chiral monoclinic P 1 2_1 1 space group.

The chirality transfer is further observed on the distortion of bismuth halide octahedra. From SCXRD structures, we find that for iodide structures, the Bi-I distances vary between ~2.9 and ~3.3 Å, and for bromide structures, the Bi-Br distances (from ~2.7 to ~3.1 Å) are a little bit shorter than Bi-I bonds, due to the smaller Br atom size (Fig. A1). Besides, the bond length distortion index and bond angle variance are two important factors in determining perovskite octahedra distortion (*53*). For an ideal octahedron with full symmetry, both values should be 0. However, in our chiral bismuth halide samples, bromide and iodide samples show large distortion degrees (Table B2) in both bond angles and lengths. (R)-$CHEA_4Bi_2Br_{10}$ and (R)-$CHEA_4Bi_2I_{10}$ crystals show almost twice larger bond length distortion index values (0.034-0.044) than the corresponding values observed in other low-dimensional non-chiral

perovskites (*54*), indicating broken symmetry of octahedra structure due to chirality transfer. It is important to note that, both crystals also exhibit the largest bond angle variance of 15.84 (iodide) and 25.05 (bromide) degrees, which are comparable in their values to other chiral lead-halide perovskites (*55*).

In order to fabricate high-quality chiral perovskite films, we simply dissolve chiral perovskite single crystal samples inside N,N′-dimethylformamide (DMF) to get chiral perovskite precursor solutions. After spin-coating the resulting solution and a follow-up annealing process (100 °C, 10 min), we obtain smooth and high-quality perovskite thin films with a thickness of around 100 nm. XRD measurements confirm that as-prepared thin films show a similar crystal structure as their single crystals, while with a preferred (002) plane (Fig. 4.3).

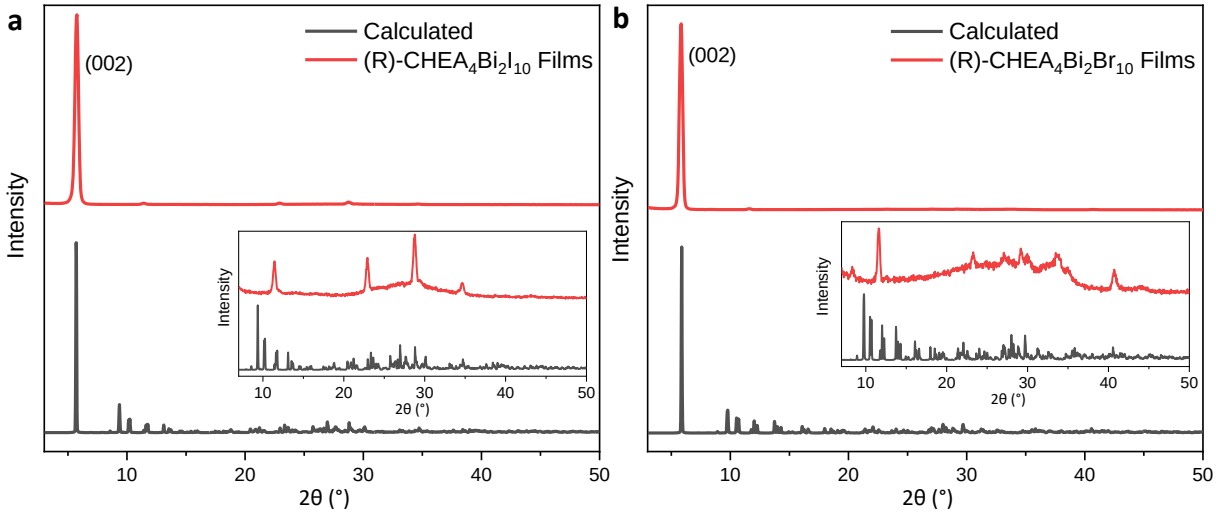

Fig. 4. 3. Powder X-ray diffraction pattern of (R)-$CHEA_4Bi_2I_{10}$ (a) and (R)-$CHEA_4Bi_2Br_{10}$ (b) spin-coating films (red line) and the patterns (black line) simulated from the single-crystal structures. The inset shows the same XRD patterns but in different regions. Evidently, the spin-coating films possess a structure that prefers growing along the (002) facet compared with that of single crystals.

To identify the structure variations in mixed-halide samples, we compared the XRD patterns between (R)- and (S)-$CHEA_4Bi_2Br_xI_{10-x}$ mixed-halide films (x = 10, 9.5, 9, 5, 3, and 0). As depicted in Fig. 4.4, consistent with SCXRD results, the diffraction patterns collected from all chiral (R) films show a good overlap with (S) samples, indicating the same crystal structures in different chirality samples. Importantly, when the bromide to iodide ratios decrease from 10 to 0, we observe obvious patterns shifting, especially at the (002) plane, to

lower 2Theta degree by ~0.12°, indicating the broadening of lattice due to the involvement of more large iodide atoms inside crystal structures. For the diffraction patterns at 2Theta degrees higher than 10°, there are some patterns (40-45°) that vanish when we increase iodide concentrations, while the diffraction intensities are much smaller than the signals at the (002) plane.

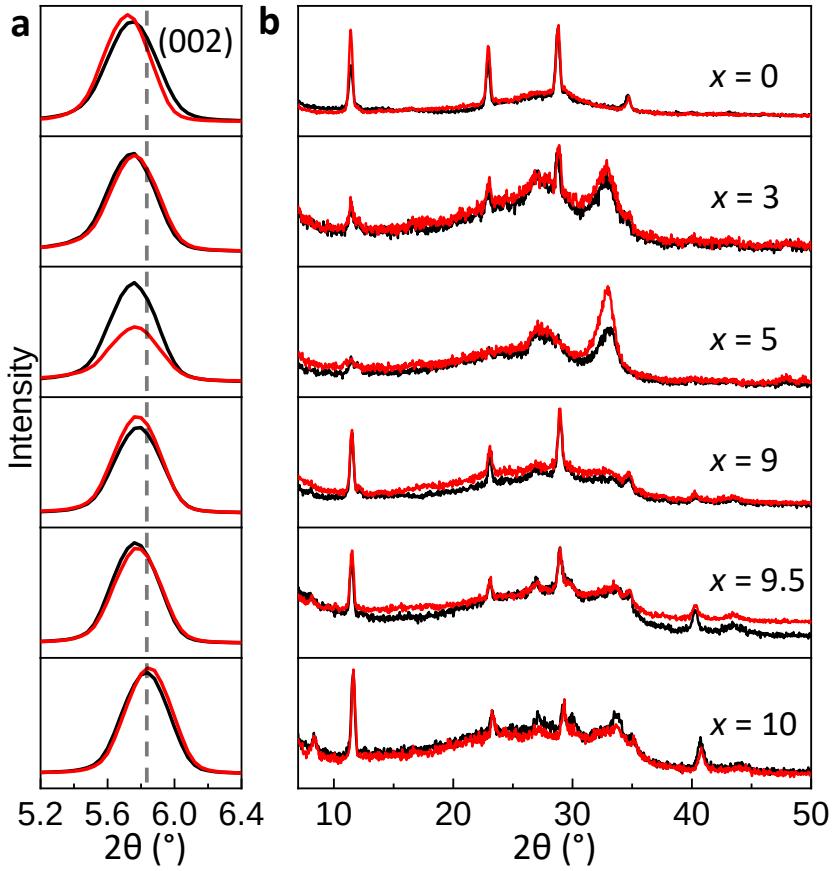

Fig. 4. 4. Powder X-ray diffraction pattern of R/S-CHEA$_4$Bi$_2$Br$_x$I$_{10-x}$ spin-coating films (x = 0 to 10). The characteristic XRD patterns are expanded in two diffraction regions, from 5.2 to 6.4° (a), and from 7 to 50° (b). With the increase of the x value, the down-field shifted diffraction peaks demonstrate larger iodide ions are successfully involved in the bismuth structure.

4.2.2 Chirality transfer in band structures

To further understand the influence of chirality transfer on material properties, we employed density-functional theory (DFT) calculations to study their band structures. Both (R)- and (S)-CHEA$_4$Bi$_2$Br$_{10}$ show a similar single crystal structure, and thus they should have the same band structures. As shown in Fig. 4.5, chiral (R)-CHEA$_4$Bi$_2$Br$_{10}$ samples show little

dispersion at both conduction band and valence band structures compared to other prototypical metal-halide perovskites (*56*). The conduction band is composed of Bi 6p and Br 4p orbitals, while the valence band is formed by Br 4p and Bi 6s orbitals. Besides, the (R)-$CHEA_4Bi_2Br_{10}$ samples show an indirect bandgap (2.49 eV) at two different regions in the Brillouin zone. However, due to the low degree of dispersion of current band structures, we find the direct gap (2.50 eV) features are almost similar to the indirect one, which suggests that our chiral bismuth halide sample is essentially a direct-gap material. In addition, like in other perovskite materials, there is no contribution from organic molecules in band edge structures (Fig. A2).

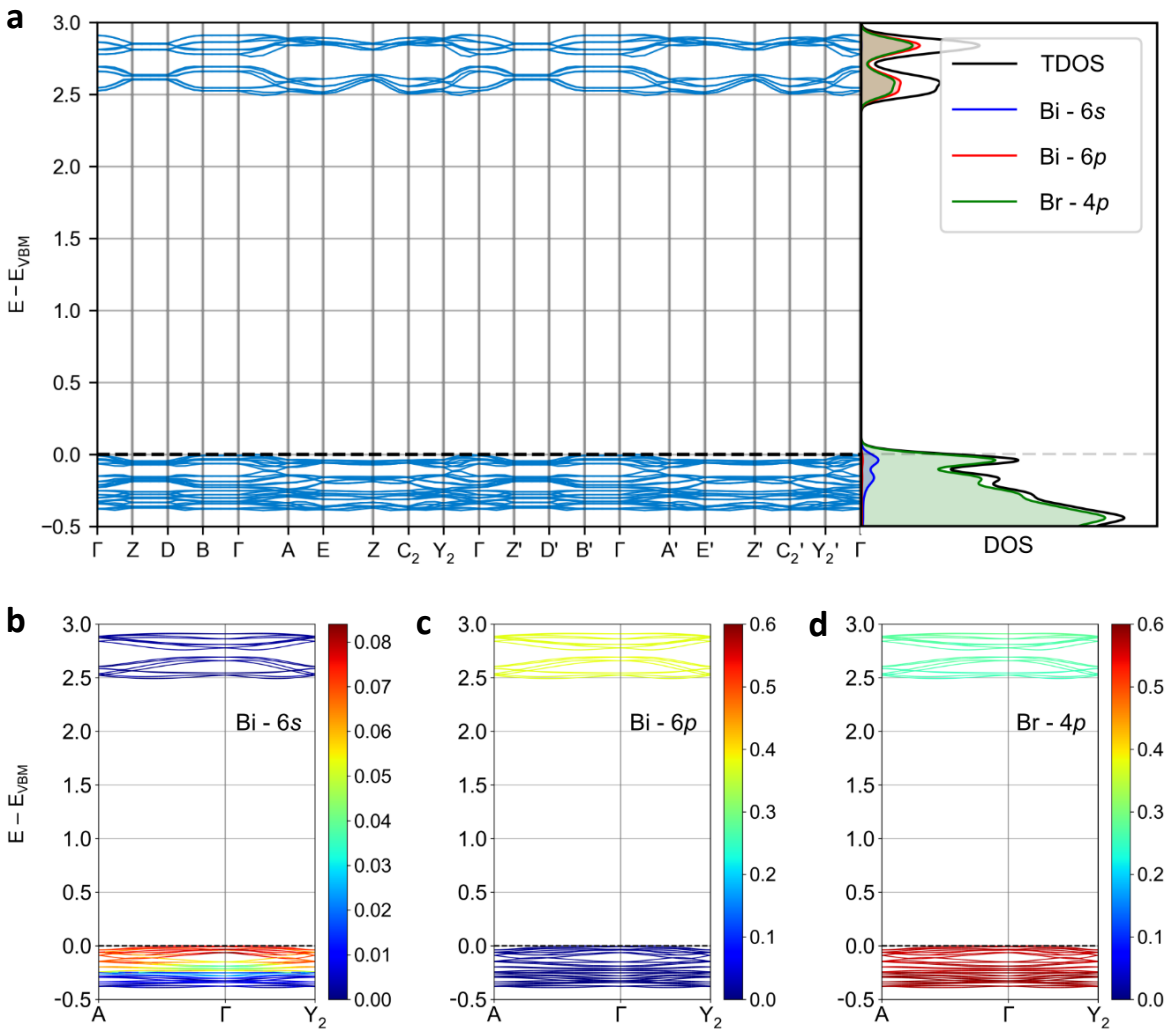

Fig. 4. 5. DFT calculation of the electronic structure of (R)-$CHEA_4Bi_2Br_{10}$ at the PBE+SOC level of theory. a, Band structure along the high-symmetry path of the first Brillouin zone of the chiral monoclinic P 1 2_1 1 space group (left panel). Total (TDOS) and projected density of states showing the Bi-6s and Br-4p contributions to the VBM, and the Bi-6p and Br-4p contributions to the CBM (right panel). **b-d**, The band structure projected on

the Bi-6s (b), Bi-6p (c) and Br-4p (d) orbitals is also shown. The color code signifies the projection of the Kohn-Sham wave functions onto spherical harmonics, and suggests that the VBM is formed mostly by Br-4p orbitals with a small contribution of Bi-6s (see the difference in the scale of the color bar), while the CBM is formed by Bi-6p and Br-4p orbitals. DFT calculations were performed by Dr. Sebastián Caicedo-Dávila and Prof. David Egger.

From the results above, we know the bandgap structure of chiral bismuth halide samples is predominantly determined by Bi 6p and Br 4p orbitals. Thus, by changing the halide composition, the band structure and optical properties of chiral bismuth halide samples would be tuned accordingly. Further, according to the Rashba effect, the high asymmetry material structure would cause spin-polarized band structures. In our chiral bismuth halide materials, SCXRD measurements confirmed the strong distortion in bismuth halide octahedra. Taking into account spin-orbital coupling, we find that clear spin polarization happens at the band edge positions (Fig. 4.6). In chiral bismuth-halide perovskite, the difference in the chirality of (R)- and (S)-compound induces opposite spin textures of band edges. Such polarized band structures should generate strong chiral optical features, such as CD or CPL signals.

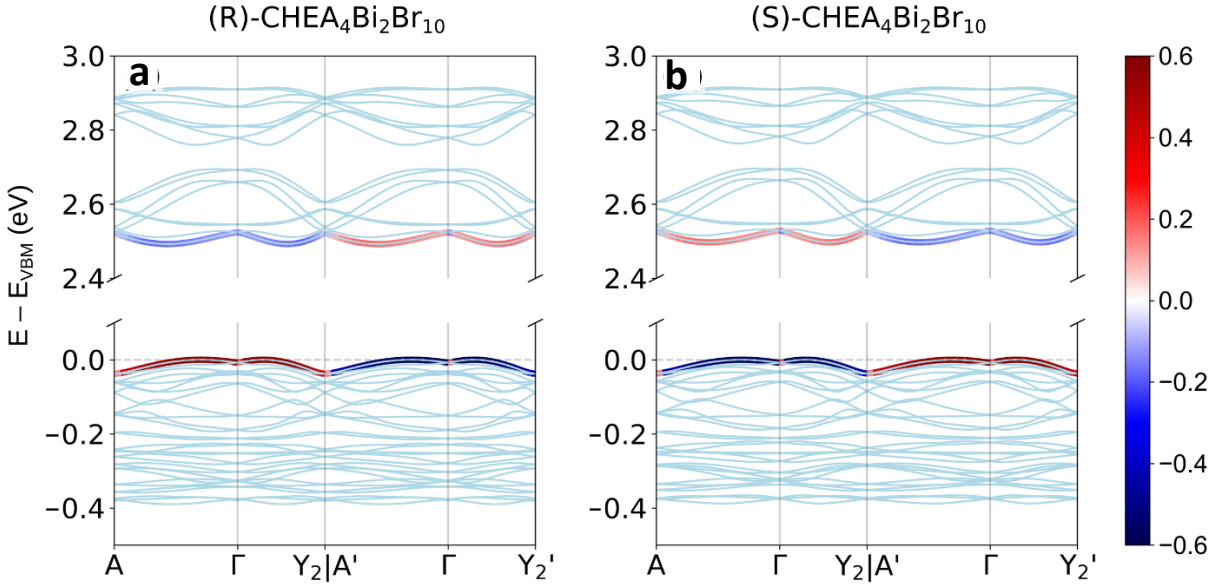

Fig. 4. 6. Band structures along the high-symmetry paths that include VBM and CBM for (a) (R)-$CHEA_4Bi_2Br_{10}$ and (b) (S)-$CHEA_4Bi_2Br_{10}$. The spin polarization, calculated as the spin expectation value or projected magnetization along the x-axis, S_x, is color-coded and plotted for the highest valence band and lowest conduction band. Note that the spin polarization is opposite for the different chiralities, and that it is dominated by the x and z components (see Fig. A3 for polarization along other axes). DFT calculations were performed by Dr. Sebastián Caicedo-Dávila and Prof. David Egger.

4.2.3 Color-tuneable circular dichroism in chiral (R/S)-$CHEA_4Bi_2Br_xI_{10-x}$ films

Due to the unique distorted crystal structures and spin-polarized band edges, we believe our chiral bismuth halide films would show interesting optical features. We first investigate the steady-state absorption spectra of mix-halide (R/S)-$CHEA_4Bi_2Br_xI_{10-x}$ (x = 0 to 10) films. Similar to the XRD results, chiral (R) and (S) samples show the same absorption signals (Fig. 4.7a). When we gradually increase the iodide concentrations, the absorption band located at ~380 nm (x = 10) continuously shifts to higher wavelengths up until ~495 nm (x = 0). We also find chiral bismuth halide samples show much weaker and broader PL intensities at room temperature compared to other lead-halide perovskites (*7*, *57*). Such broad PL features likely result from trapped excitons, which is further confirmed by temperature-dependent and fluence-dependent PL measurements (Fig. A4 and Fig. A5). Besides, combined with absorption results, the red-shifted PL signals of chiral bismuth halide samples with increased iodide concentration demonstrate that the change of bromide and iodide rations in chiral bismuth halides samples effectively tunes their bandgap positions, changing their optical properties.

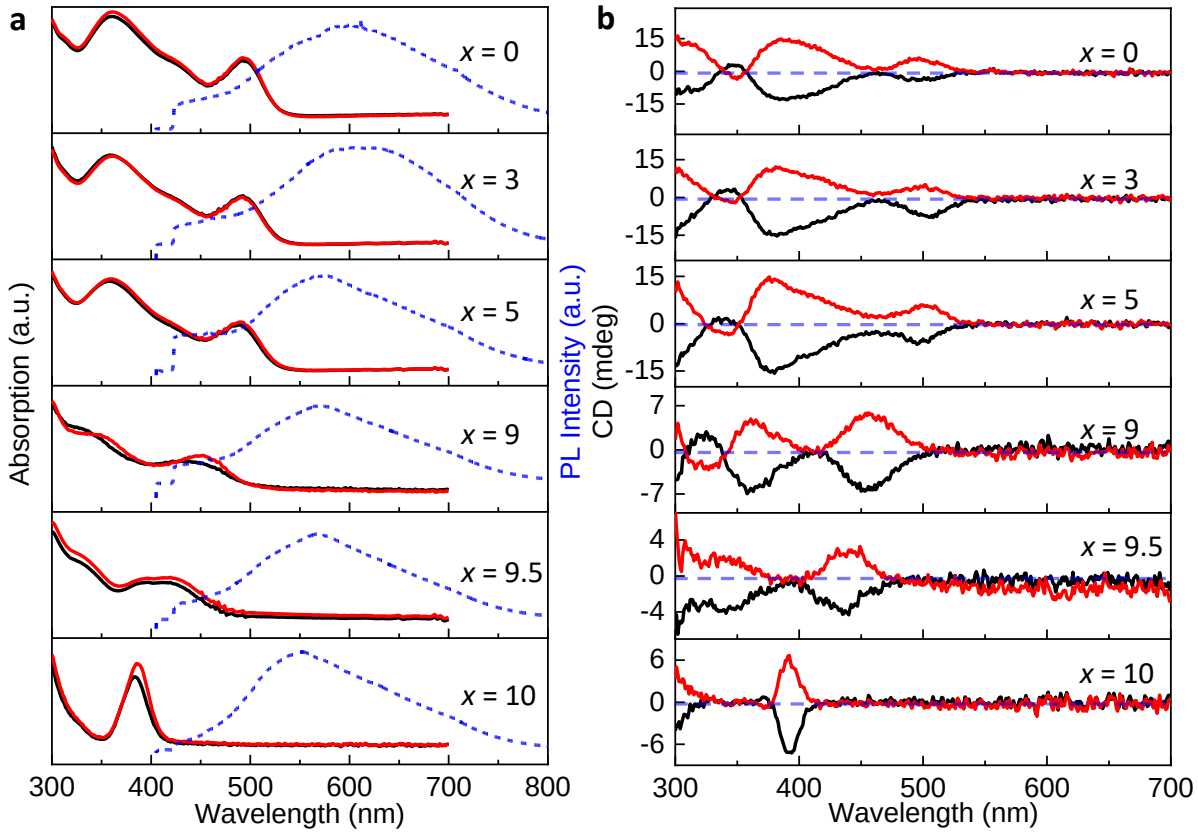

Fig. 4. 7. Optical properties of chiral lead-free bismuth halide films. a,b, Room-temperature absorption (solid lines), PL (blue dotted lines) (a) and CD spectra (b) of (R)/(S)-

$CHEA_4Bi_2Br_xI_{10-x}$ (x = 0 to 10) films. The black and red solid lines represent the results acquired from (R)- and (S)- spin-coating films, respectively. The blue dashed lines indicate PL results obtained from (R)- drop-casting films. Evidently, by changing the ratios between bromide and iodide, CD signals of (R)/(S)-$CHEA_4Bi_2Br_xI_{10-x}$ films shift simultaneously with absorption bands, but with smaller shifts of PL peaks.

Considering the existence of chiroptical features in our chiral samples, we further use CD spectroscopy to detect their CD signals. Notably, chiral (R) and (S) samples show obvious CD signals at the same band positions with opposite signals, while there is no CD signal in racemic samples (equal mixture of chiral (R) and (S) samples, Fig. 4.8). This is the direct evidence for the chirality transfer from chiral molecules to chiral bismuth halide structures. Also, with increasing iodide concentration, the CD signals undergo unambiguously redshifts to 500 nm (Fig. 4.7). The corresponding anisotropy-factor (g_{CD} value) plots of CD signal are shown in Fig. A6, which quantifies chirality without additional effects from film thickness or optical path length. We observe the same trends in g_{CD} value as in CD spectra. Thus, by changing the bromide and iodide ratios in our mix-halide chiral bismuth halide films, they exhibit different absorption and PL features with controllable wavelengths. Such bandgap modulation further results in color-tunable CD signals from 300 nm to 500 nm. With such color-tunable CD signals, our chiral bismuth halide samples should be a suitable material for circularly polarized photodetector applications (*13*, *47*, *58–60*). We tried CPL measurements on our chiral bismuth halide samples at low temperature. However, no obvious polarization was detected on PL features (Fig. A7). We think the main reason for weak CPL signals in our chiral bismuth halide samples is due to their low PL efficiency. Then the dominant polarization state may be located in dark state, which cannot be observed by PL measurements.

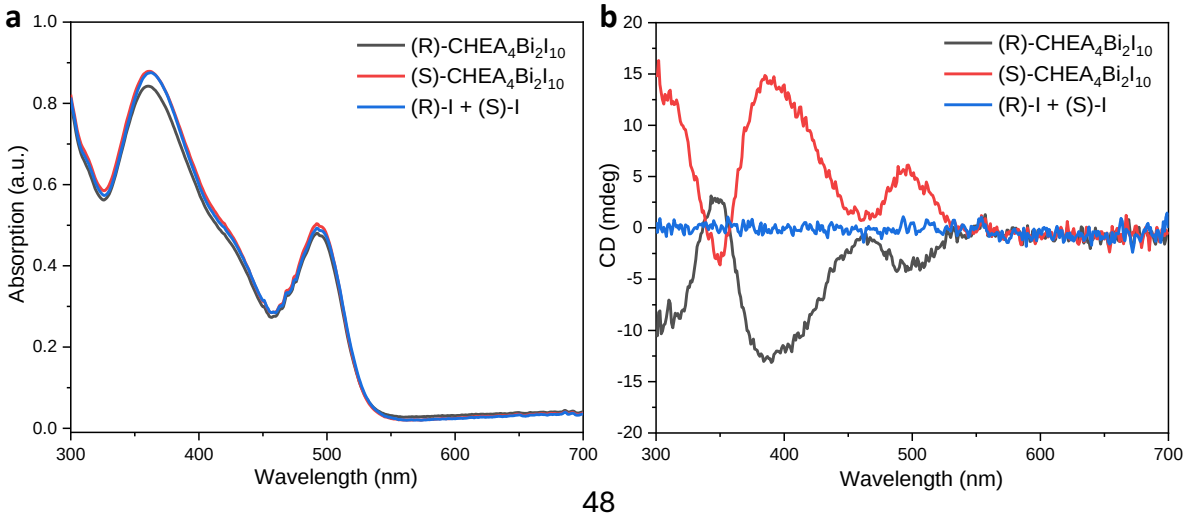

Fig. 4. 8. Circular dichroism (a) and absorption spectra (b) of (R), (S)-CHEA$_4$Bi$_2$I$_{10}$, and the mixture of them (containing an equal amount of (R) and (S)-CHEA$_4$Bi$_2$I$_{10}$) thin films. The disappearance of the CD signal in the mixture sample further demonstrates the enantiomer property of chiral (R) and (S)-CHEA$_4$Bi$_2$I$_{10}$ molecules.

4.2.4 Exciton dynamics in chiral bismuth halide films

To further understand the charge of carrier dynamics in chiral bismuth halide films, we performed transient absorption spectroscopy measurements. Here, we use a linear pump (385 nm) with a fluence of 13 μJ/cm^2 to excite (R)-CHEA$_4$Bi$_2$I$_{10}$ samples, and broadband white light to probe TA signals. As shown in Fig. 4.9a, obvious ground state bleaching (GSB) signals were observed at sample band edge positions (~495 nm), which were surrounded by two strong photoinduced absorption (PIA) signals. Similar TA results were also found in other bismuth-based perovskite materials (*61*, *62*), indicating the formation of photoinduced bound excitons.

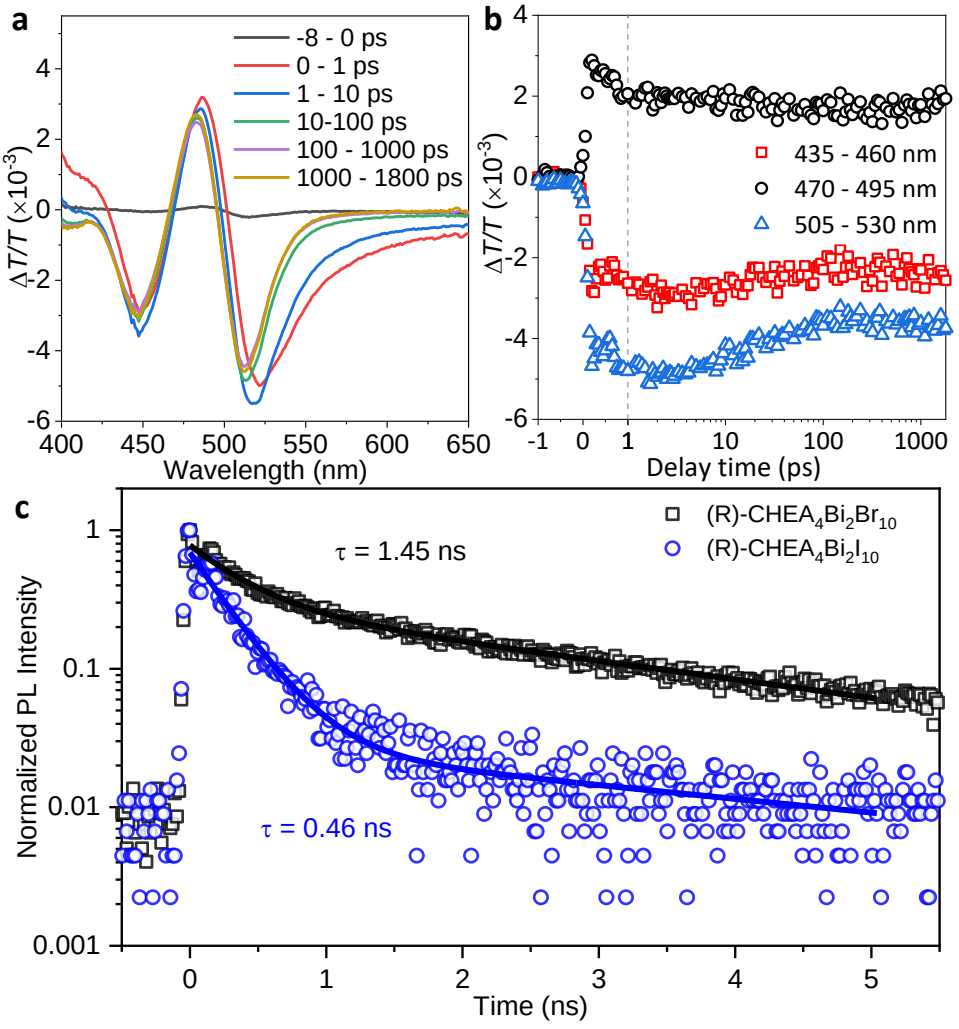

Fig. 4. 9. Charge carrier dynamics in chiral lead-free (R)-$CHEA_4Bi_2I_{10}$ films. Transient absorption (TA) and kinetics (a, b) obtained from (R)-$CHEA_4Bi_2I_{10}$ spin-coating films. (d) Time-correlated single photon counting spectra of (R)-$CHEA_4Bi_2I_{10}$ and (R)-$CHEA_4Bi_2Br_{10}$ drop-casting films collected at 600 nm. It is clear that, (R)-$CHEA_4Bi_2I_{10}$ films have extremely long TA decay in the microsecond range.

We further extract the TA recombination kinetics at GSB and PIA wavelengths and plot them in Fig. 4.9b. There is a fast TA signal decay at GSB wavelength over the first ps, which should relate to the hot carrier cooling process (*63*). Both GSB and PIA signals show long-lived carrier lifetime, with unchangeable TA signals after 100 ps until our instrument detection limit (2 ns). The same long-lived excitons were also observed in mixed-halide samples with blue-shifted spectra (Fig. A8 and Fig. A9). These results prove our chiral lead-free bismuth halide (R)-$CHEA_4Bi_2Br_xI_{10-x}$ samples have a long-lived exciton lifetime beyond ns resolution. Fig. 4.9c compares the time-resolved PL kinetics between (R)-$CHEA_4Bi_2I_{10}$ and (R)-$CHEA_4Bi_2Br_{10}$ drop-casting films. We use time-correlated single photon counting (TCSPC) kinetic measurements to detect the PL decay, and the PL decay signals were collected at 600 nm, where large trap PL signals were observed. We find that (R)-$CHEA_4Bi_2Br_{10}$ film has a longer PL lifetime with a fitting value of 1.45 ns, while the PL lifetime of (R)-$CHEA_4Bi_2I_{10}$ film is ~0.46 ns. Interestingly, the PL decay is much faster than the TA decay, which is also a reasonable result. With TA measurements, we detect all the carrier recombination channels, including radiative and nonradiative decay channels. However, for the PL measurements, we can only monitor the radiative decay channels. Such mismatching result confirmed the formation of long-lived self-trapped excitons in our chiral bismuth halide samples, with forbidden radiative transitions (*64*).

We further use long-term TA spectroscopy measurements with ns resolution to check the full carrier decay channel of our chiral bismuth halide samples. As shown in Fig. 4.10, both GSB and PIA signals show the same decay trends and their dominant TA signals vanished during the initial microsecond, and only small amounts of signals stay unchangeable for the rest of our detections till hundreds of microseconds, indicating the much smaller amount of non-radiative loss in our materials. In general, the long-term TA measurements proved that the long-lived excitons in our chiral bismuth halide samples exist for a few microseconds at room temperature, providing us with a necessary platform for longer spin polarization lifetimes.

Thus, our next step would be the polarization lifetime investigation on chiral bismuth halide samples.

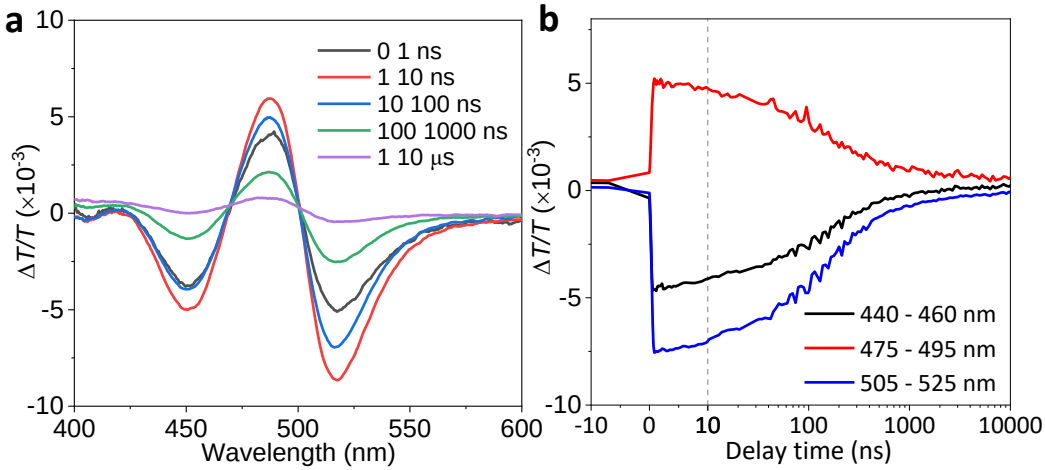

Fig. 4. 10. Long-term TA spectroscopy measurements on chiral lead-free (S)-CHEA$_4$Bi$_2$I$_{10}$ films. TA spectra (a) and kinetics (b) obtained with nanosecond resolution. The measurements were performed under 385 nm excitation with a fluence of ~280 µJ/cm^2.

4.2.5 Polarization dynamics in chiral bismuth halide films

We then use circularly polarized TA spectroscopy to understand the polarization dynamics on chiral bismuth halide films at room temperature. We use a circularly polarized pump to excite the samples and a circularly polarized probe to detect the polarization degrees in TA signals (Fig. 4.11a). Linear polarizers and quarter waveplates were used here to change the linearly polarized laser to circular polarization. For the co- and counter-polarized pump-probe signals (Fig. 4.11b), there has been a large energy separation and intensity difference between the two spectra from time zero, and such separation also persists until a few ns. We further extract the exciton polarization degrees (P(t)) from the PIA regions and plot the corresponding polarization kinetics using the following equation (*65*),

$$P(t) = \frac{\Delta T/T_{counter} - \Delta T/T_{co}}{\Delta T/T_{counter} + \Delta T/T_{co}} \quad (25)$$

where $\Delta T/T_{counter}$ and $\Delta T/T_{co}$ represent the TA intensity under counter or co-polarized pump-probe configurations, respectively. As shown in Fig. 4.11c, we find a dramatic TA intensity difference between co and counter-polarized configurations. The exciton polarization degree is quickly increased to 80% around time zero, and then gradually decreases to 40%, and stabilizes at 2 ns, which suggests our perovskites would have a larger polarization degree after circularly polarized excitation and also notably long polarization lifetime beyond ns resolution.

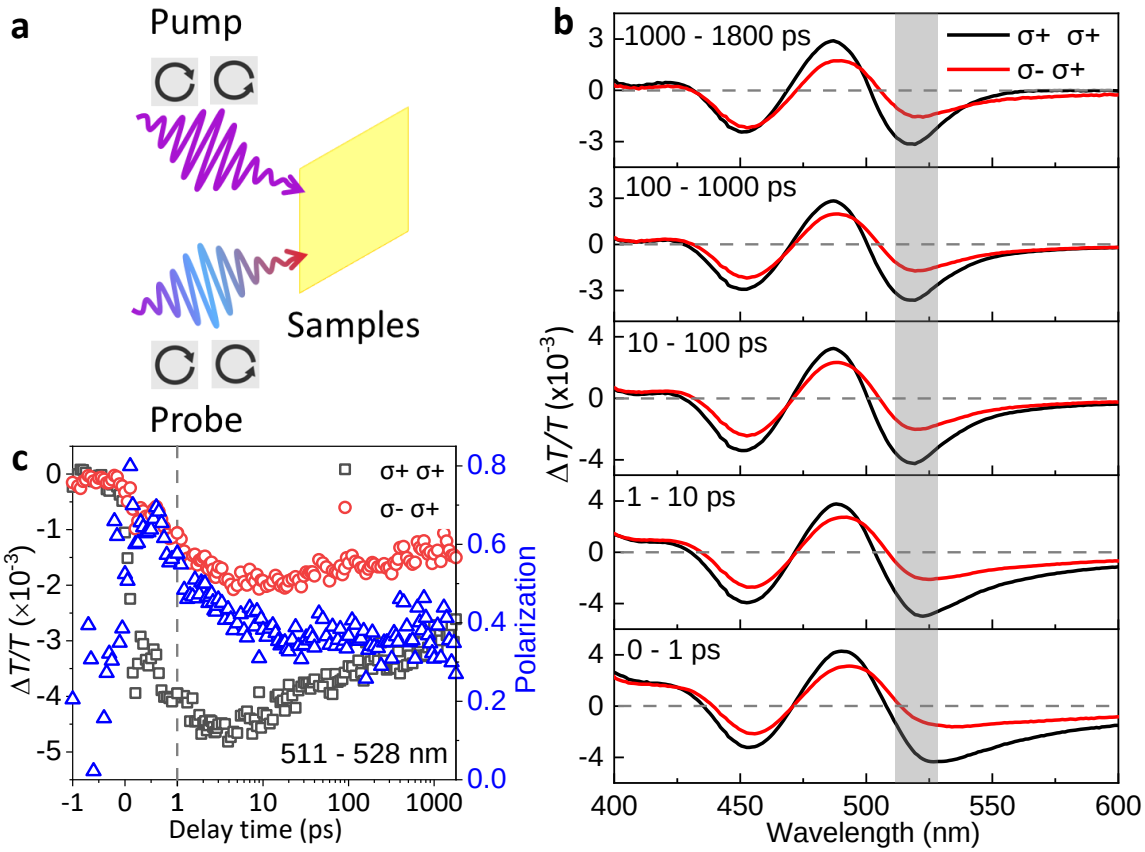

Fig. 4. 11. Circularly polarized TA (CTA) measurements on (R)-CHEA$_4$Bi$_2$I$_{10}$ film. a, Schematics of CTA measurement configurations. **b,** Evolution of circular polarized TA spectra with both circular polarized pump and probe. The red and blue lines represent the different polarized directions as indicated. **c,** Corresponding TA kinetics for the different polarized configurations at the gray range in (b). The spin relaxation kinetics are also calculated and plotted in blue triangle-shaped dots. Apparently, (R)-CHEA$_4$Bi$_2$I$_{10}$ films possess extremely long spin relaxation time.

Usually, in nonchiral perovskite materials, the polarization states were generated by circularly polarized pump excitation (*66*). However, we find that the chiral perovskite would generate intrinsic polarized excitons due to their distorted octahedral structure and spin-polarized band structure. To measure such intrinsic exciton polarization, we also use a linearly polarized pump to excite the samples and a circularly polarized probe to detect the TA signals (Fig. 4.12a). For linear excitation, the energy separation and intensity difference between left-hand and right-hand probe spectra is much smaller (Fig. 4.12b), compared to circularly polarized excitations. Such separation also starts from zero pump-probe delay. It persists until the limit

of our detection (2 ns), which confirmed the long-lived intrinsic excitation polarization existing in the synthesized chiral lead-free perovskites.

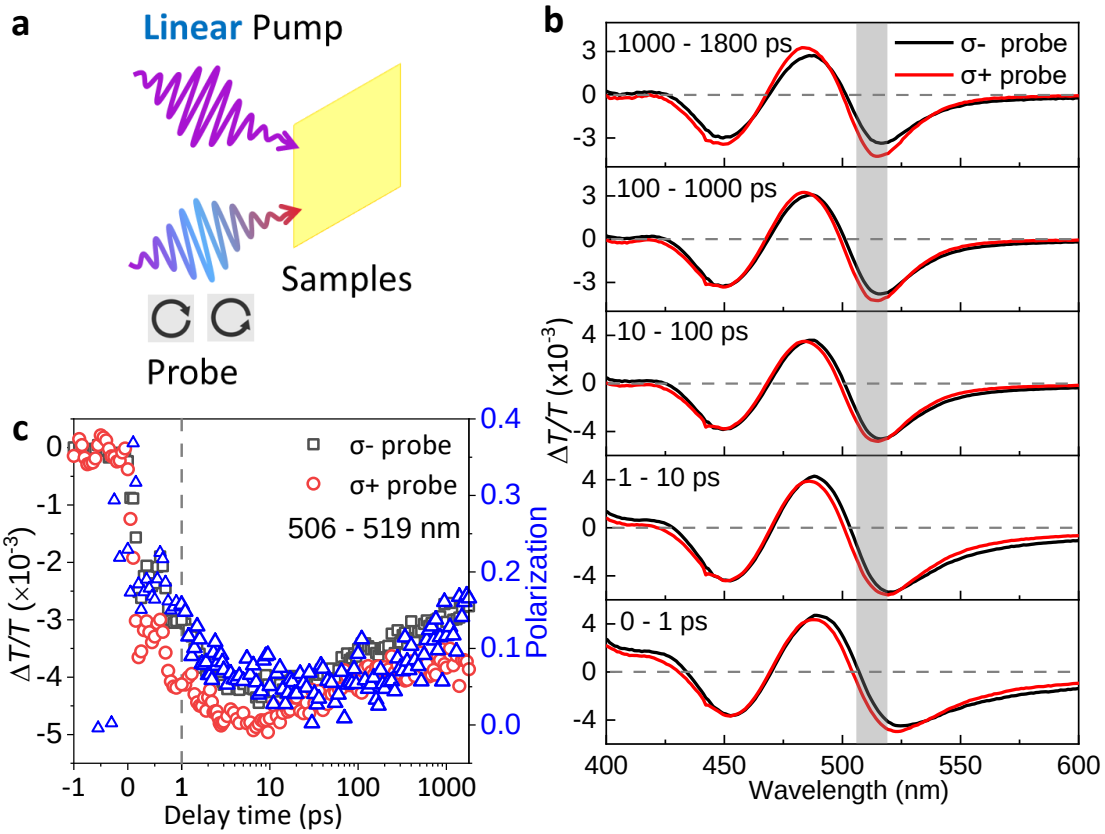

Fig. 4. 12. Circularly polarized TA (CTA) measurements on (R)-CHEA$_4$Bi$_2$I$_{10}$ film. a, Schematics of CTA measurement with linear excitations. **b,** Evolution of circular polarized TA spectra with linear pump and circular polarized probe. The red and blue lines represent the different polarized directions as indicated. **c,** Corresponding TA kinetics for the different polarized configurations at the gray range in (b). The spin relaxation kinetics are also calculated and plotted in blue triangle-shaped dots.

The polarization degree under linear excitation was also calculated and plotted in Fig. 4.12c. Compared to circularly polarized excitation, under liner excitation, chiral bismuth halide samples show a smaller polarization degree of ~35% at zero delay, which gradually decreases to 10% at 2 ns. We performed CTA measurements on racemic bismuth-based perovskites to further validate our measurements. Under linear excitations (Fig. A10), there is no obvious energy separation between left-handed and right-handed detections for racemic samples since zero delay. Under circularly polarized excitation, additionally, we find a tiny CTA intensity difference at the PIA region for racemic samples at time zero. The polarization vanishes fast

over the first ps, which should only relate to circularly polarized excitations. All these results proved the accuracy of our CTA measurements, and there are intrinsic long-lived polarized excitations (>2 ns) in our chiral bismuth halide samples.

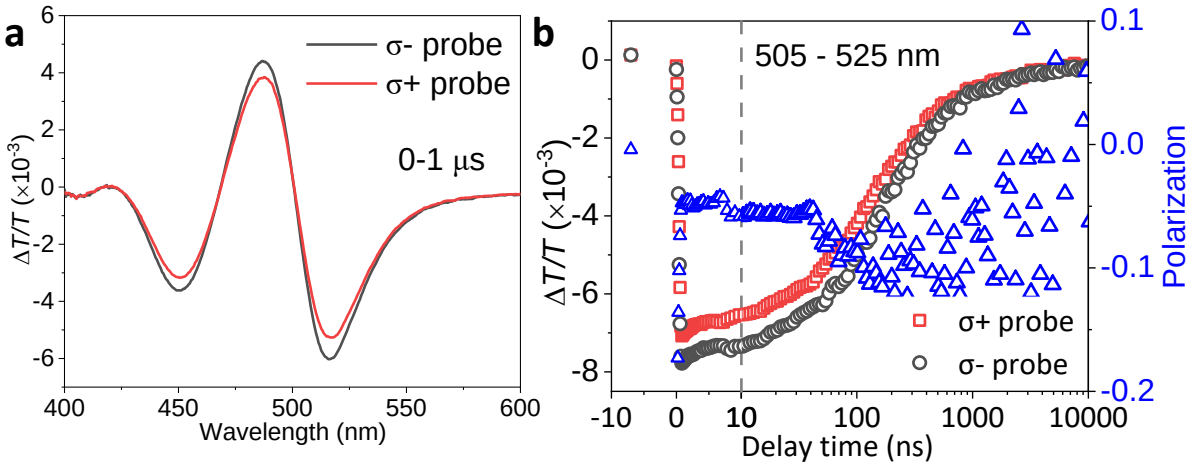

Fig. 4. 13. Long-term circularly polarized TA measurements on (S)-CHEA$_4$Bi$_2$I$_{10}$ film. a, CTA spectra with linear pump and circularly polarized probe. The signals were collected in the first microsecond. The red and blue lines represent the different polarized directions as indicated. **b,** Corresponding TA kinetics for the different polarized configurations at PIA regions. The spin relaxation kinetics are also calculated and plotted in blue triangle-shaped dots.

We performed long-term CTA measurements on (S)-CHEA$_4$Bi$_2$I$_{10}$ film to determine the polarization lifetime in our chiral bismuth halide samples. Under linear excitations, we find large CTA intensity differences between right-handed and left-handed probes at both PIA and GSB regions (Fig. 4.13a), and such intrinsic polarization lasts for a few microseconds. The corresponding CTA kinetics and polarization degrees were plotted in Fig. 4.13b. For chiral (S) samples, the polarization degree shows a negative signal, compared to (R) samples (Fig. 4.12), confirming the dominant photons in chiral (S) samples are left-handed photons, opposite to chiral (R) samples. Besides, chiral (S) samples show a large polarization degree of ~20% at first ns, and then quickly decreases and stabilizes to ~10% after 100 ns, which shows a good consistency to the stabilized polarization degree (~10%) we observed in short-term CTA measurements. Thus, we can conclude from the long-term CTA measurements that our chiral bismuth halide samples generate long-lived polarized excitons with a microseconds-long polarization lifetime.

To prove the optical polarization states we measured in our chiral bismuth halide samples are real spin-related states, we further compared their Faraday rotation signals on chiral and racemic samples. For Faraday rotation measurements, we used a circularly polarized pump (343 nm) to excite the samples and detect the variation of linear polarization of the probe beam (800 nm). Under circular polarization, the spin polarizations in our chiral bismuth halide samples create an optical-induced magnetic field, which would then turn the direction of the probe beam by the Faraday effect. As shown in Fig. A12, similar to CTA kinetics, we find a much longer spin polarization lifetime existing in chiral bismuth-based samples compared to racemic samples. This result confirms that the long-lived polarization states we observed in our chiral bismuth halide samples contain optical-induced spin-related effects.

4.3 Conclusion

In summary, in this work, we report the fabrication of a series of novel chiral lead-free (R)/(S)-$CHEA_4Bi_2Br_xI_{10-x}$ (x = 0 - 10) semiconductors, which shows color tunable circular dichroism from 300-500 nm. By detailed crystal structure analysis and DFT calculations, we find the highly distorted crystal structures are the main reason for the spin-polarized band edge structures in our chiral bismuth halide materials due to strong spin-orbital coupling and Rashba effects. More importantly, chiral bismuth halide samples show extremely long TA decay, reaching a microsecond time range. Upon the combination of long-lived excitons and their chirality features, chiral bismuth halide films inherently exhibit an extremely long polarization lifetime of tens of microseconds at room temperature without magnetic fields. We think the spin-polarized band edge structure in our chiral materials, which provides an initial strong exciton polarization state, together with the long-lived carrier lifetime of lead-free bismuth-based samples, which can further preserve such polarization state for a longer time, are the dominant explanation for such long polarization lifetime in our materials. Further work on the fluence/temperature-dependent CTA or magnetic-optic measurements may offer us a better understanding of the underlying mechanism behind such a long-lived polarization lifetime. Our demonstration of color-tunable optical properties of chiral lead-free perovskites opens a new avenue for the future development of high-performance, nontoxic spintronic materials.

Chapter 5: Effective Chirality Funnels Induce Circularly Polarized Photoluminescence in Chiral Low-Dimensional Hybrid Perovskite Heterostructures

The structural and optoelectronic characteristics of chiral hybrid metal-halide perovskites, e.g. markedly distorted crystal structures, significant Rashba splitting, spin-filtering effect, and robust chiroptical properties, have sparked considerable interest. These features offer valuable advantages across various applications, including nonlinear optoelectronics, encryption, and quantum information technologies. Current research endeavors in chiral perovskites primarily focus on discovering increasingly distorted chiral structures to enhance circular dichroism or achieve greater degrees of CPL.

In this chapter, we investigate the chirality transfer and excited state dynamics in chiral low-dimensional perovskite/PbI_2 heterostructures, which provides a promising way to achieve both long-lived polarized photo-carriers and bright CPL on non-chiral materials. By controlling the fabrication conditions, we can tune the preferential crystal orientations of our chiral perovskite films, as monitored by in-situ X-ray diffraction and grazing incident wide-angle X-ray scattering measurements, which we find to change the corresponding PbI_2 heterostructures. We use transient chiroptical spectroscopy to resolve charge carrier and chirality transfer processes in heterostructures at both room and cryogenic temperatures. We observe rapid carrier transfer from chiral perovskite phases to PbI_2 heterostructures, which is critical for achieving both high PL intensities and substantial degrees of polarization. Our current work starts a general strategy to explore a wide range of chiroptical heterostructure materials based on effective chirality transfer for future chiroptical applications beyond the limits of chiral perovskite itself, such as, low conductivity or weak PL intensity at room temperature.

This chapter explores effective chirality transfer within chiral low-dimensional perovskite/PbI_2 heterostructures, offering a promising avenue for achieving enduring polarized photo-carriers and vibrant CPL in non-chiral materials. Through precise control of fabrication conditions, we manipulate the preferential crystal orientations of chiral perovskite films, as evidenced by in-situ X-ray diffraction and grazing incident wide-angle X-ray scattering measurements, consequently altering their corresponding perovskite-PbI_2

heterostructures. Employing transient chiroptical spectroscopy, we delve into comprehending charge carrier and chirality transfer processes within these heterostructures across the room and cryogenic temperatures. Notably, we identify rapid carrier transfer from chiral perovskite phases to PbI_2 heterostructures as a crucial factor for achieving high PL intensities and significant degrees of polarization.

The work in this chapter is based on an unpublished manuscript. See details below.

S. Liu, J. Zerhoch, M. W. Heindl, C. Zhang, T. Kodalle, K. Sun, A. Shcherbakov, S. Bodnar, C. Jandl, A. Pöthig, I. D. Sharp, P. Müller-Buschbaum, C. M. Sutter-Fella, F. Deschler. Chirality Funnels in Low-Dimensional Hybrid Perovskite Heterostructures for Circularly Polarized Photoluminescence. (to be submitted)

5.1 Background

Hybrid metal-halide perovskites have shown great potential for future commercialized optoelectronic applications, e.g. light-emitting diodes (*57, 67*), photodetectors (*16, 47*), solar cells (*25*), and lasers (*68*), because of their excellent emission quantum efficiency, promising charge-transport capability, strong defect tolerance, and low-cost solution-processed fabrications. By changing the organic and inorganic components, hybrid perovskite materials provide much broader opportunities to vary their crystal structures, band-edge electronic structures, and optical properties. Owing to tuneable compositions, variable bandgap, and strong spin-orbit coupling, hybrid perovskites are of particular interest for multifunctional applications, such as circularly polarized light generation and detection (*7, 69, 70*), second harmonic generation(*71*), piezoelectric (*72, 73*), magnetic (*74*), and spintronic characteristics (*75, 76*). It has been reported that, by simply including chiral organic molecules inside hybrid perovskite frameworks, highly distorted perovskite crystal structures form, which belongs to one of Sohncke space groups, referred to as chiral perovskites (*11, 77*). Chiral perovskites usually exhibit interesting chiroptical features due to their chiral crystal structures and broken inversion symmetry (*11, 78*).

There are two main mechanisms for the formation of chiral perovskites. One is using the chiral organic molecules as chiral ligands for chiral perovskite nanocrystals (*15, 79, 80*), which mostly show a high PL intensity due to quantum confinements but a relatively low degree of opto-polarizations. Another way is the formation of chiral perovskite crystal structures using chiral organic cations. However, the introduction of chirality into perovskite structures would lead to the formation of low-dimensional perovskites because of large chiral organic groups, which generally decreases their conductivity, photoluminescence quantum efficiencies (PLQE) and increases the trap concentrations due to strong electron-phonon coupling (*6, 7*). Only a few chiral perovskites show a high PLQE at room temperature (*7*). Chiral two-dimensional (2D) layered perovskites are well-known for their high degree of circularly polarized photoluminescence (CPL) polarization from single crystal or exfoliated crystal samples (*7, 69, 73*). The degree of CPL polarization for thin film samples remains low at room temperature (10^{-3} or 10^{-4}) and 10^{-2} at cryogenic temperature (*81, 82*). The possible reason may be the chirality loss during single crystals being converted to polycrystalline thin films. Additionally, most reported works about chiral one-dimensional (1D) chain perovskites focus on their strong CD signals, which can be transferred to circularly polarized light

detection (*16*, *47*). Due to disconnected face-sharing octahedral chains, chiral 1D perovskites show relatively weak PL intensities at room temperature, and there is almost no CPL report from chiral 1D perovskites, which strongly hinders their optoelectronic applications.

Recently, Ruddlesden-Popper 2D layered perovskites have emerged as a new platform for exploring high-performance heterostructure optoelectronic devices (*27*, *83*). Due to their unique quantum well structures and intrinsic dielectric confinements, 2D perovskite crystals can be considered as general van der Waals structures, like traditional 2D transition metal dichalcogenides (TMDs), which can be easily modified by mechanical exfoliation and stacking. There are also chiral 2D perovskite/TMD heterostructures reported in recent times (*84*), which show an interesting chirality transfer from chiral perovskite to TMD structures, resulting in a high degree of CPL polarization at low temperatures. However, the fabrication of 2D perovskite heterostructures requires crucial fabrication conditions, and their precise control in a microscopic environment is difficult. Moreover, due to the low stability and fragility of perovskite materials, the exfoliation, transfer, and stack of 2D perovskites are still uncontrollable and less efficient.

Chiral 1D perovskite can differentially absorb circularly polarized light but not efficiently emit light (*14*, *78*). Here, we use a simple solution-processed method to fabricate chiral perovskite/PbI_2 heterostructure thin films that effectively transfer the chiral properties of chiral perovskite to PbI_2 heterostructures. This results in both broad CD signals covering 300-550 nm and a large degree of CPL polarization at low temperature (~4%), comparable to most pure chiral perovskite thin films.

5.2 Result and Discussion

5.2.1 Structure characterizations of chiral one-dimension perovskites

We prepare chiral 1D perovskite (R/S)-$EAPbI_3$ (EA = α-ethylbenzylamine) single crystals by a slow cooling-down process. In short, after fully dissolving (R/S)-EA and PbO in HI solution at 95 °C, we controlled the cooling rate of the reaction solution by 1 °C per hour till room temperature. Large needle-sharp single crystals formed gradually. Single-crystal XRD measurements identify the 1D chain structures of chiral perovskites (see detailed crystal structure results in Table B3), with face-sharing PbI_2 chains and alternatively surrounded

chiral organic molecules (Fig. 5.1a). The Orthorhombic P $2_12_12_1$ crystal structure of our chiral 1D perovskites belongs to one of Sohncke space groups (*11*), supporting the chirality transfer from chiral organics to inorganic lead halide octahedra.

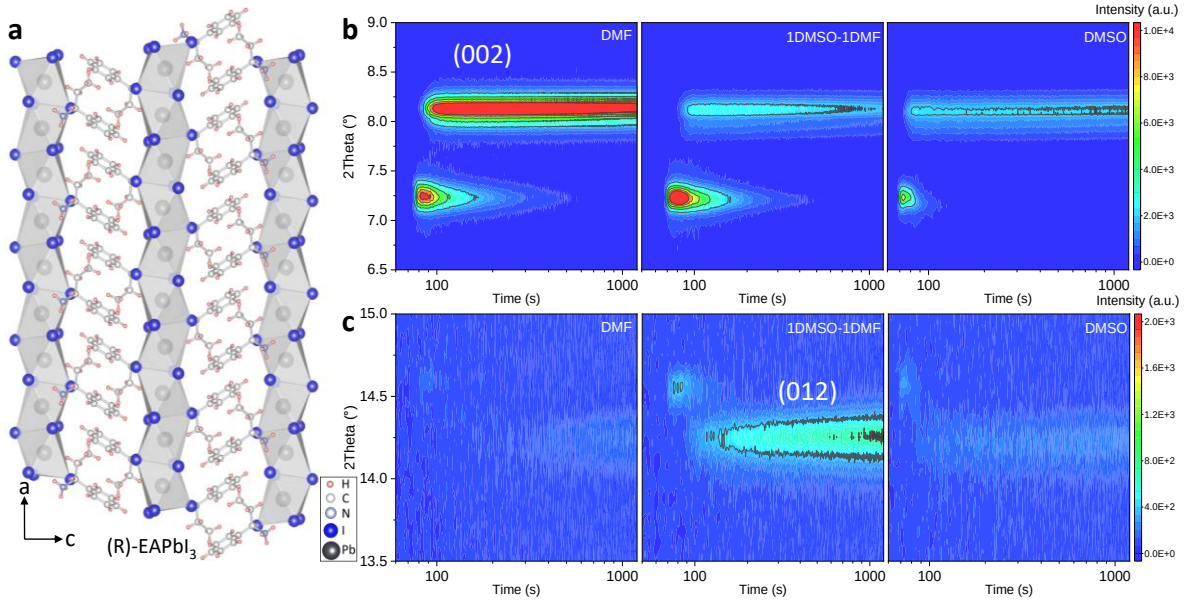

Fig. 5. 1. Structure characterization of chiral 1D perovskites. a, Single-crystal X-ray structure of (R)-EAPbI$_3$. **b, c,** In-situ XRD maps of chiral perovskite thin films monitoring spin-coating (before 60 s) and annealing process (after 60 s). The films were fabricated using three different solvents: DMF, DMSO, and DMF-DMSO mixture. The XRD patterns are expanded in two regions, 6.5 to 9.0° (b), and 13.5 to 15.0° (c).

We then further converted single-crystal samples to high-quality polycrystalline thin films. Simple solution-based spin-coating methods were employed. Here, we used three different solvents (DMF, DMSO, and DMSO-DMF mixture) to dissolve perovskite single crystals to see how solvents impact the film structures and morphologies. The obtained precursor solutions were directly spin-coated on pre-cleaned glass substrates. We performed in-situ XRD measurements to monitor the crystallization process of perovskite films. As depicted in Fig. 5.1b and 5.1c (wide range in-situ XRD results were shown in Fig. A13), no obvious diffraction pattern formed at the initial 60 s during the spin-coating process. When the hot annealing started after 60 s, an intermediate state located at 7.3° emerged first and gradually vanished at ~300 s for DMF and DMSO-DMF mixtures and dimmish quickly for pure DMSO solution at ~100 s. Importantly, the (002) facet of chiral 1D perovskites at 8.2° appears at ~100 s and stabilized until the end of our detection. Much higher (002) facet diffraction intensities were observed in the pure DMF solution compared to the other two

solutions. Besides, the (012) facet located at 14.3° showed up after 100 s for DMSO-DMF mixtures and relatively weaker signals for DMSO solutions, while much lower signals were found in pure DMF solutions. This is clear evidence that different spin-coating solutions result in different preferred crystal orientations in film structures. We further compared the XRD diffraction patterns of spin-coated films with simulated patterns from single-crystal structures (Fig. 5.2). Compared to single-crystal structures, chiral 1D perovskite films show similar diffraction patterns with a dominate (002) facet, indicating the well-formed high-quality 1D perovskite structures on substrates. Notably, there is no diffraction pattern belonging to PbI_2 structures for all three solvents, proving the absence of pure PbI_2 bulk phase in our chiral perovskite films.

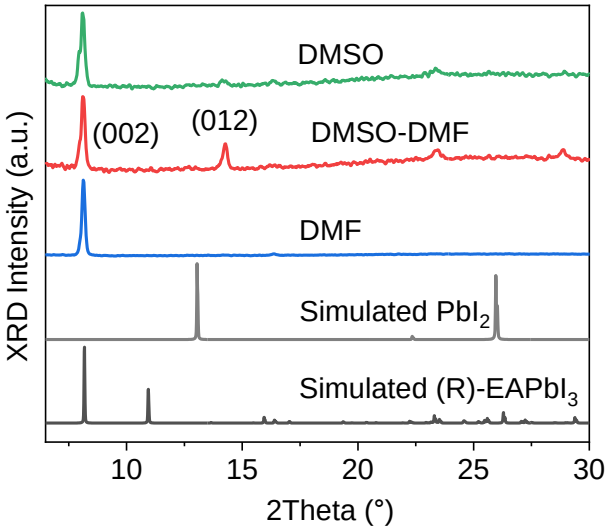

Fig. 5. 2. Comparison of XRD pattern between films prepared with different solvents. All the films were annealed at 100 °C for 10 mins.

To further investigate the crystal orientation of chiral perovskite films, we performed GIWAXS measurements based on synchrotron radiation. Only noticeable diffraction rings were observed for the perovskite spin-coated films with a room-temperature casting process (Fig. A14a), indicating strong randomness of crystal orientations in perovskite films. However, for the perovskite films with 10 mins of hot annealing (Fig. 5.3a and b), we find lots of Bragg spots formed and distributed along the diffraction rings, revealing the different preferential crystal orientations in chiral perovskite films. All three solutions' dominant (002) facets show a preferred out-of-plane orientation (Fig. A14). Additionally, for DMSO-DMF mixture and DMSO solutions, there are also small parts of the (002) phase located on the substrates with in-plane orientations, which may explain their relatively weaker (002) phase intensities observed in in-situ XRD (Fig. 5.1b). We also find an additional (011) phase

showing in-plane orientation for the DMF solution, while for the DMSO-DMF mixture, such (011) phase shows more random orientations along the whole diffraction ring. Thus, according to synchrotron GIWAXS measurements, we conclude that different spin-coating solutions clearly changed the crystal orientations of the perovskite films, with the major (002) phase growing along out-of-plane direction for all three solutions, but a part of (002) or (011) planes still remaining random for DMSO-DMF mixture and DMSO solutions. Similar trends can also be found in atomic force microscope (AFM) morphology measurements. Different solvents lead to different surface morphologies of perovskite films, which may also relate to their surface crystallization orientations (Fig. A15).

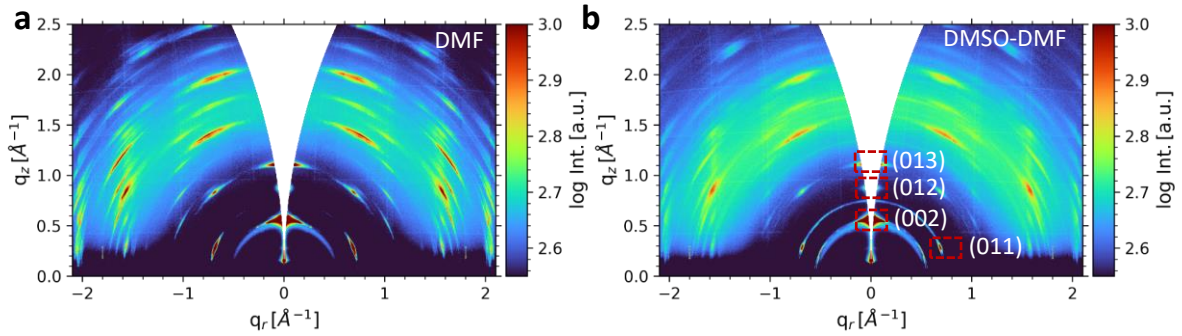

Fig. 5. 3. GIWAXS maps for perovskite films fabricated with DMF (a) and DMSO-DMF mixture solutions (b).

5.2.2 Optical characteristics of chiral perovskite films

Considering interesting and tuneable structures and morphologies of chiral perovskite films controlled by the solvents, we further study the variation of their optical features. Steady-state absorption spectra show that chiral perovskite films exhibit a sharp absorption peak at ~378 nm for all three solvents (Fig. 5.4a), which indicates a similar band position in comparison to other 1D perovskites (*14*, *16*, *85*). Interestingly, DMF and DMSO-DMF films have a long tail from 450 nm to 550 nm, which may relate to the impurity states existing in chiral perovskite films (*86*). Fig. 5.4b presents the circular dichroism (CD) results of chiral 1D perovskite films. The main CD signals of chiral perovskite films were located at absorption band positions (~378 nm), demonstrating an executory chirality transfer from chiral organic molecules to perovskite bandgap structures. Besides, different solutions caused obvious CD signal variations, and perovskite films using DMF solvents show a maximum CD signal. The same results were also observed in their absorption anisotropy factor (g_{abs}) plots (Fig. A16), which are independent of film thickness and absorption intensities (*11*, *87*).

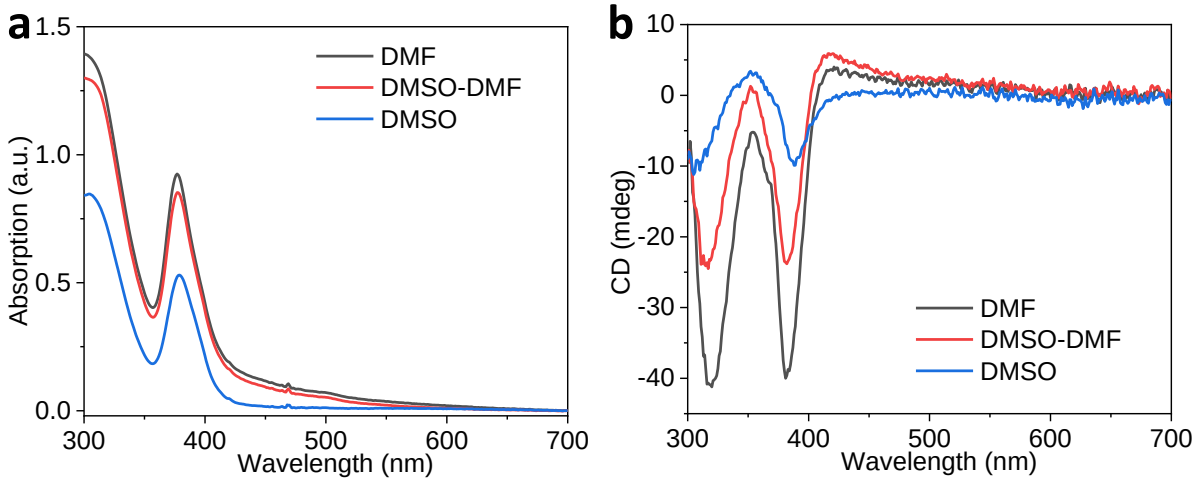

Fig. 5. 4. General optical features of chiral perovskite thin films. (a-c) Steady-state room-temperature Uv-vis absorption (a) and CD (b) spectra of chiral perovskite thin films.

We further study the PL features of chiral perovskite films. Under 340 nm excitations, there is no PL signal at the band edge (~378 nm) for all chiral 1D perovskite films with different solvents (Fig. A17), which is a reasonable result since most reported chiral 1D perovskites did not show band edge PL due their face-sharing disconnected octahedral chains and flat band structures (*14*, *16*). Interestingly, in our chiral perovskite films, a relatively weak PL band shows up at ~510 nm (Fig. 5.5). Besides, there is also a broad PL feature located from 550 nm to 650 nm, which attributes to the trap exciton signals. Different solvents changed the intensities of such trap PL signals, with the highest trap intensities in DMF films and the lowest trap intensities in DMSO-DMF films.

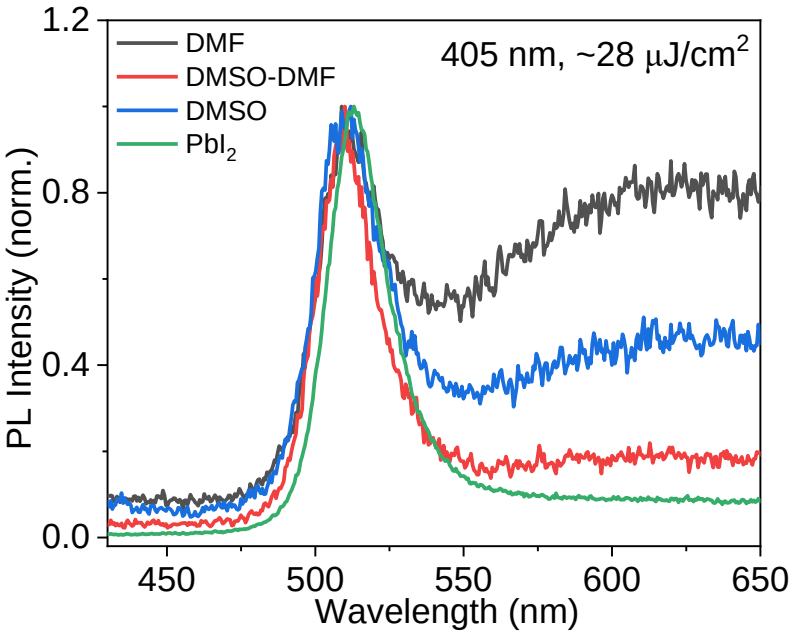

Fig. 5. 5. Room-temperature photoluminescence spectra of chiral perovskite thin films.

To understand the origin of the PL peak at 510 nm, we use the same spin-coating conditions to prepare pure PbI_2 thin films. The PbI_2 films show an overlapping PL feature at ~510 nm, as in chiral perovskite films. However, XRD and GIWAXS measurements confirmed there is no pure PbI_2 phase in chiral perovskite films (Fig. 5.2). Thus, we infer that such PL peak (at 510 nm) originates from chiral perovskite/PbI_2 heterostructure. During the spin-coating and annealing process, part of the PbI_2 precursors may stay in or be coupled with chiral 1D perovskite structures, which might slightly change the crystal structure of PbI_2 or form PbI_2 nanoparticles but keep their PL features at room temperature.

To further study the evolution of this interesting ~510 nm feature, we performed transient absorption (TA) spectroscopy measurements on chiral perovskite films (Fig. 5.6). Two ground-state bleach (GSB) signals were observed from TA spectroscopy. One (GSB1) located at ~378 nm belongs to 1D perovskite band edge feature, and the other one (GSB2) at ~495 nm should relate to ~510 nm PL features with large Stokes shifts (*88*).

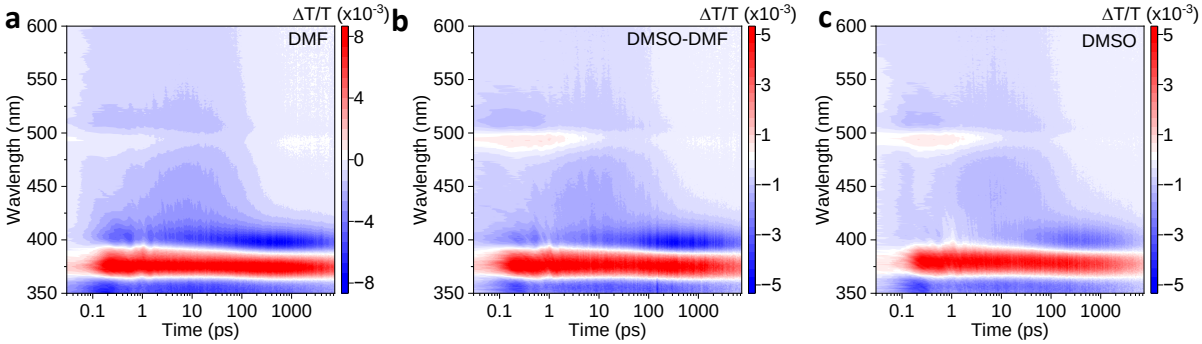

Fig. 5. 6. Transient absorption color maps of chiral perovskite samples using DMF (a), DMSO-DMF mixture (b), and DMSO solvents (c). The samples were pumped by a 340 nm laser (~178 μJ/cm^2).

We also prepared one reference sample without a hot annealing process. Corresponding TA spectra indicate no GSB2 phase formed (Fig. 5.7a). For other chiral perovskite films with different solvents and a 10 min hot-annealing process, we find both DMSO-DMF and DMSO films show a stronger GSB2 TA signal than DMF films. Taking all this information together, we know the GSB2 phase only shows up after the hot-annealing process, and different solvents result in different GSB2 phase intensities. GIWAXS measurements indicate that the obvious phase appearing after hot-annealing is the (012) facet, compared to room-temperature casted films (Fig. A14), and in-situ XRD measurements prove the main

difference between films using different solvents also comes from (012) phase (Fig. 5.1). Hence, we infer that the GSB2 signals observed in chiral perovskite samples should be highly related to chiral perovskite (012) crystal phase, which may provide a better crystal orientation for chiral perovskite/PbI_2 heterostructure formation. TA kinetics further confirmed that GSB1 has a much longer carrier lifetime than that of GSB2 (Fig. 5.7b). The rising signals after 100 ps for GSB2 are derived from the carrier transfer from GSB1 signals, which show a fast decay after hundreds of ps. Time-correlated single-photon counting (TCSPC) measurements were also used here to characterize the PL decay of such 510 nm PL feature, which exhibits a short PL lifetime ~257 ps (Fig. A18). No transferring process was detected in TCSPC measurements, possibly due to its low ns resolution or the transferring process mainly happening in dark states such that they only be detected in TA measurements (*89*, *90*).

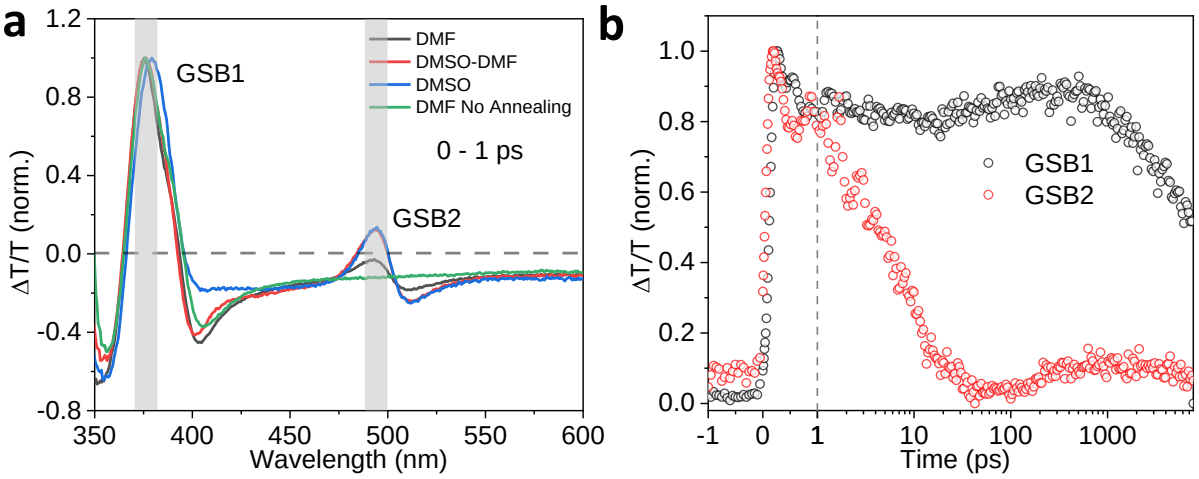

Fig. 5. 7. TA results collected from chiral 1D perovskite films. a, Comparison of TA spectra (initial 1 ps) between films prepared by different solvents. One of the samples was fabricated without a hot-annealing process. The rest of the films were annealed at 100 °C for 10 mins. Grey regions indicate two GSB signals. **b,** TA kinetics extracted from two GSB regions (DMF films). The GSB2 kinetics were calibrated by the broad photoinduced absorption signals next to it (550-560 nm).

5.2.3 Polarization dynamics in chiral 1D perovskite/PbI_2 heterostructures

We further employed circularly polarized TA (CTA) spectroscopy to investigate the polarization dynamics of our chiral perovskite thin films at room temperature. Different from CTA measurements on non-chiral materials, which need circularly polarized excitations to

create polarized carriers, we here use a linear pump to excite the chiral perovskites that intrinsically generate photo-excited polarized carriers due to their highly distorted chiral crystal structures (6). A circularly polarized probe was used to detect the intensity difference between left-handed and right-handed TA signals. Fig. 5.8a-c show the CTA spectra collected from chiral perovskite thin films with three different solutions. All three films exhibit obvious intensity differences at GSB1 regions (~378 nm) over initial ps, which should relate to intrinsic chirality features of chiral 1D perovskites. The extracted decay kinetics from GSB1 (372-382 nm) were plotted in Fig. A19. Both DMF and DMSO-DMF mixture films show a long-lived polarization lifetime (a few ns) for chiral 1D perovskite phases. In contrast, the polarization in DMSO films only lasts ~1 ps. Besides, we discover the GSB2 phase, which we attribute to chiral perovskite/PbI_2 heterostructures, showing a non-negligible difference between σ^+ and σ^- probes for DMF-DMSO mixture film (Fig. 5.8b), indicating in turn successful chirality transfer from chiral 1D perovskites to PbI_2 heterostructures. Unexpectedly, GSB2 phases for DMF and DMSO films didn't exhibit a clear polarization.

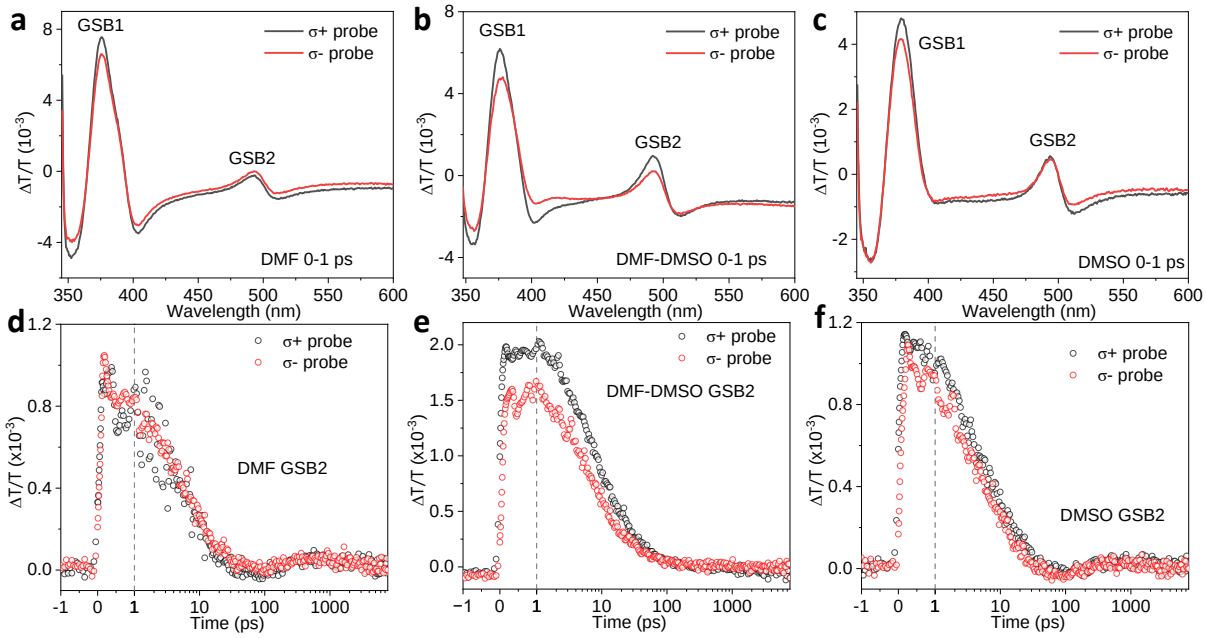

Fig. 5. 8. Polarization dynamics of chiral perovskite thin films. a-c, CTA spectra (0-1 ps) collected from DMF (a), DMF-DMSO mixture (b), and DMSO (c) based chiral perovskite thin films. Linear pump at 340 nm (~178 μJ/cm^2) was used to excite the samples. Circularly polarizer right-handed (σ^+) and left-handed (σ^-) probes were used to detect TA signals. **d-f,** CTA kinetics collected from GSB2 regions in Fig. 3a-c, respectively.

We further collect the CTA kinetics from GSB2 regions (490-500 nm). Since the GSB2 signal is located on a broad photoinduced absorption (PIA) signal covering 400 to 600 nm, we calibrate the GSB2 signals with their adjacent PIA signals (550-560 nm) and plot the calibrated CTA kinetics in Fig. 5.8d-f. We observe almost no difference between σ^+ and σ^- probes GSB2 kinetics for DMF and DMSO films, while DMSO-DMF films have a relatively longer polarization lifetime, reaching ~100 ps. Therefore, it is reasonable to conclude that the solvent for thin film fabrication is an important factor to not only control the optical polarization of chiral perovskite intrinsic band phases but also the chirality transfer between chiral perovskites and their heterostructures.

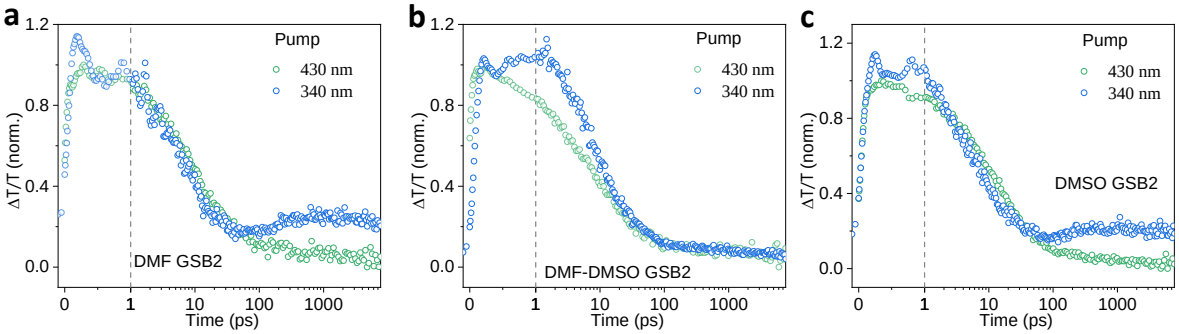

Fig. 5. 9. Comparison of linear TA kinetics at GSB2 regions under 340 nm and 430 nm excitations. The TA kinetics were obtained from films using DMF (a), DMSO-DMF mixture (b), and DMSO solutions (c).

To further explain the chirality transfer process inside chiral perovskite heterostructures, we use two different pump wavelengths to excite chiral perovskite films. Apart from the TA signals collected under a 340 nm excitation, which would excite GSB1 at ~378 nm first, facilitating carrier transfer from GSB1 to GSB2 (~378 nm), we can also directly obtain GSB2 signals by using a 430 nm excitation. No broad long-lived PIA signal showing up above GSB2 signals proved no GSB1 state generation under 430 nm excitations (Fig. A20). Accordingly, no transfer process is happening under 430 nm excitations (*91*). We then compare the TA kinetics obtained from GSB2 regions under 340 nm and 430 nm excitations (Fig. 5.9). The difference between them should indicate the carrier transfer process. We find a small hot-carrier cooling process occurring before 0.5 ps under 340 nm excitations. For DMF films (Fig. 5.9a), the decay kinetics almost overlap between 340 nm and 430 nm pumps from 0.5 ps to 100 ps. The rising up of TA signals under 340 nm excitations takes place after 100 ps, which confirms the carrier transfer in DMF films comes about after 100 ps. The same

trends were also noticed in DMSO films (Fig. 5.9c). Differently, for DMF-DMSO mixture film (Fig. 5.9b), the TA signals under 340 nm excitations increase significantly over the initial 10 ps, compared to TA signals under 430 nm excitations. Such results prove that carrier transfer from GSB1 to GSB2 phases in DMF-DMSO mixture films happens fast at first 10 ps. Based on the aforementioned results, we think the main reason for DMF-DMSO mixture films featuring a large and long-lived polarization state is that fast carrier transfer efficiently delivers the polarized photons from chiral 1D perovskite phase (GSB1) to PbI_2 heterostructure (GSB2) before the depolarization process becomes dominate. For DMF or DMSO films, carrier transfer happens after 100 ps, at which point the polarization of carriers in GSB1 already decays heavily (Fig. A19).

5.2.4 Low-temperature optical features in chiral 1D perovskite/PbI_2 heterostructures

Given that effective chirality transfer in chiral perovskite/PbI_2 heterostructures enables long-lived polarized states, we attempt to explore CPL properties on our chiral perovskite films. Nevertheless, we didn't observe obvious CPL signals at room temperature due to the low PL intensities of chiral perovskite films. Interesting PL features were detected at cryogenic temperatures. Fig. 5.10a shows the temperature-dependent PL spectra of chiral perovskite films using DMSO-DMF mixture as spin-coating solvents. A sharp PL peak at ~498 nm becomes dominant when the sample temperature goes to 5 K, which is a large blue shift of PL emission compared to PL features at room temperature (~510 nm). Additionally, the dramatic increase in PL intensity and decrease in PL peak width indicate strong electron-phonon interactions in our chiral perovskite/PbI_2 heterostructures.

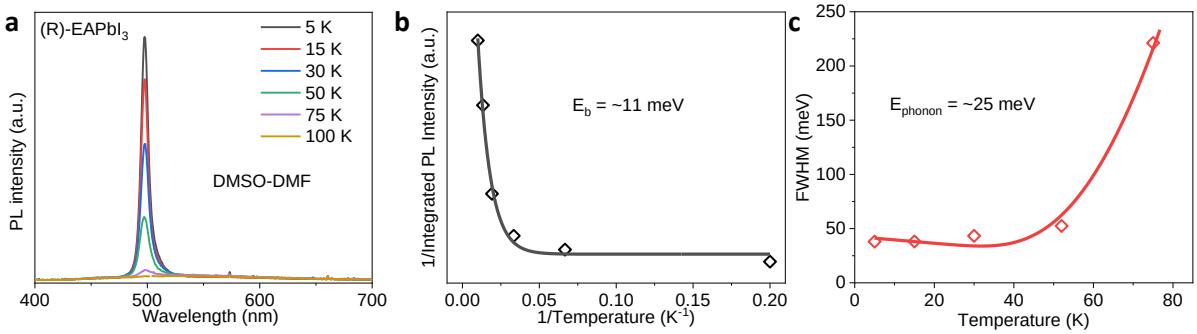

Fig. 5. 10. Low-temperature chiroptical characteristics of chiral perovskite thin films. a-c, Temperature-dependent PL spectra (a), corresponding integrated PL intensity (b), and FWHM as a function of temperature (c) for chiral perovskite films. The samples were excited at 395 nm with a pump fluence of ~5 μJ/cm^2.

To quantitatively understand electron-phonon coupling in the heterostructure, we extract the integrated PL intensity and full width at half maximum (FWHM) of PL peaks from temperature-dependent spectra and plot them as a function of temperature (Fig. 5.10b and 5.10c). In Fig. 5.10b, the integrated PL (I_{PL}) was fitted by the following equation (*73*),

$$I_{PL}(T) = \frac{I_0}{1+Aexp(-E_b/k_BT)} \quad (26)$$

where E_b is the activation energy, also known as excitonic binding energy, k_B is the Boltzmann constant, A is a fitting constant, and I_0 is the integrated intensity of PL peak at 0 K. The fitted E_b value is only ~11 meV, which is much smaller than in low-dimensional perovskite materials (hundreds of meV) (*92*, *93*). The sharp PL feature at ~500 nm originates from chiral perovskite/PbI_2 heterostructures rather than chiral 1D perovskite itself. This result also explains the low PL intensity of our samples at room temperature because excitons with such a small E_b value would have a higher probability of dissociating before their radiative decay. We also describe the broadening of FWHM by the equation below (Fig. 5.10c) (*94*, *95*),

$$\Gamma(T) = \Gamma_0 + \gamma_{ac}T + \gamma_{LO}/\left[\exp\left(\frac{E_{phonon}}{k_BT}\right) - 1\right] \quad (27)$$

where the first term Γ_0 represents a temperature-independent inhomogeneous broadening term, which is related to disorder in material size or composition (*94*). The second and last terms are homogeneous PL broadening terms caused by acoustic and longitudinal optical (LO) phonons scattering, respectively. E_{phonon} is the extracted LO phonon energy. The detailed fitting results are shown in Table B4. Due to the low acoustic weight value (γ_{ac} = ~0.31 meV), the main contribution for emission broadening in current samples should derive from LO phonon scattering (*96*). Besides, the fitting phonon energy is ~25 meV, which is comparable value to the perovskite materials (*28*, *97*)Such small phonon energy indicates that more phonons would be generated at room temperature, which may be a scattering centre for non-radiative decay, consistent with the low PL intensity we observed at room temperature.

We compare the PL spectra of chiral perovskite films using different spin-coating solvents at low temperature (5 K, Fig. 5.11a). It is important to note that the PL intensity at ~500 nm of all chiral perovskite films is strongly increased compared to background PbI_2 bulk films at 5 K. On the other hand, the FWHM of PbI_2 PL (~75 meV) is almost double than that of chiral perovskite films (~38 meV), corroborating the 500 nm PL feature in chiral perovskite film is not simply from pure PbI_2 bulk phase. We think the substantial increase in PL intensity of

chiral perovskite films may be due to the additional carrier transfer from the perovskite phase to PbI_2 heterostructures. As expected, DMSO-DMF films show a much larger PL intensity at ~500 nm than pure DMSO, DMF films, which can also be explained by fast carrier transfer happening in DMSO-DMF films as we observed from TA spectroscopy (Fig. 5.8). The fast carrier transfer at initial time can efficiently enable a large proportion of carriers to go to PbI_2 heterostructure phase, before they turn to non-radiative decay channel, like forming traps and defects, and then decay radiatively. Except for the 500 nm PL peak, we find another broad PL feature from 550 nm to 800 nm showing only in DMF films, which should be similar trap signals as we observed at room temperature (Fig. 5.5). Different spin-coating solvents change the crystallization of perovskite films, which may also cause different traps or defects intensities in films.

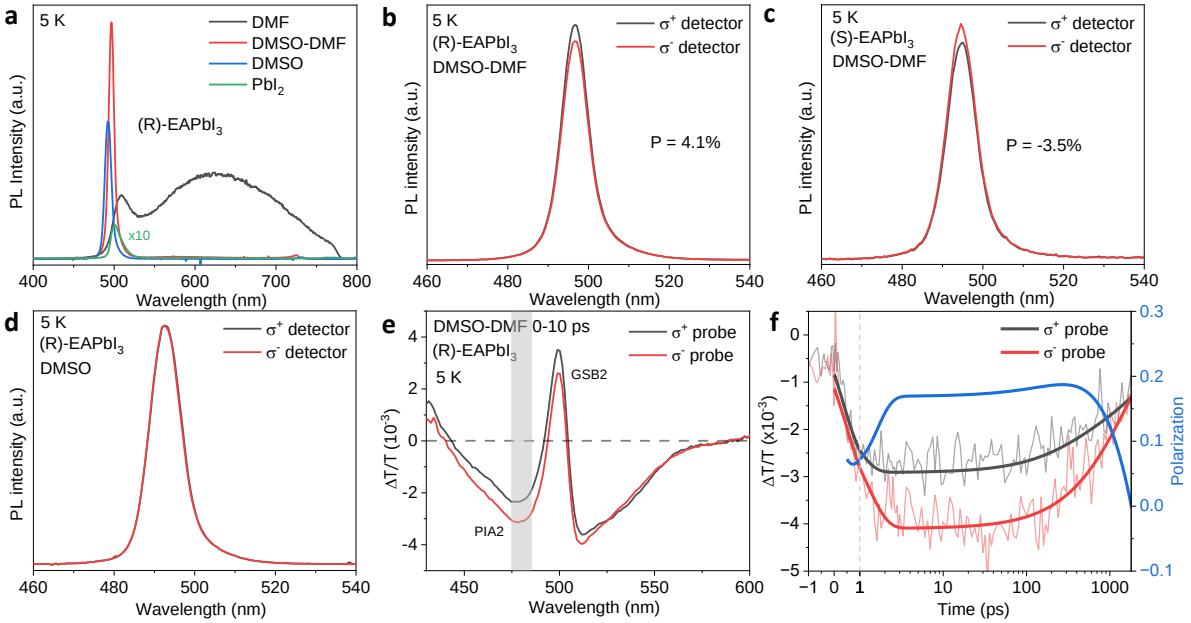

Fig. 5. 11. Low-temperature chiroptical characteristics of chiral perovskite thin films. a, Comparison of PL spectra between DMF, DMSO-DMF mixture, and DMSO based films at 5K. **b, c,** Low-temperature CPL spectra of chiral perovskite (R)-EAPbI3 (b) and (S)-EAPbI3 (c) thin films using DMSO-DMF mixture as solvent. **d,** CPL spectra of chiral perovskite films using DMSO solvents. **e, f,** CTA spectra (e) and kinetics (f) of chiral perovskite films using DMSO-DMF mixture as solvent at 5 K. The CTA kinetics were collected from PIA signals (grey region). A 390 nm excitation beam with a fluence of ~14 μJ/cm^2 was used to pump the samples.

With quite strong PL intensities at low temperatures, we carry out CPL measurements on our chiral perovskite films at 5 K. Here, we use a linear excitation to pump the samples and a quarter waveplate with a 45° polarizer to select σ^+ and σ^- PL signals into the camera. Each measurement was taken 5 times to get an average result. For DMSO-DMF films, clear intensity differences were detected for chiral (R) and (S)-$EAPbI_3$ films, which also show a flipping intensity difference between σ^+ and σ^- detections (Fig. 5.11b and 5.11c). We calculate the degree of CPL polarization (P) by following the equation.

$$P = \frac{I_{\sigma+} - I_{\sigma-}}{I_{\sigma+} + I_{\sigma-}} \tag{28}$$

Here, $I_{\sigma+}$ and $I_{\sigma-}$ represent the integrated PL intensity between σ^+ and σ^- detections. (R) and (S)-$EAPbI_3$ films exhibit similar polarization (~4%) but reversed signs. In principle, chiral two-dimensional layered perovskite single crystals or exfoliating flakes would have a large degree of polarization (dozens of percent) at cryogenic or room-temperature (*7, 69, 73*). The most reported chiral perovskite thin films only show a g factor at the order of 10^{-3} or 10^{-4} (*11, 15, 78, 81, 98*), which are much smaller values compared to the degree of polarization we obtained from our last chiral perovskite/PbI_2 heterostructures. Both pure DMSO and DMF chiral perovskite films didn't show obvious PL intensity difference at ~500 nm between σ^+ and σ^- detections (Fig. 5.11d and A21a), which is in good consistency with their low TA polarization degree, caused by slow and inefficient carrier chirality transfer (Fig. 5.8). Interestingly, there is an unusual polarization showing at broad trap PL from 550 to 750 nm in DMF films (Fig. A21a). To understand this unusual PL polarization, we use and cool down the racemic $EAPbI_3$ single crystal sample to eliminate the influence from both chirality and the PL features at 500 nm due to PbI_2 heterostructures. We remove the quarter waveplate in front of the camera for CPL measurements and only rotate the linear polarizer before the camera to measure the linear polarization of PL. No sharp PL features at 500 nm approve such PL features only coming from PbI_2 heterostructures in thin films as well (Fig. A21b). Similar and strong linear polarizations were noted for racemic $EAPbI_3$ single crystals, which may be caused by strong anisotropy in their crystal structures. Thus, we think the unusual polarization for trap PL in DMF films should also originate from their strong linear polarization.

To study the polarization dynamics of chiral perovskite films at low temperatures, we also performed CTA measurements on chiral perovskite films using DMSO-DMF solvents at 5 K.

Different with room temperature TA signals, the GSB2 signals (495-505 nm) for PbI_2 heterostructures become quite stronger and also live longer till a few ns (Fig. 5.12).

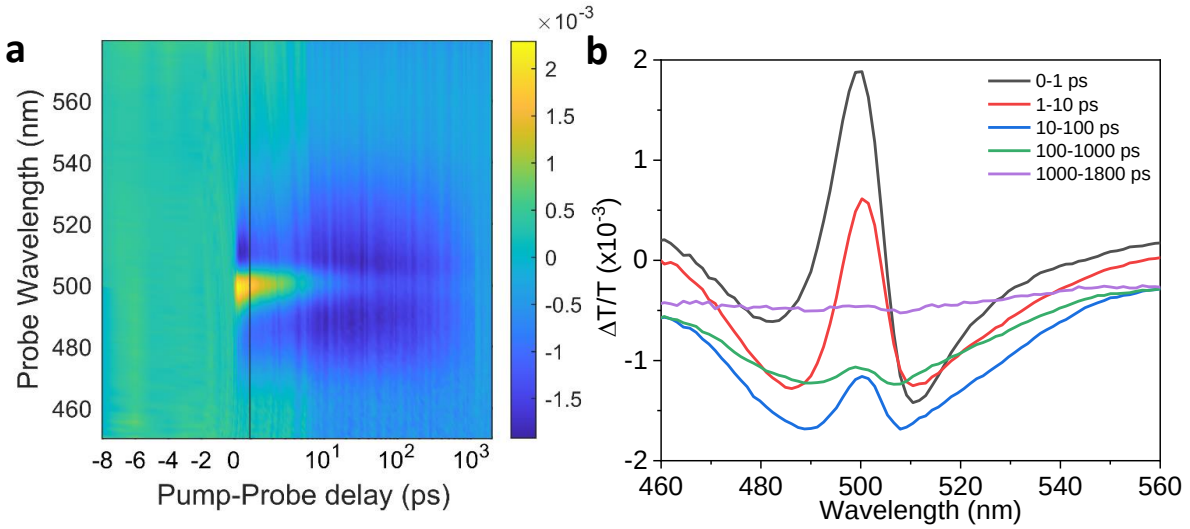

Fig. 5. 12. Low-temperature TA measurements on chiral perovskite films. TA color map (a) and corresponding spectra (b) obtained from chiral perovskite films (DMSO-DMF mixture) at 5 K.

The presence of broad PIA signals from 460 – 560 nm confirms the existence of carrier transfer from the high-energy phase (chiral perovskite phase). Similar to low-temperature CPL measurements, large polarizations between σ^+ and σ^- probes were found at GSB2 regions (Fig. 5.11e). The polarization for GSB2 lasts for a longer time at low temperatures and goes to zero at ~1 ns (Fig. A22), which explains the large degree of CPL we obtained at cryo-temperature. Because the GSB2 signals live longer till the end of our detection and co-exist with negative broad PIA signals, it is hard to calibrate the GSB2 signal at low temperatures and fit its decay kinetics. We choose the PIA2 regions (475-485 nm) as alternatives for polarization kinetics plotting. As depicted in Fig. 5.11f, the blue curve is the calculated degree of polarization of CTA signals, according to the same equation we used for CPL polarization calculations, while here, $I_{\sigma+}$ and $I_{\sigma-}$ represent the TA intensity under σ^+ and σ^- probes. The difference between σ^+ and σ^- probes is pretty small at first ps, and then the degree of polarization increases quickly from 1 to 4 ps, and stabilizes from 4 ps to hundreds of ps, reaching high polarization degree ~0.2. Such rising polarization kinetics strongly prove that the chirality efficiently transfers from chiral perovskite states into PbI_2 heterostructures, which gives them a long-lived polarized state. The polarization decreases fast after ~300 ps, gradually decreasing to 0 after 1 ns. All these results show the great potential of chiral

perovskite films for controllable chirality transfer into PbI_2 heterostructures, resulting in bright CPL and long-lived polarization states at cryo-temperature.

5.3 Conclusion

In summary, we grow new types of low-dimensional chiral perovskite (R/S)-$EAPbI_3$ single crystals. Single crystal XRD measurements prove the formation of chiral crystal structures belonging to Sohncke space groups. In-situ XRD and GIWAXS measurements indicate the different solvents we used for the spin-coating process change the crystal orientations in chiral perovskite films, which helps us to control both absorption and CD signals of chiral 1D perovskite films. The formation of (012) phases in DMSO-DMF films provides a suitable framework for PbI_2 heterostructures to engage in, which generates a new PL feature at ~500 nm. Transient optical spectroscopy measurements confirm that, by simply controlling the spin-coating solvents, we can drive the fast and effective chirality transfers and energy funneling from chiral perovskite phases to PbI_2 heterostructures, which possess a long-lived polarized excited state with bright circularly polarized emissions at cryo-temperatures. We further fabricated another two types of novel chiral 1D perovskite films using two different chiral organic molecules, which also show the same heterostructure features at ~500 nm (Fig. A23), indicating such results are the general trends in chiral 1D perovskite films. Our finding of chiral perovskite heterostructures with controllable chirality transfer provides a new avenue for circularly polarized light generation, broadening the material ranges for future non-linear optoelectronics and spintronics applications.

Chapter 6: Bright Circularly Polarized Photoluminescence in Chiral Layered Two-Dimensional Perovskites

Chiral 2D hybrid organic-inorganic halide perovskites, which take advantage of both unique chirality features and exceptional optoelectronic properties, are emerging spintronic materials. However, chiral perovskites with highly distorted crystal structures usually exhibit low PL efficiency, which strongly hinders their photonic applications, e.g., LEDs.

In this chapter, upon careful structure design of chiral organic molecules, we successfully fabricated chiral two-dimension (2D) (R/S/Rac)-3BrMBA$_2$PbI$_4$ (3BrMBA = 1-(3-Bromphenyl)-ethylamine) perovskites as single crystals and thin films, which not only obtain a high photoluminescence quantum efficiency of 39%, but show strong circular dichroism at band edge position and strong circularly polarized photoluminescence at room temperature. We use single-crystals x-ray diffraction and density-functional theory to understand the chirality transfer from chiral crystal structures to spin-polarized band structures. By using time-resolved spectroscopy, we observed improved photoluminescence yields and exceptional chiral optical properties in our chiral 2D perovskites, compared to previously reported chiral perovskites and reference 4BrMBA samples. We attribute such superior properties to the dominantly fast radiative recombination and long-lived polarized excitons in our 2D perovskites. The current work will pave the way for the design of high-performance perovskite optoelectronic devices with spin-polarized features based on the structure engineering of organic cations.

This chapter is based on a published work (*7*), *Shangpu Liu, et al. Bright circularly polarized photoluminescence in chiral layered hybrid lead-halide perovskites. Science Advances,* ***9****, eadh5083 (2023)*.

6.1 Background

With the development of quantum mechanics, the spin of charged particles is gradually recognized as a novel functional carrier for information transport and manipulation, which would benefit from intrinsic spin characteristics, such as low energy consumption and large memory density. The spintronic applications, which combine three information carriers (electron charge, photon, and electron spin), have already been promoted to large-scale commercial industries, resulting in a variety of functional devices, including data storage and processing devices (*99*) Given that the performance of spintronic devices mainly depends on efficient spin injections and detections (*100*). The design of new spintronic materials is the current research priority. The traditional spintronic devices are mostly based on magnetic materials or materials with strong spin-orbit coupling (SOC), which would produce polarized spin states under a magnetic field or external spin injection. Due to the discovery of the chiral-induced spin selectivity (CISS) effect recently, chiral organic molecules have proved themselves as room-temperature spin filters (*101*). The CISS effect can be extended to other solid-state chiral materials, such as organic-inorganic hybrid metal halide perovskites (HMHPs), to enable intrinsic spin injection inside the materials, further widening current spintronic applications.

HMHP semiconductors are attractive optoelectronic materials owing to their excellent physical properties, such as high charge-carrier mobility, long carrier lifetime, color-tunable bandgap, and superior photoluminescence quantum efficiency (PLQE). These outstanding features make HMHPs highly desirable materials for solar cells, photodetectors, lasers, and light-emitting diodes (LED) applications (*23*, *34*, *68*). Compared to three-dimensional perovskites, two-dimensional (2D) perovskites with more stable structures and stronger quantum confinement have obtained intense research attention. Besides, because of numerous available organic cations and metal halides, 2D HMHPs feature superb compositional and structural diversity, which offers good platforms for the involvement of multi functionalities, for instance, piezoelectricity, ferroelectricity, magnetic properties, and chirality features (*73*, *102*). However, it is still a leading challenge to preserve the efficient optical properties of HMHPs while introducing novel functionalities by using relatively large and complicated organic molecules or replacing the lead atoms with other transition metals, which would further limit their practical applications.

Chirality is a ubiquitous attribute in nature. A chiral material features fully broken symmetry, while its mirror image cannot overlap with itself. Chiral organic molecules usually exhibit strong chiroptical activity due to their unique asymmetry structures, such as amine acid, DNA, and other natural products. By employing chiral molecules as organic cations in 2D HMHPs, chirality would be further transferred into the perovskite network. Except for the colloidal nanocrystal system, wherein chirality would transfer via surface ligands modification, the chirality transfer mechanism for HMHPs would mainly drive from chiral-induced crystallization. Thus, HMHPs, with the addition of chiral molecules, would form a chiral crystal structure with the highly distorted octahedral framework, which belongs to one of Sohncke space groups with strong chiral optical properties, such as circular dichroism (CD) and circularly polarized photoluminescence (CPL) (*14*, *82*, *103*). The superior optoelectronic performance of HMHPs then provides a good complement to break the photovoltaic limitation from pure chiral molecules due to poor electrical properties (*104*). Besides, HMHPs, which possess strong spin-orbit coupling, large Rashba splitting, and long polarization lifetime (*11*), make them suitable supporting materials for spintronic applications. Consequently, the excellent polarization features of chiral perovskite with intrinsic spin injection achieve plenty of room-temperature spintronics applications, including spin-LED or circularly polarized light detectors (*67*, *105*).

However, 2D HMHPs usually exhibit low PLQE at room temperature because of the existence of nonradiative dark or defect states. Not to mention that, from previously reported work, the introduction of chiral organic cation into perovskite would further decrease the PLQE value (*82*) The existence of competition between the polarization degree and the PL efficiency is still the main problem for their spintronic photovoltaic applications.

6.2 Result and Discussion

6.2.1 Chirality transfer in crystal structures

In recently reported work, chiral MBA_2PbI_4 (MBA = methylbenzylammonium) perovskite is the most common chiral perovskite, which has a strong CPL at low temperatures (*69*). Lots of work focused on finding different derivatives of MBA organic molecules, such as 4Br, Cl, FMBA, to form novel chiral perovskites (*11*, *78*, *106*). They usually added another halide atom at the opposite position of the amino group on the aromatic ring, which would trigger

different optical properties of chiral perovskite. From current work, we find that not only the type of halide atom but also the position of the halide atom on the aromatic ring is an important factor in controlling the chiroptical properties of formed chiral perovskites. Thus, we try to change the position of the Br atom on the aromatic ring from para- to meta-position (Fig. 6.1), which shows a higher dissymmetry in their organic structures, and successfully generate novel chiral 2D layered perovskite (R/S)-3BrMBA$_2$PbI$_4$.

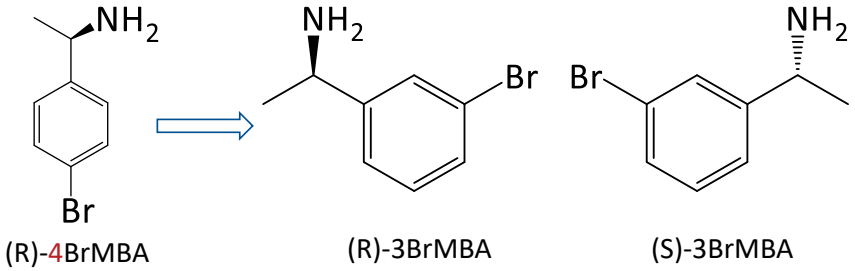

Fig. 6. 1. Chemical structures of chiral organic enantiomers (R)-4BrMBA and (R/S)-3BrMBA.

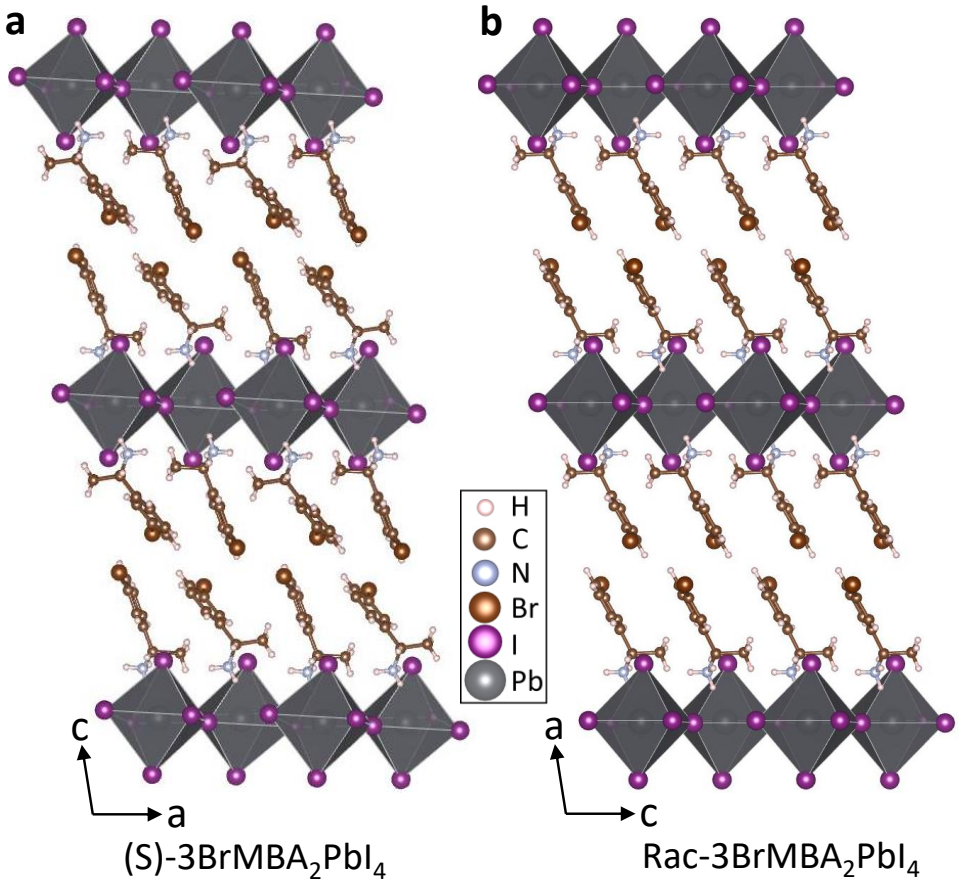

Fig. 6. 2. Single-crystal structure of 2D (S/Rac)-3BrMBA$_2$PbI$_4$ perovskites. a,b, Crystal structure of (S)-3BrMBA$_2$PbI$_4$ and Racemic-3BrMBA$_2$PbI$_4$ single-crystal structures.

A hydrothermal approach with controlled cooling rates was used to prepare chiral perovskite single crystals. We use single crystal x-ray diffraction (XRD) to identify their crystal structure, which shows the chiral perovskite samples crystallize in the P 2_1 space group with a distorted chiral crystal structure (Fig. 6.2). At the same time, the broken symmetry is absent for their corresponding racemic (Rac) crystals with a centrosymmetric structure (Detailed structure information in Table B5). Besides, the P 2_1 space group also belongs to one of Sohncke space group (*11*), proving our chiral 2D perovskite possesses a chiral crystal structure. Further, the bond length distortion index (D) and bond angle variance degree (σ^2) quantify the distortion degree of perovskite octahedron (detailed calculations in Table B6), which would be both 0 with full symmetry. Compared to the racemic sample (D = 0.006, σ^2 = 20.87), chiral (S)-3BrMBA$_2$PbI$_4$ shows a twice larger distortion index of 0.012, and a much higher angle variance value of 31.91, which is also relatively large value compared to other chiral 2D perovskites(*55*) All the current results prove that the introduction of new chiral organic molecules into the perovskite framework contributes to the strong distortion of PbI_2 octahedral structures.

We then transferred the chiral perovskite single crystal into perovskite thin films by spin-coating methods. In short, the single crystal samples were first dissolved inside DMF solvent, which was then directly spin-coated on glass substrates. After annealing at 100 °C for 10 mins, yellow perovskite thin films formed on top of glass substrates with a thickness of ~100 nm. We performed XRD measurements on as-obtained thin films (Fig. 6.3), which show well-overlapped diffraction patterns as single-crystal results, confirming the successful transfer of chiral perovskite single-crystal structure into thin-film structures.

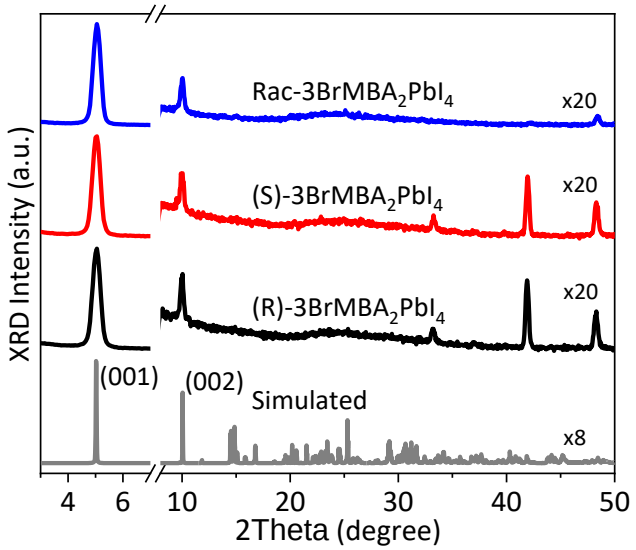

Fig. 6. 3. X-ray diffraction (XRD) patterns of chiral (R/S)-3BrMBA$_2$PbI$_4$ and Racemic-3BrMBA$_2$PbI$_4$ thin films. XRD results indicated thin film samples show a similar structure as a single crystal, with a preferred (001) plane orientation.

6.2.2 Steady-state chiroptical characterizations

In our current research, we use spin-coated thin films to investigate the general optical properties of chiral and racemic 2D perovskites. Steady-state linear absorption spectra reveal that the excitonic peak for both chiral enantiomers, (R) and (S)-3BrMBA$_2$PbI$_4$, coincides at 488 nm. In contrast, the racemic samples display an excitonic peak that is red-shifted to 500 nm as depicted in Fig. 6.4a. This significant redshift of approximately 60 meV underscores the more pronounced structural distortions induced by the chiral organic cations within these chiral perovskites compared to other chiral perovskite structures (*103*, *107*, *108*).

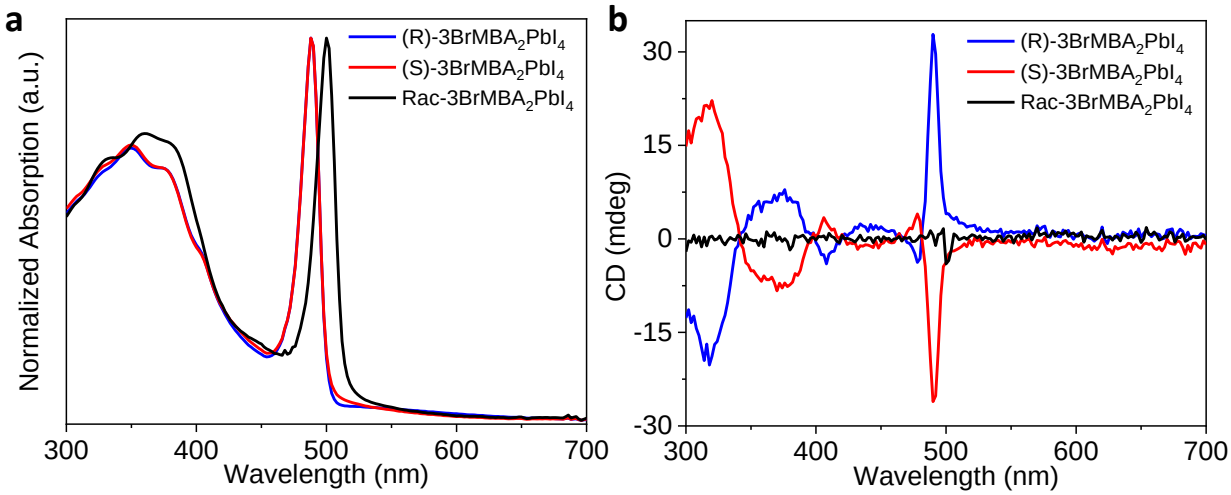

Fig. 6. 4. Comparison of general optical properties between chiral (R/S)-3BrMBA$_2$PbI$_4$ and Rac-3BrMBA$_2$PbI$_4$. a, b, Linear absorption (a) and circular dichroism spectra (b) of 2D perovskite thin films.

Neumann–Curie principle (*109*, *110*), explaining the relationship between structure symmetry and their physical properties, further enables our perovskite materials with a chiral crystal structure, which belongs to Sohncke space groups, to exhibit chiral optical properties. We then performed CD measurements on our chiral perovskites, which indicate the chiral enantiomer features of chiral (R) and (S)-3BrMBA$_2$PbI$_4$, with clear opposite CD signals from 300 nm to 550 nm, but racemic samples show no signals (Fig. 6.4b). The highest CD values of chiral perovskites are exactly located at their absorption excitonic peak position, which

elucidates the actual chirality transfer from chiral crystal structures to the band structures.

Fig. 6.5 presents the linear PL spectroscopy results of chiral and racemic 2D perovskite thin films at room temperature. Coherently, chiral (R) and (S)-3BrMBA$_2$PbI$_4$ exhibit similar PL features with a sharp excitonic emission at ~496 nm, and the PL peak of Rac-3BrMBA$_2$PbI$_4$ locates at ~508 nm. Both of them are slightly redshifted compared to their corresponding absorptions due to Stokes shift. TCSPC measurements show that the PL decays of chiral and racemic samples are the same (Fig. A24). Importantly, under 405 nm excitation with a fluence of 132.7 mW/cm^2, and 6 times repeated experiments, we find the PLQE value of pure chiral 2D perovskite thin films achieves 19% (±5%), and such value further increases to 39% (±4%) for their single crystal samples. This champion optical result indicates the dominantly radiative recombination channels in our chiral 2D perovskites, which is abnormal behavior compared to other chiral 2D perovskites with symmetry-broken structures (*82*).

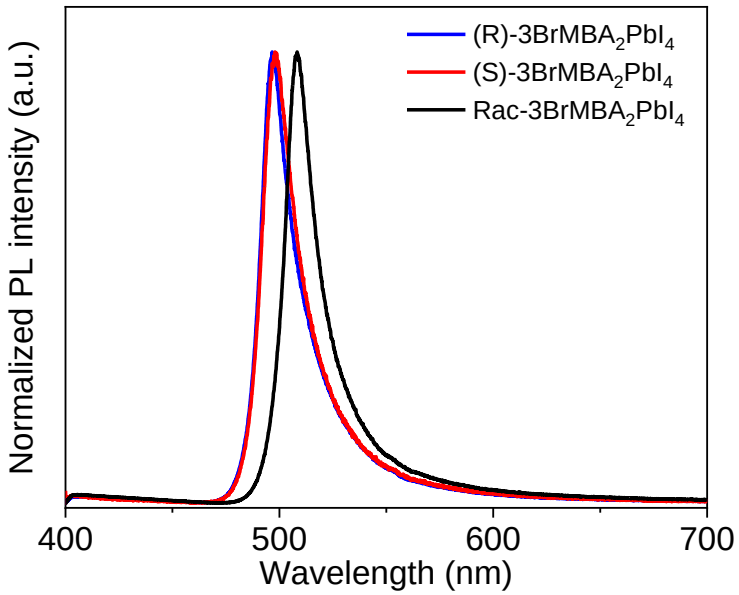

Fig. 6. 5. Comparison of general optical properties between chiral (R/S)-3BrMBA$_2$PbI$_4$ and Rac-3BrMBA$_2$PbI$_4$. Linear PL spectra of 2D perovskite thin films.

Upon their superior optical performance and highly distorted structures, we further use flat single-crystal samples (Fig. A25) for circularly polarized PL measurements at room temperature. We pumped the samples with a linear excitation at 405 nm, and the generated emission was passed through a quarter waveplate and a Wollaston prism pair to separate the right-handed and left-handed circularly polarized emissions. Then, after a 45° linear polarizer,

right-handed and left-handed emissions were simultaneously collected by one camera but at different regions to get a better comparable result. Both $MAPbBr_3$ and Rac-3BrMBA$_2$PbI$_4$ samples were used to calibrate the spectra (Fig. A26). Fig. 6.6 shows the CPL results collected from (R), Rac, and (S)-3BrMBA$_2$PbI$_4$ single crystal samples, respectively. Each plot is the average result from 5 different spots on single crystals. We observe significant intensity differences between right-handed and left-handed detectors, and the spectral differences for (R) and (S)-3BrMBA$_2$PbI$_4$ crystals, which feature opposite chiralities, can also flip their sign as in CD spectra. Rac-3BrMBA$_2$PbI$_4$ crystals show almost the same PL intensity between right-handed and left-handed detections. Further, the polarization degrees of CPL can be expressed as,

$$P_{CPL} = \frac{I_{\sigma+} - I_{\sigma-}}{I_{\sigma+} + I_{\sigma-}} \tag{29}$$

where $I_{\sigma+}$and $I_{\sigma-}$ are the integrated PL intensity with right-handed and left-handed detectors, respectively. The calculated P_{CPL} of chiral (R) and (S)-3BrMBA$_2$PbI$_4$ crystals at room temperature are ~52% and ~34 %, respectively, which is almost three times as large as previously reported strong CPL value from chiral 2D perovskite (R)-MBA$_2$PbI$_4$ at low temperature (*103*), further confirming the successful chiral-induced polarization in our chiral 2D perovskites.

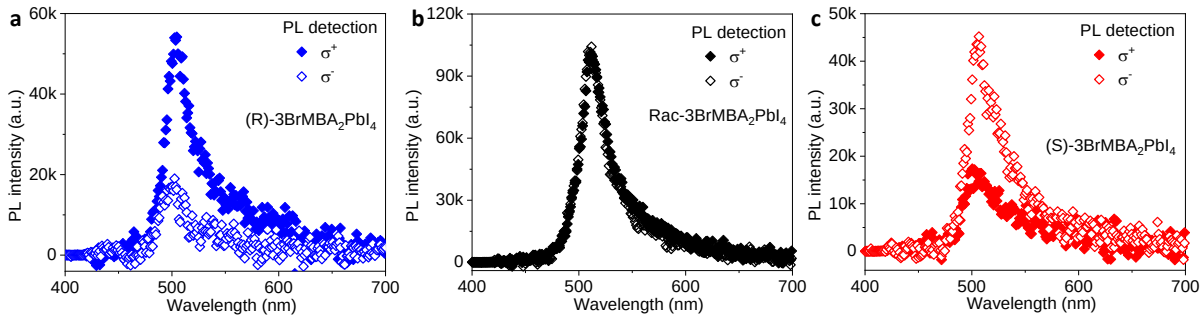

Fig. 6. 6. Comparison of chiroptical properties between chiral (R/S)-3BrMBA$_2$PbI$_4$ and Rac-3BrMBA$_2$PbI$_4$. a-c, Circularly polarized PL (CPL) spectra of (R/S)-3BrMBA$_2$PbI$_4$ and Rac-3BrMBA$_2$PbI$_4$ single crystals at room temperature. CPL results were obtained under linear excitation at 405 nm, and σ^+ and σ^- signals were detected simultaneously on different regions of the camera. Chiral (R) and (S) crystals exhibit opposite CPL signals, but racemic samples show comparable σ^+ and σ^- signals, confirming that crystalline chirality successfully induces chiroptical properties.

We further investigate the PL and CPL measurement on chiral 2D perovskite at low temperatures considering the strong phonon-phonon interactions at room temperature. For low-temperature measurements, we find a clear increase in PL intensity and a large decrease in PL width at 4 K (Fig. 6.7a). Another broad PL feature shows at a higher wavelength position, which we attribute to trapped exciton signals. Interestingly, there is clearly an increased intensity difference between left-handed and right-handed PL detections at free exciton positions (Fig. 6.7b) compared to room temperature measurements. At the same time, overlapped PL signals were observed at trapped exciton positions, confirming that polarization mainly stays at free excitons. When excitons are localized, they may lose their polarizations.

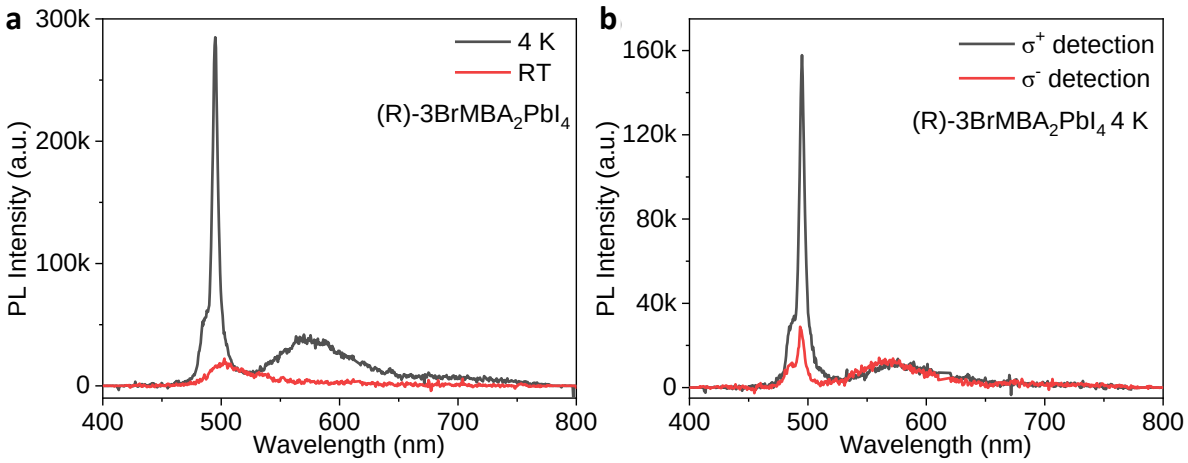

Fig. 6. 7. PL and CPL measurements at cryogenic temperatures. **a,** Comparison of PL spectra from chiral (R)-3BrMBA$_2$PbI$_4$ samples at different temperatures. **b,** CPL spectra of chiral (R)-3BrMBA$_2$PbI$_4$ samples obtained at 4 K.

6.2.3 Time-resolved charge carrier recombination

From our current work, we find our chiral perovskites show strong CD signals at the absorption band position and the largest CPL degree up to ~50% at room temperature under linear excitations. Furthermore, PL efficiency measurements confirm our chiral perovskites also exhibit a high degree of PLQE values, reaching 39% at room temperature. Such high PL polarization degree and large PLQE value obtained at room temperature, to the best of our knowledge, are first reported record values in chiral perovskite systems. In order to understand that both high PL efficiency and large polarization degree are simultaneously acquired in our chiral perovskites, we then performed transient absorption (TA) spectroscopy

measurements to study their charge carrier decay channels.

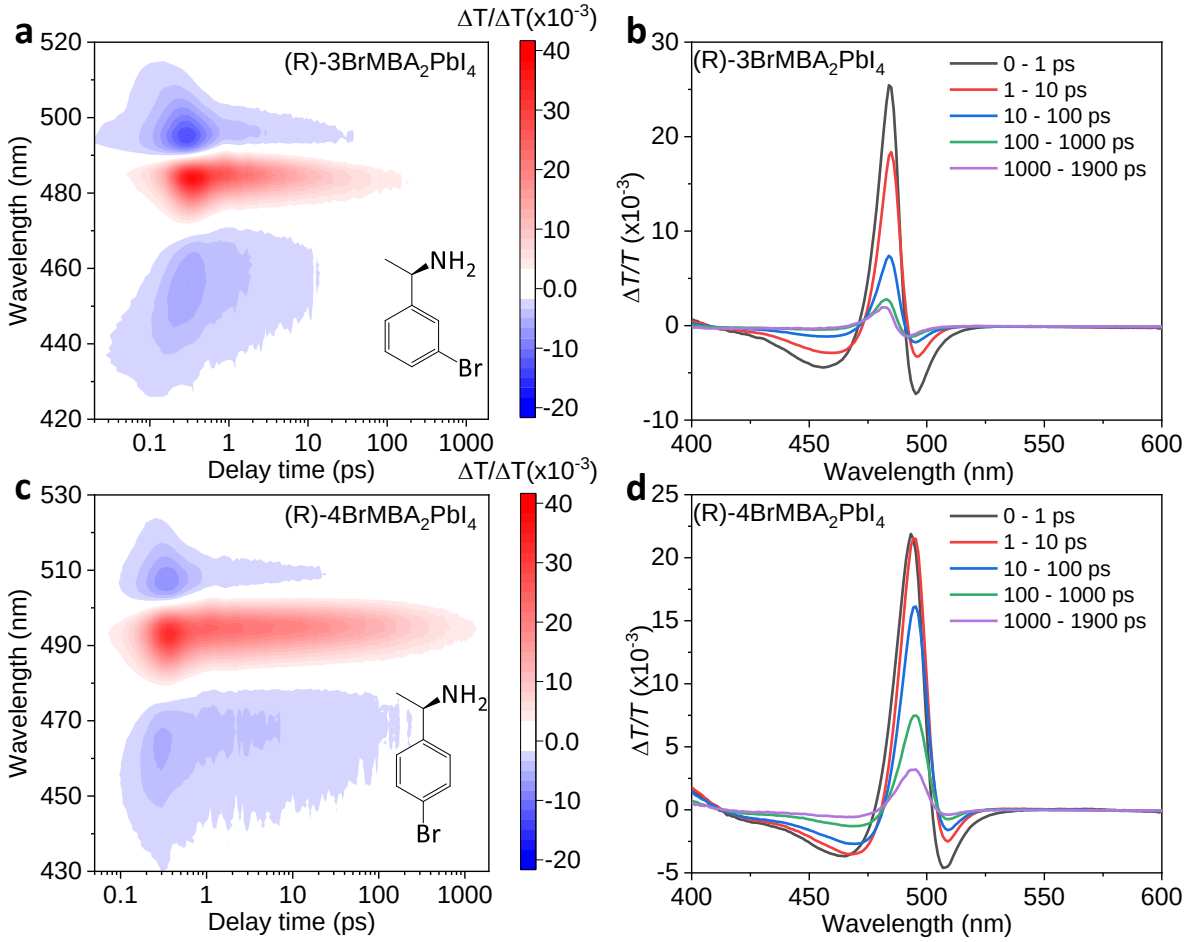

Fig. 6. 8. Charge carrier dynamics of chiral perovskite thin films. a, c, Transient absorption (TA) maps, and **b, d,** time-resolved spectra of (R)-3BrMBA$_2$PbI$_4$ and (R)-4BrMBA$_2$PbI$_4$ thin films, respectively. TA spectra were collected under 385 nm excitation with a pump fluence of ~1 μJ/cm^2.

Fig. 6.8a and 6.8c compare the TA color maps obtained from (R)-3BrMBA$_2$PbI$_4$ and (R)-4BrMBA$_2$PbI$_4$ spin-coated films, with the same excitation wavelength at 385 nm and pump fluence of ~1 μJ/cm^2. (R)-4BrMBA$_2$PbI$_4$ films are used as reference samples. Both of them show ground state bleach (GSB) signals at the absorption band edge positions, and two photoinduced absorption (PIA) signals are located on both sides of GSB. The evolutions of their TA spectra from 0 to 1900 ps are further presented in Fig. 6.8b and 6.8d. We find that the TA signals of (R)-3BrMBA$_2$PbI$_4$ are blue-shifted compared to these of (R)-4BrMBA$_2$PbI$_4$, which are ascribed to more distorted structures with (R)-3BrMBA cations (*111*). Similar trends can also be found in their steady-state absorption and PL spectra (Fig. A27). More importantly, it is noticeable that the TA decay at the GSB regions of (R)-3BrMBA$_2$PbI$_4$ is

exceptionally fast than that of the (R)-4BrMBA$_2$PbI$_4$ sample. Their decay kinetics at GSB regions are plotted together in Fig. 6.9a for comparison. Considering the complicated configurations of the current TA signals, tetra-exponential decay was used to get the best fit here (detailed fit results in Table B7). The average TA lifetime of (R)-3BrMBA$_2$PbI$_4$ and (R)-4BrMBA$_2$PbI$_4$ is about 150 ps and 400 ps, respectively. In addition to the relatively fast radiative decay, we find the main reason for the shorter decay lifetime of (R)-3BrMBA$_2$PbI$_4$ is the suppressed nonradiative decay, which usually exhibits a longer lifetime. For both (R)-3BrMBA$_2$PbI$_4$ and (R)-4BrMBA$_2$PbI$_4$, the fitted nonradiative decay lifetime is ~1700 ps. But the amplitude of the nonradiative decay of (R)-3BrMBA$_2$PbI$_4$ is ~8%, which is almost 3-fold smaller than that of (R)-4BrMBA$_2$PbI$_4$ (~21%). We count this as the key evidence for the high PLQE value of (R)-3BrMBA$_2$PbI$_4$ samples with heavily suppressed nonradiative decay. Fluence-dependent TA kinetics indicate the nonradiative decay can be further shrunk to ~6% with increased fluence (Fig. A28a). The difference in optical performance between (R)-3BrMBA2PbI4 and (R)-4BrMBA$_2$PbI$_4$ also indicates the structure symmetry of organic cations is an important factor in controlling the performance of chiral HMHPs.

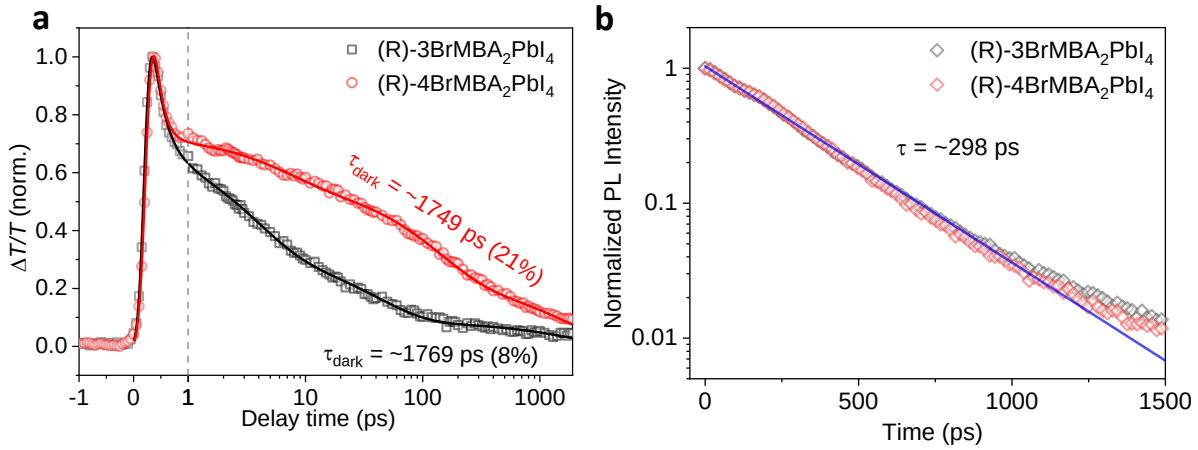

Fig. 6. 9. Charge carrier dynamics of chiral perovskite thin films. a, Transient absorption recombination kinetics at GSB regions, and **b,** time-correlated single photon counting (TCSPC) kinetics of (R)-3BrMBA$_2$PbI$_4$ and (R)-4BrMBA$_2$PbI$_4$ thin films, respectively. TA spectra were collected under 385 nm excitation with a pump fluence of ~1 μJ/cm^2, while TCSPC measurements were performed with photoexcitation at 405 nm (~10 μJ/cm^2).

Fig. 6.9b shows the time-correlated single photon counting (TCSPC) kinetic plots of (R)-3BrMBA$_2$PbI$_4$ and (R)-4BrMBA$_2$PbI$_4$ thin films. Their PL decay kinetics are extracted at excitonic PL peak positions and can overlap with each other at the same pump fluence (405 nm, ~10 μJ/cm^2), which fit well with the monoexponential decay at the initial 1200 ps with a

fitted lifetime of ~298 ps. Unlike TA spectra would investigate the kinetics of all photocarriers, including nonradiative decay (*90*), which would be a suitable tool to detect dark or defect state changes in our 2D chiral perovskites, the PL decay only detects the radiative recombination, which would explain the difference results we obtained from TA and TCSPC measurements. Furthermore, the unnormalized TCSPC intensity difference between (R)-3BrMBA$_2$PbI$_4$ and (R)-4BrMBA$_2$PbI$_4$ with the same collection time also indicates a much brighter emission of (R)-3BrMBA$_2$PbI$_4$ (Fig. A29). Fluence-dependent TCSPC measurements (Fig. A28b) indicate that the PL lifetime would gradually decrease with enlarged fluence and then stabilize after ~10 μJ/cm^2), which is consistent with TA results. Generally, low fluence would result in the population of dark or defect states, which further increases the nonradiative decay and extends the decay lifetime. From the results above, we conclude that, upon cation engineering, chiral 3BrMBA$_2$PbI$_4$ with a more distorted chiral crystal structure would severely minimize non-radiative losses, which further results in efficient, brighter emissions.

6.2.4 Time-resolved polarization dynamics

For the purpose of interpreting the high CPL degree at room temperature, CTA spectroscopy measurements were performed to explore the exciton polarization kinetics of chiral 2D perovskite thin films. Compared to the linear TA measurements, linear polarizers and quarter waveplates were further used to control the circularly polarized directions of pump and probe beams. TA spectra and kinetics showing the difference between counter and co-polarized spectra collected from (R)-3BrMBA$_2$PbI$_4$ enantiomers were depicted in Fig. 6.10a and 6.10b, respectively.

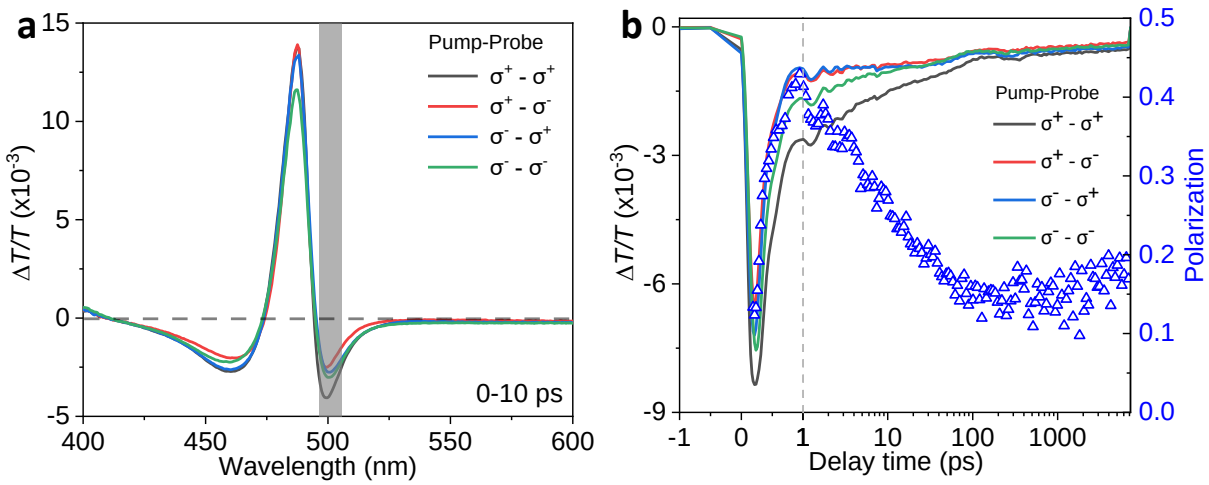

Fig. 6. 10. Circularly polarized transient absorption (CTA) spectroscopy of chiral (R)-3BrMBA$_2$PbI$_4$ perovskites under 385 nm excitation with a pump fluence of ~2.5 μJ/cm^2. **a, b,** CTA spectra and kinetics showing the difference between four circularly polarized configurations. The different polarization configurations are indicated (σ^+ (right-handed) or σ^- (left-handed)). The spectra results are the average results for the initial 10 ps. The decay kinetics are extracted within the gray spectral ranges in (a), and the polarization relaxation kinetics between black and red curves are calculated and plotted as blue triangles.

Under σ^+ or σ^- excitation at 385 nm (~1 μJ/cm^2), (R)-3BrMBA$_2$PbI$_4$ shows a clear difference between σ^- and σ^+ probes at both GSB regions and PIA regions, confirming the existence of polarized states after photoexcitation. Compared to the counter-polarized pump-probe configuration, the TA signals with co-polarized configurations always show higher intensities, as we expected. However, in nonchiral systems measured in co-polarized TA configurations, signals from co- and counter-polarized pump-probe display the same depolarization kinetics (*65*, *66*). Unexpectedly, for our chiral (R)-3BrMBA$_2$PbI$_4$, signals from co- and counter-polarized pump-probe configurations show different depolarization kinetics and TA signals, with right-handed pump and right-handed probe exhibiting higher intensities, indicating the existence of intrinsic polarization in chiral materials. This is also reasonable because, in addition to the polarized states generated from circularly polarized photo-excitations, the chiral perovskite itself would initially produce polarized states according to the Rashba effect due to the highly distorted structures with broken inversion symmetry.

We further extracted the decay kinetics at PIA regions from CTA spectra and calculated their polarization degree (P_{CTA}). The following equations determined the polarization degree of CTA signals,

$$P_{CTA} = \frac{\Delta T/T_{counter} - \Delta T/T_{co}}{\Delta T/T_{counter} + \Delta T/T_{co}} \quad (30)$$

where $\Delta T/T_{counter}$ and $\Delta T/T_{co}$ are the TA signals with counter and co-polarized configurations, respectively. Fig. 6.10b compares the PIA delay kinetics with different polarization configurations for chiral (R)-3BrMBA$_2$PbI$_4$, with their polarization degree plotted in blue triangles. Since time zero, the polarization degree of (R)-3BrMBA$_2$PbI$_4$ shows a positive signal, and gradually increases to ~45% at first ps, and decay slowly over 100 ps, and then stabilizes at ~20% until the end of detection (~8 ns). Such room-temperature long-lived polarization lifetime is the largest value observed in lead halide perovskite systems at

room temperature(*38*, *40*).

In order to detect intrinsic polarized states of chiral perovskites, we applied a linearly polarized pump to excite the chiral perovskites. Then we detected the TA signals with circularly polarized probes. As expected, chiral (R)-3BrMBA$_2$PbI$_4$ exhibits different decay kinetics for right-handed and left-handed probes without the efforts of circularly polarized excitation (Fig. 6.11a). The degree of polarization between right-handed and left-handed probes starts from 0% at time zero and increases to the maximum positive value of ~15% during the initial 1 ps, after which it decays to ~10% at 7 ns.

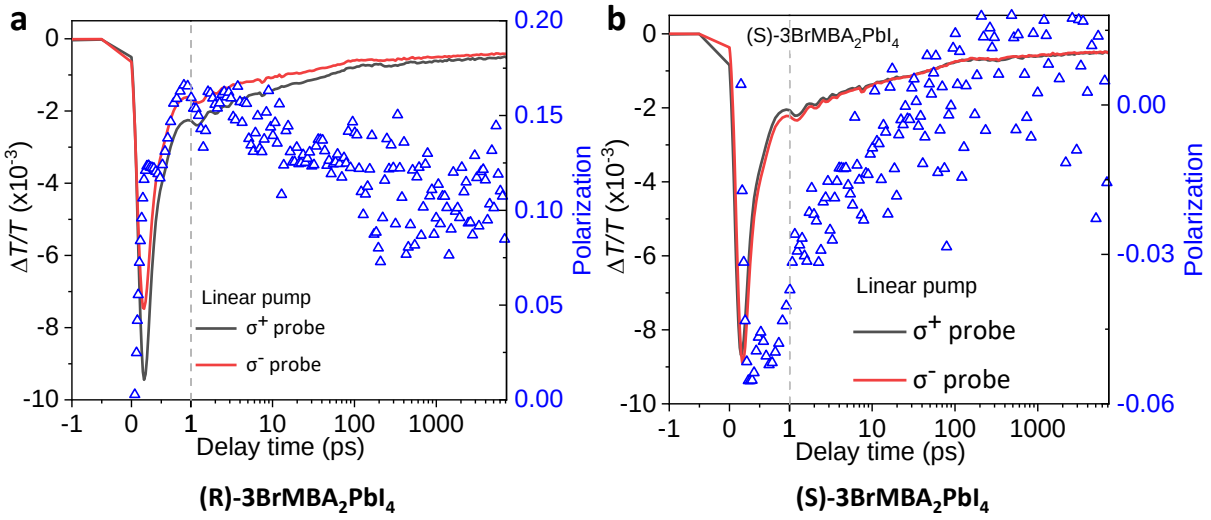

Fig. 6. 11. Circularly polarized transient absorption (CTA) spectroscopy of chiral (R/S)-3BrMBA$_2$PbI$_4$ perovskites, under 385 nm excitation with a pump fluence of ~2.5 μJ/cm^2. **a, b,** Comparison of TA kinetics with linear pump and circularly polarized probes, collected from chiral (R) and (S)-3BrMBA$_2$PbI$_4$ films.

Also, we performed CTA spectroscopy measurements on chiral (S)-3BrMBA$_2$PbI$_4$ samples with linear pump and circularly polarized probes (Fig. 6.11b), which indicate the dominant population states in chiral (S)-3BrMBA$_2$PbI$_4$ samples are left-handed photons with negative values for the degree of polarization, which shows a good consistency to room-temperature CPL results. Apparently, different chirality directions of (R) and (S)-3BrMBA$_2$PbI$_4$ result in reversed profiles between σ^+ and σ^- TA kinetics, demonstrating the strong exciton polarization in chiral 2D perovskites with intrinsic spin injections. The dominant spin polarization directions in chiral materials can be determined by their chirality directions, which is the main reason for the opposite CTA signals for (R) and (S)-enantiomers. More importantly, we find the σ^+ photons decay much slower than σ^- photons in chiral (R) samples,

which would further result in the population of σ^+ photons.

Besides, we found the degrees of polarization for chiral perovskites (R)-3BrMBA2PbI4 samples didn't go to zero at the limit of our short-term TA measurements; we further performed circularly polarized TA measurements up to microsecond time delays on chiral perovskites. Clearly, under circularly polarized excitation, the difference between co- and counter-polarized TA signals persists for as long as 2 μs (Fig. 6.12). This 2 μs polarization lifetime in our materials is the longest value observed in lead halide perovskite systems. According to the results above, we think the long-lived chirality-dependent polarized excitons in chiral perovskites, which exist even longer than their fast PL radiative decay lifetime (Fig. 6.9), would be the key explanation for the high and efficient CPL results at room temperature.

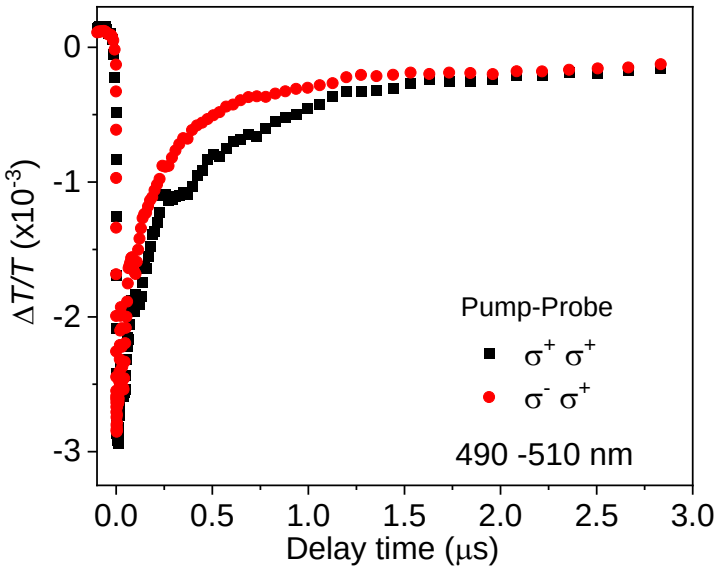

Fig. 6. 12. Long-term CTA kinetics obtained from PIA regions. At room temperature, chiral (R)-3BrMBA$_2$PbI$_4$ shows different depolarization kinetics for σ^+ and σ^- states.

6.2.5 Spin-polarized band structure in chiral 2D perovskites

To find the reason for their high PLQE value and large degree of CPL, we also performed DFT calculations on chiral perovskite (R) and Rac-3BrMBA$_2$PbI$_4$ samples. The band structure analysis of the racemic compound (Fig. 6.13a and A30) illustrates a direct band gap at the Y point within the Brillouin zone, which is a general characteristic of 2D perovskites (*112*, *113*). The valence band maximum (VBM) primarily comprises iodine 5p orbitals with

lead 6s contributions, while the conduction band minimum (CBM) is predominantly lead 6p orbitals with minor iodine 5p contributions (Fig. 6.13b and A31). For chiral compound (S)-3BrMBA$_2$PbI$_4$, notably, the band gap widens by 100 meV due to increased structural distortion, consistent with observed blue shifts in absorption and PL spectra. An important part is the splitting of conduction bands induced by Rashba coupling in (S)-3BrMBA$_2$PbI$_4$ band structure (Fig. 6.13c and A32), as a consequence of the loss of centrosymmetry and large spin-orbit coupling (SOC) in lead halide compounds (*114*). In the valence band, the observed effect is subtle, characterized by a slight shift of the VBM in k-space, denoted as k_R, which is smaller than 0.01 Å^{-1}, with an energy splitting of 0.50 meV. This results in a Rashba parameter α_{VBM} = 0.08 eV·Å. Conversely, the impact is significantly more pronounced in the conduction band, evident in a notable displacement of the CBM away from the B point (0.02 Å^{-1}) and a 75 meV energy splitting, with a substantial Rashba parameter of α_{CBM} = 2.21 eV·Å. This finding aligns well with previously computed parameters in lead-iodide perovskites (*115*). We further consider the in-plane inter-octahedral distortion angle β (Pb-I-Pb bond angle) disparity $\Delta\beta = \beta_{max} - \beta_{min}$ for chiral materials, which is the relevant structural descriptor for the Rashba effect (*116*). It's worth noting that such a substantial computed Rashba parameter correlates with the significant disparity in the β angle within the structure of (S)-3BrMBA$_2$PbI$_4$ ($\Delta\beta$ = 11.9°). This places it among compounds with $\Delta\beta$ > 11°, known to exhibit considerable spin-splitting. Thus, DFT calculations confirm that compared to racemic perovskites, the asymmetry structure of chiral perovskite induces clear spin split at conduction band position, which would of course generate strong chiroptical features, like large CPL.

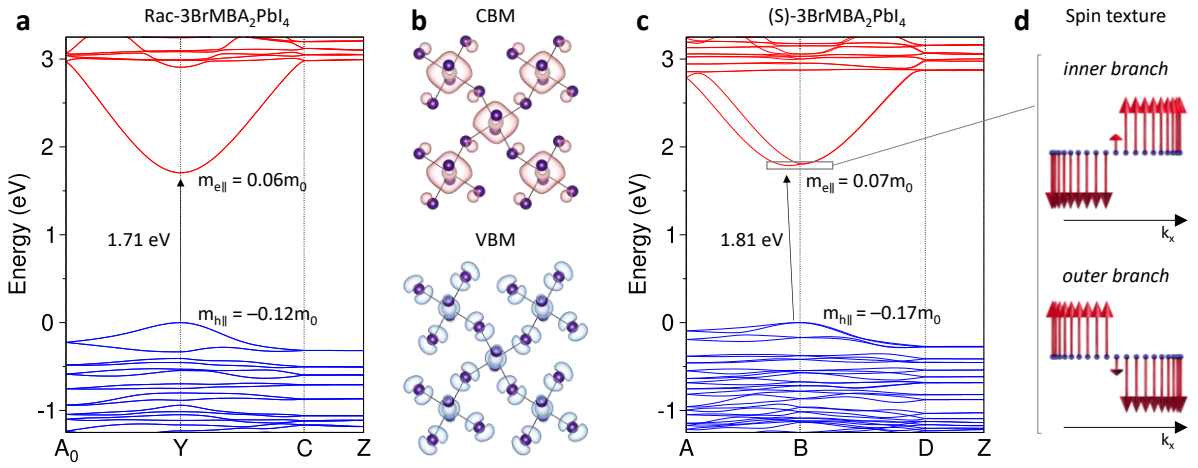

Fig. 6. 13. Electronic structure of 2D (S/Rac)-3BrMBA$_2$PbI$_4$ perovskites. a, c, DFT computed band structures of Rac-3BrMBA$_2$PbI$_4$ and (S)-3BrMBA$_2$PbI$_4$, respectively. In-plane hole (m_{hll}) and electron (m_{ell}) effective masses are computed at the valence and conduction band edges. **b,** Partial charge density taken at the valence band maximum (VBM) and conduction band minimum (CBM). **d,** Spin textures computed for the (S) structure in the (k_x,k_y) plane for the inner and outer branches of the conduction bands. DFT calculations were performed by Dr. Mikaël Kepenekian, Dr. Claudine Katan, and Dr. Jacky Even.

6.2.6 Chiral perovskite applications

Considering the strong chiroptical properties of our 2D chiral perovskites, we try to use them for chiroptical applications. Because we find large circular dichroism signals covering 300 to 500 nm. We fabricated a circularly polarized photodetector based on our chiral 2D perovskites, which show a large polarization between right-handed and left-handed light absorption (Fig. 6.14). We also try to make circularly polarized perovskite light-emitting diodes using our bright chiral 2D perovskites. However, the resulting electroluminescence is too weak and unstable, which makes it hard to detect reliable circularly polarized electroluminescence (Fig. A33). The main problem should be the weak conductivity of pure chiral 2D perovskite. Further introducing a 3D phase inside the chiral perovskite structure may improve the device properties.

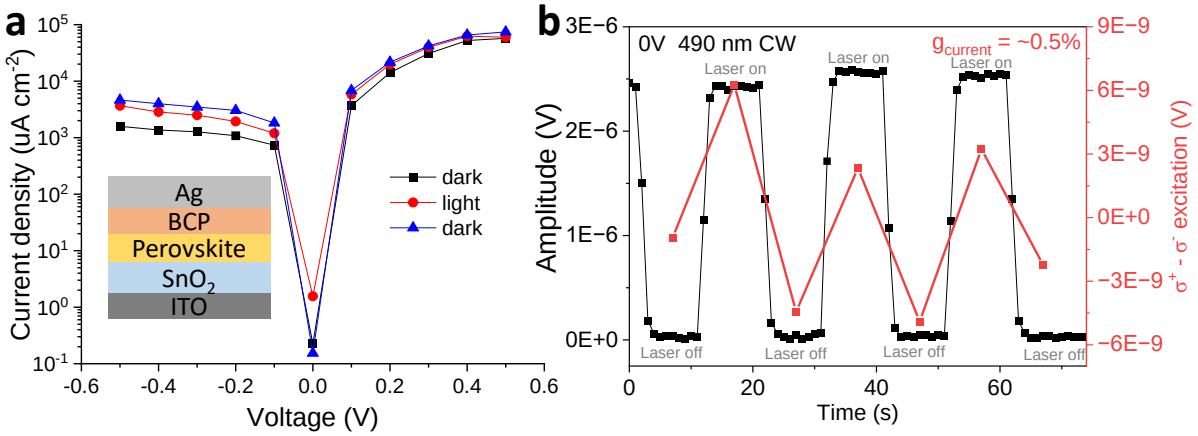

Fig. 6. 14. Device characterizations of chiral layered perovskite photodetectors. a, Current density−voltage curves of chiral perovskite (R)-3BrMBA2PbI4 based device. Inset of Fig. a is the corresponding photodetector device structure. **b,** Comparison of total photocurrent response (black curve) and circularly polarized photocurrent (red curve) of our chiral photodetectors. Photoelastic modulator and lock-in detector were used here to measure

small circularly polarized photocurrent values. The average $g_{current}$ of our chiral circularly polarized photodetector is ~0.5%.

6.3 Conclusion

In summary, we design and fabricate novel chiral 2D HMHP (R/S)-3BrMBA$_2$PbI$_4$ (3BrMBA = 1-(3-Bromphenyl)-ethylamine) as single crystals and thin films. SCXRD confirmed the formation of chiral perovskite structures with highly distorted octahedra. We further investigate their chiroptical properties by CD and CPL measurements, and we find our chiral perovskites show strong CD signals at absorption band position and largest CPL degree up to ~50% at room temperature under linear excitations. Furthermore, PL efficiency measurements confirm our chiral perovskites also exhibit a high degree of PLQE values, reaching 39% at room temperature. Such high PL polarization degrees and large PLQE values obtained at room temperature are first reported record values in chiral perovskite systems. In order to understand that both high PL efficiency and large polarization degree are simultaneously acquired in our chiral perovskites, we perform transient absorption (TA) spectroscopy measurements to study their charge carrier decay channels, which demonstrate that (R)-3BrMBA$_2$PbI$_4$ with a dominant fast radiative decay are the main reason for their superior optical performance, especially compared with (R)-4BrMBA$_2$PbI$_4$ (4BrMBA = 1-(4-Bromphenyl)-ethylamine). The difference in optical performance between (R)-3BrMBA$_2$PbI$_4$ and (R)-4BrMBA$_2$PbI$_4$ also indicates the structure symmetry of organic cations is an important factor in controlling the performance of chiral HMHPs. Circularly polarized TA measurements further confirm the polarized excitons in our chiral perovskite live longer than their PL lifetime, which would result in an efficient polarized PL. The DFT calculations also indicate the existence of evident opposite spin textures induced by chirality at band edge regions. Our demonstration of efficient chiroptical features in chiral 2D perovskite will provide a new avenue for the design of high-performance spintronic materials with efficient optical properties.

Chapter 7: Circularly Polarized Light-Emitting Diodes Using Chiral Hybrid Perovskite Heterostructure Emitters

The generation of light with the special property of circular polarization is desired for a wide range of applications, such as displays, telecommunication, and sensing. Next-generation lighting technologies aim to improve the efficiency of light generation, use the complex properties of light for advanced sensing, or exploit the quantum nature of light for information technologies.

In this chapter, we fabricate efficient and highly-polarized circularly polarized perovskite light-emitting diodes (CPeLEDs), directly using chiral hybrid metal-halide perovskite heterostructure as an emitting layer, which inherently shows bright emission with large polarization. The chiral perovskite emitter is made by adding chiral organic precursors (R/S)-3BrMBA (3BrMBA = 1-(3-Bromphenyl)-ethylamine) into three-dimensional $(FA_{0.7}MA_{0.1}GA_{0.2})_{0.87}Cs_{0.13}PbBr_3$ perovskite matrix. Using confocal photoluminescence mapping and transient optical measurements, we find the addition of chiral organic group results in the formation of chiral nanostructures in 3D perovskite films, which induces strong chirality and preserves the excellent charge transport features of 3D perovskites. The resulting CPeLED reaches an external quantum efficiency of ~10% with a brightness higher than 220,000 cd m^{-2} and a large degree of polarization of ~20%. We expect that our current work will greatly impact emerging display applications and quantum information technology developments.

The work in this chapter is based on the submitted results, which are still under the peer review process. See details below.

S. Liu, Y. Li, S. Bodnar, J. Zerhoch, J. A. Gessner, P. Kollenz, A. Shcherbakov, G. May, N. Solhtalab, M. W. Heindl, U. W. Paetzold, F. Deschler. Bright Circularly Polarized Light-Emitting Diodes Using Chiral Lead-Halide Perovskite Heterostructure Emitters. 2024 (under review)

7.1 Background

Light-emitting diodes (LED) are optoelectronic devices that convert electricity into photons. Tailoring the properties of the generated light, e.g., color, phase, or polarization, is a material and technology challenge. However, such ability is crucial for applications, e.g., sensing, information storage, or lasing. For the generation of circularly polarized light, a traditional way is producing unpolarized light in a commercial LED first and then using photonic structures, like circular polarizers, to induce circular polarization. This existing solution is inherently energetically inefficient since up to 50% of the generated electro-luminescence (EL) is discarded in the process. Thus, the use of bright light emitters that generate circularly polarized light intrinsically would be a vastly preferred solution, which, however, has proven challenging with existing material systems (*67*, *117*).

Most efforts in the research of circularly polarized light generation have been made to find more twisted chiral photonic structures or semiconductor materials with large chirality (*7*, *11*, *15*, *69*, *76*, *118*, *119*). However, creating such chirality in the electronic states of semiconductor materials is a material problem since available high-performance optoelectronic material systems are rarely transformable into chiral structures without hampering their semiconducting properties by forming defect states, such as inorganic, high-performance crystalline materials, or are difficult to fabricate into films with high conductivity and charge densities for maximum brightness, like organic, amorphous materials. The material class of solution-processable hybrid metal-halide perovskites has emerged as next-generation semiconductor materials for optoelectronics (*57*, *120*, *121*). These materials show exceptional tolerance in their electronic states to defects and crystal strain, which underpins bright emission in light-emitting devices and long-lived charge carriers for photovoltaic energy conversion. These excellent material properties can be used to synthesize chiral semiconductor materials with superior performance over existing chiral organic and inorganic systems.

Metal-halide chiral perovskites exhibit several promising polarization features, like large circular dichroism (CD) and circularly polarized photoluminescence (CPL), which make them suitable platforms for many applications, e.g. circularly polarized photodetectors (*16*, *47*), LED (CPLED) (*15*, *122*) or spin-filters using chiral-induced spin-selectivity (CISS) effects (*67*). There are two main strategies to fabricate chiral perovskites. Both of them

require large chiral organic amine groups to replace small organic cations to form low-dimensional chiral perovskite single-crystal structures or as chiral ligands to produce perovskite nanocrystals. Low-dimensional chiral perovskites usually show large CD or CPL values. However, due to their weak conductivity, it is hard to use them for optoelectronic applications, while chiral perovskite nanocrystals generally exhibit higher brightness but relatively weak polarization. Hence, there is little report about CPeLED using chiral perovskite emitter (*11*, *78*).

It has been reported that chiral perovskite materials can be used as spin-filter in LED devices for room-temperature spin LED (*67*, *123*). Circularly polarized EL (CEL) is generated due to the CISS effect. The resulted EL only shows a very low degree of polarization (smaller than 3%). In this work, we try to fabricate a novel CPeLED based on a chiral perovskite emitter, which may give us better opportunities to reach efficient circularly polarized electroluminescence.

7.2 Result and Discussion

7.2.1 Circularly polarized light-emitting diode performance

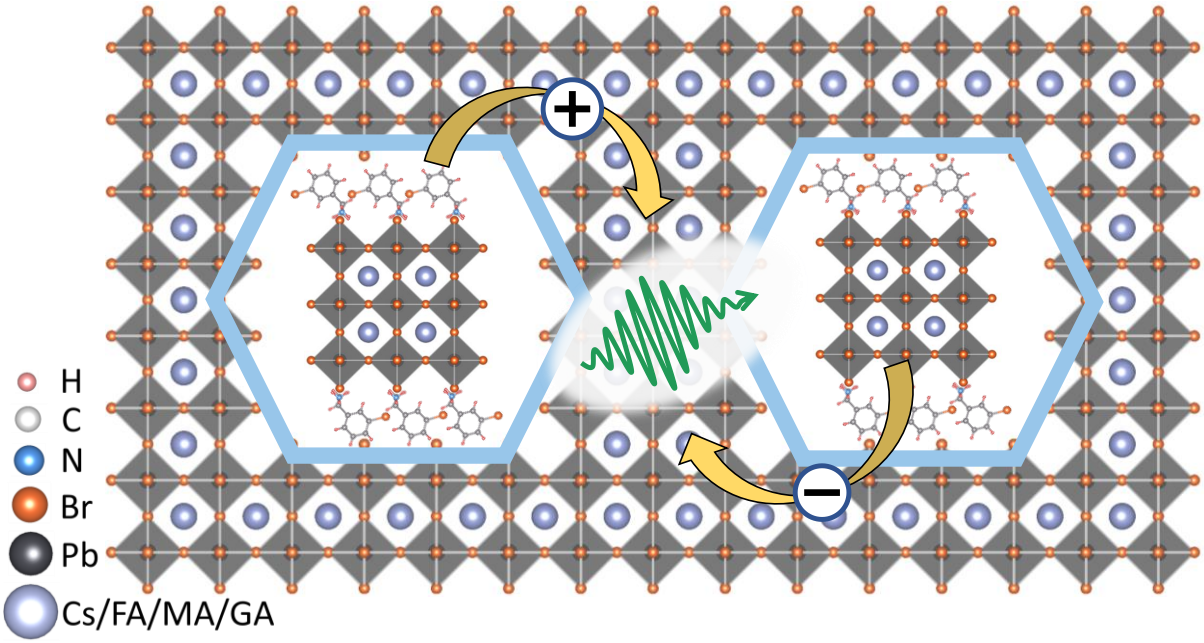

Fig. 7. 1. Schematic illustration of in-situ 3D perovskite structures functionalized by chiral ligands (R/S-1-(3-Bromphenyl)-ethylamine). FA: formamidinium; MA: methylammonium; GA: guanidinium.

The chiral perovskite thin films were prepared using spin-coating methods. Considering LED applications, it is required to fabricate structures that can transport charges efficiently from the injection layers to make them recombine efficiently. For this, we develop a heterostructure system of chiral quasi-2D perovskite nanostructures for polarized charge carrier injection within 3D bulk perovskite (Fig. 7.1). To fabricate these heterostructures, we follow a solution-based in-situ nanocrystal formation route that results into an exceptionally high luminescence yield, which is a necessary part for the integration of hybrid perovskites into efficient LEDs (*57, 120*). We further advance this approach by including nanocrystalline domains of our bright chiral perovskite emitter materials into a 3D bulk perovskite material that serves as charge transport material for efficient electroluminescence. We choose the same 3D $(FA_{0.7}MA_{0.1}GA_{0.2})_{0.87}Cs_{0.13}PbBr_3$ perovskites as 3D bulk materials and use chiral organic precursors (R)-3BrMBA (3BrMBA = 1-(3-Bromphenyl)-ethylamine) as chiral additives. Such chiral (R)-3BrMBA organic group is a suitable organic component of the hybrid perovskites, to unlock bright, and strongly circularly polarized photoluminescence (*7*). The efficient energy funneling in the chiral nanoparticle emitters has been reported before (*15, 122*), which ensures bright and strongly polarized luminescence in our heterostructures.

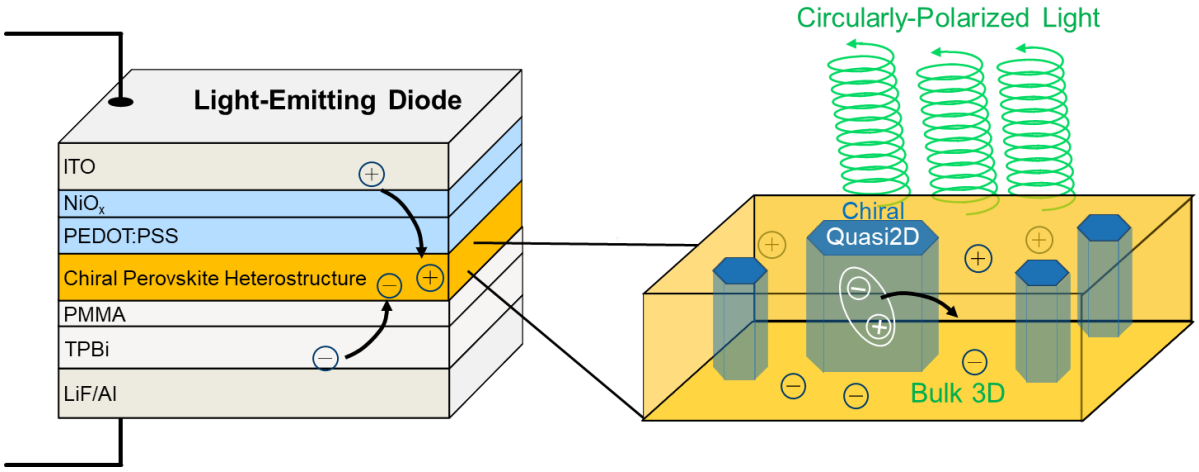

Fig. 7. 2. Schematics of CPeLED structures using chiral perovskite emitter. ITO, indium tin oxide; PEDOT, poly(3,4-ethylenedioxythiophene); TPBi, 1,3,5-Tris(1-phenyl-1H-benzimidazol-2-yl)benzene.

We fabricated CPeLED based on chiral perovskite heterostructure systems. Fig. 7.2 shows the general LED structure we used for CEL generation. Bi-layer NiO/Poly(3,4-

ethlyenedioxythiophene)polystyrene sulfonate (PEDOT:PSS) servers as the hole injection layer, TPBi as the electron injection layer, and LiF/Al as the cathodes. It is important to note that a thin layer of Poly(methyl methacrylate) (PMMA) is also spin-coated on top of the perovskite layer to balance the electron/hole injection.

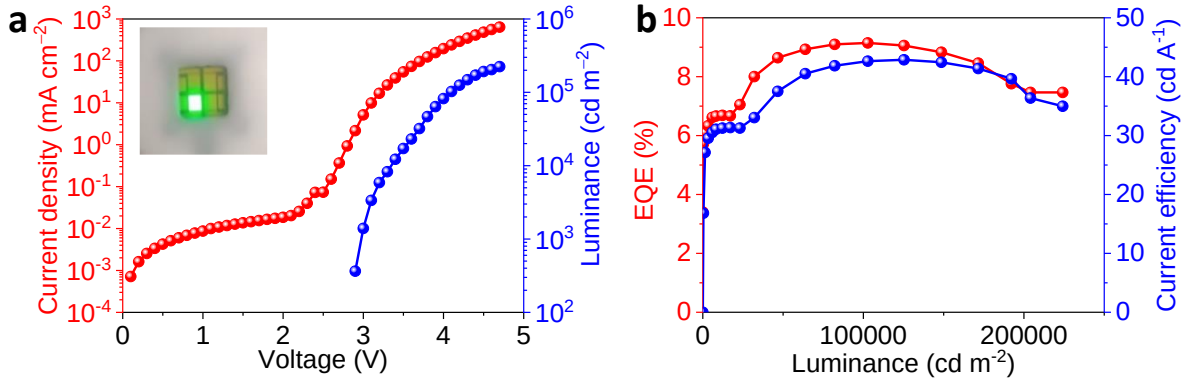

Fig. 7. 3. Electroluminescence Characteristics of CPeLEDs. a, Current density (red) and luminance (blue) versus voltage curves. Inset, photograph of a working device. **b,** EQE (red) and current efficiency (blue) versus luminance curves.

We further plotted the current density-luminance-voltage curves of our chiral perovskite LEDs in Fig. 7.3a. The chiral perovskite LEDs show a maximum EQE of ~9.2% (Fig. 7.3b), which is a relatively high value compared to reference pure 3D perovskites without any chiral organic precursors (smaller than 1%, Fig. A34) and other CPeLEDs based on chiral materials (*67*, *117*, *122*, *124*). Noticeably, our chiral perovskite LEDs exhibit bright electroluminescence centered at ~542 nm with narrow full width at half maximum (FWHM, ~20 nm), demonstrating the high purity of generated green light (Fig. A35).

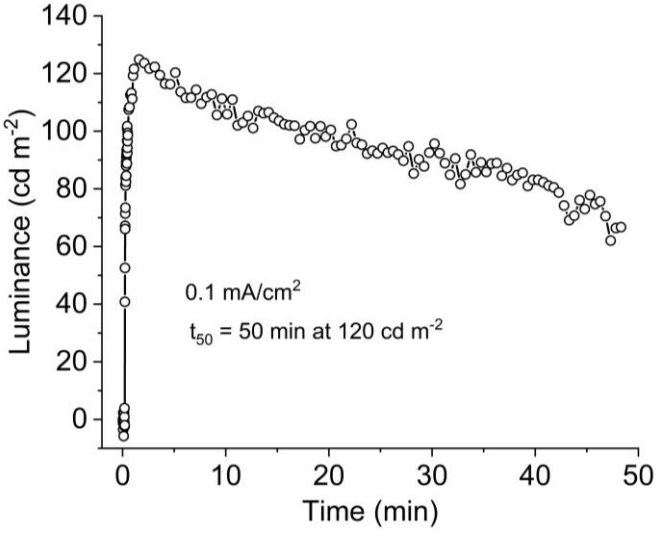

Fig. 7. 4. Operating stability of CPeLEDs based on chiral perovskite heterostructures. The measurements were performed under a constant current of 0.1 mA/cm^2.

We first used UV-curable glue and transparent glass for the CEL measurements to encapsulate LED devices. Besides, the device lifetime (the time to a drop of 50% in the light emission intensity) of our CPeLED is higher than 50 min, which allows for us to collect reliable CEL data (Fig. 7.4). During the running of CPeLED devices, we set the generated EL through a photoelastic modulator (PEM), which modulates the polarization of light between right-handed (σ^+) and left-handed (σ^-) with a frequency of 84 KHz (Fig. 7.5). A 45° linear polarizer was placed after PEM to cut one handedness of the light. Then, a 980 Hz chopper was used to provide reference input for lock-in detectors. The resulting light was further passed through a monochromator and then collected the signals using an avalanche photodiode (APD). Importantly, two lock-in detectors with different frequencies (980 Hz for chopper, 84 KHz for PEM) were used to record the total EL and CEL (difference between σ^+ and σ^- circularly polarized EL) simultaneously to avoid influence from sample degradation.

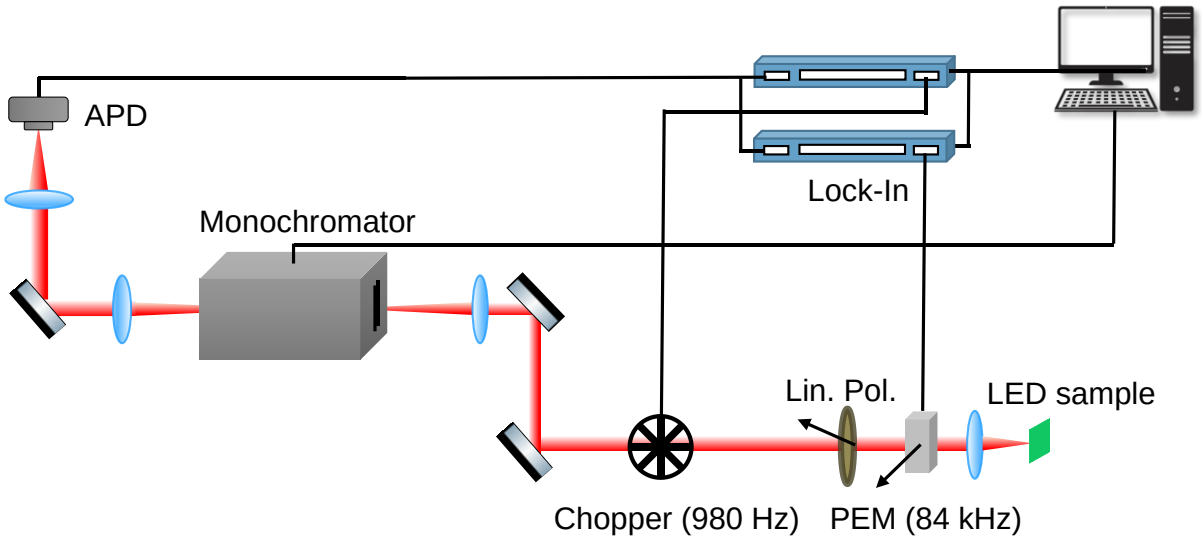

Fig. 7. 5. Optical layout of circularly polarized electroluminescence measurement configurations. PEM, photoelastic modulator; Lin. Pol., linear polarizer; APD, avalanche photodiode.

From lock-in detectors, we find clear CEL signals from 530 nm to 560 nm (Fig. 7.6a). Quantitatively, the degree of CPeLED polarization (P_{CEL}) was calculated using the following equation,

$$P_{CEL} = \frac{A_{CEL}}{A_{EL}} \tag{31}$$

where A_{CEL} and A_{EL} are the amplitudes of CEL and total EL signals, respectively. The highest P_{CEL} of our chiral perovskite LED reaches ~20% at ~545 nm. We further compared both efficiency (EQE) and the degree of EL polarization (P_{CEL}) with other recently reported circularly polarized LEDs (*5*, *15*, *67*, *117*, *122*, *125–128*) (Fig. 7.6b). We find that although organic LEDs can reach high polarization, the EQE value is pretty low due to the dark triplet generation. On the other hand, inorganic LEDs may reach high polarization but require strong magnetic fields and work under cryogenic temperatures. The performance of our chiral perovskite heterostructure LEDs is not only much superior compared to other perovskite LEDs, but they can reach a high degree of EL polarization and large EQE value at the same time without the need for magnetic fields. All these results have further proved our chiral perovskite heterostructures pave the way for room-temperature display and spintronic applications, which can achieve an efficient and highly polarized EL at the same time.

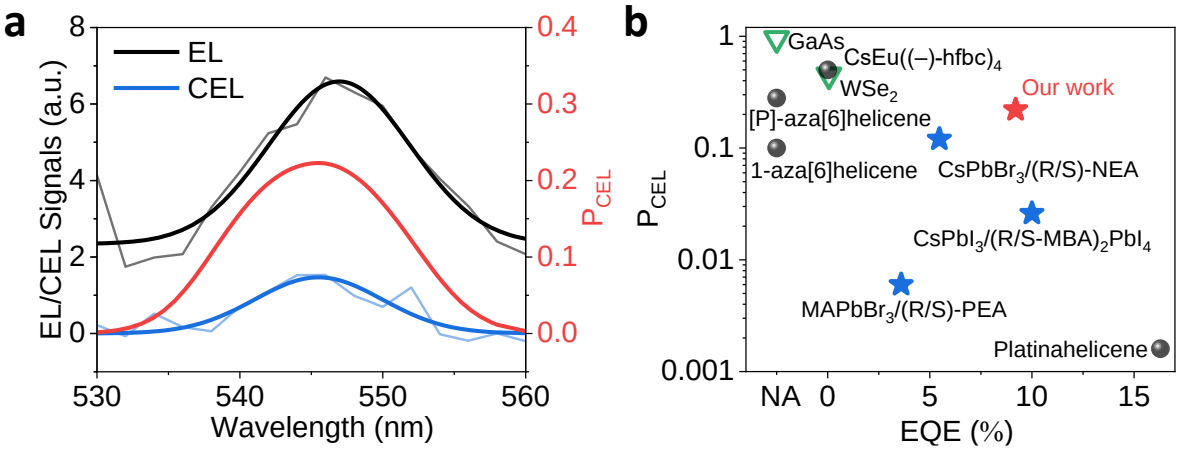

Fig. 7. 6. a, EL (black curve), and circularly polarized EL (CEL, blue curve) spectra of CPeLEDs measured by two lock-in amplifiers simultaneously. The polarization degree of CPeLEDs was also calculated as a red curve. **b,** Comparison of the degree of circularly-polarized electroluminescence (CEL) polarization and external quantum efficiency (EQE) values for recently reported promising circularly polarized LEDs (5, 15, 67, 117, 122, 125–128).

7.2.2 Chiral nanostructures formation on 3D perovskite matrix

To elucidate the formation of chiral perovskite heterostructure structures while involving chiral organic molecules, we utilize atomic force microscopy (AFM) to investigate their morphology evolution. Compared to the pristine 3D perovskite films (Fig. 7.7a), we observe a few nanoflake structures formed on top of perovskite clusters on chiral perovskite films

(Fig. 7.7b). We believe this is clear evidence for the formation of heterostructures. 3D bulk perovskites work as host structures homogenously distributed on the substrate for efficient charge transport. Chiral quasi-2D perovskite nanostructures would act as chirality injection sites randomly allocated in the whole materials. Further increasing the concentration of chiral additives, more quasi-2D nanostructures were found in Fig. 7.7c, as expected.

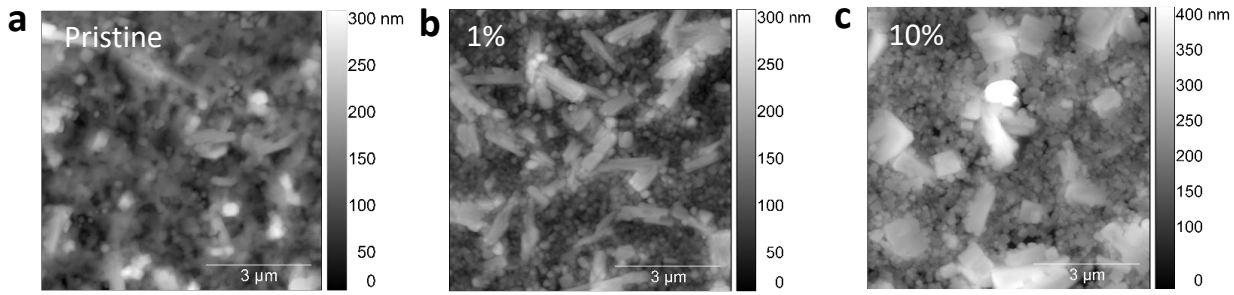

Fig. 7. 7. Morphology of chiral perovskite heterostructure films. a-c, Atomic force microscope (AFM) images of pristine (a), 1% (R)-3BrMBA (b), and 10% (R)-3BrMBA (c) treated samples. 1% and 10% are the ratios of (R)-3BrMBA to $PbBr_2$.

Besides, confocal PL image measurements also proved the formation of chiral domains on 3D perovskite films. Pure 3D perovskite films show a uniform PL distribution on the whole substrate (Fig. 7.8a). For the 1% and 10% (R)-3BrMBA treated samples, we find obvious PL inhomogeneous regions (blue regions in Fig. 7.8b and 7.8c), which show slightly blue-shifted emissions, compared to the yellow regions. We attribute such blue regions to the chiral quasi-2D nanostructures we observed from AFM images, with broadening bandgap structures. Their blue-shifted PL further enables the successful charge transfer from the high-energy domain with efficient chirality injections to 3D bulk perovskites, resulting in bright and strongly polarized luminescence. Consistent with the AFM results, more blue-shift quasi-2D domains were observed in 10% (R)-3BrMBA samples.

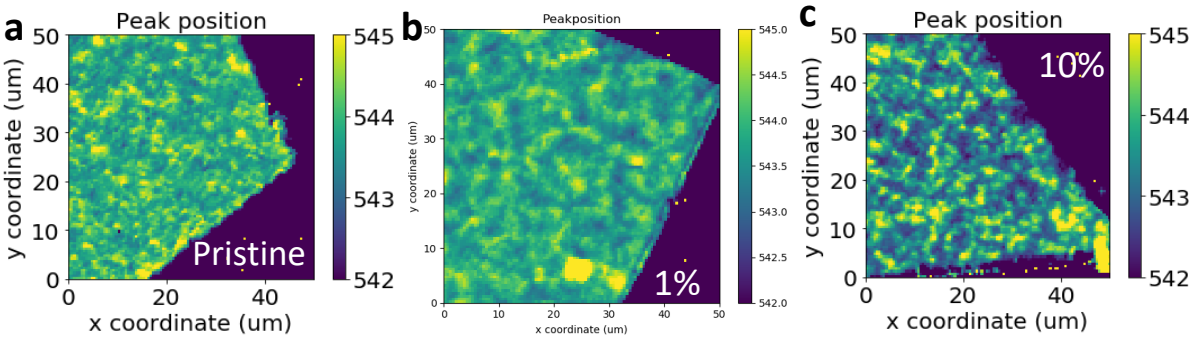

Fig. 7. 8. Confocal PL images of 3D perovskites with 0 (a), 1% (R)-3BrMBA (b), and 10% (R)-3BrMBA (c) additives. Obviously, chiral quasi-2D nanodomain formed with the addition of chiral organic molecules, which shows a blue-shifted PL compared to bulk 3D perovskite phases.

We further employ time-resolved PL (TRPL) to track the potential short-lived phases in chiral perovskite heterostructure films. Under 355 nm excitations (~24 nJ/cm^2), we find two obvious PL features located at ~510 nm and ~535 nm (Fig. 7.9), which we attribute to chiral quasi-2D domains and bulk 3D perovskite phases, respectively.

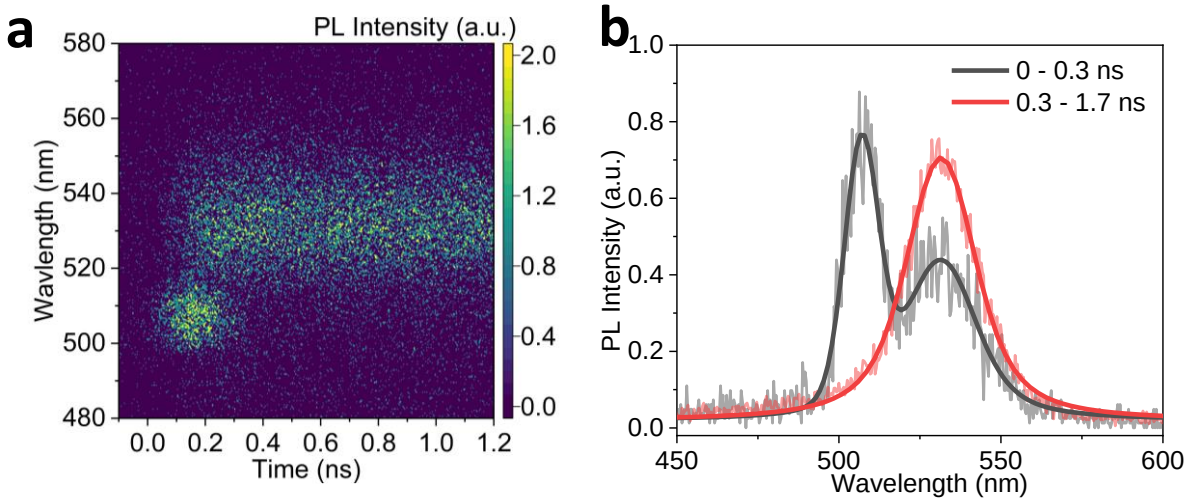

Fig. 7. 9. Time-resolved PL color maps (a) and spectra (b) of perovskite heterostructures with 1% (R)-3BrMBA additives. The measurements were performed under 355 nm excitations with a low fluence of ~24 nJ/cm^2.

We further plot their corresponding PL decay kinetics in Fig. 7.10. We notice that the PL signal of chiral domains located at ~510 nm vanishes fast over the initial ~300 ps. At the same time, 3D perovskite phases show a small rise this time, confirming the successful carrier transfer from high-energy chiral domains to low-energy 3D phases. The 3D perovskite phase also shows a long-lived bright state, which stays unchangeable until the end of our detection (~1.7 ns). We also perform TRPL measurements under higher fluence (Fig. A36), which show a much-diminished chiral domain (~510 nm) with a shorter PL lifetime. We think high fluence would result in fast radiative decay of chiral domains, which may compete with their carrier transfer channel to 3D phases. Besides, we use transient absorption spectroscopy (TA) to detect additional phase formation in our chiral perovskite films, like 2D or quasi-2D phases. For the samples with low (R)-3BrMBA concentrations (below 10%), only one

dominant TA feature was observed at ~540 nm, which should be ascribed to the 3D perovskite phase. The weak quasi-2D phases were covered by a strong PIA signal next to 540 nm (Fig. A37). However, excess amounts of (R)-3BrMBA (larger than 50%) induced additional TA features before 450 nm, which should belong to 2D or low-layered quasi-2D phases. Thus, for better conductivity and higher brightness, our CPeLED fabrication only uses low (R)-3BrMBA doping concentrations.

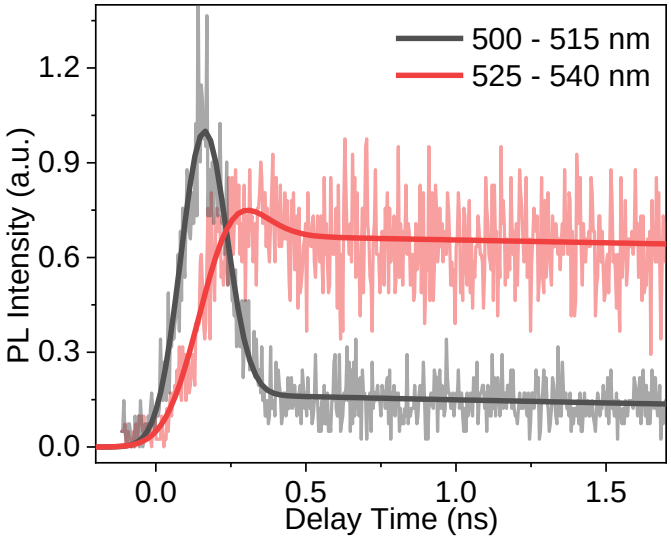

Fig. 7. 10. Luminescent property of chiral perovskite films. Time-resolved PL kinetics of perovskite heterostructures with 1% (R)-3BrMBA additives.

7.2.3 Room-temperature chiroptical characteristics of chiral perovskite heterostructures

We also investigate chiral perovskite films' general structure and optical features with different amounts of chiral additives. Fig. 7.11a shows X-ray diffraction (XRD) results of spin-coated perovskite films. 1% chiral molecules treated samples show almost the same diffraction patterns as that of pure 3D films. Predictably, further increasing the chiral molecule amounts leads to the diminishing of the 3D phase at ~15° and ~30° and the rise of the low-dimensional phase before 10°. The same trends were obtained from absorption spectroscopy measurements (Fig. 7.11b). Importantly, all chiral perovskite films with (R) or (S) additives have well-overlapping diffraction patterns and absorption spectra, indicating identical crystal structures with identical optical properties but opposite chirality. As shown in Fig. 7.11c, chiral (R) and (S) additives result in opposite CD signals covering whole spectra regions we detected (300-700 nm), revealing the success of chirality transfer from chiral organic molecules into chiral heterostructures.

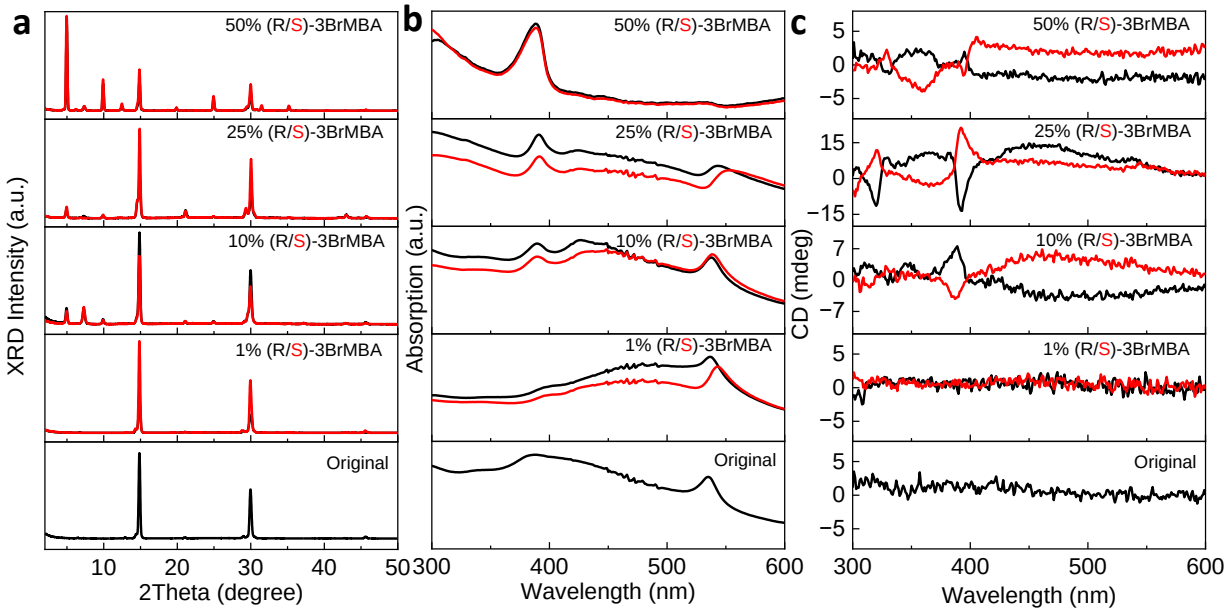

Fig. 7. 11. Steady-state chiroptical characterizations. a-c, XRD (a), absorption (b), and CD spectra of original, 1%, 10%, 25%, and 50% (R/S)-3BrMBA treated samples.

We further study the PL characteristics of chiral perovskite films at room temperature. Under 405 nm excitations with large spot size ~300 μm, we notice that chiral perovskite films with increasing chiral additives show gradually blue-shifted PL features (Fig. 7.12), which are ascribed to the enhanced confinement effect of formed chiral quasi-2D phases as we already observed in their confocal PL images. We performed PLQE measurements on our chiral perovskite films. Upon a 405 nm excitation (100 mW/cm^2), we find that the 1% chiral additives treated sample produces the highest PLQE value, reaching ~24%, which is almost twice as high as the value obtained from original 3D perovskite films (~14%). Besides, more chiral additives, like 10%, result in a slight decrease in PLQE value (~20%).

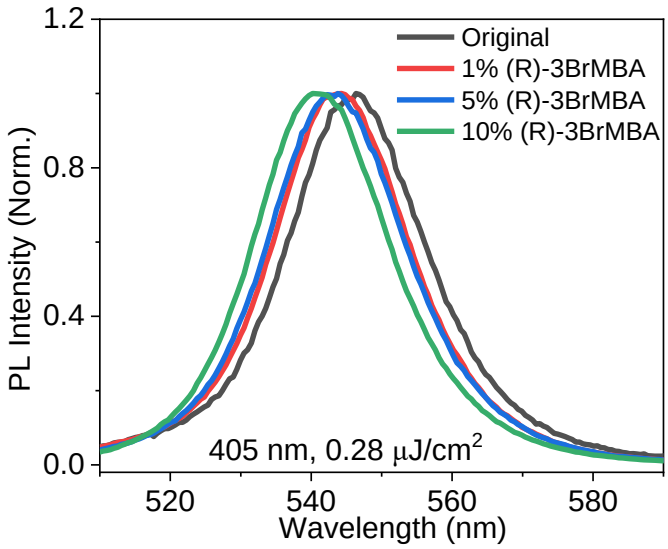

Fig. 7. 12. Normalized room-temperature PL spectra chiral perovskites with 0, 1%, 5%, and 10% (R)-3BrMBA additives.

For CPL measurements on chiral perovskite films, we employed the same optical configurations we used for CEL measurements, while a 450 nm continuous-wave laser was used to excite the samples. All the CPL measurements were performed at room temperature without external magnetic fields. In order to compare the CPL results quantitively, we calculated the CPL anisotropy factor (g_{CPL}) based on the equation as below.

$$g_{CPL} = \frac{2 \times A_{CPL}}{A_{PL}} \tag{32}$$

Here, A_{CPL} and A_{PL} represent the amplitudes of CPL and total PL signals collected from two lock-in detectors (one for PEM, one for chopper) at the same time.

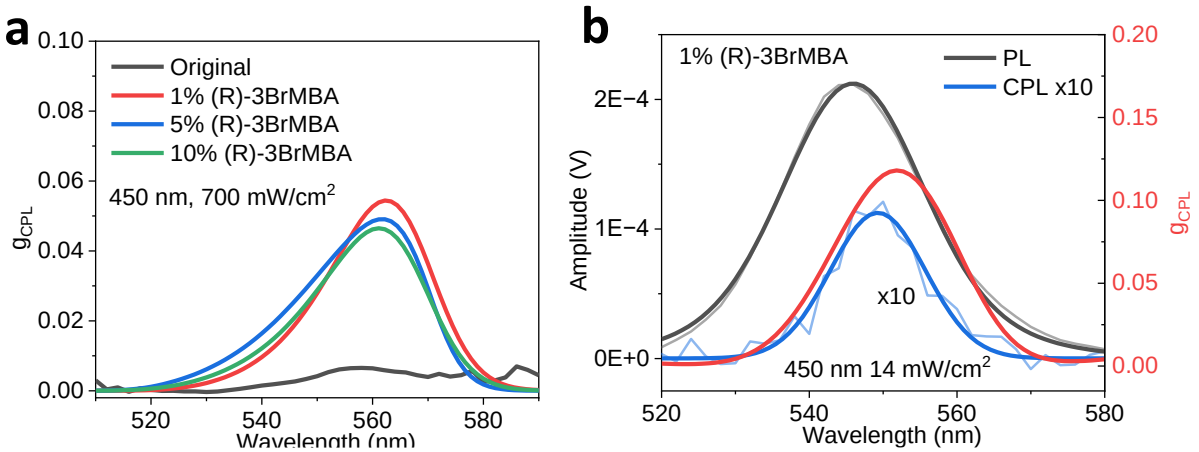

Fig. 7. 13. Steady-state chiroptical characterizations. a, Room-temperature CPL spectra chiral perovskites with 0, 1%, 5%, and 10% (R)-3BrMBA additives. **b,** CPL spectra of 1% (R)-3BrMBA treated samples under weak excitation power.

As plotted in Fig. 7.13a, no obvious CPL signals, only background signals, were observed in original 3D perovskite films, while samples with chiral additives show much stronger g_{CPL} values from 530 to 580 nm. Unexpectedly, higher amounts of chiral additives result in decreased g_{CPL} values. A possible reason for decreased g_{CPL} is that all the generated CPL signals should come from 3D bulk phases. The increased amount of chiral additives results in the broadening of their bandgap due to increased confinements, which may further block the efficient chirality transfer from quasi-2D chiral phases to 3D perovskite phases. Moreover, we note that the CPL signals of our chiral perovskites would increase a lot when we use low excitation power. By gradually decreasing excitation power during CPL measurements, our chiral perovskite films reach a maximum g_{CPL} value of ~0.12 at ~550 nm (Fig. 7.13b), which is at least one order of magnitude larger than previously reported top values for chiral perovskite (*81, 98, 129, 130*). Importantly, we find the CPL signals are slightly red-shifted compared to their PL signals, which corroborates that the CPL signals should predominantly originate from red-shifted bulk 3D phases. Therefore, our chiral perovskite films show both a high PLQE value and a large degree of CPL polarization, demonstrating a great platform for CPeLED applications.

7.2.4 Charge carrier dynamics and time-resolved polarization kinetics in chiral perovskite heterostructures

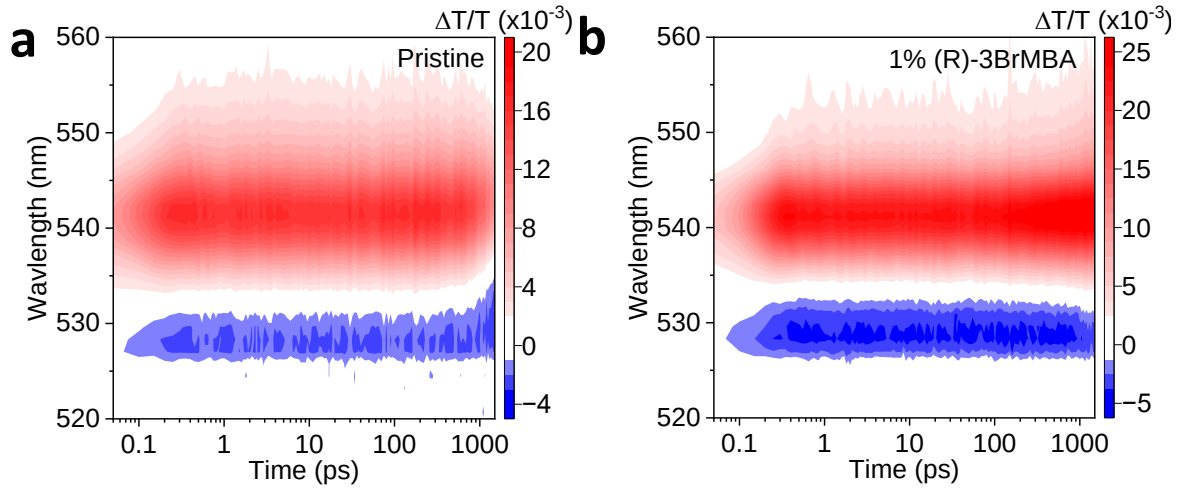

Fig. 7. 14. Linear transient absorption (TA) color maps of pristine (a) and 1% (R)-3BrMBA treated samples (b). TA measurements were performed under 515 nm excitations (0.57 μJ/cm^2).

To understand the high PLQE value and significant degree of PL polarization in our chiral perovskite films, we further investigate their charge carrier dynamics via TA spectroscopy. As shown in Fig. 714a and 7.14b, perovskite films with or without chiral additives both exhibit a long-lived carrier lifetime. We extracted their decay kinetics at ground-state bleaching (GSB) regions (535 - 455 nm), and plotted both of them in Fig. 7.15 for comparison. At low excitation fluence, TA signals of chiral perovskite films show a small increase, while pristine 3D samples have a fast decrease after 100 ps. This is clear evidence for charge transfer inside chiral perovskite film from chiral quasi-2D perovskites to bulk 3D phases, resulting in a much longer carrier lifetime. Fluence-dependent TA measurements indicate that the carrier lifetime would gradually decrease with increasing fluence, which is also a general trend for 3D perovskites (Fig. A38) (*131*).

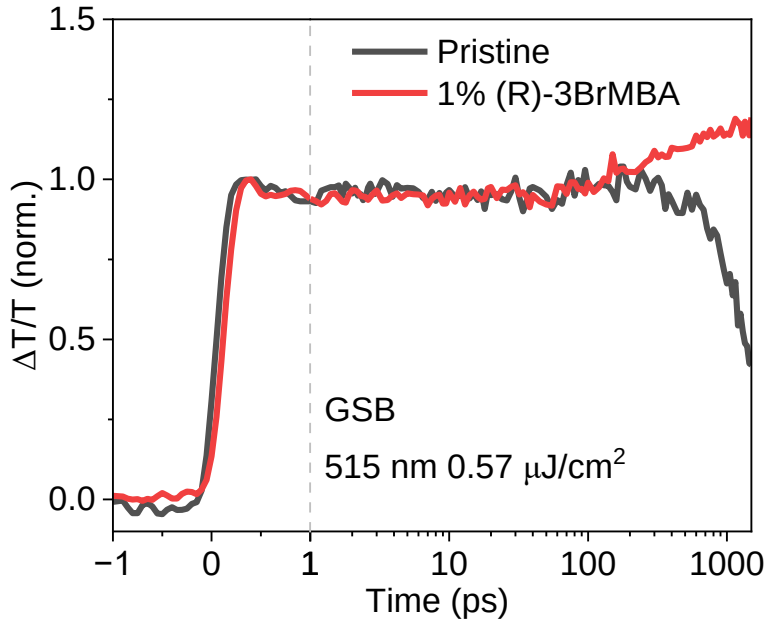

Fig. 7. 15. Comparison of TA kinetics (GSB regions) obtained from pristine and 1% (R)-3BrMBA treated samples. TA measurements were performed under 515 nm excitations (0.57 μJ/cm^2).

Long-term TA measurements were also used here to detect the whole recombination process. As illustrated in Fig. 7.16, chiral perovskite films show much long-lived TA signals with a

fitted average lifetime of ~167 ns, while only ~99 ns for pristine 3D perovskites (see fitting details in Table B8). Time-resolved PL measurements further confirmed that chiral perovskite films have a longer radiative recombination lifetime than that of pristine 3D films. The fitted average PL lifetimes for chiral perovskite and original thin films are ~161 ns and ~102 ns (Fig. A39), respectively, which are both super close to the lifetimes we obtained from TA measurements. Such results indicate our chiral perovskite samples have a dominantly radiative recombination channel (*7*, *131*, *132*). Further increasing the chiral additive amount to 10% caused the diminution of PL lifetimes (Fig. A40), which also explains the reduction of their PLQE values.

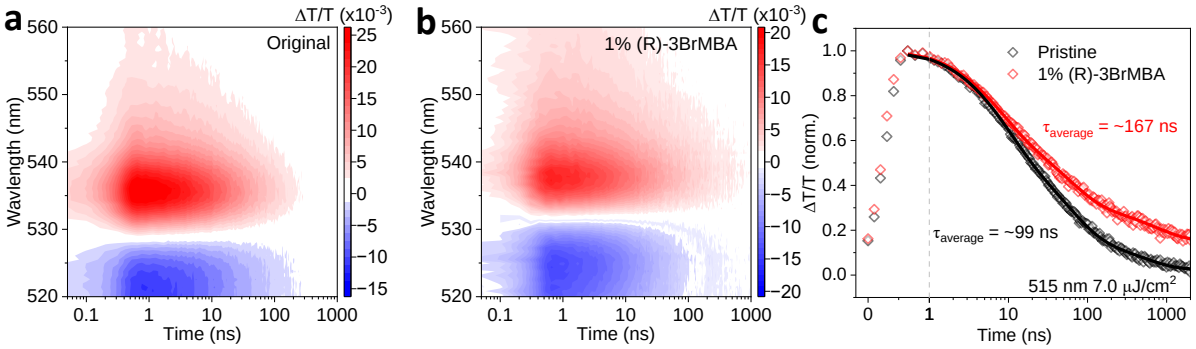

Fig. 7. 16. Charge carrier dynamics. a, b, Long-time TA color maps of original and 1% (R)-3BrMBA treated samples. **c,** Comparison of TA kinetics (GSB regions) obtained from pristine and 1% (R)-3BrMBA treated samples.

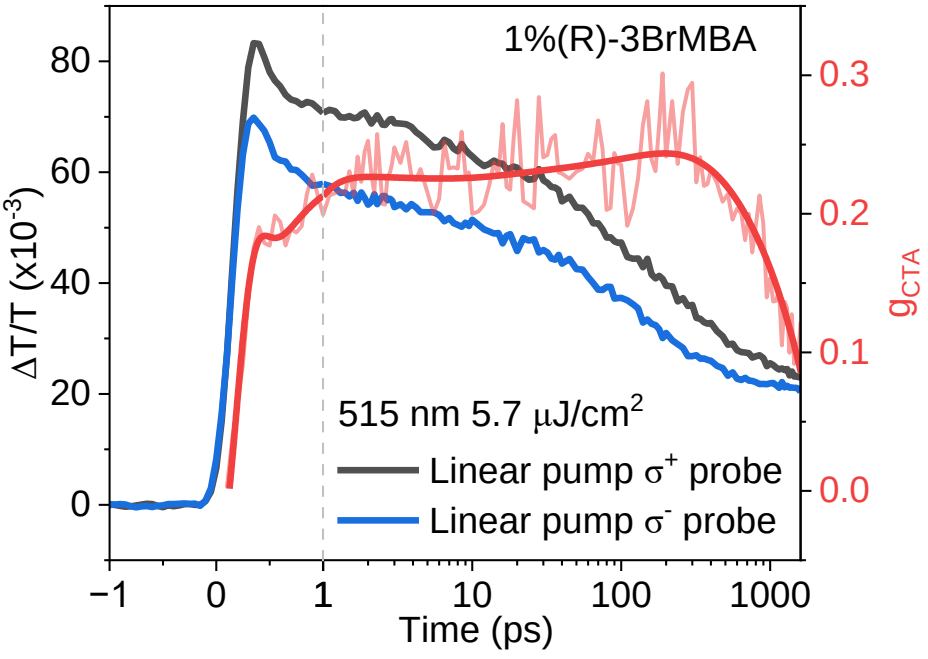

Fig. 7. 17. Circularly polarized TA (CTA) kinetics extracted from GSB regions of 1% (R)-3BrMBA treated samples. The g_{CTA} kinetics are highlighted as red data. The corresponding pump wavelength and fluence are depicted in the figure.

Furthermore, we performed circularly polarized TA (CTA) spectroscopy measurements on our chiral perovskite films to explore their time-resolved polarization dynamics. In contrast to general CTA measurements, in which carrier polarization was created by circularly polarized excitations, for chiral perovskite films, we use linear excitations to pump the samples and circularly polarized probes to detect the intrinsic photo-generated polarization. Fig. 7.17 shows the CTA decay kinetics excerpted from the GSB region of chiral perovskite films, which manifest apparent differences between σ^+ and σ^- detections. The polarization degree in TA signals can be calculated using the following equation,

$$g_{CTA} = \frac{2\times(\Delta T/T_{\sigma+} - \Delta T/T_{\sigma-})}{\Delta T/T_{\sigma+} + \Delta T/T_{\sigma-}} \quad (33)$$

where $\Delta T/T_{\sigma+}$ and $\Delta T/T_{\sigma-}$ are the TA signals with σ^+ and σ^- probes, respectively. Chiral perovskite films experience a gradually increasing polarization degree at an initial 100 ps (gCTA = ~25%), confirming the existence of a chirality transfer process. Then, the degree of CTA polarization slowly decreases to ~10% at 2 ns. Moreover, in order to verify the contribution of the resulting polarization only related to sample chirality, we have performed the same CTA measurements on racemic (Rac)-3BrMBA treated perovskite sample as a comparison. Without chirality in our perovskite films, TA polarization degree quickly went to zero at first ps (Fig. A41).

We also performed time-resolved CPL measurements to interpret the chirality transfer process in chiral perovskite films (355 nm excitations, 60 nJ/cm^2). For the first 0.2 ns, we observe a large intensity difference between σ^+ and σ^- detections at both 510 nm and 535 nm (Fig. 7.18a), which should relate to the fast chirality transfer from chiral domains to 3D perovskites. A high g_{CPL} value of ~21% was obtained at the initial time. After 0.2 ns, the PL features of chiral domains at 510 nm fully disappeared (Fig. 7.18b), while the intensity difference at ~535 nm was kept with a smaller g_{CPL} value of ~9%. Such value is not only consistent with the value we obtained from steady-state CPL measurements but notably, the time-resolved g_{CPL} values we obtained here are also close to the g_{CTA} values we acquired from CTA measurements at certain time scales, further proving the accuracy of our optical

polarization results. As a result, our chiral perovskite films, which have long-lived polarized photo-excited carriers and dominant radiative recombination channels, explained their increased PLQE values and large optical polarization results well.

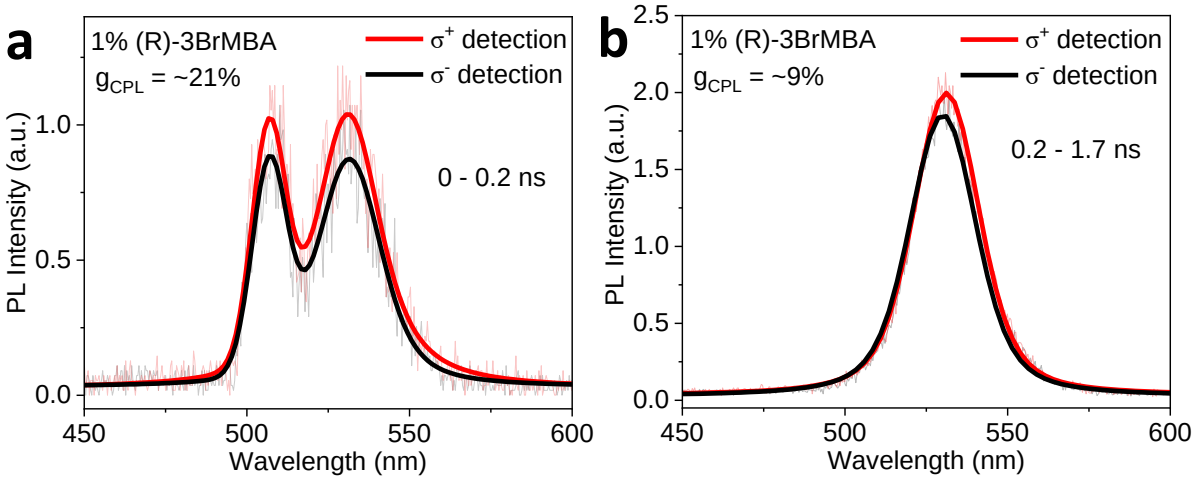

Fig. 7. 18. Polarization-dependent charge carrier recombination dynamics. a, b, Time-resolved circularly polarized photoluminescence (CPL) spectra of 1% (R)-3BrMBA treated samples with different time scales 0-0.2 ns (a) and 0.2-1.7 ns (b). The measurements were performed under 355 nm excitations with a fluence of ~60 nJ/cm^2.

7.2.5 Holographic TA microscope measurements on chiral heterostructures

For investigating the charge carrier transport happening in between the chiral quasi-2D domains and 3D phases, we performed ultrafast transient holographic imaging (*32*, *33*) in a wide-field configuration on the 1% (R)-3BrMBA treated and on the original pure 3D samples for comparison. The recorded signal is the spatial distribution of the transient absorption signal, which is collected by a 400 nm with ~30 µJ/cm^2 fluence excitation and probing at 530 nm, with a 10 nm band-pass filter for both pump and probe pulses.

To interpret TA holographic data, we utilized principle component analysis (PCA) to identify kinetics with various time constants. Fig. 7.19 illustrates three components of these kinetics in both samples. While the first temporal component behaves similarly in both the original and 1% (R)-3BrMBA treated samples, the second and long-lived components exhibit different kinetics. The long-lived component operates on a time scale beyond our measurement capabilities (~1.6 ns).

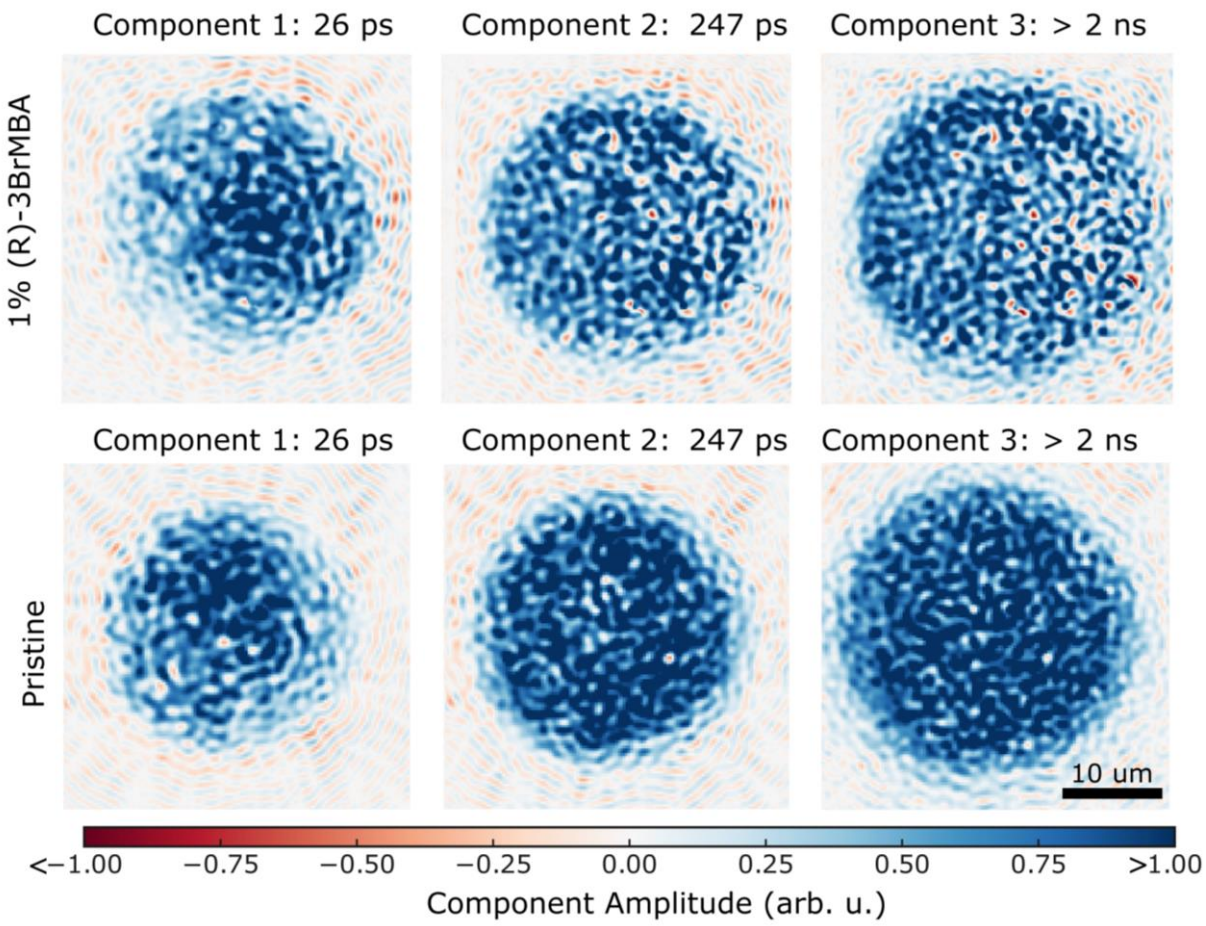

Fig. 7. 19. Spatial-resolved charge carrier dynamics. a, b, Holographic TA microscope images collected from 1% (R)-3BrMBA treated (a), and pristine samples (b). Each time component was obtained by applying principle component analysis. The blue area corresponds to the pumped area, while the probe illuminates the entire field of view. The TA microscope measurements were performed under 400 nm excitations with a fluence of 30 μJ/cm^2, and probed at ~530 nm.

We observe a positive (blue) and a negative (red) signal within the pumped region in chiral samples, attributed to 3D phases and chiral quasi-2D domains, respectively. For detailed analysis, we applied an intensity mask to component 2 in Fig. 7.19, to separate the region with position and negative kinetics and plotted their corresponding average scale behaviors in Fig. 7.20. Notably, more heterostructures form in the red region of the 1% (R)-3BrMBA samples compared to pure 3D samples. Additionally, kinetics in blue and red regions have opposite signs in the 1% (R)-3BrMBA samples, indicating carriers funneling from higher to lower energy domains. The negative long-lived PIA signals in red regions relate to carrier

transfer from chiral domains (~510 nm, Fig. A42 and A43) (*91*). Compared with the original samples, the red curve remains zero in the measured time window of ~1.6 ns, suggesting only one kinetics occurs here.

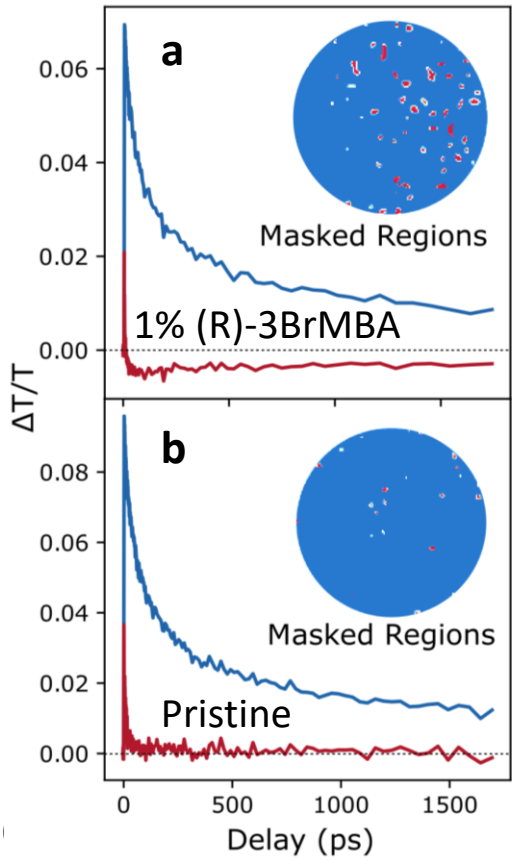

Fig. 7. 20. Spatial-resolved TA kinetic plots for 1% (R)-3BrMBA treated (a) and pristine 3D samples (b). Blue and red curves indicate the two different kinetics recognized by applying the mask on component 2 in Fig. 7.19a and 7.19b. The inset contains their corresponding masked images.

Our current work demonstrates the monolithic LED for generating circularly polarized light by utilizing the achiral/chiral bulk heterostructure emitters. Our data suggest that the carrier transfer from chiral quasi-2D phases to 3D bulk perovskite domain is responsible for the circularly polarized light emission, which is more suited for efficient CPeLEDs with high polarization degree than the spin-selective strategy (*67*). Engineering the heterostructure thin films to boost the PLQE will be the future focus in terms of more efficient CPeLED. Meanwhile, regulating the heterostructure interface and homogenizing the distribution of chiral domains could benefit the carrier transfer process and generate a higher polarization degree from CPeLED.

7.3 Conclusion

In summary, our discovery of bright circularly polarized emission in these novel chiral perovskite films, with quantum yields of ~25% and polarization as high as ~15%, presents a disruptive step in the performance of chiral emitters that was not achievable in most existing semiconductor materials (*5, 11, 67, 82, 119, 127*). The hybrid perovskites are fabricated by solution-processing and self-assembly to form polycrystalline thin films with high crystal structure quality and low impact of defects/strain on their electronic states. AFM and confocal PL image measurements reveal that the addition of chiral molecules inside 3D perovskite structures forms chiral quasi-2D perovskite nanocrystal and 3D bulk phase heterostructures. The formation of chiral nanostructure provides an efficient charge and chirality transfer into bulk 3D systems, while 3D perovskite structure keeps their excellent charge-transport properties. We further translate these exciting new material properties into optoelectronic devices, particularly CPeLEDs, for generating circularly polarized light. Consequently, efficient and highly-polarized CPeLEDs with a maximum EQE of ~9.2%, a maximum luminance of ~220,000 cd m^{-2}, and a large degree of EL polarization of ~20% were obtained. To summarize, our novel CPeLEDs made out of chiral perovskite host-guest structures offer an exciting novel direction for future high-performance, low-energy display, and spintronic applications.

Outlook

This thesis work focused on fabricating chiral metal-halide perovskite in different dimensions to find the most suitable structures for spintronics applications. First, we tried 0D chiral lead-free bismuth halide perovskite with disconnected octahedral dimers, in which the combination of the advantages from both chirality (intrinsic polarization injection) and lead-free perovskites (long carrier lifetime), results in longer polarization lifetime, reaching a few microseconds at room temperature. Such results are at least two orders of magnitude larger than the polarization lifetime reported in other perovskite spintronic materials (*17*, *65*, *75*, *133*). However, due to the disconnected octahedron and strongly localized excitons, it did not show any PL features at room temperature, which hinders our further applications. Then we turn our focus to chiral 1D chain perovskites, which show usually large CD signals (*14*, *16*). We find weak PL signals in chiral 1D perovskite films located at ~500 nm, which we attribute to the PbI_2 nanoparticles/chiral perovskite heterostructures. The heterostructure films show large CPL signals (~5%) at low temperature 5 K. Using ultrafast transient chiroptical spectroscopy measurements, we find the efficient chirality transfer from chiral 1D perovskite into PbI_2 heterostructure is the main reason for their large CPL signals.

However, 1D chiral perovskite did not show strong CPL at room temperature, which is still not a reasonable material for real application part. Then, we moved our focus to 2D chiral layered perovskite. From previously reported work, we know it is always hard to get both strong chirality and high PLQE simultaneously. There is a competition between them. If we introduce the chiral organic molecules inside the perovskite structure, in some cases, the distortion of perovskite would kill its photoluminescence. However, in our work, we find that the structure of chiral organic molecules is an important factor in getting both high PLQE and a large degree of CPL. We change the position of the halide atom on the aromatic ring from para to meta position and successfully introduce chiral organic molecules (R/S)-3BrMBA into PbI_2 structures to form a novel chiral 2D layered perovskites (R/S)-3BrMBA$_2$PbI$_4$, which gives us a bright CPL value at room temperature. We use transient chiroptical measurements to understand the mechanism behind such bright CPL values, and we find that a dominant fast radiative decay channel coupled with a long-lived polarization lifetime is the main contribution. We further transfer our 2D chiral perovskite into circularly polarized photodetectors, which show a detection polarization of ~0.5%, consistent with their CD

values. Due to the low conductivity of pure 2D chiral perovskites, the circularly polarized perovskite LEDs based on chiral 2D perovskites didn't show stable and strong electroluminescence.

Thus, we further introduce chiral organic molecules (R/S)-3BrMBA into 3D perovskite structures, PL mapping, and transient holographic images measurements confirmed the formation of chiral nano heterostructure of quasi-2D perovskites and 3D bulk phases. Quasi-2D perovskite phases work as polarization injection layers, which efficiently transfer their polarized excitons to 3D bulk phases, which serve as charge transfer layers, emitting bright and highly polarized luminescence. Circularly polarized perovskite LED based on chiral perovskite heterostructure emitters show a high degree of electroluminescence polarization of ~20%, a considerable EQE value of ~9% with a strong brightness of 220,000 cd m^2. Our current research provides a visible way for future optical and spintronic applications.

For next-step plan, there are some potential interesting projects:

1. Turning the LEDs structure to balance the carrier transfer would be an easy way to improve our CPeLEDs performance.
2. Using passivation additives to increase the stability and device lifetime of CPeLEDs for long-term applications.
3. Turning the halide ratios inside CPeLEDs perovskite layers to reach color-tunable CPeLEDs.
4. Trying different chiral organic molecules to reach the highest degree of electroluminescence polarization.

Appendix A Supplemental Figures

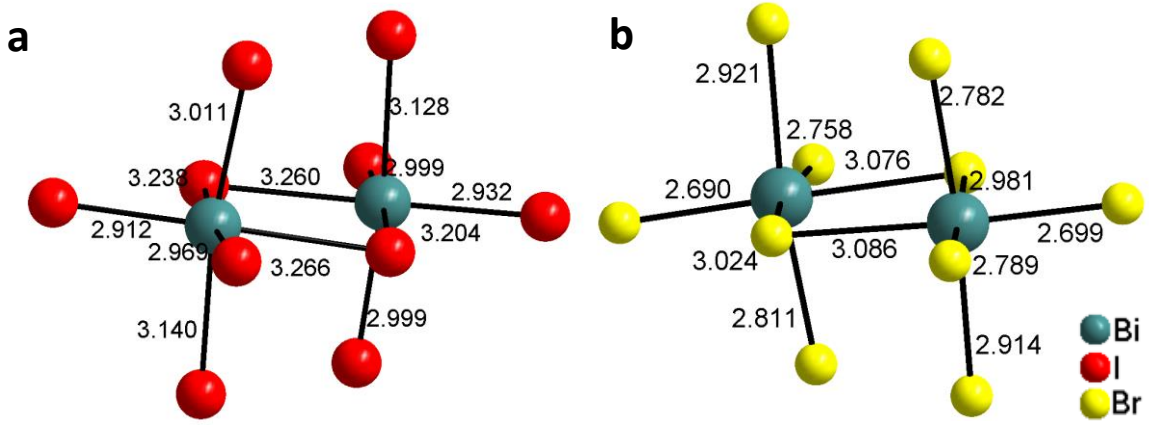

Fig. A1. The Bi coordination sphere of (R)-CHEA$_4$Bi$_2$I$_{10}$ (a) and (R)-CHEA$_4$Bi$_2$Br$_{10}$ crystals (b). The values of the bond distances are indicated in Ångstroms.

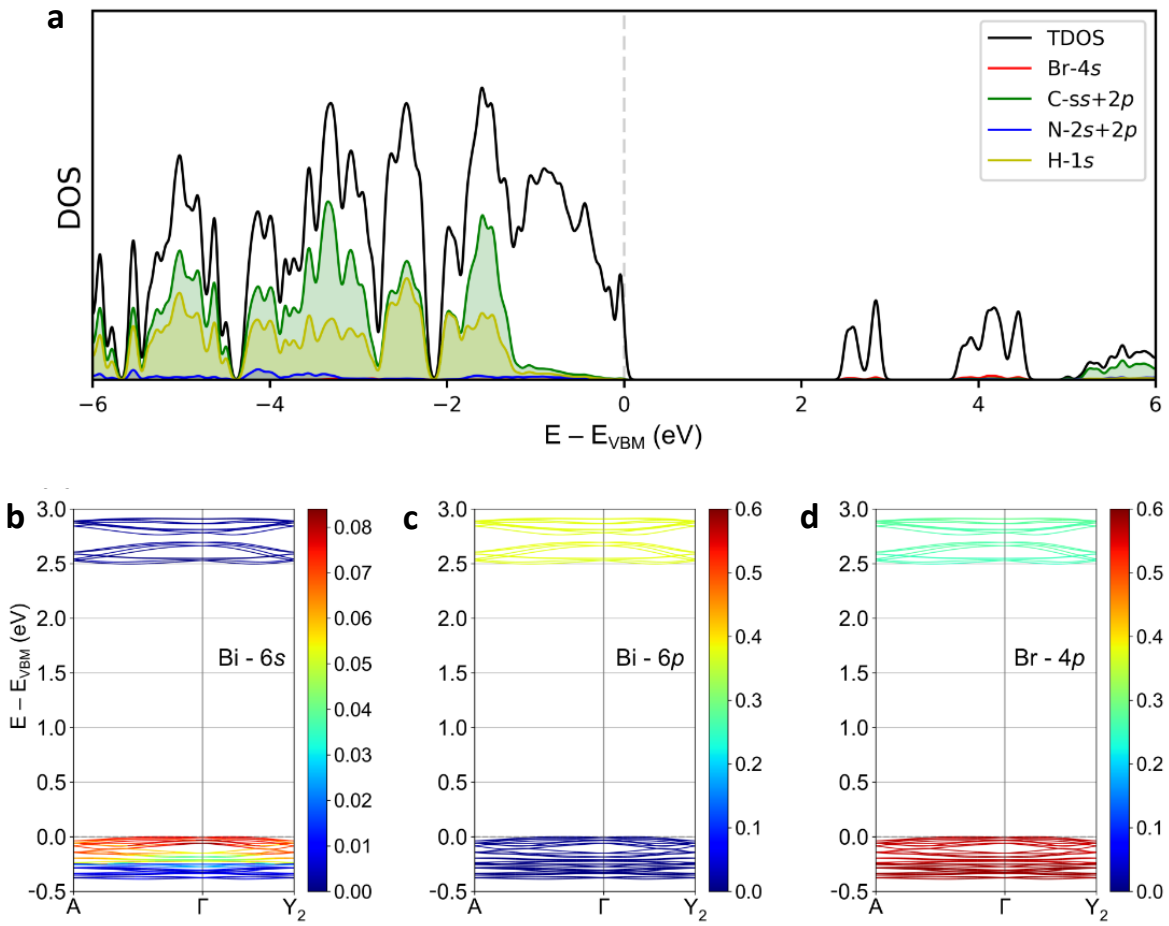

Fig. A2. **DFT calculation results on chiral bismuth halide samples.** (a) Projected density of states of (R)-$CHEA_4Bi_2Br_{10}$ showing the contribution of the organic molecules to the band structure deep away from the band edges. Band structure projected on the (b) Bi-6s, (c) Bi-6p and (d) Br-4p orbitals for the (S)-$CHEA_4Bi_2Br_{10}$. The band structure and orbital composition of the S-handed compound is very similar to the R-handed one, discussed in the main text.

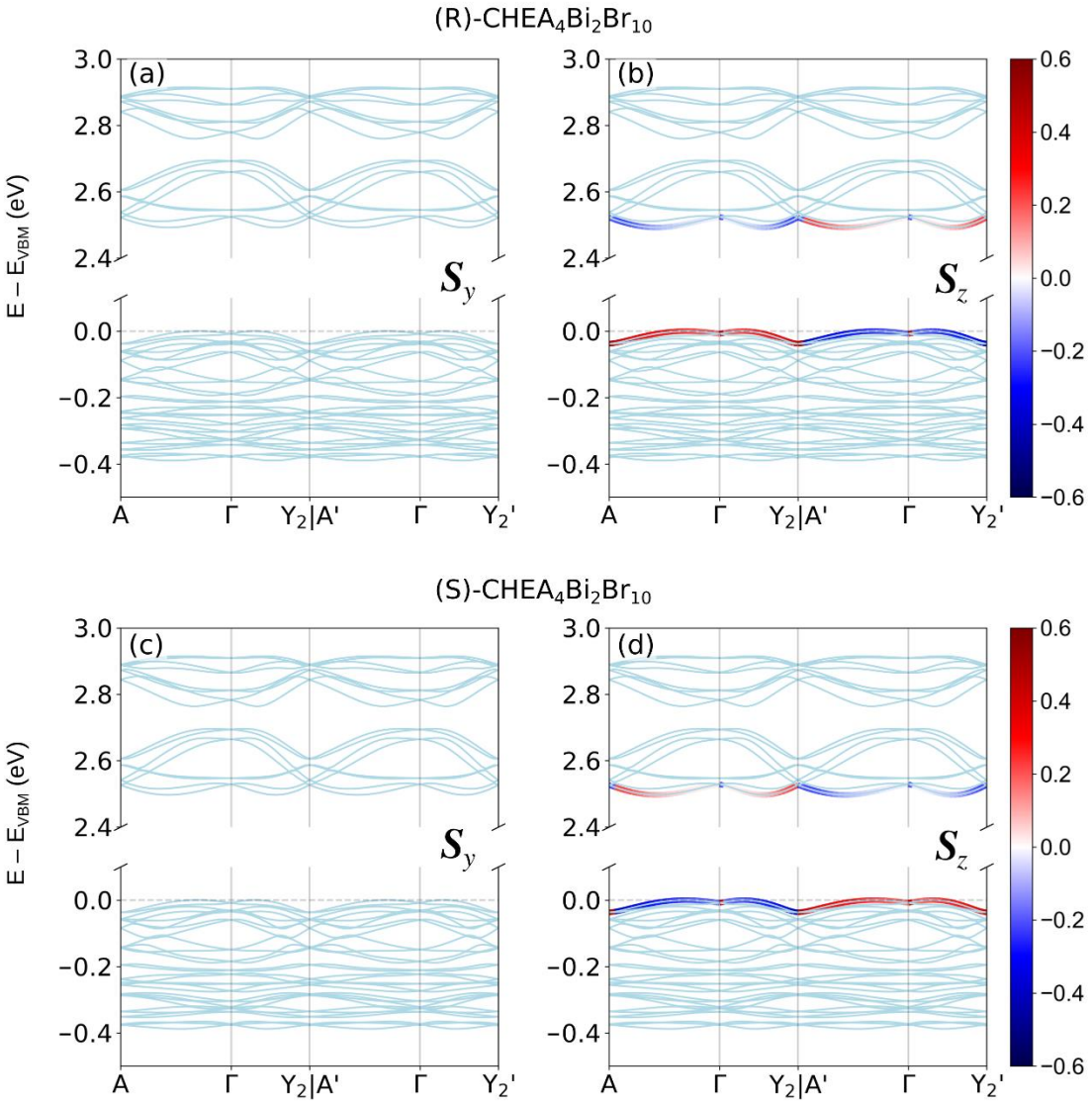

Fig. A3. Band structures along high-symmetry paths for (a-b) (R)-$CHEA_4Bi_2Br_{10}$ and (c-d) (S)-$CHEA_4Bi_2Br_{10}$. The spin polarization along the y and z axes, S_y and S_z, of the highest valence band and lowest conduction band is color-coded. Note that along the y axis there is no spin polarization.

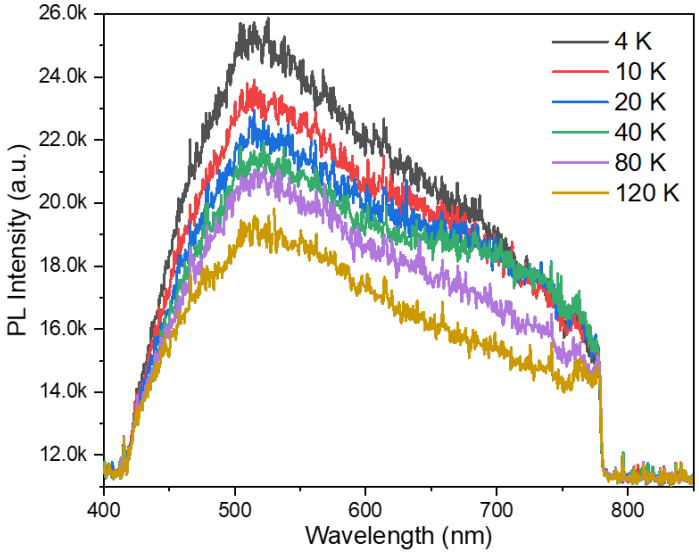

Fig. A4. **Temperature-dependent PL spectra of a drop-cast (R)-$CHEA_4Bi_2Br_{10}$ film.**

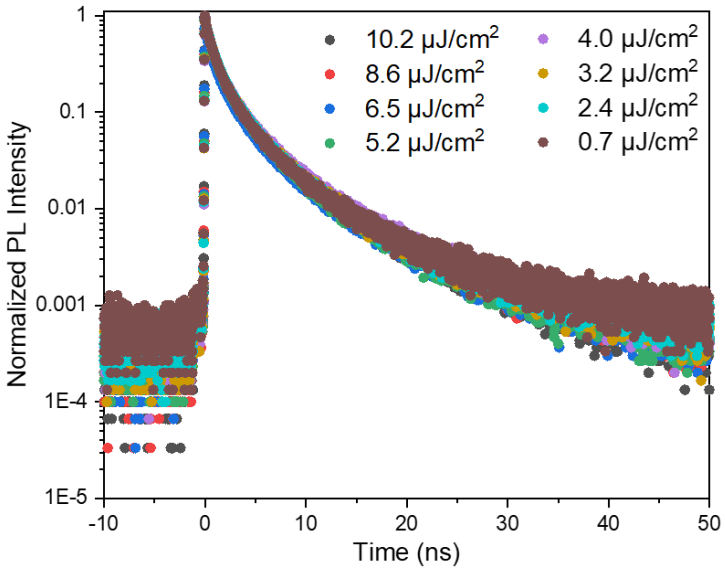

Fig. A5. **Fluence-dependent PL kinetics of a drop-cast (R)-$CHEA_4Bi_2Br_{10}$ film.** ND filters were used to control the incident laser power at a constant repetition rate.

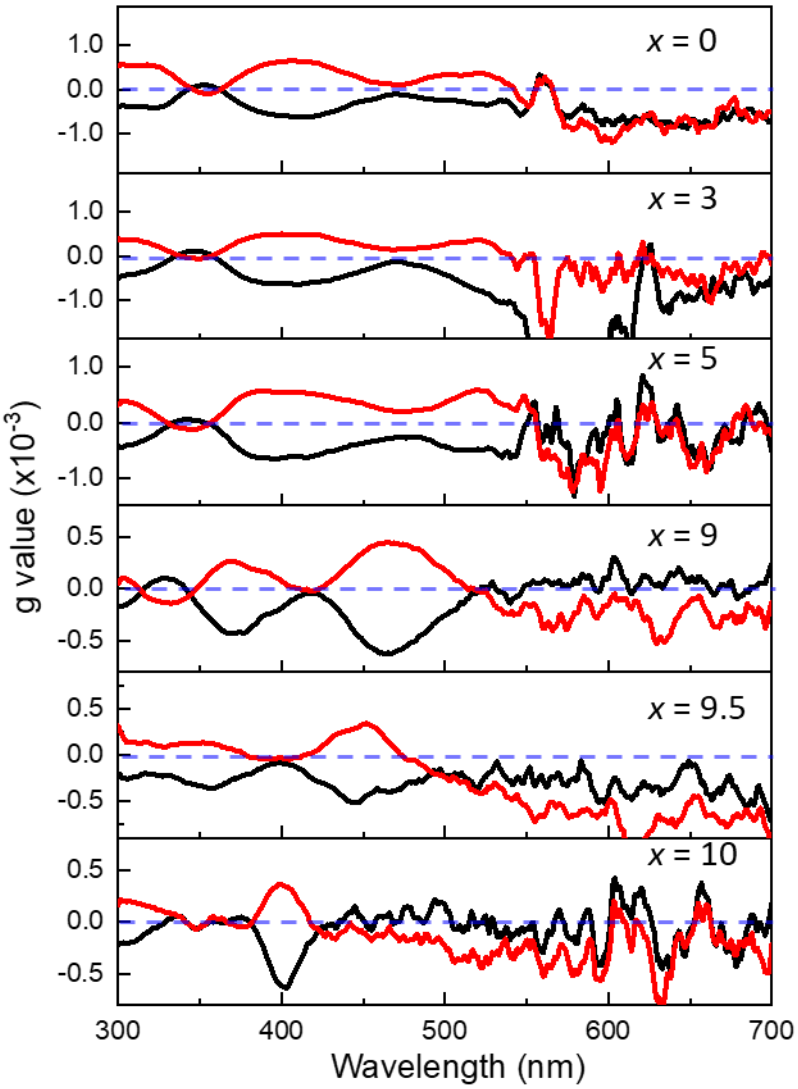

Fig. A6. **The anisotropy factor (g_{Abs} value) of (R)/(S)-CHEA$_4$Bi$_2$Br$_x$I$_{10-x}$ (x = 0 to 10) films.** The black and red solid lines represent the results acquiring from spin-coated films comprising (R)- and (S)- enantiomers, respectively. The g_{Abs} values show the same trends as the curves in the CD spectra.

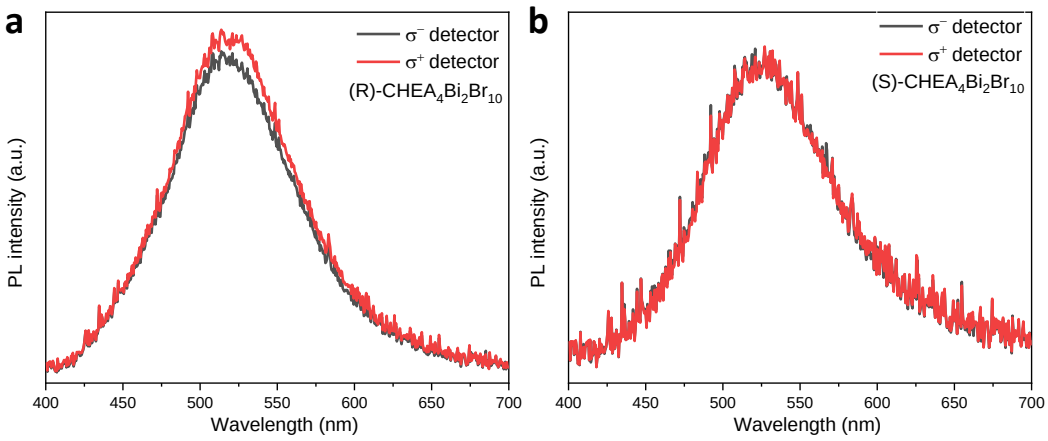

Fig. A7. Circularly polarized PL spectra of (R)-$CHEA_4Bi_2Br_{10}$ (a) and (S)-$CHEA_4Bi_2Br_{10}$ drop-casted films (b). Under a linear excitation (385 nm) at 5 K, both (R)- and (S)-$CHEA_4Bi_2Br_{10}$ show low CPL degree, less than 2%.

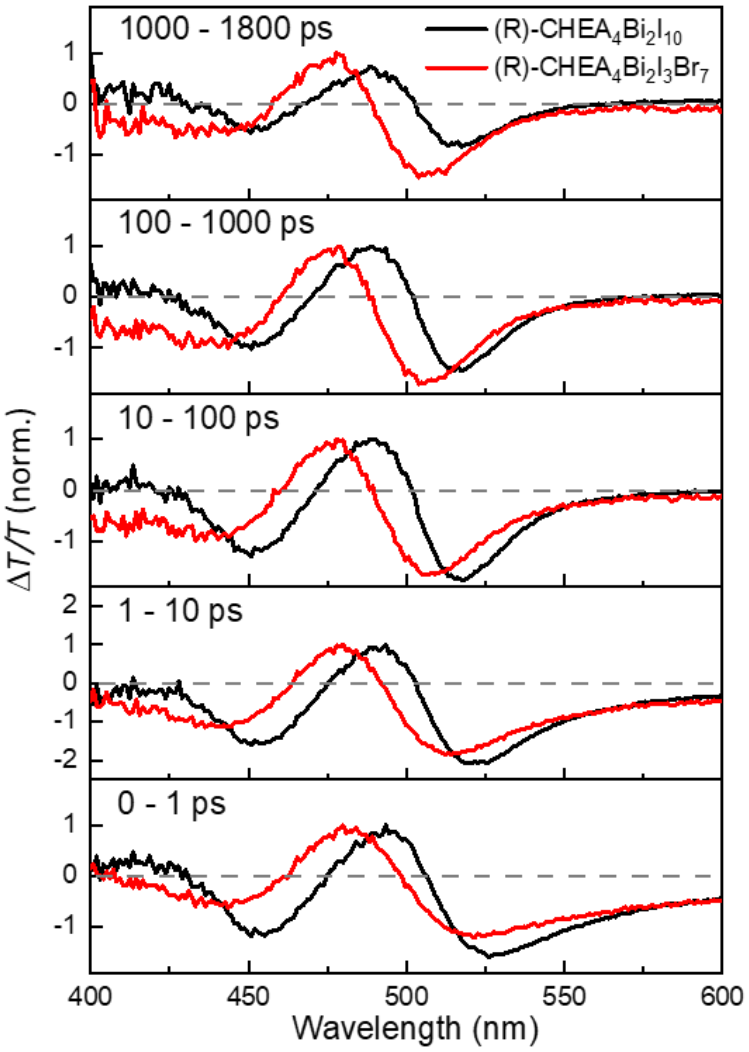

Fig. A8. **Comparison of TA spectra between mixed halide thin films.** The black and red solid lines represent the results acquired from (R)-$CHEA_4Bi_2I_{10}$ and (R)-$CHEA_4Bi_2I_3Br_7$, respectively. As expected, (R)-$CHEA_4Bi_2I_3Br_7$ is characterized by blue-shifted TA signals, compared with those from (R)-$CHEA_4Bi_2I_{10}$.

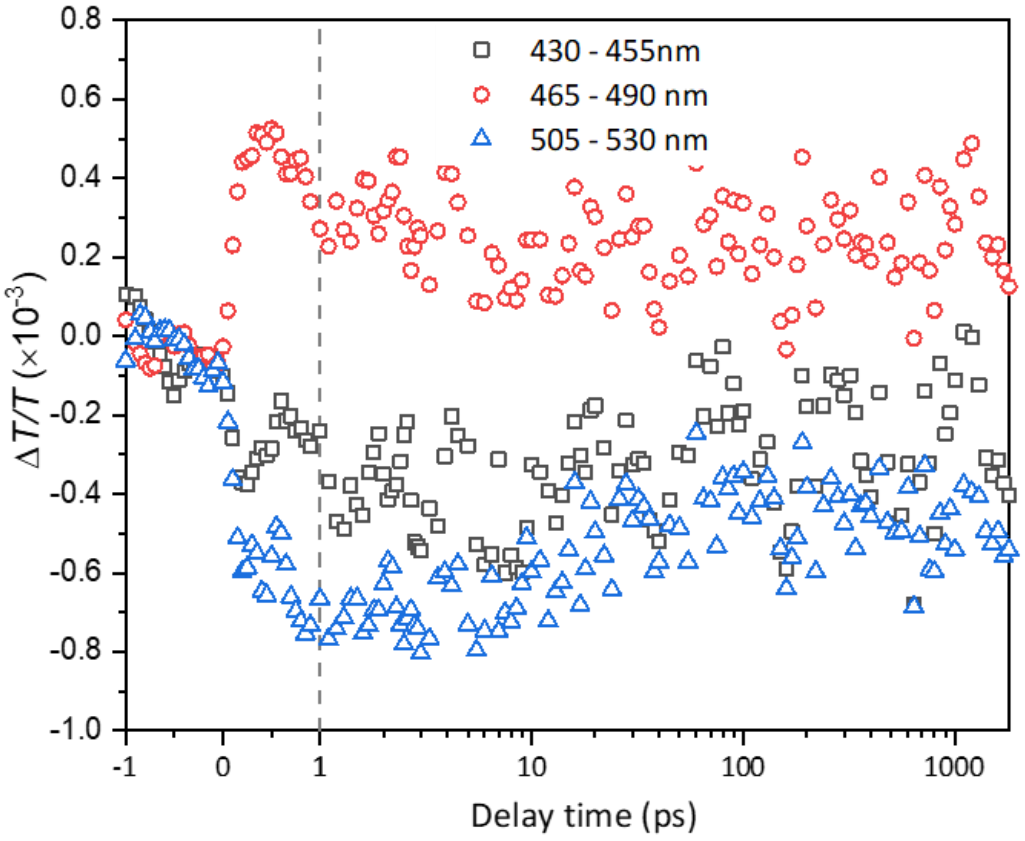

Fig. A9. **Transient absorption kinetics from (R)-CHEA$_4$Bi$_2$I$_3$Br$_7$ thin films**, which show similar trends compared to those from (R)-CHEA$_4$Bi$_2$I$_{10}$.

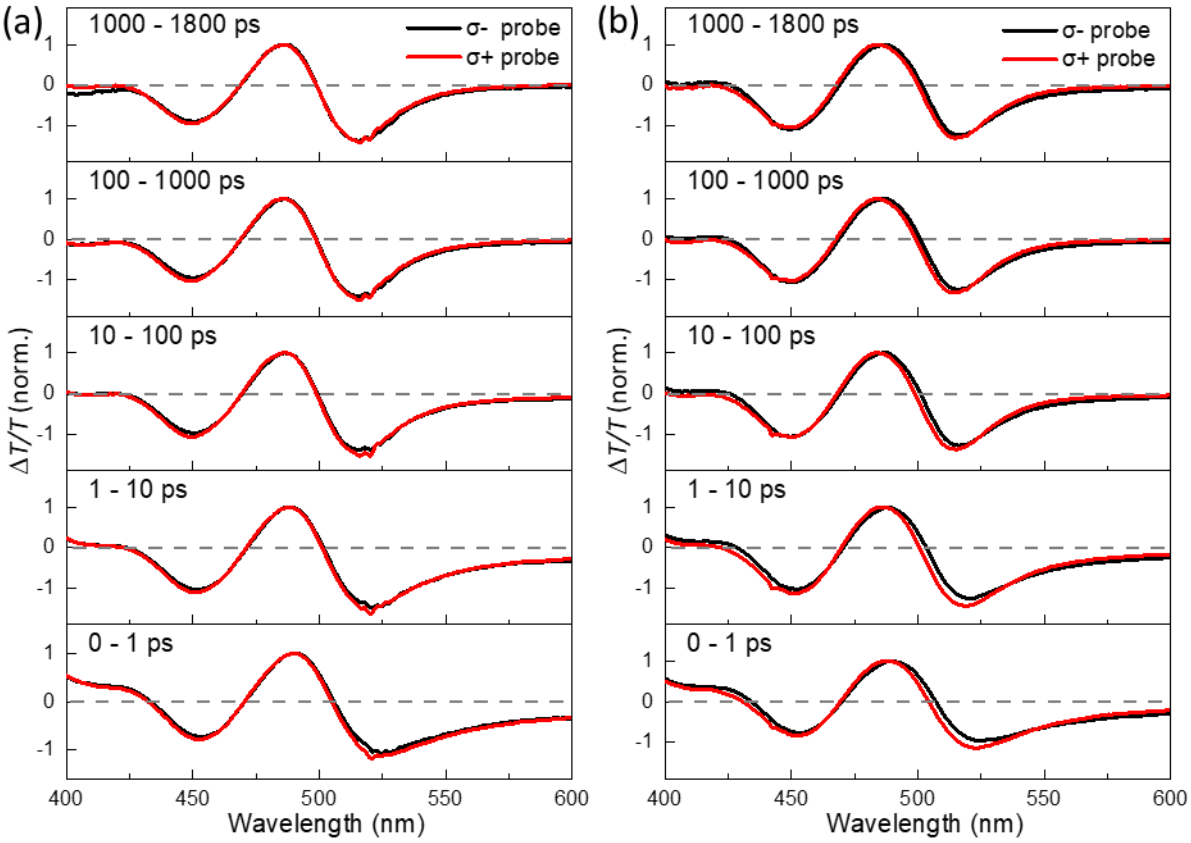

Fig. A10. Comparison of normalized circularly polarized TA spectra with linear pump and circularly polarized probe between racemic (a) and chiral (R)-$CHEA_4Bi_2I_{10}$ films (b).

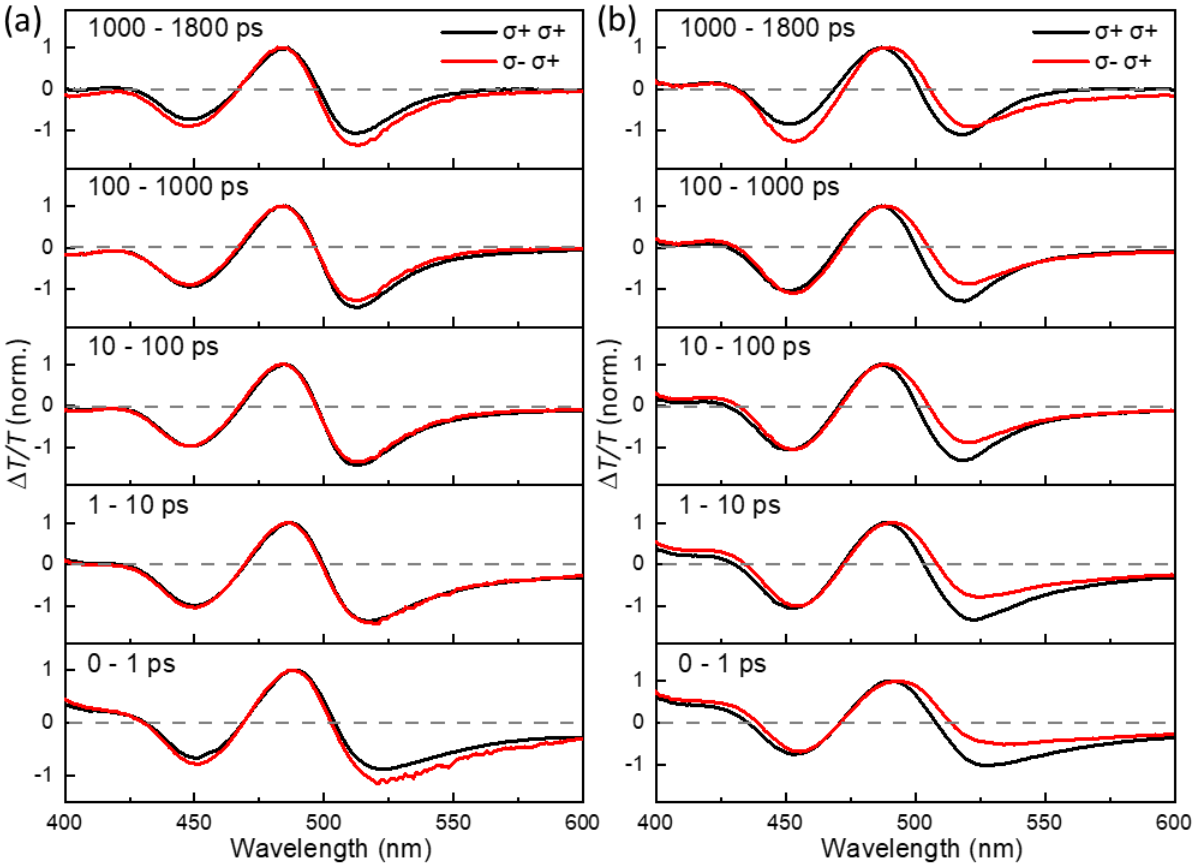

Fig. A11. **Comparison of normalized circularly polarized TA spectra with both circularly polarized pump and probe** between racemic (a) and chiral (R)-CHEA$_4$Bi$_2$I$_{10}$ films (b).

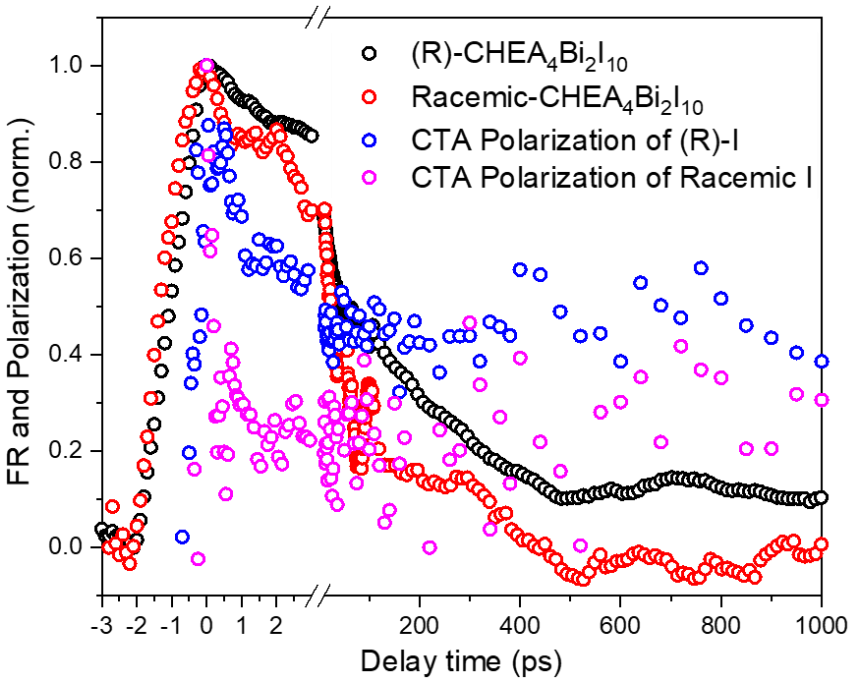

Fig. A12. Faraday rotation kinetics of (R)-$CHEA_4Bi_2I_{10}$ and racemic-$CHEA_4Bi_2I_{10}$ films. The Faraday rotation signals were obtained with circularly polarized pump excitation at 343 nm (~22 μJ/cm^2), and linear polarized probe beam at 800 nm to get rid of TA signals. The probe beam was further passed over a Wollaston prism, and detected by a pair of balanced photodiodes. The black and red dots represent the Faraday kinetics from chiral (R)-$CHEA_4Bi_2I_{10}$ and racemic-$CHEA_4Bi_2I_{10}$, respectively. The polarization relaxation kinetics of (R)-$CHEA_4Bi_2I_{10}$ and racemic samples extracted from CTA in PIA regions are plotted as blue and purple dots as a comparison. Faraday rotation measurements indicate the chiral (R)-$CHEA_4Bi_2I_{10}$ apparently exhibits longer spin lifetime than racemic samples, and further prove there is a spin-related effect in the polarization measurement results.

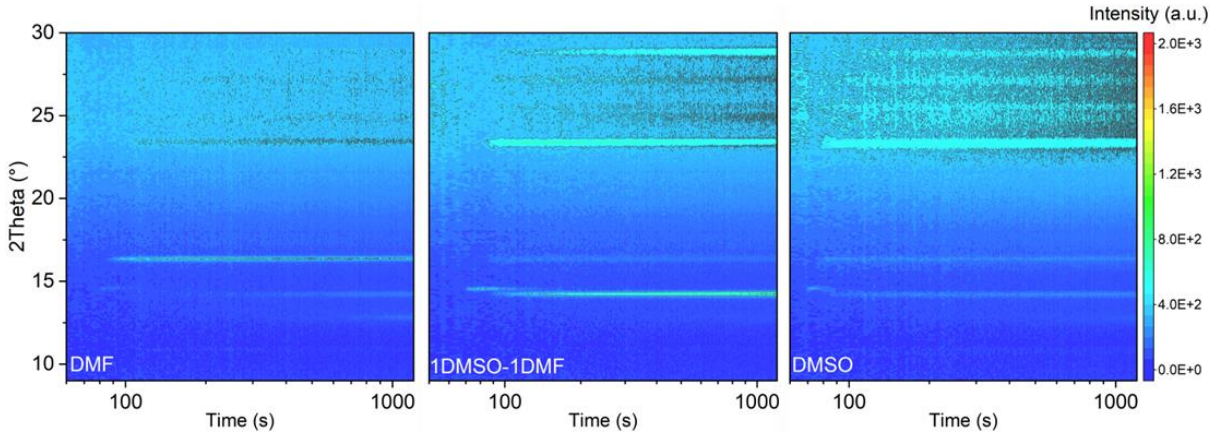

Fig. A13. In-situ XRD maps monitoring three different perovskite thin films formation.

The XRD patterns cover a broad region from 9° to 50°.

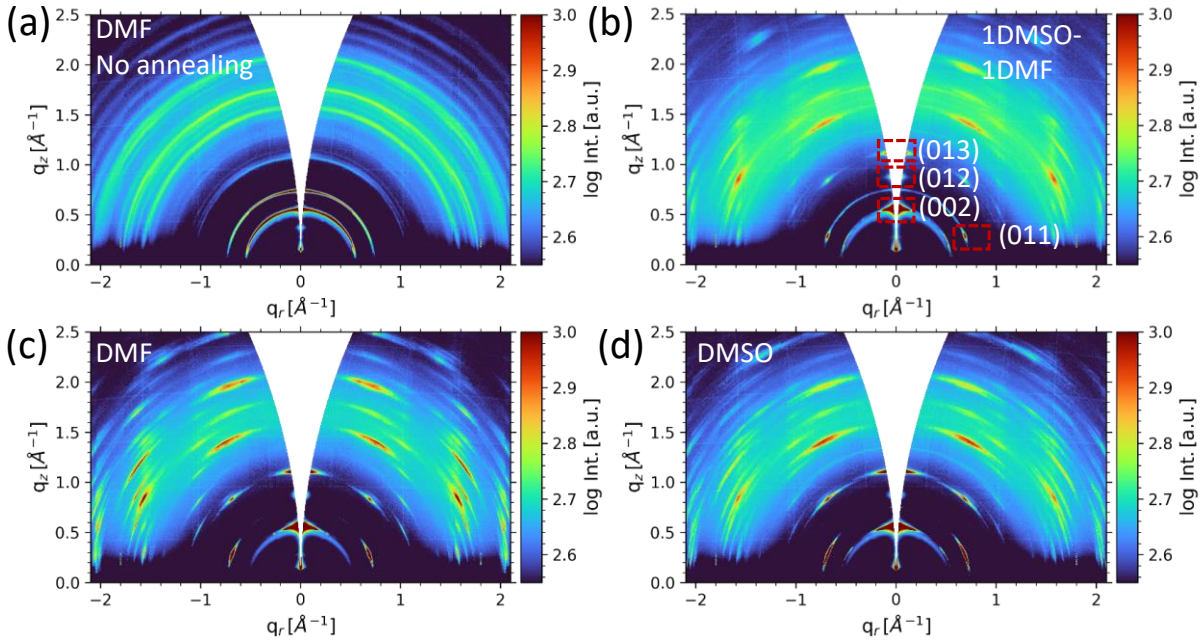

Fig. A14. **GIWAXS measurements on chiral perovskites film.** GIWAXS maps of perovskite films fabricated using DMF solvents (a) without hot-annealing process, DMSO-DMF mixture (b), DMF (c) and DMSO solvents (d). The later three samples were all annealing at 100 °C for 10 mins.

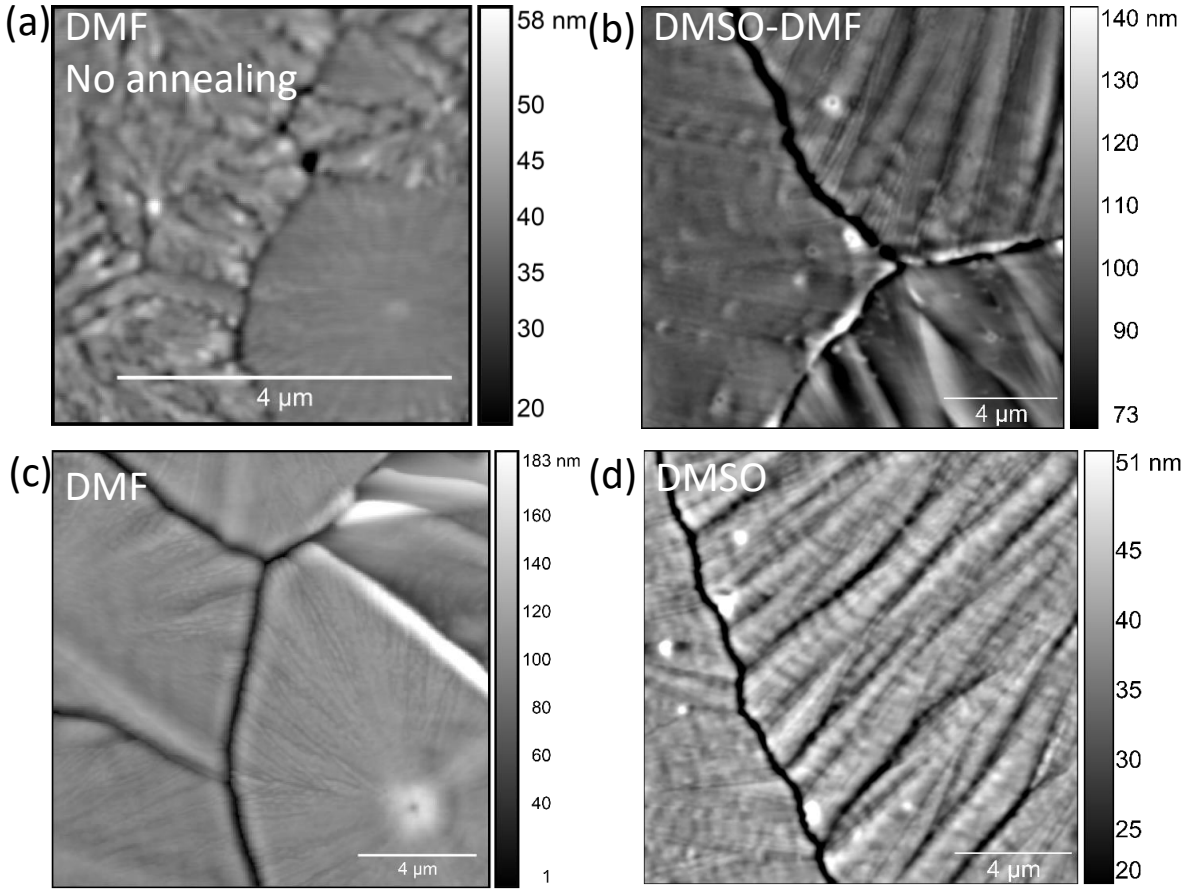

Fig. A15. AFM images of chiral perovskite films. The results were collected from perovskite films fabricated using DMF solvents (a) without hot-annealing process, DMSO-DMF mixture (b), DMF (c) and DMSO solvents (d). The later three samples were all annealing at 100 °C for 10 mins.

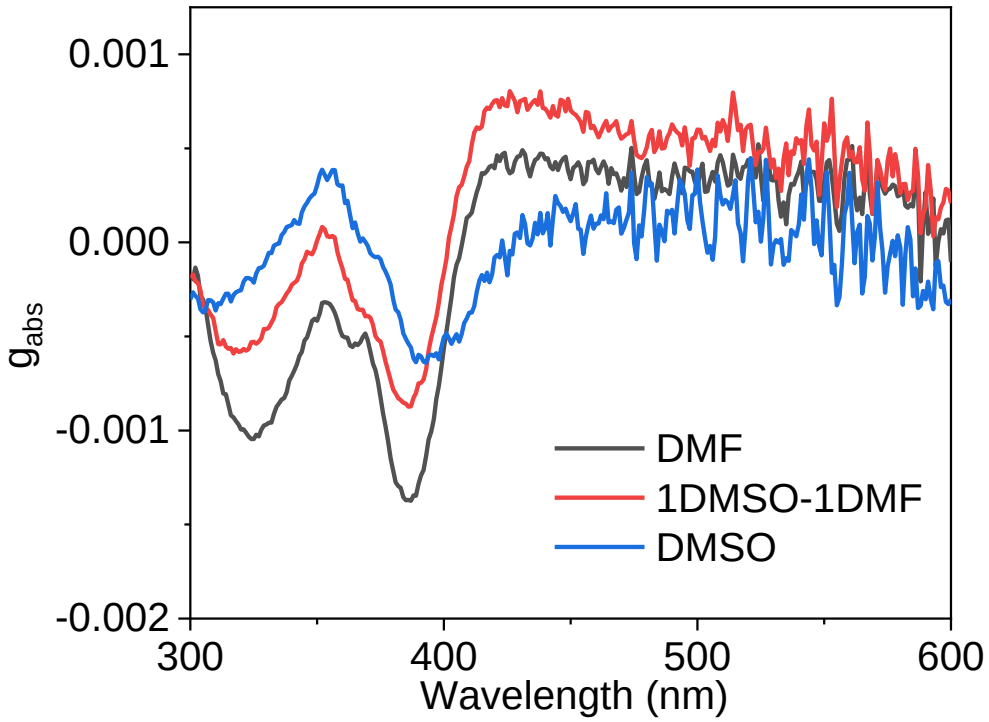

Fig. A16. **The anisotropy factor (g_{abs} value) of chiral perovskite films.** The perovskite films were prepared using three different solutions.

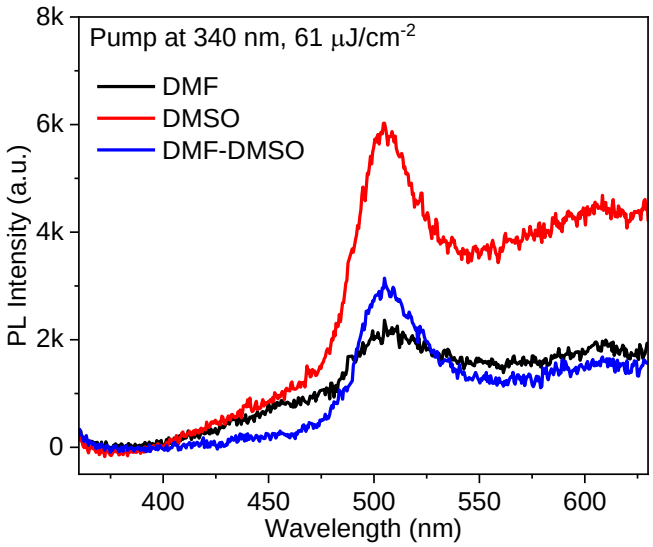

Fig. A17. **Room temperature PL spectra of chiral (R)-EAPbI$_3$ perovskite films.** The PL measurements were performed under 340 nm excitation and were collected from films produced using three different solvents, as indicated in the legend.

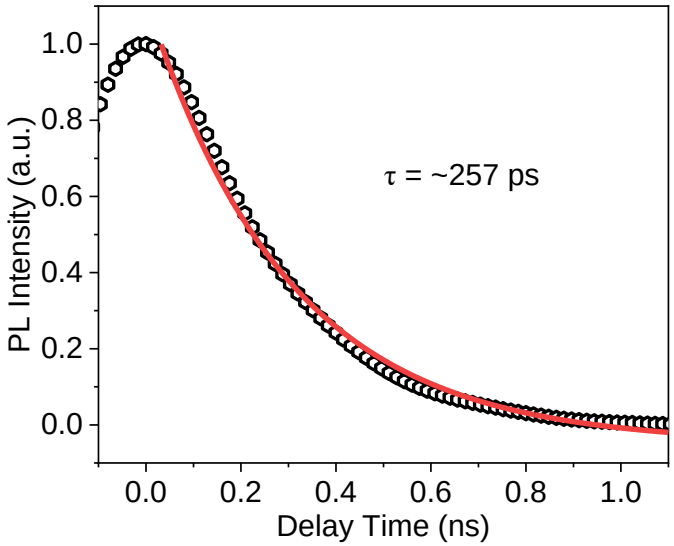

Fig. A18. TCSPC kinetics were obtained at 505 nm (DMF films). A 405 nm excitation beam with a fluence of ~10 μJ/cm^2 was used to pump the samples.

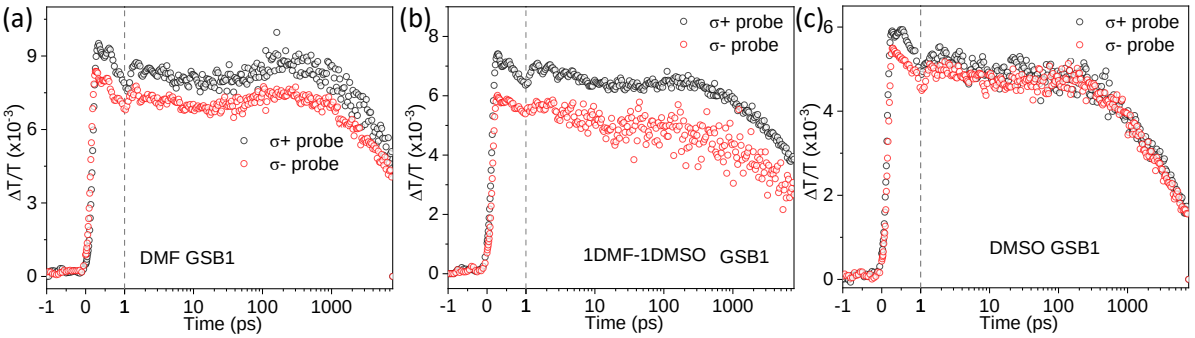

Fig. A19. CTA kinetics collected from GSB1 regions in Fig. 5.8a-c.

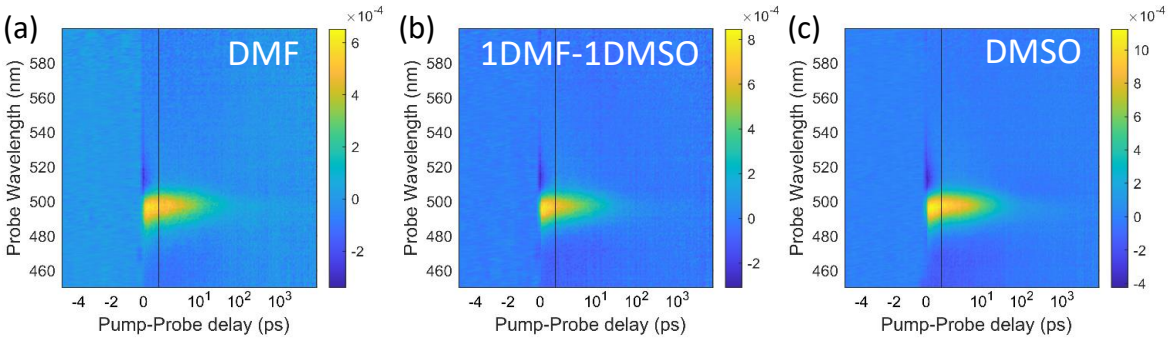

Fig. A20. **TA color maps of chiral perovskite samples using DMF (a), DMSO-DMF mixture (b), and DMSO solvents (c).** The excitation wavelength is 430 nm to avoid the generation of GSB1 signals (~378 nm).

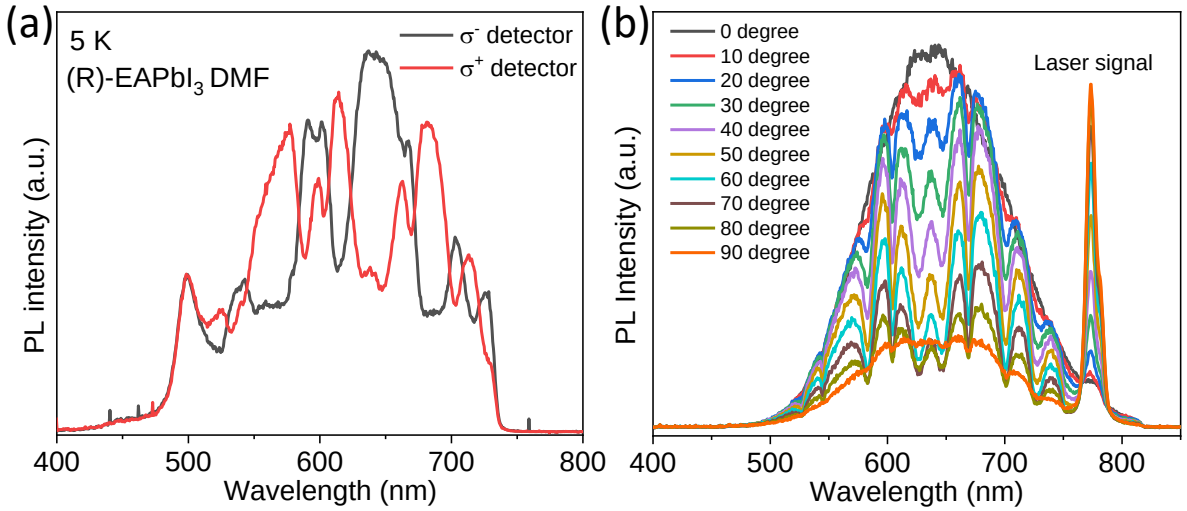

Fig. A21. **CPL measurements on chiral perovskite samples.** (a) Low temperature CPL spectra collected from chiral perovskite thin films using DMF solvents. (b) Linear polarized PL measurements obtained from $EAPbI_3$ single crystals at 5 K.

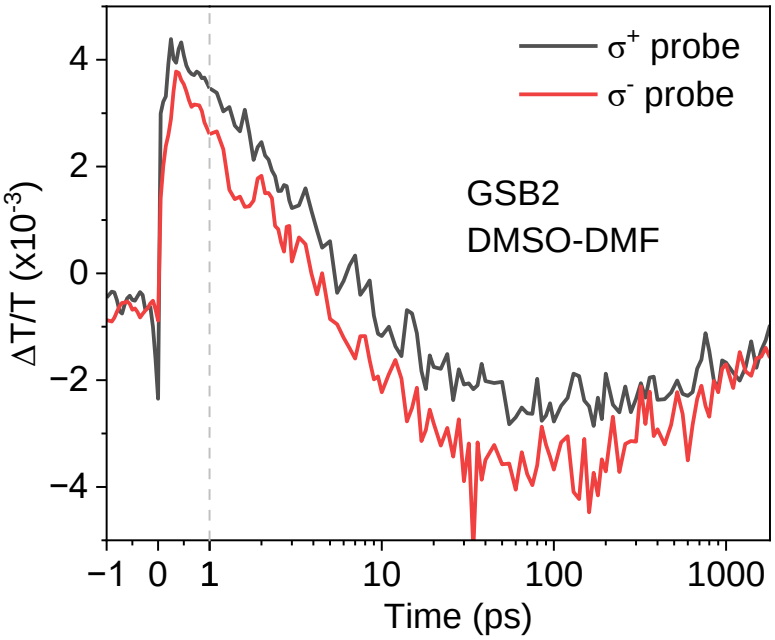

Fig. A22. Low temperature CTA kinetics obtained from GSB2 regions in Fig. 5.11e.

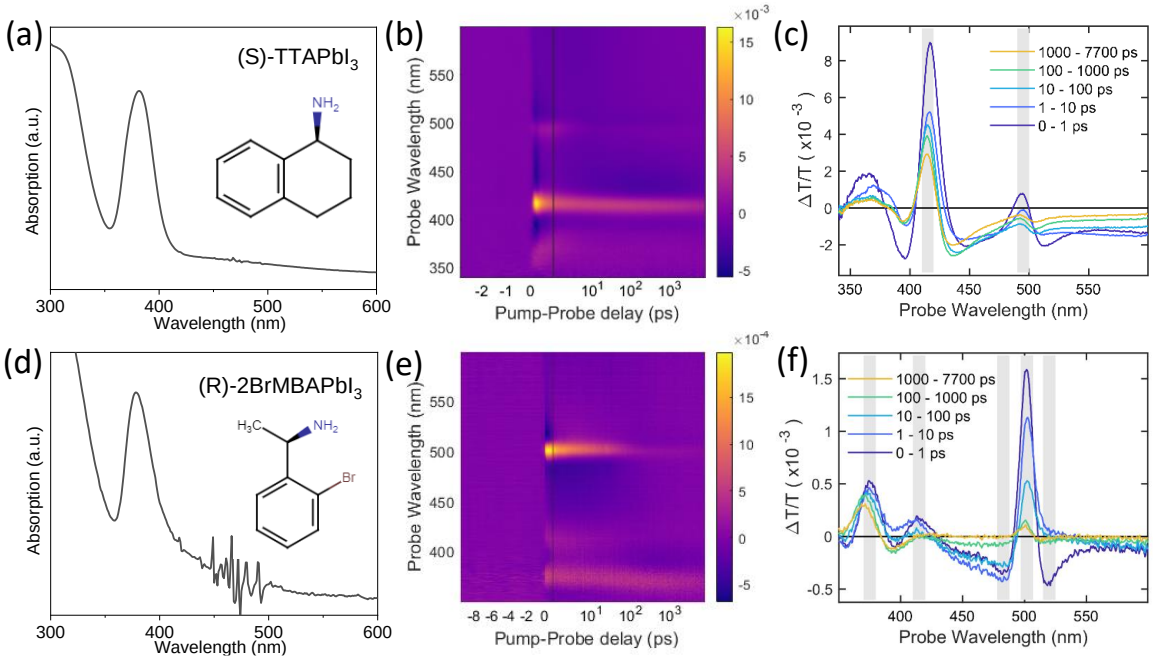

Fig. A23. **Optical properties of other chiral 1D perovskite thin films.** Absorption spectra (a, d), TA color maps (b, e), and TA spectra (c, f) collected from chiral 1D perovskite (S)-TTAPbI$_3$ and (R)-2BrMBAPbI$_3$, respectively. TTA represents 1,2,3,4-Tetrahydro-1-naphthylamine, and 2BrMBA represents 1-(2-Bromophenyl)ethylamine. Their corresponding molecule structures are depicted in the Fig. a and d.

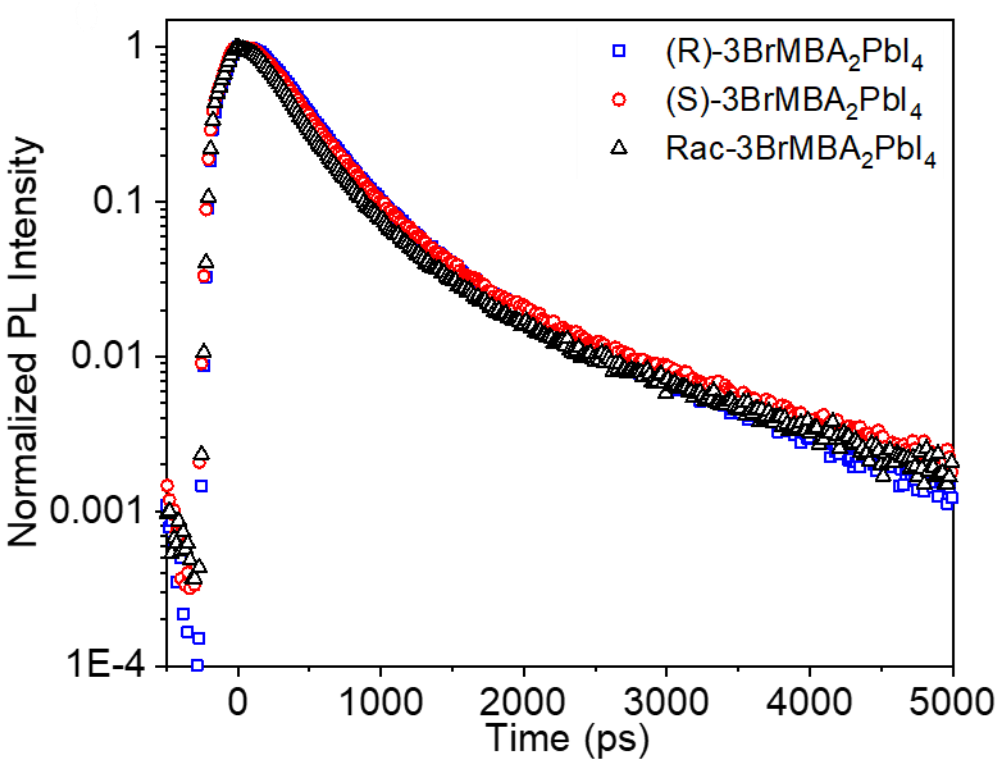

Fig. A24. TCSPC kinetics of (R/S)-3BrMBA$_2$PbI$_4$ and Rac-3BrMBA$_2$PbI$_4$ thin films. Each measurement was collected at their respective PL band positions with photoexcitation at 405 nm and an excitation fluence of ~0.5 μJ/cm^2.

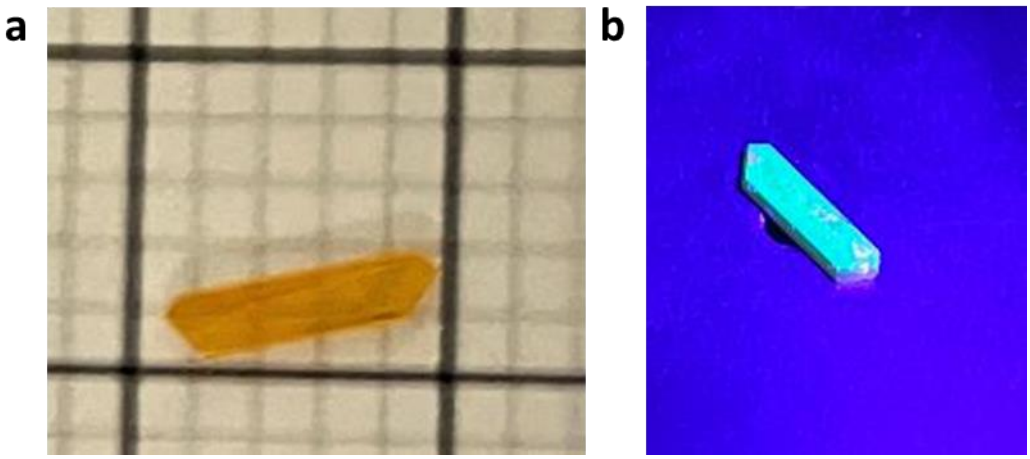

Fig. A25. Photographs of chiral (S)-3BrMBA$_2$PbI$_4$ single crystal on millimeter-grid paper (a) and under UV light photoexcitation (b).

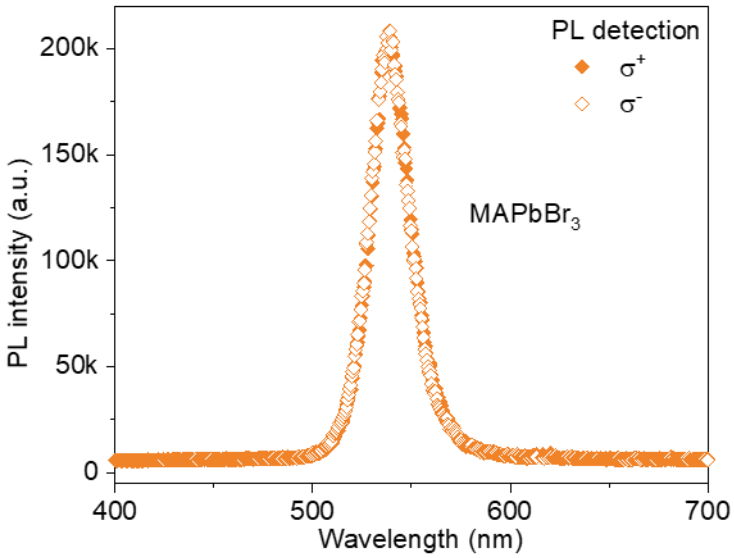

Fig. A26. **Circularly polarized PL spectra of $MAPbBr_3$ thin films at room temperature.** CPL results were obtained under the same conditions as chiral 2D perovskite for comparison.

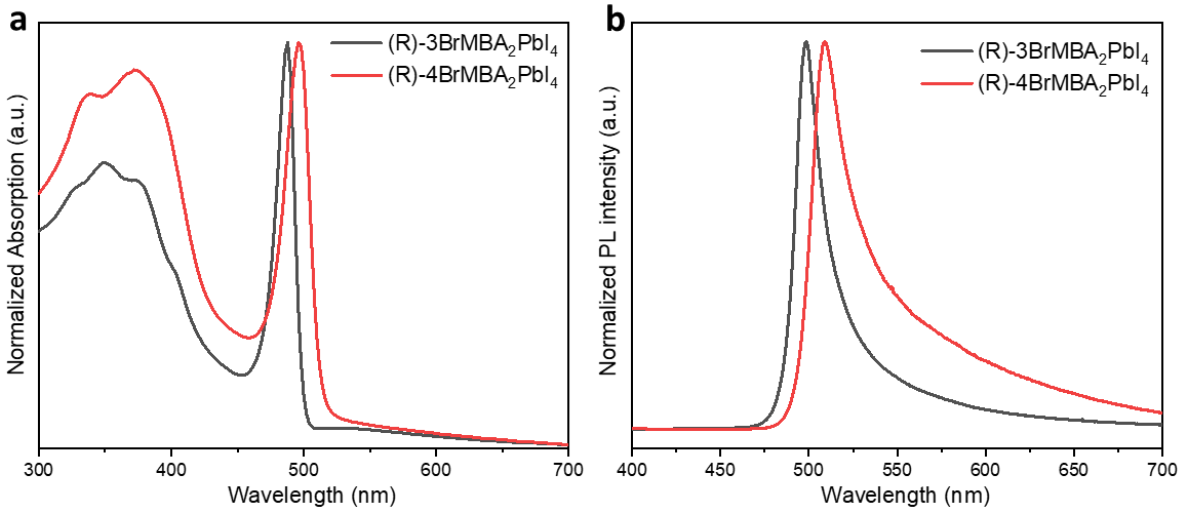

Fig. A27. Linear absorption (a) and PL (b) spectra of chiral (R)-3BrMBA$_2$PbI$_4$ and (R)-4BrMBA$_2$PbI$_4$ thin films. Compared with (R)-4BrMBA$_2$PbI$_4$, more distorted (R)-3BrMBA$_2$PbI$_4$ shows blue shifted signals in both absorption and PL spectra.

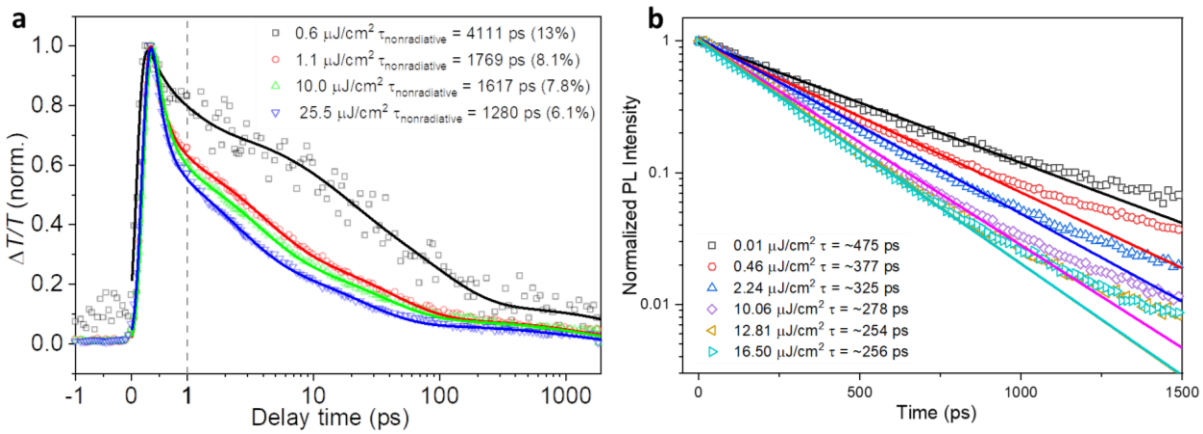

Fig. A28. (a) Fluence dependent TA kinetics plots obtained from GSB region of chiral (R)-3BrMBA$_2$PbI$_4$. (b) Fluence dependent TCSPC kinetics of (R)-3BrMBA$_2$PbI$_4$ thin films at 500 nm.

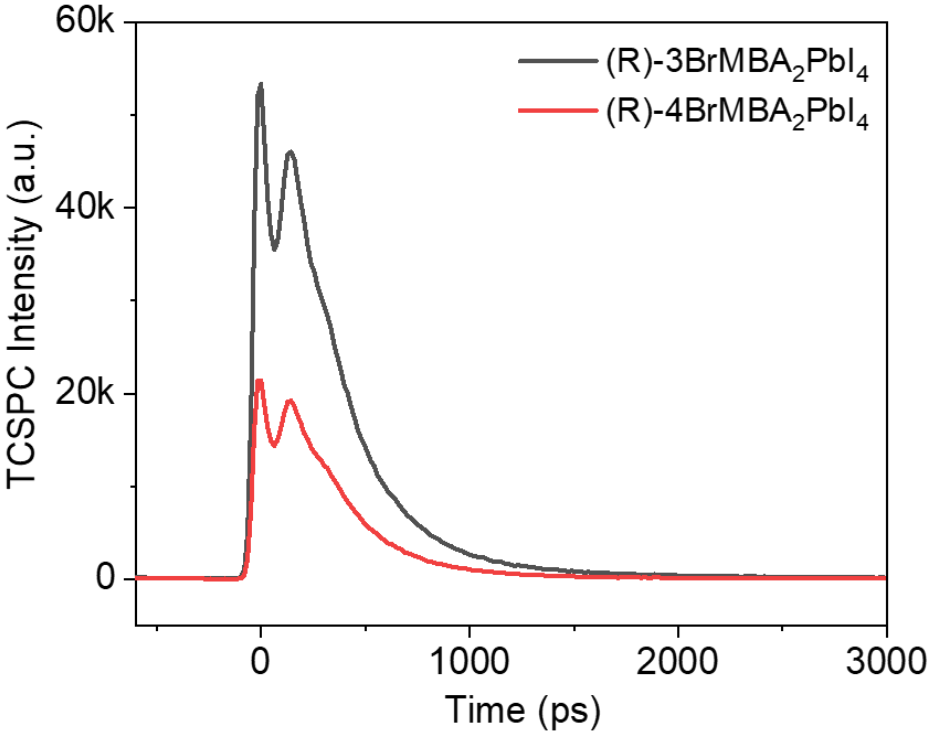

Fig. A29. Original TCSPC kinetics of (R)-3BrMBA$_2$PbI$_4$ and (R)-4BrMBA$_2$PbI$_4$ thin films, which is collected at their corresponding PL band positions under the same excitation conditions (405 nm, ~10 μJ/cm^2), with fixed signal accumulation time of 60 s.

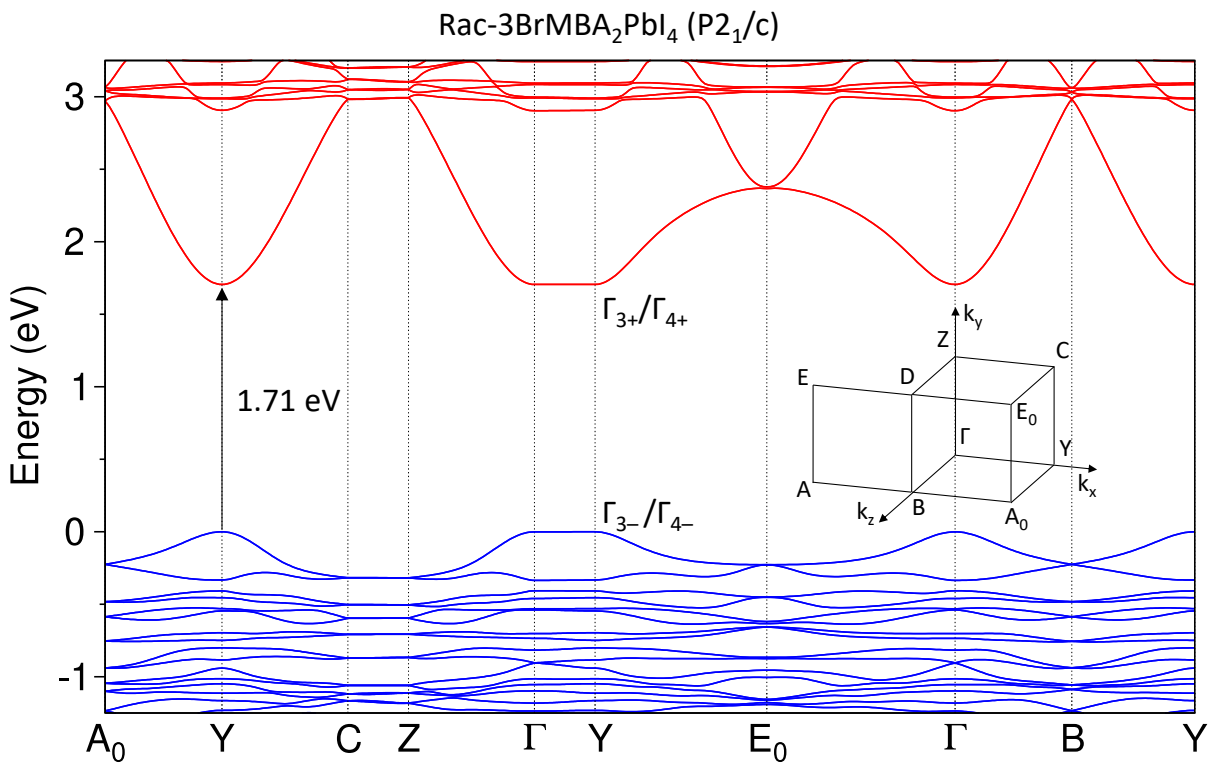

Fig. A30. DFT computed band structures of Rac-3BrMBA$_2$PbI$_4$. The irreducible representations at Y are marked. The inset shows the Brillouin zone for the P2$_1$/c group. A direct band gap of 1.71 eV is found at Y.

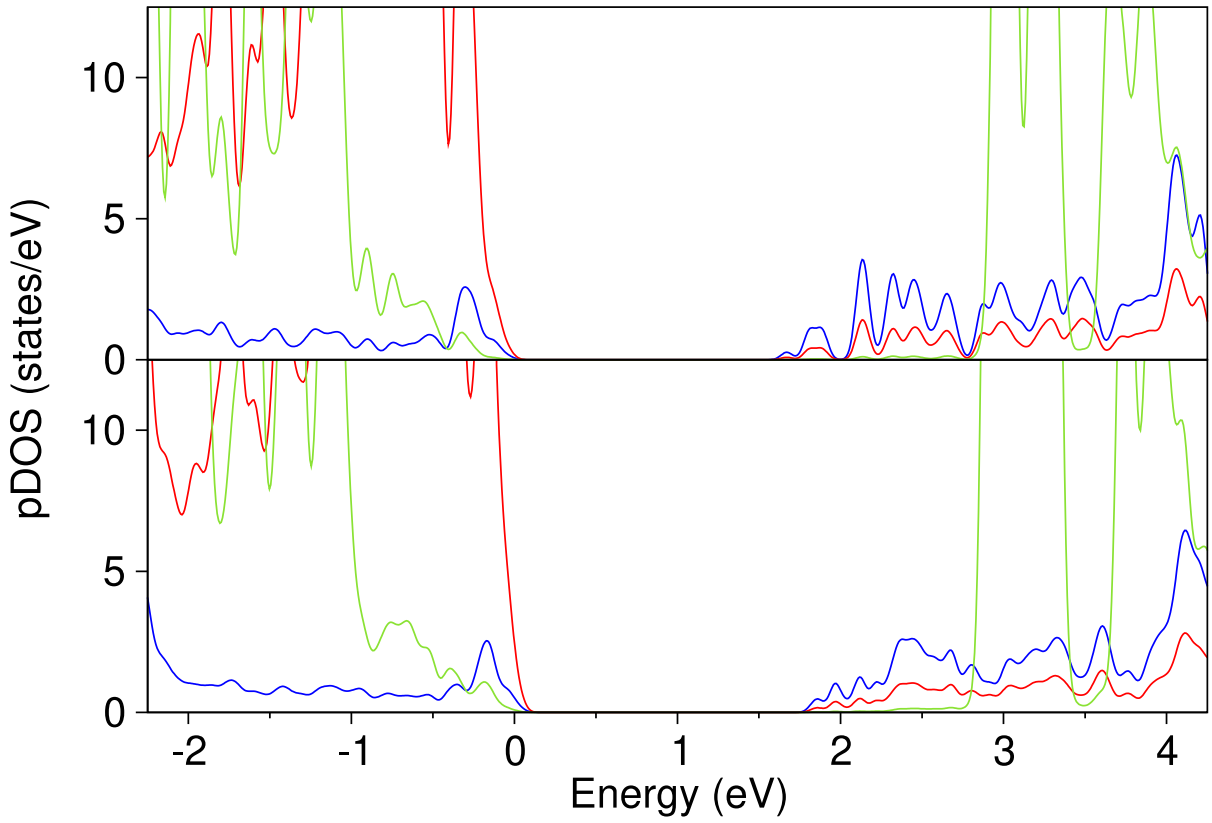

Fig. A31. Density of states projected over Pb (blue lines), I (red lines) and 3BrMBA (green lines) states for Rac-3BrMBA$_2$PbI$_4$ (top) and (S)-3BrMBA$_2$PbI$_4$ (bottom).

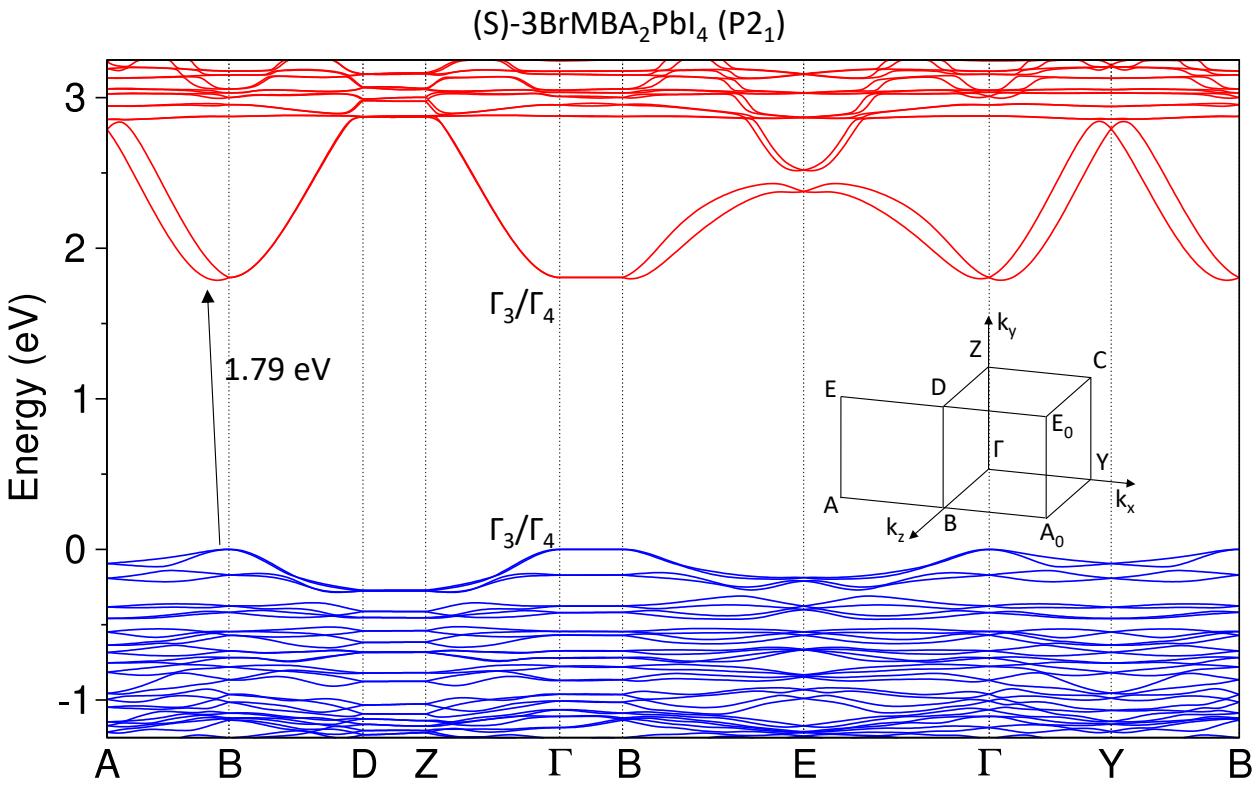

Fig. S32. DFT computed band structures of (S)-3BrMBA$_2$PbI$_4$. The irreducible representations at Γ are marked. The inset shows the Brillouin zone for the P2$_1$ group. Both VBM and CBM move away from B because of the Rashba splitting observable on the B-A path, resulting in a slightly indirect band gap of 1.79 eV.

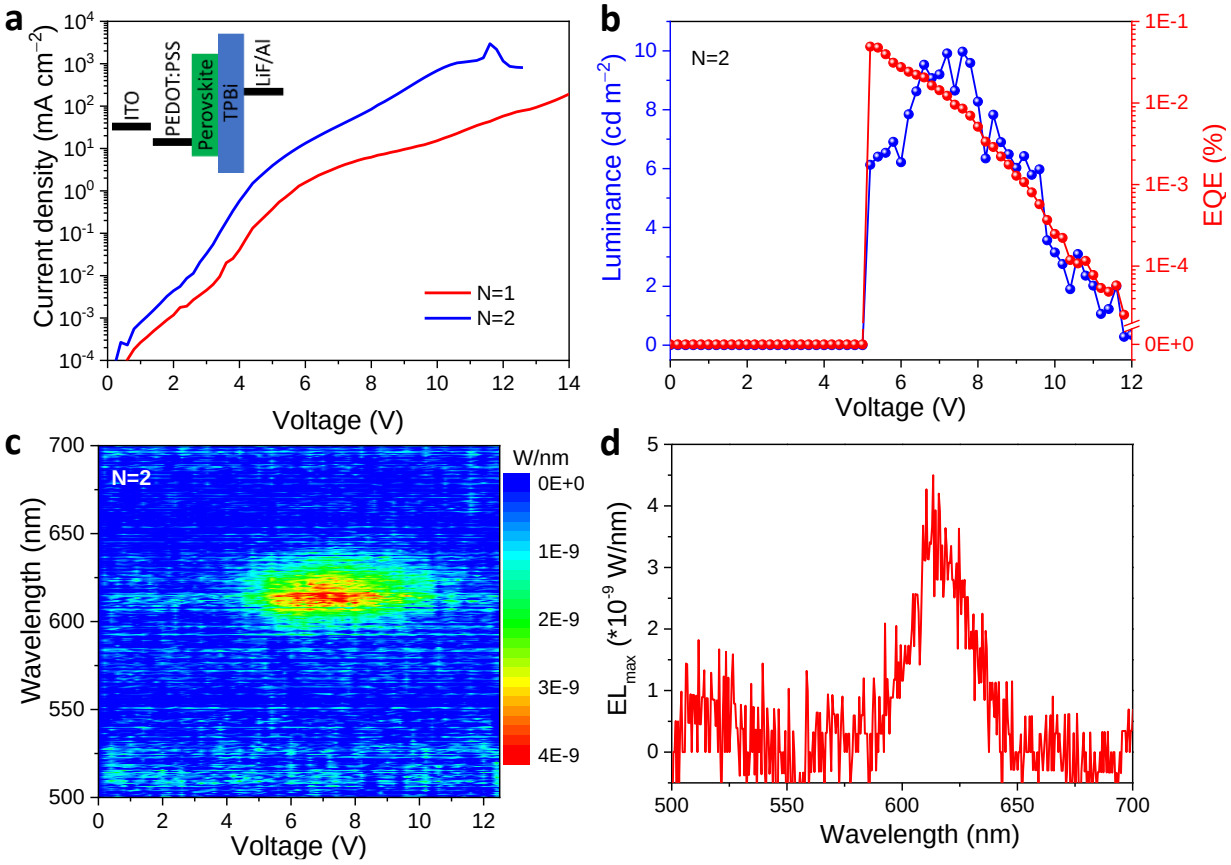

Fig. A33. Device characterizations of chiral layered perovskite LED. (a) Current density−voltage curves of chiral perovskite ((R)-3BrMBA$_2$PbI$_4$)(CsPbBr$_3$)$_{N-1}$ (N = 1 or 2). Inset is the corresponding LED device structure. (b) Luminance–voltage, EQE−voltage, and (c, d) electroluminescence maps and spectra of N = 2 sample.

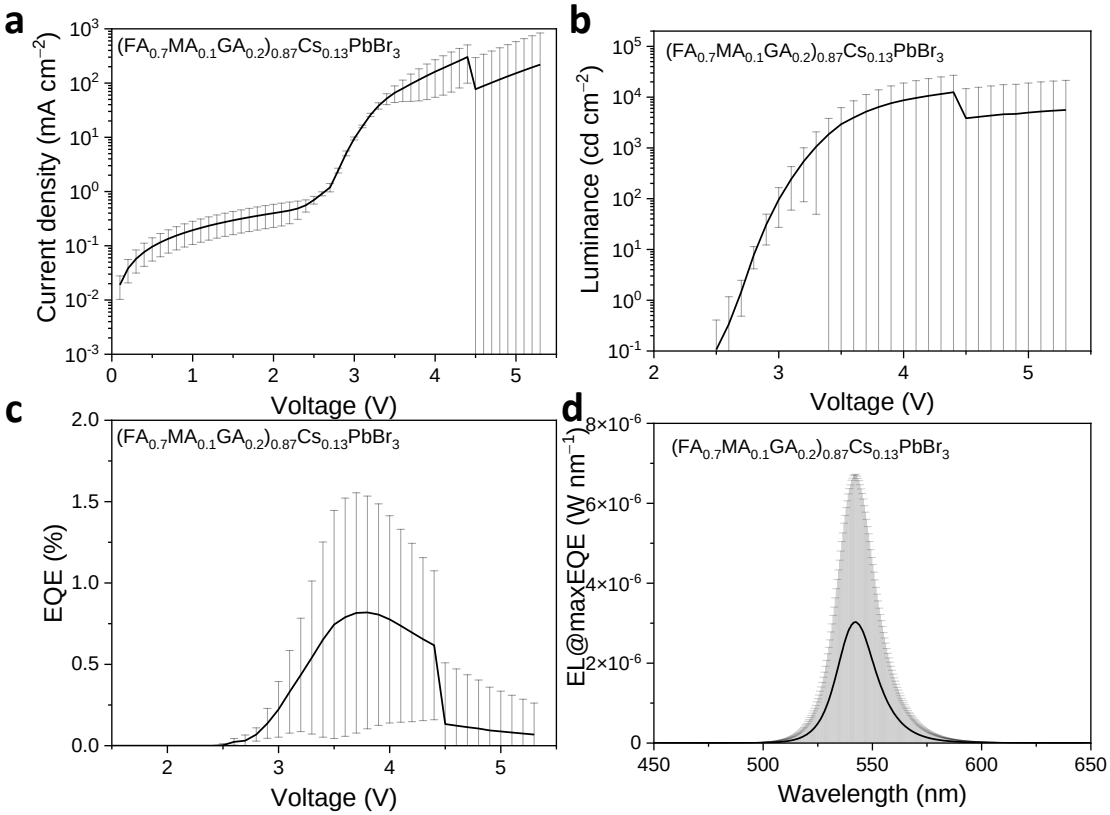

Fig. A34. **LED performance based on pure 3D $(FA_{0.7}MA_{0.1}GA_{0.2})_{0.87}Cs_{0.13}PbBr_3$ perovskites. a,** Current density versus voltage curve. **b,** luminance versus voltage curve. **c,** EQE versus voltage curve. **d,** EL spectra of perovskite LED devices under maximum EQE conditions.

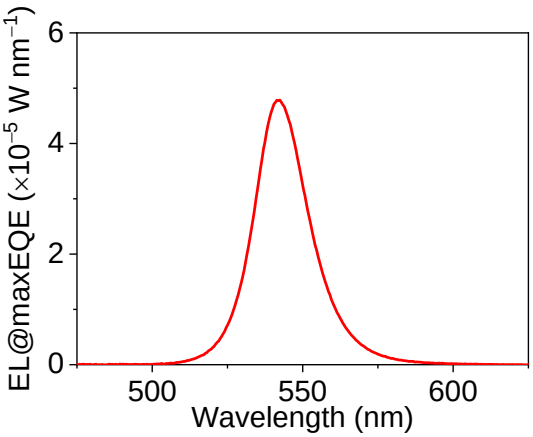

Fig. A35. EL spectra of chiral perovskite LED devices under maximum EQE conditions.

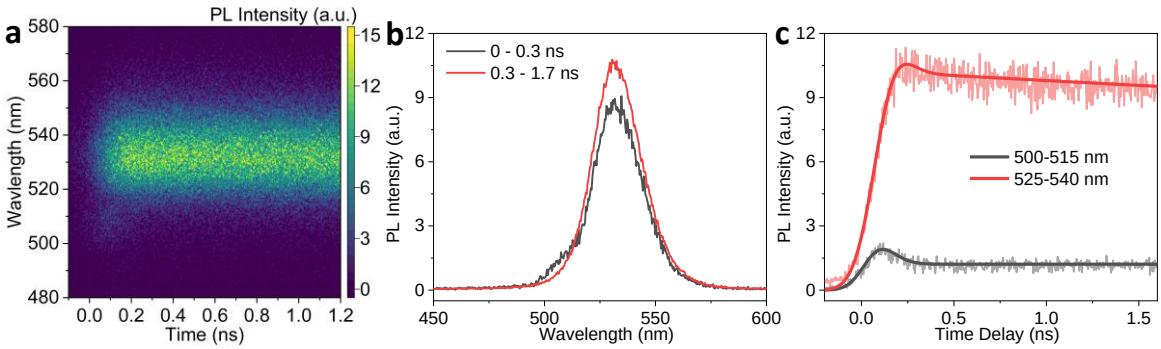

Fig. A36. Time resolved PL color maps (a), spectra (b), and kinetics (c) of perovskite heterostructures with 1% (R)-3BrMBA additives. The measurements were performed under 355 nm excitations with a fluence of 0.3 μJ/cm^2.

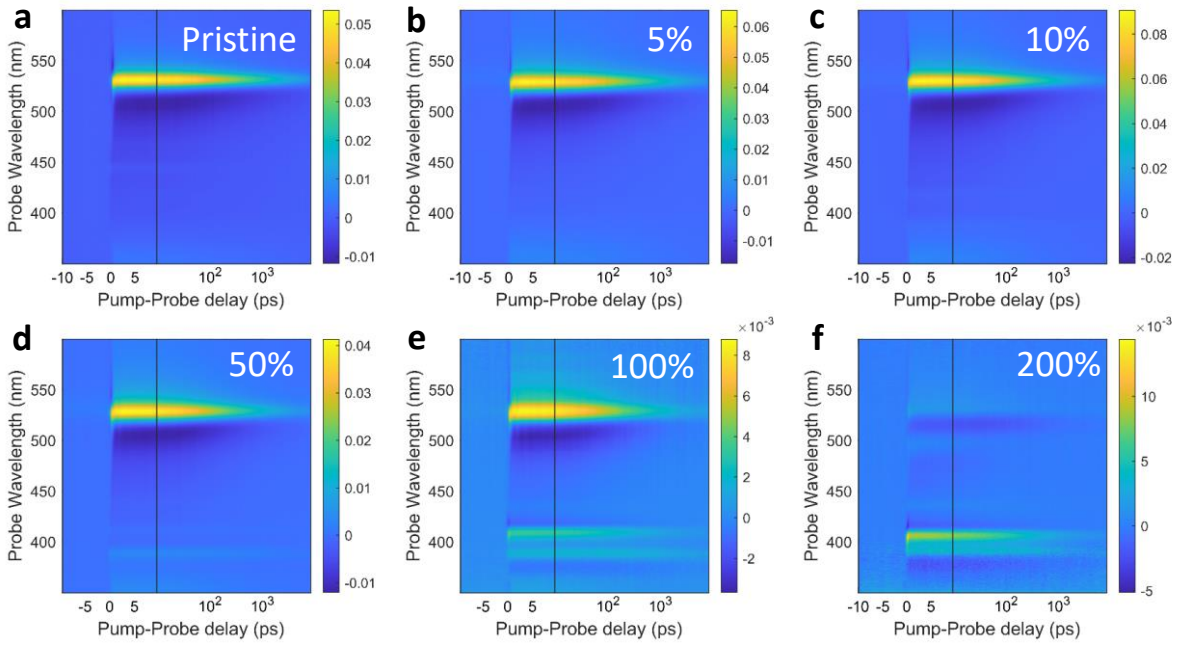

Fig. A37. TA color maps of pristine (a), 5% (b), 10% (c), 50% (d), 100% (e) and 200% (R)-3BrMBA (f) treated 3D perovskites. The excitation wavelength for current TA measurements is 340 nm with a fluence of ~141 μJ/cm^2 to monitor all possible phase information.

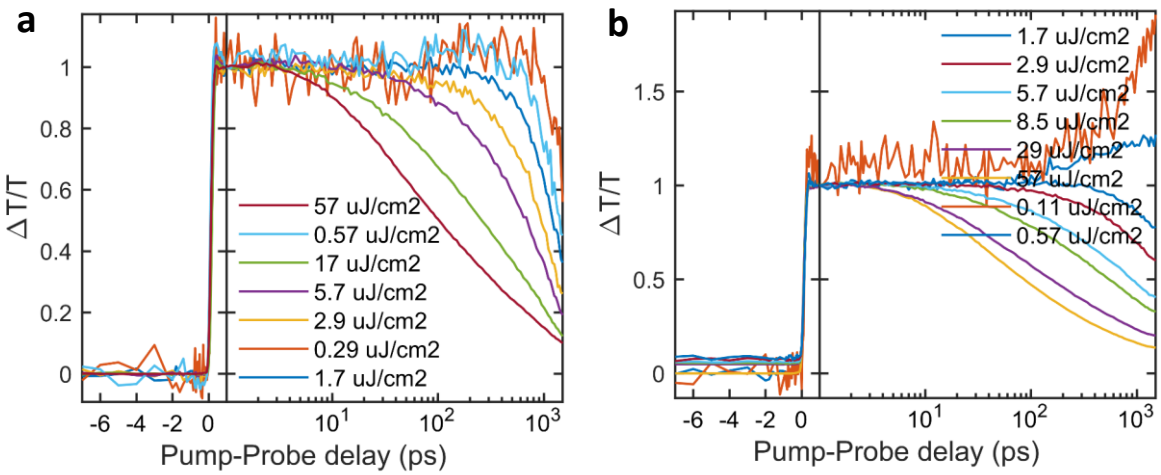

Fig. A38. **Fluence dependent TA kinetics plots**, obtained from GSB region of pristine (a) and 1% (R)-3BrMBA treated (b) 3D perovskite samples.

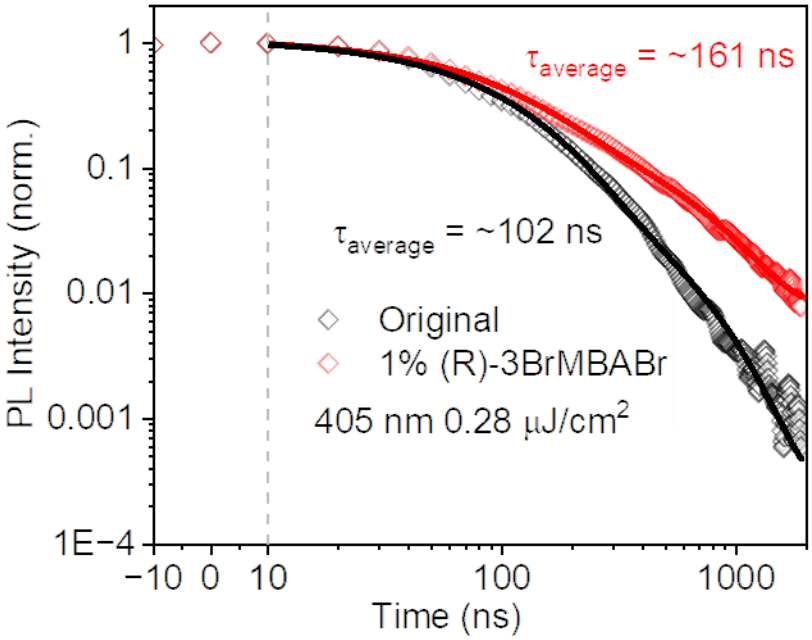

Fig. A39. Comparison of PL decay kinetics between original and 1% (R)-3BrMBA treated samples.

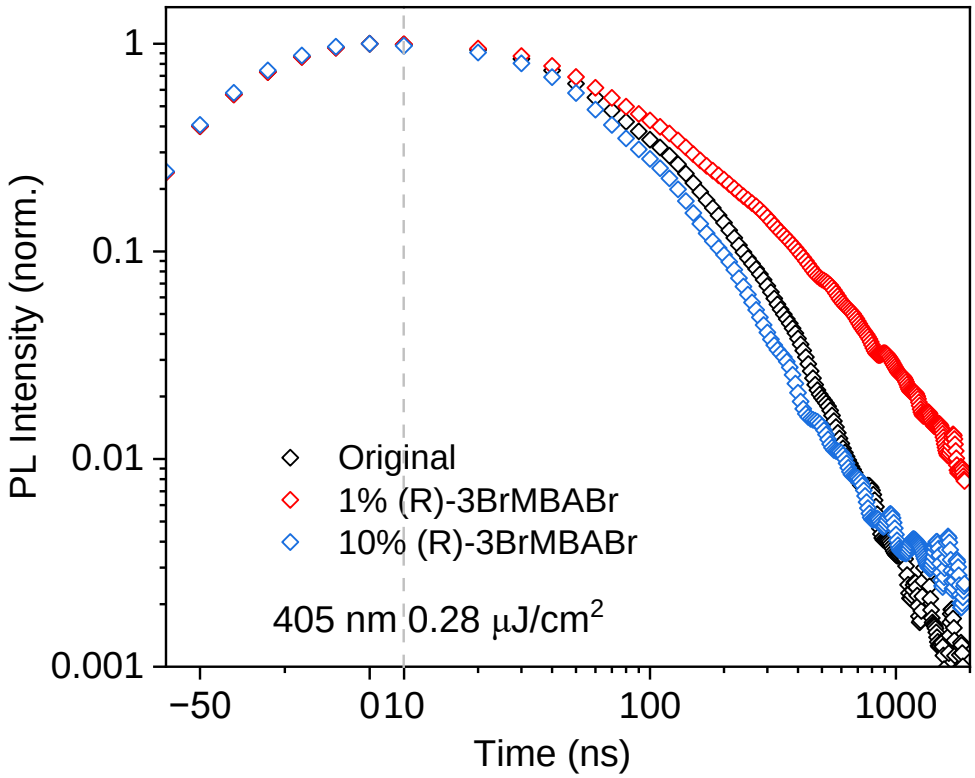

Fig. A40. Comparison of time resolved PL kinetics between pristine (a), 1% (b), and 10% (R)-3BrMBA treated (c) 3D perovskite samples.

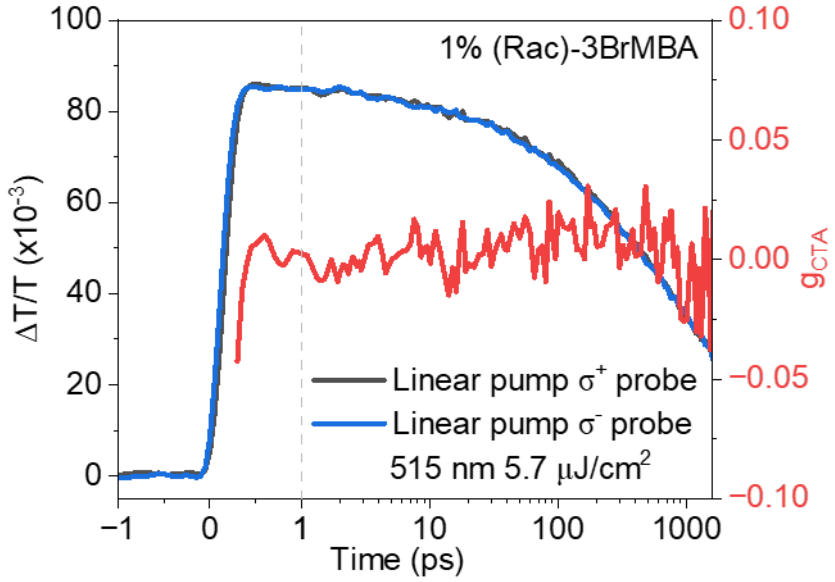

Fig. A41. CTA kinetics extracted from GSB regions of 1% (Rac)-3BrMBA treated samples. The corresponding pump wavelengths and fluences were depicted in the figures.

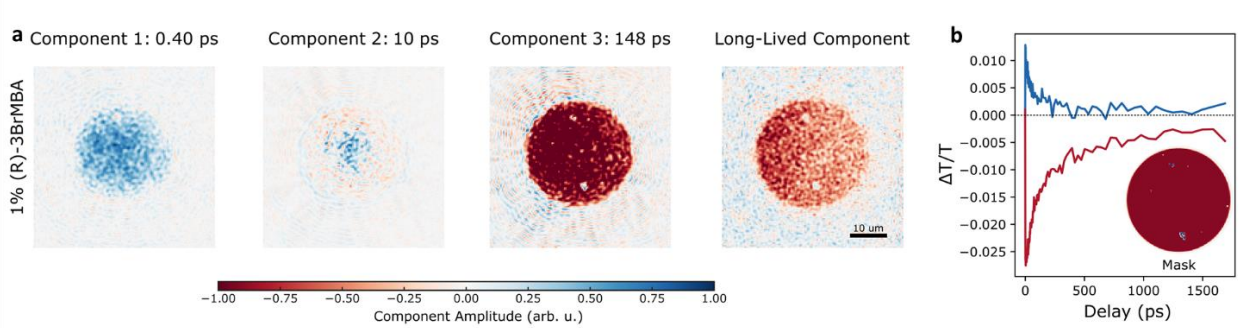

Fig. A42. Spatial-resolved charge carrier dynamics. a, Holographic TA microscope images collected from 1% (R)-3BrMBA treated. Each time component was obtained by applying principle component analysis. The blue or red area corresponds to the pumped area, while the probe illuminates the entire field of view. The TA microscope measurements were performed under 400 nm excitations with a fluence of 30 μJ/cm^2, and probed at ~510 nm. **b,** Spatial-resolved TA kinetic plots for 1% (R)-3BrMBA treated samples. Blue and red curves indicate the two different kinetics recognized by applying the mask on component 3 in Fig. a. The inset contains their corresponding masked images.

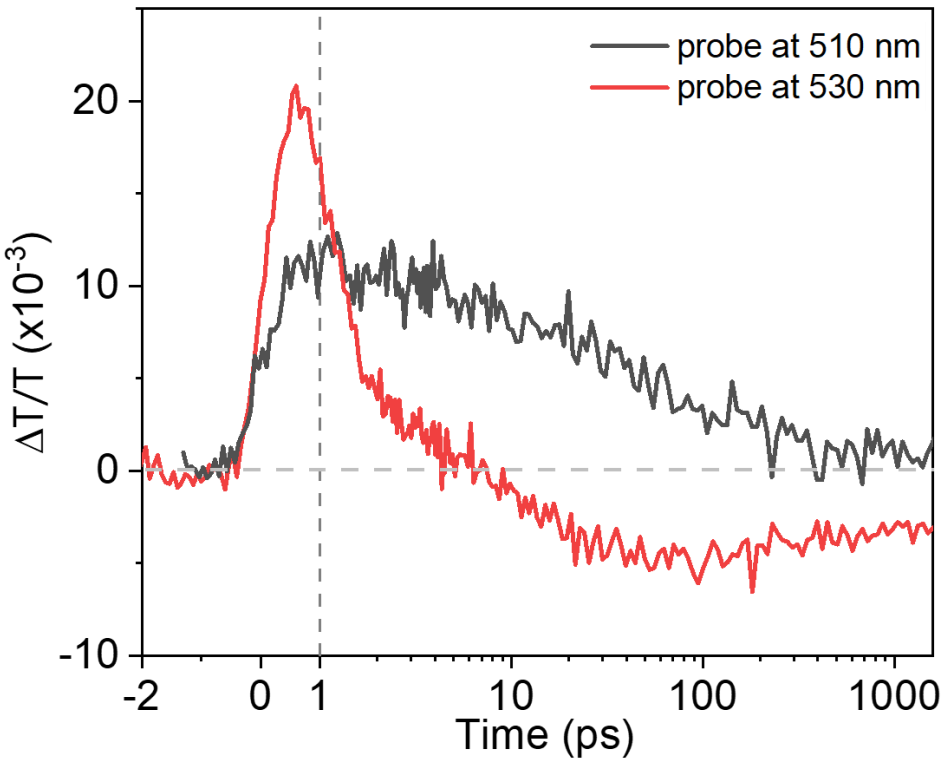

Fig. A43. Comparison of holographic TA kinetics probed at 510 nm and 530 nm of 1% (R)-3BrMBA treated samples. The black curve was collected from the positive masked regions when probed at 510 nm (Fig. A42b), representing the GSB kinetics of chiral quasi-2D perovskite domains. The red curve was collected from the negative masked regions when probed at 530 nm (Fig. 4c), representing the PIA kinetics of chiral domains. Such fast-decay GSB and long-lived PIA kinetics are the main evidence for the carrier transfer from chiral quasi-2D perovskite domains to bulk 3D phases.

Appendix B Supplemental Tables

Table B1. Crystallographic data for (R)-$CHEA_4Bi_2I_{10}$ and (R/S)-$CHEA_4Bi_2Br_{10}$.

	(R)-$CHEA_4Bi_2I_{10}$	(R)-$CHEA_4Bi_2Br_{10}$	(S)-$CHEA_4Bi_2Br_{10}$
Empirical Formula	$C_{64}H_{144}Bi_4I_{20}N_8$	$C_{64}H_{144}Bi_4Br_{20}N_8$	$C_{64}H_{144}Bi_4Br_{20}N_8$
Temperature, K	100	100	100
Formula Weight, g/mol	4399.78	3459.98	3459.98
Crystal System	monoclinic	monoclinic	monoclinic
Space group	P 1 2_1 1	P 1 2_1 1	P 1 2_1 1
a, Å	13.2206(5)	12.7299(10)	12.7080(10)
b, Å	13.8313(5)	13.1847(10)	13.2439(8)
c, Å	31.5088(13)	30.524(3)	30.566(2)
α, °	90	90	90
β, °	101.079(2)	100.298(3)	100.480(3)
γ, °	90	90	90
Volume, $Å^3$	5654.3(4)	5040.7(7)	5058.6(6)
Z	2	2	2
Density (calculated), g/cm^3	2.584	2.280	2.272
Absorption coefficient,	11.7	14926	14.873

mm^{-1}			
F(000)	3952	3232	3232
Radiation	MoK_α (λ = 0.71073)	MoK_α (λ = 0.71073)	MoK_α (λ = 0.71073)
2θ range for data collection, °	3.69 to 52.744	3.844 to 61.11	3.75 to 51.364
Reflections collected	294825	145333	91763
Independent reflections	23124 [R_{int} = 0.0882, R_{sigma} = 0.0414]	30360 [R_{int} = 0.0693, R_{sigma} = 0.652]	18339 [R_{int} = 0.0547, R_{sigma} = 0.0460]
Data/restraints/parameters	23124/1/858	30360/13/846	18339/1/840
Goodness of fit on F^2	1.070	1.023	1.065
Final R indexes [I>2σ(I)]	R_1 = 0.0279, wR_2 = 0.0499	R_1 = 0.0343, wR_2 = 0.065	R_1 = 0.0325, wR_2 = 0.0745
Final R indexes (all data)	R_1 = 0.0345, wR_2 = 0.0528	R_1 = 0.0415 wR_2 = 0.0671	R_1 = 0.0352, wR_2 = 0.0754
CCDC number	2129957	2129958	2175452

Table B2. Octahedral distortion calculation for (R)-$CHEA_4Bi_2I_{10}$ and (R)-$CHEA_4Bi_2Br_{10}$.

		Bond length distortion index	Bond angle variance degrees^2
(R)-$CHEA_4Bi_2I_{10}$	$Bi(1)I_6$	0.0405	4.57
	$Bi(2)I_6$	0.0341	9.26
	$Bi(3)I_6$	0.0356	9.41
	$Bi(4)I_6$	0.0363	15.84
(R)-$CHEA_4Bi_2Br_{10}$	$Bi(1)Br_6$	0.0414	4.09
	$Bi(2)Br_6$	0.0352	23.09
	$Bi(3)Br_6$	0.0421	25.05
	$Bi(4)Br_6$	0.0441	14.94

The distortion degree of bismuth halide octahedral structures is quantified according to Lu's work (*108*). Specifically, the bond length distortion index (D) and bond angle variance degrees (σ^2) are calculated by following equations:

$$D = \frac{1}{6}\sum_{i=1}^{6}\frac{|d_i - d_0|}{d_0}$$

$$\sigma^2 = \frac{1}{11}\sum_{i=1}^{12}(\theta_i - 90)^2,$$

where d_i is the corresponding Bi-I bond distance, d_0 represents the average Bi-I bond length, and θ_i means I-Bi-I bond angle in octahedral structures. All these values can be obtained from single crystal XRD data.

Table B3. Crystallographic data for (R)-EAPbI$_3$.

	(R)-EAPbI$_3$
Empirical Formula	$C_9H_{14}I_3NPb$
Temperature, K	100(2) K
Formula Weight, g/mol	724.10
Crystal System	Orthorhombic
Space group	*P* 2_1 2_1 2_1
a, Å	8.1004(4)
b, Å	8.7167(5)
c, Å	21.6184(11)
α, °	90
β, °	90
γ, °	90
Volume, Å^3	1526.45(14)
Z	4
Density (calculated), g/cm^3	3.151
Absorption coefficient, mm^{-1}	17.091
F(000)	1264
Radiation	MoK$_\alpha$ (λ = 0.71073)
2θ range for data collection, °	2.25 to 28.75
Reflections collected	70309
Independent reflections	3875 [R(int) = 0.0427]
Data/restraints/parameters	3875/3/129
Goodness of fit on F^2	1.153
Final R indexes [I>2σ(I)]	R_1 = 0.0160, wR_2 = 0.0366
Final R indexes (all data)	R_1 = 0.0161, wR_2 = 0.0367

Table B4. Fit results of FWHM plots as a function of temperature.

	Γ_0	γ_{ac}	γ_{LO}	E_{phonon}
Chiral perovskite/PbI_2 heterostructure	~43 meV	~0.31 meV	~8590 meV	~25 meV

Table B5. Crystallographic data for (S)-3BrMBA$_2$PbI$_4$ and Rac-3BrMBA$_2$PbI$_4$.

	(S)-3BrMBA$_2$PbI$_4$	Rac-3BrMBA$_2$PbI$_4$
Empirical Formula	$C_{16}H_{22}Br_2I_4N_2Pb$	$C_{16}H_{22}Br_2I_4N_2Pb$
Temperature, K	103(2) K	105(2) K
Formula Weight, g/mol	1116.96	1116.96
Crystal System	Monoclinic	monoclinic
Space group	*P* 1 2_1 1	*P* 1 $2_1/c$ 1
a, Å	9.1551(5)	17.6377(17)
b, Å	8.2245(5)	8.3785(7)
c, Å	17.7782(10)	9.1449(9)
α, °	90	90
β, °	99.051(3)	98.973(3)
γ, °	90	90
Volume, Å^3	1321.96(13)	1334.9(2)
Z	2	2
Density (calculated), g/cm^3	2.806	2.779
Absorption coefficient, mm^{-1}	14.079	13.942
F(000)	992	992
Radiation	MoK$_\alpha$ (λ = 0.71073)	MoK$_\alpha$ (λ = 0.71073)
2θ range for data collection, °	2.25 to 25.35	2.34 to 25.34
Reflections collected	138706	63180
Independent reflections	4737 [R(int) = 0.0433]	2432 [R_{int} = 0.0575]
Data/restraints/parameters	4737/1/231	2432/0/117
Goodness of fit on F^2	1.050	1.103
Final R indexes [I>2σ(I)]	R_1 = 0.0127, wR_2 = 0.0254	R_1 = 0.0226, wR_2 = 0.0600
Final R indexes (all data)	R_1 = 0.0130, wR_2 = 0.0256	R_1 = 0.0244, wR_2 = 0.0629

CCDC number	2222721	2222720

Table B6. Octahedral distortion calculation for (S)-3BrMBA$_2$PbI$_4$ and Rac-3BrMBA$_2$PbI$_4$.

	Pb-I Bond length	D	σ^2
(S)-3BrMBA$_2$PbI$_4$	3.1489(3) 3.1816(4) 3.2084(4) 3.1757(3) 3.1833(4) 3.3085(3)	0.012	31.91
Rac-3BrMBA$_2$PbI$_4$	3.1763(4) 3.1973(3) 3.2273(4) 3.1763(4) 3.1973(3) 3.2273(4)	0.006	20.87

The bond length distortion index (D) and bond angle variance degrees (σ^2) are calculated by following equations:

$$D = \frac{1}{6}\sum_{i=1}^{6}\frac{|d_i - d_0|}{d_0}$$

$$\sigma^2 = \frac{1}{11}\sum_{i=1}^{12}(\theta_i - 90)^2,$$

where d_i is the corresponding Bi-I bond distance, d_0 represents the average Bi-I bond length, and θ_i means I-Bi-I bond angle in octahedral structures. All these values can be obtained from single crystal XRD data.

Table B7. Fit results of the decay kinetics in the GSB regions of (R)-3BrMBA$_2$PbI$_4$ and (R)-3BrMBA$_2$PbI$_4$.

TA kinetics Fitting	Amplitude	Decay lifetime (ps)
(R)-3BrMBA$_2$PbI$_4$	0.37	τ_1 = ~0.23
	0.32	τ_2 = ~3.5
	0.23	τ_3 = ~40.2
	0.08	τ_{dark} = ~1769.3
(R)-4BrMBA$_2$PbI$_4$	0.34	τ_1 = ~0.14
	0.14	τ_2 = ~6.5
	0.33	τ_3 = ~131.24
	0.21	τ_{dark} = ~1749.4

Table B8. Fit results of the decay kinetics in the GSB regions of pristine and 1% (R)-3BrMBA treated 3D perovskite samples.

TA kinetics Fitting	Amplitude	Decay lifetime (ns)
$(FA_{0.7}MA_{0.1}GA_{0.2})_{0.87}Cs_{0.13}PbBr_3$	0.43	τ_1 = ~8.2
	0.42	τ_2 = ~55.2
	0.15	τ_3 = ~481.6
		$\tau_{average}$ = ~99.0
$(FA_{0.7}MA_{0.1}GA_{0.2})_{0.87}Cs_{0.13}PbBr_3$: 1% (R)-3BrMBA	0.41	τ_1 = ~6.9
	0.39	τ_2 = ~54.1
	0.20	τ_3 = ~715.4
		$\tau_{average}$ = ~167.0

Bibliography

1. NREL, “Best Research-Cell Effciencies” (https://www.nrel.gov/pv/cell-efficiency.html, 2024).
2. G. Niu, X. Guo, L. Wang, Review of recent progress in chemical stability of perovskite solar cells. *J Mater Chem A Mater* **3**, 8970–8980 (2015).
3. W. Bai, T. Xuan, H. Zhao, H. Dong, X. Cheng, L. Wang, R. J. Xie, Perovskite Light-Emitting Diodes with an External Quantum Efficiency Exceeding 30%. *Advanced Materials* **35**, 2302283 (2023).
4. J. Ye, A. Ren, L. Dai, T. K. Baikie, R. Guo, D. Pal, S. Gorgon, J. E. Heger, J. Huang, Y. Sun, R. Arul, G. Grimaldi, K. Zhang, J. Shamsi, Y. T. Huang, H. Wang, J. Wu, A. F. Koenderink, L. Torrente Murciano, M. Schwartzkopf, S. V. Roth, P. Müller-Buschbaum, J. J. Baumberg, S. D. Stranks, N. C. Greenham, L. Polavarapu, W. Zhang, A. Rao, R. L. Z. Hoye, Direct linearly polarized electroluminescence from perovskite nanoplatelet superlattices. *Nat Photonics*, doi: 10.1038/s41566-024-01398-y (2024).
5. N. Nishizawa, K. Nishibayashi, H. Munekata, Pure circular polarization electroluminescence at room temperature with spin-polarized light-emitting diodes. *PNAS* **114**, 1783–1788 (2017).
6. S. Liu, M. W. Heindl, N. Fehn, S. Caicedo-Dávila, L. Eyre, S. M. Kronawitter, J. Zerhoch, S. Bodnar, A. Shcherbakov, A. Stadlbauer, G. Kieslich, I. D. Sharp, D. A. Egger, A. Kartouzian, F. Deschler, Optically induced long-lived chirality memory in the color-tunable chiral lead-free semiconductor (R)/(S)-CHEA4Bi2BrxI10−x (x= 0−10). *J. Am. Chem. Soc.* **144**, 14079–14089 (2022).
7. S. Liu, M. Kepenekian, S. Bodnar, S. Feldmann, M. W. Heindl, N. Fehn, J. Zerhoch, A. Shcherbakov, A. Pöthig, Y. Li, U. W. Paetzold, A. Kartouzian, I. D. Sharp, C. Katan, J. Even, F. Deschler, Bright circularly polarized photoluminescence in chiral layered hybrid lead-halide perovskites. *Sci. Adv.* **9**, eadh5083 (2023).
8. W. Friedrich, P. Knipping, M. Laue, In Sitzungsberichte der Math. Phys. Klasse (Kgl.) Bayerische Akademie der Wissenschaften. 303–322 (1912).
9. Thomas J., The birth of X-ray crystallography. *Nature* **491**, 186–187 (2012).
10. W. L. Bragg, Proc. Cambr. Phil. Soc. **17**, 43–57 (1913).

11. G. Long, R. Sabatini, M. I. Saidaminov, G. Lakhwani, A. Rasmita, X. Liu, E. H. Sargent, W. Gao, Chiral-perovskite optoelectronics. *Nat. Rev. Mater.* **5**, 423–439 (2020).
12. L. Sohncke, *Entwickelung Einer Theorie Der* (Teubner, 1879; http://books.google.com).
13. L. Wang, Y. Xue, M. Cui, Y. Huang, H. Xu, C. Qin, J. Yang, H. Dai, M. Yuan, A Chiral Reduced-Dimension Perovskite for an Efficient Flexible Circularly Polarized Light Photodetector. *Angewandte Chemie* **132**, 6504–6512 (2020).
14. Y. Hu, F. Florio, Z. Chen, W. Adam Phelan, M. A. Siegler, Z. Zhou, Y. Guo, R. Hawks, J. Jiang, J. Feng, L. Zhang, B. Wang, Y. Wang, D. Gall, E. F. Palermo, Z. Lu, X. Sun, T.-M. Lu, H. Zhou, Y. Ren, E. Wertz, R. Sundararaman, J. Shi, A chiral switchable photovoltaic ferroelectric 1D perovskite. *Sci. Adv* **6**, eaay4213 (2020).
15. C. Ye, J. Jiang, S. Zou, W. Mi, Y. Xiao, Core-shell three-dimensional perovskite nanocrystals with chiral-induced spin selectivity for room-temperature spin light-emitting diodes. *J. Am. Chem. Soc.* **144**, 9707–9714 (2022).
16. A. Ishii, T. Miyasaka, Direct detection of circular polarized light in helical 1D perovskite-based photodiode. *Sci. Adv* **6**, eabd3274 (2020).
17. A. Privitera, M. Righetto, F. Cacialli, M. K. Riede, Perspectives of Organic and Perovskite-Based Spintronics. *Adv Opt Mater* **9** (2021).
18. G. Grancini, M. K. Nazeeruddin, Dimensional tailoring of hybrid perovskites for photovoltaics. *Nat. Rev. Mater.* **4**, 4–22 (2019).
19. M. D. Smith, H. I. Karunadasa, White-Light Emission from Layered Halide Perovskites. *Acc Chem Res* **51**, 619–627 (2018).
20. R. Yang, R. Li, Y. Cao, Y. Wei, Y. Miao, W. L. Tan, X. Jiao, H. Chen, L. Zhang, Q. Chen, H. Zhang, W. Zou, Y. Wang, M. Yang, C. Yi, N. Wang, F. Gao, C. R. McNeill, T. Qin, J. Wang, W. Huang, Oriented Quasi-2D Perovskites for High Performance Optoelectronic Devices. *Advanced Materials* **30** (2018).
21. J. W. Lee, Z. Dai, T. H. Han, C. Choi, S. Y. Chang, S. J. Lee, N. De Marco, H. Zhao, P. Sun, Y. Huang, Y. Yang, 2D perovskite stabilized phase-pure formamidinium perovskite solar cells. *Nat Commun* **9** (2018).
22. N. G. Park, Perovskite solar cells: An emerging photovoltaic technology. *Materials Today* **18**, 65–72 (2015).
23. L. M. Pazos-Outón, M. Szumilo, R. Lamboll, J. M. Richter, M. Crespo-Quesada, M. Abdi-Jalebi, H. J. Beeson, M. Vrućinić, M. Alsari, H. J. Snaith, B. Ehrler, R. H. Friend,

F. Deschler, Photon recycling in lead iodide perovskite solar cells. *Science (1979)* **351**, 1430–1433 (2016).

24. G. Longo, S. Mahesh, L. R. V. Buizza, A. D. Wright, A. J. Ramadan, M. Abdi-Jalebi, P. K. Nayak, L. M. Herz, H. J. Snaith, Understanding the Performance-Limiting Factors of Cs2AgBiBr6Double-Perovskite Solar Cells. *ACS Energy Lett* **5**, 2200–2207 (2020).
25. D. Yu, M. Pan, G. Liu, X. Jiang, X. Wen, W. Li, S. Chen, W. Zhou, H. Wang, Y. Lu, M. Ma, Z. Zang, P. Cheng, Q. Ji, F. Zheng, Z. Ning, Electron-withdrawing organic ligand for high-efficiency all-perovskite tandem solar cells. *Nat Energy*, doi: 10.1038/s41560-023-01441-2 (2024).
26. T. Wu, Y. Wang, Z. Dai, D. Cui, T. Wang, X. Meng, E. Bi, X. Yang, L. Han, Efficient and stable CsPbI3 solar cells via regulating lattice distortion with surface organic terminal groups. *Adv. Mater.* **31**, 1900605 (2019).
27. E. Shi, B. Yuan, S. B. Shiring, Y. Gao, Akriti, Y. Guo, C. Su, M. Lai, P. Yang, J. Kong, B. M. Savoie, Y. Yu, L. Dou, Two-dimensional halide perovskite lateral epitaxial heterostructures. *Nature* **580**, 614–620 (2020).
28. J. Y. Park, R. Song, J. Liang, L. Jin, K. Wang, S. Li, E. Shi, Y. Gao, M. Zeller, S. J. Teat, P. Guo, L. Huang, Y. S. Zhao, V. Blum, L. Dou, Thickness control of organic semiconductor-incorporated perovskites. *Nat Chem* **15**, 1745–1753 (2023).
29. Y. Lin, Y. Zhong, Y. Lin, J. Lin, L. Pang, Z. Zhang, Y. Zhao, X. Y. Huang, K. Z. Du, White light emission in 0D halide perovskite [(CH3)3S]2SnCl6·H2O crystals through variation of doping ns2 ions. *Frontiers of Optoelectronics* **17** (2024).
30. M. A. Reus, L. K. Reb, A. F. Weinzierl, C. L. Weindl, R. Guo, T. Xiao, M. Schwartzkopf, A. Chumakov, S. V. Roth, P. Müller-Buschbaum, Time-Resolved orientation and phase analysis of lead halide perovskite film annealing probed by in situ GIWAXS. *Adv Opt Mater* **10**, 2102722 (2022).
31. G. Albano, G. Pescitelli, L. Di Bari, Chiroptical Properties in Thin Films of π-Conjugated Systems. *Chem Rev* **120**, 10145–10243 (2020).
32. M. Liebel, F. V. A. Camargo, G. Cerullo, N. F. van Hulst, Ultrafast transient holographic microscopy. *Nano Lett* **21**, 1666–1671 (2021).
33. M. Hörmann, F. Visentin, A. Zanetta, J. Osmond, G. Grancini, N. F. van Hulst, M. Liebel, G. Cerullo, F. V. A. Camargo, High-sensitivity visualization of ultrafast carrier diffusion by wide-field holographic microscopy. *Ultrafast Science* **3** (2023).
34. Y. Dong, Y. K. Wang, F. Yuan, A. Johnston, Y. Liu, D. Ma, M. J. Choi, B. Chen, M. Chekini, S. W. Baek, L. K. Sagar, J. Fan, Y. Hou, M. Wu, S. Lee, B. Sun, S. Hoogland,

R. Quintero-Bermudez, H. Ebe, P. Todorovic, F. Dinic, P. Li, H. T. Kung, M. I. Saidaminov, E. Kumacheva, E. Spiecker, L. S. Liao, O. Voznyy, Z. H. Lu, E. H. Sargent, Bipolar-shell resurfacing for blue LEDs based on strongly confined perovskite quantum dots. *Nat Nanotechnol* **15**, 668–674 (2020).

35. M. K. Jana, S. M. Janke, D. J. Dirkes, S. Dovletgeldi, C. Liu, X. Qin, K. Gundogdu, W. You, V. Blum, D. B. Mitzi, Direct-Bandgap 2D Silver-Bismuth Iodide Double Perovskite: The Structure-Directing Influence of an Oligothiophene Spacer Cation. *J Am Chem Soc* **141**, 7955–7964 (2019).
36. M. L. Aubrey, A. Saldivar Valdes, M. R. Filip, B. A. Connor, K. P. Lindquist, J. B. Neaton, H. I. Karunadasa, Directed assembly of layered perovskite heterostructures as single crystals. *Nature* **597**, 355–359 (2021).
37. Z. Huang, S. R. Vardeny, T. Wang, Z. Ahmad, A. Chanana, E. Vetter, S. Yang, X. Liu, G. Galli, A. Amassian, Z. V. Vardeny, D. Sun, Observation of spatially resolved Rashba states on the surface of CH3NH3PbBr3single crystals. *Appl Phys Rev* **8**, 031408 (2021).
38. W. Liang, Y. Li, D. Xiang, Y. Han, Q. Jiang, W. Zhang, K. Wu, Efficient optical orientation and slow spin relaxation in lead-free CsSnBr3 perovskite nanocrystals. *ACS Energy Lett.* **6**, 1670–1676 (2021).
39. G. Garcia-Arellano, G. Trippé-Allard, L. Legrand, T. Barisien, D. Garrot, E. Deleporte, F. Bernardot, C. Testelin, M. Chamarro, Energy Tuning of Electronic Spin Coherent Evolution in Methylammonium Lead Iodide Perovskites. *Journal of Physical Chemistry Letters* **12**, 8272–8279 (2021).
40. Z. Chen, G. Dong, J. Qiu, Ultrafast pump-probe spectroscopy—a powerful tool for tracking spin-quantum dynamics in metal halide perovskites. *Adv. Quantum Technol.* **4**, 2100052 (2021).
41. K. Zhang, J. Zhao, Q. Hu, S. Yang, X. Zhu, Y. Zhang, R. Huang, Y. Ma, Z. Wang, Z. Ouyang, J. Han, Y. Han, J. Tang, W. Tong, L. Zhang, T. Zhai, Room-Temperature Magnetic Field Effect on Excitonic Photoluminescence in Perovskite Nanocrystals. *Advanced Materials* **33**, 2008225 (2021).
42. J. M. Richter, K. Chen, A. Sadhanala, J. Butkus, J. P. H. Rivett, R. H. Friend, B. Monserrat, J. M. Hodgkiss, F. Deschler, Direct Bandgap Behavior in Rashba-Type Metal Halide Perovskites. *Advanced Materials* **30** (2018).
43. M. K. Jana, R. Song, H. Liu, D. R. Khanal, S. M. Janke, R. Zhao, C. Liu, Z. Valy Vardeny, V. Blum, D. B. Mitzi, Organic-to-inorganic structural chirality transfer in a

2D hybrid perovskite and impact on Rashba-Dresselhaus spin-orbit coupling. *Nat. Commun.* **11**, 4699 (2020).

44. M. Kepenekian, R. Robles, C. Katan, D. Sapori, L. Pedesseau, J. Even, Rashba and Dresselhaus effects in hybrid organic-inorganic perovskites: from basics to devices. *ACS Nano* **9**, 11557–11567 (2015).
45. G. Szulczewski, S. Sanvito, M. Coey, A spin of their own. *Nat Mater* **8**, 693–695 (2009).
46. S. Reineke, M. Thomschke, B. Lüssem, K. Leo, White organic light-emitting diodes: Status and perspective. *Rev Mod Phys* **85**, 1245–1293 (2013).
47. C. Chen, L. Gao, W. Gao, C. Ge, X. Du, Z. Li, Y. Yang, G. Niu, J. Tang, Circularly polarized light detection using chiral hybrid perovskite. *Nat Commun* **10**, 1927 (2019).
48. Y.-H. Kim, Y. Zhai, H. Lu, X. Pan, C. Xiao, E. A. Gaulding, S. P. Harvey, J. J. Berry, Z. Valy Vardeny, J. M. Luther, M. C. Beard, Chiral-induced spin selectivity enables a room-temperature spin light-emitting diode. *Science (1979)* **371**, 1129–1133 (2021).
49. B. Vargas, R. Torres-Cadena, D. T. Reyes-Castillo, J. Rodríguez-Hernández, M. Gembicky, E. Menéndez-Proupin, D. Solis-Ibarra, Chemical Diversity in Lead-Free, Layered Double Perovskites: A Combined Experimental and Computational Approach. *Chemistry of Materials* **32**, 424–429 (2020).
50. H. Lei, D. Hardy, F. Gao, Lead-free double perovskite Cs2AgBiBr6: fundamentals, applications, and perspectives. *Adv. Funct. Mater.* **31**, 2105898 (2021).
51. D. Cortecchia, H. A. Dewi, J. Yin, A. Bruno, S. Chen, T. Baikie, P. P. Boix, M. Grätzel, S. Mhaisalkar, C. Soci, N. Mathews, Lead-Free MA2CuClxBr4-x Hybrid Perovskites. *Inorg Chem* **55**, 1044–1052 (2016).
52. F. Giustino, H. J. Snaith, Toward Lead-Free Perovskite Solar Cells. *ACS Energy Lett* **1**, 1233–1240 (2016).
53. T. Schmitt, S. Bourelle, N. Tye, G. Soavi, A. D. Bond, S. Feldmann, B. Traore, C. Katan, J. Even, S. E. Dutton, F. Deschler, Control of Crystal Symmetry Breaking with Halogen-Substituted Benzylammonium in Layered Hybrid Metal-Halide Perovskites. *J Am Chem Soc* **142**, 5060–5067 (2020).
54. X. Li, Y. Fu, L. Pedesseau, P. Guo, S. Cuthriell, I. Hadar, J. Even, C. Katan, C. C. Stoumpos, R. D. Schaller, E. Harel, M. G. Kanatzidis, Negative Pressure Engineering with Large Cage Cations in 2D Halide Perovskites Causes Lattice Softening. *J Am Chem Soc* **142**, 11486–11496 (2020).

55. M. K. Jana, R. Song, Y. Xie, R. Zhao, P. C. Sercel, V. Blum, D. B. Mitzi, Structural descriptor for enhanced spin-splitting in 2D hybrid perovskites. *Nat. Commun.* **12** (2021).

56. J. P. Yang, M. Meissner, T. Yamaguchi, X. Y. Zhang, T. Ueba, L. W. Cheng, S. Ideta, K. Tanaka, X. H. Zeng, N. Ueno, S. Kera, Band Dispersion and Hole Effective Mass of Methylammonium Lead Iodide Perovskite. *Solar RRL* **2**, 1800132 (2018).

57. J. S. Kim, J. M. Heo, G. S. Park, S. J. Woo, C. Cho, H. J. Yun, D. H. Kim, J. Park, S. C. Lee, S. H. Park, E. Yoon, N. C. Greenham, T. W. Lee, Ultra-bright, efficient and stable perovskite light-emitting diodes. *Nature* **611**, 688–694 (2022).

58. Y. Zhao, M. Dong, J. Feng, J. Zhao, Y. Guo, Y. Fu, H. Gao, J. Yang, L. Jiang, Y. Wu, Lead-Free Chiral 2D Double Perovskite Microwire Arrays for Circularly Polarized Light Detection. *Adv Opt Mater* **10**, 2102227 (2022).

59. D. Li, X. Liu, W. Wu, Y. Peng, S. Zhao, L. Li, M. Hong, J. Luo, Chiral Lead-Free Hybrid Perovskites for Self-Powered Circularly Polarized Light Detection. *Angewandte Chemie - International Edition* **60**, 8415–8418 (2021).

60. Z. Liu, C. Zhang, X. Liu, A. Ren, Z. Zhou, C. Qiao, Y. Guan, Y. Fan, F. Hu, Y. S. Zhao, Chiral Hybrid Perovskite Single-Crystal Nanowire Arrays for High-Performance Circularly Polarized Light Detection. *Advanced Science* **8**, 2102065 (2021).

61. M. Scholz, O. Flender, K. Oum, T. Lenzer, Pronounced Exciton Dynamics in the Vacancy-Ordered Bismuth Halide Perovskite (CH3NH3)3Bi2I9 Observed by Ultrafast UV-vis-NIR Transient Absorption Spectroscopy. *Journal of Physical Chemistry C* **121**, 12110–12116 (2017).

62. R. Kentsch, M. Scholz, J. Horn, D. Schlettwein, K. Oum, T. Lenzer, Exciton Dynamics and Electron-Phonon Coupling Affect the Photovoltaic Performance of the Cs2AgBiBr6 Double Perovskite. *Journal of Physical Chemistry C* **122**, 25940–25947 (2018).

63. M. B. Price, J. Butkus, T. C. Jellicoe, A. Sadhanala, A. Briane, J. E. Halpert, K. Broch, J. M. Hodgkiss, R. H. Friend, F. Deschler, Hot-carrier cooling and photoinduced refractive index changes in organic-inorganic lead halide perovskites. *Nat Commun* **6** (2015).

64. B. Wu, W. Ning, Q. Xu, M. Manjappa, M. Feng, S. Ye, J. Fu, S. Lie, T. Yin, F. Wang, T. Wee Goh, P. Cholakkal Harikesh, Y. Kang Eugene Tay, Z. Xiang Shen, F. Huang, R. Singh, G. Zhou, F. Gao, T. Chien Sum, Strong self-trapping by deformation potential

limits photovoltaic performance in bismuth double perovskite. *Sci Adv* **7**, eabd3160 (2021).

65. S. A. Bourelle, R. Shivanna, F. V. A. Camargo, S. Ghosh, A. J. Gillett, S. P. Senanayak, S. Feldmann, L. Eyre, A. Ashoka, T. W. J. Van De Goor, H. Abolins, T. Winkler, G. Cerullo, R. H. Friend, F. Deschler, How exciton interactions control spin-depolarization in layered hybrid perovskites. *Nano Lett.* **20**, 5678–5685 (2020).
66. S. A. Bourelle, F. V. A. Camargo, S. Ghosh, T. Neumann, T. W. J. van de Goor, R. Shivanna, T. Winkler, G. Cerullo, F. Deschler, Optical control of exciton spin dynamics in layered metal halide perovskites via polaronic state formation. *Nat Commun* **13** (2022).
67. Y.-H. Kim, Y. Zhai, H. Lu, X. Pan, C. Xiao, E. A. Gaulding, S. P. Harvey, J. J. Berry, Z. Valy Vardeny, J. M. Luther, M. C. Beard, Chiral-induced spin selectivity enables a room-temperature spin light-emitting diode. *Science (1979)* **371**, 1129–1133 (2021).
68. C. Qin, A. S. D. Sandanayaka, C. Zhao, T. Matsushima, D. Zhang, T. Fujihara, C. Adachi, Stable room-temperature continuous-wave lasing in quasi-2D perovskite films. *Nature* **585**, 53–57 (2020).
69. J. Ma, C. Fang, C. Chen, L. Jin, J. Wang, S. Wang, J. Tang, D. Li, Chiral 2D perovskites with a high degree of circularly polarized photoluminescence. *ACS Nano* **13**, 3659–3665 (2019).
70. D. Di Nuzzo, L. Cui, J. L. Greenfield, B. Zhao, R. H. Friend, S. C. J. Meskers, Circularly polarized photoluminescence from chiral perovskite thin films at room temperature. *ACS Nano* **14**, 7610–7616 (2020).
71. C. Yuan, X. Li, S. Semin, Y. Feng, T. Rasing, J. Xu, Chiral Lead Halide Perovskite Nanowires for Second-Order Nonlinear Optics. *Nano Lett* **18**, 5411–5417 (2018).
72. Y. M. You, W. Q. Liao, D. Zhao, H. Y. Ye, Y. Zhang, Q. Zhou, X. Niu, J. Wang, P. F. Li, D. W. Fu, Z. Wang, S. Gao, K. Yang, J. M. Liu, J. Li, Y. Yan, R. G. Xiong, An organic-inorganic perovskite ferroelectric with large piezoelectric response. *Science (1979)* **357**, 306–309 (2017).
73. Y. Qin, F. F. Gao, S. Qian, T. M. Guo, Y. J. Gong, Z. G. Li, G. D. Su, Y. Gao, W. Li, C. Jiang, P. Lu, X. H. Bu, Multifunctional chiral 2D lead halide perovskites with circularly polarized photoluminescence and piezoelectric energy harvesting properties. *ACS Nano* **16**, 3221–3230 (2022).
74. T. Neumann, S. Feldmann, P. Moser, A. Delhomme, J. Zerhoch, T. van de Goor, S. Wang, M. Dyksik, T. Winkler, J. J. Finley, P. Plochocka, M. S. Brandt, C. Faugeras, A.

V. Stier, F. Deschler, Manganese doping for enhanced magnetic brightening and circular polarization control of dark excitons in paramagnetic layered hybrid metal-halide perovskites. *Nat. Commun.* **12**, 3489 (2021).

75. Q. Wei, Z. Ning, Chiral perovskite spin-optoelectronics and spintronics: toward judicious design and application. *ACS Mater. Lett.* **3**, 1266–1275 (2021).
76. H. Lu, J. Wang, C. Xiao, X. Pan, X. Chen, R. Brunecky, J. J. Berry, K. Zhu, M. C. Beard, Z. Valy Vardeny, Spin-dependent charge transport through 2D chiral hybrid lead-iodide perovskites. *Sci. Adv* **5**, eaay0571 (2019).
77. J. Ahn, E. Lee, J. Tan, W. Yang, B. Kim, J. Moon, A new class of chiral semiconductors: Chiral-organic-molecule-incorporating organic-inorganic hybrid perovskites. *Mater Horiz* **4**, 851–856 (2017).
78. J. Ma, H. Wang, D. Li, Recent Progress of Chiral Perovskites: Materials, Synthesis, and Properties. *Advanced Materials* **33**, 2008785 (2021).
79. Z. N. Georgieva, B. P. Bloom, S. Ghosh, D. H. Waldeck, Imprinting Chirality onto the Electronic States of Colloidal Perovskite Nanoplatelets. *Advanced Materials* **30**, 1800097 (2018).
80. Z. Wen, R. Lu, F. Gu, K. Zheng, L. Zhang, H. Jin, Y. Chen, S. Wang, S. Pan, Enabling efficient blue-emissive circularly polarized luminescence by in situ crafting of chiral quasi-2D perovskite nanosheets within polymer nanofibers. *Adv Funct Mater* **33**, 2212095 (2023).
81. D. Di Nuzzo, L. Cui, J. L. Greenfield, B. Zhao, R. H. Friend, S. C. J. Meskers, Circularly polarized photoluminescence from chiral perovskite thin films at room temperature. *ACS Nano* **14**, 7610–7616 (2020).
82. G. Long, C. Jiang, R. Sabatini, Z. Yang, M. Wei, L. N. Quan, Q. Liang, A. Rasmita, M. Askerka, G. Walters, X. Gong, J. Xing, X. Wen, R. Quintero-Bermudez, H. Yuan, G. Xing, X. R. Wang, D. Song, O. Voznyy, M. Zhang, S. Hoogland, W. Gao, Q. Xiong, E. H. Sargent, Spin control in reduced-dimensional chiral perovskites. *Nat. Photon.* **12**, 528–533 (2018).
83. D. Pan, Y. Fu, N. Spitha, Y. Zhao, C. R. Roy, D. J. Morrow, D. D. Kohler, J. C. Wright, S. Jin, Deterministic fabrication of arbitrary vertical heterostructures of two-dimensional Ruddlesden–Popper halide perovskites. *Nat. Nano.* **16**, 159–165 (2021).
84. Y. Chen, J. Ma, Z. Liu, J. Li, X. Duan, D. Li, Manipulation of valley pseudospin by selective spin injection in chiral two-dimensional perovskite/monolayer transition metal dichalcogenide heterostructures. *ACS Nano* **14**, 15154–15160 (2020).

85. Z. Yuan, C. Zhou, Y. Tian, Y. Shu, J. Messier, J. C. Wang, L. J. Van De Burgt, K. Kountouriotis, Y. Xin, E. Holt, K. Schanze, R. Clark, T. Siegrist, B. Ma, One-dimensional organic lead halide perovskites with efficient bluish white-light emission. *Nat. Commun.* **8** (2017).

86. J. M. Hoffman, X. Che, S. Sidhik, X. Li, I. Hadar, J. C. Blancon, H. Yamaguchi, M. Kepenekian, C. Katan, J. Even, C. C. Stoumpos, A. D. Mohite, M. G. Kanatzidis, From 2D to 1D electronic dimensionality in halide perovskites with stepped and flat layers using propylammonium as a spacer. *J. Am. Chem. Soc.* **141**, 10661–10676 (2019).

87. Nina Berova, Koji Nakanishi, Robert W. Woody, *Circular Dichroism: Principles And* (John Wiley & Sons., 2000).

88. S. Gull, M. H. Jamil, X. Zhang, H. sing Kwok, G. Li, Stokes shift in inorganic lead halide perovskites: current status and perspective. *ChemistryOpen* **11**, e2021002 (2022).

89. S. Feldmann, S. Macpherson, S. P. Senanayak, M. Abdi-Jalebi, J. P. H. Rivett, G. Nan, G. D. Tainter, T. A. S. Doherty, K. Frohna, E. Ringe, R. H. Friend, H. Sirringhaus, M. Saliba, D. Beljonne, S. D. Stranks, F. Deschler, Photodoping through local charge carrier accumulation in alloyed hybrid perovskites for highly efficient luminescence. *Nat Photonics* **14**, 123–128 (2020).

90. R. L. Z. Hoye, L. Eyre, F. Wei, F. Brivio, A. Sadhanala, S. Sun, W. Li, K. H. L. Zhang, J. L. MacManus-Driscoll, P. D. Bristowe, R. H. Friend, A. K. Cheetham, F. Deschler, Fundamental carrier lifetime exceeding 1 μs in Cs2AgBiBr6 double perovskite. *Adv. Mater. Interfaces* **5**, 1800464 (2018).

91. J. Zhang, X. Zhu, M. Wang, B. Hu, Establishing charge-transfer excitons in 2D perovskite heterostructures. *Nat. Commun.* **11**, 2618 (2020).

92. X. Chen, H. Lu, K. Wang, Y. Zhai, V. Lunin, P. C. Sercel, M. C. Beard, Tuning Spin-Polarized Lifetime in Two-Dimensional Metal-Halide Perovskite through Exciton Binding Energy. *J. Am. Chem. Soc.* **143**, 19438–19445 (2021).

93. S. Valastro, S. Gavranovic, I. Deretzis, M. Vala, E. Smecca, A. La Magna, A. Alberti, K. Castkova, G. Mannino, Temperature-Dependent Excitonic Band Gap in Lead-Free Bismuth Halide Low-Dimensional Perovskite Single Crystals. *Adv Opt Mater*, doi: 10.1002/adom.202302397 (2023).

94. G. Morello, M. De Giorgi, S. Kudera, L. Manna, R. Cingolani, M. Anni, Temperature and size dependence of nonradiative relaxation and exciton-phonon coupling in colloidal CdTe quantum dots. *J. Phys. Chem. C* **111**, 5846–5849 (2007).

95. A. D. Wright, C. Verdi, R. L. Milot, G. E. Eperon, M. A. Pérez-Osorio, H. J. Snaith, F. Giustino, M. B. Johnston, L. M. Herz, Electron-phonon coupling in hybrid lead halide perovskites. *Nat Commun* **7** (2016).

96. H. C. Woo, J. W. Choi, J. Shin, S. H. Chin, M. H. Ann, C. L. Lee, Temperature-Dependent Photoluminescence of CH3NH3PbBr3 Perovskite Quantum Dots and Bulk Counterparts. *J. Phys. Chem. Lett.* **9**, 4066–4074 (2018).

97. Y. Lv, C. Yin, C. Zhang, X. Wang, Z. G. Yu, M. Xiao, Exciton-acoustic phonon coupling revealed by resonant excitation of single perovskite nanocrystals. *Nat Commun* **12** (2021).

98. L. Tao, H. Zhan, Y. Cheng, C. Qin, L. Wang, Enhanced circularly polarized photoluminescence of chiral perovskite films by surface passivation with chiral amines. *J. Phys. Chem. Lett.* **14**, 2317–2322 (2023).

99. A. Hirohata, K. Takanashi, Future perspectives for spintronic devices. *J Phys D Appl Phys* **47**, 193001 (2014).

100. J. F. Sierra, J. Fabian, R. K. Kawakami, S. Roche, S. O. Valenzuela, Van der Waals heterostructures for spintronics and opto-spintronics. *Nat Nanotechnol* **16**, 856–868 (2021).

101. R. Naaman, D. H. Waldeck, Chiral-induced spin selectivity effect. *J. Phys. Chem. Lett.* **3**, 2178–2187 (2012).

102. L. Guo, X. Gu, X. Zhu, X. Sun, Recent Advances in Molecular Spintronics: Multifunctional Spintronic Devices. *Advanced Materials* **31**, 1805355 (2019).

103. J. Ma, C. Fang, C. Chen, L. Jin, J. Wang, S. Wang, J. Tang, D. Li, Chiral 2D perovskites with a high degree of circularly polarized photoluminescence. *ACS Nano* **13**, 3659–3665 (2019).

104. Q. Qian, H. Ren, J. Zhou, Z. Wan, J. Zhou, X. Yan, J. Cai, P. Wang, B. Li, Z. Sofer, B. Li, X. Duan, X. Pan, Y. Huang, X. Duan, Chiral molecular intercalation superlattices. *Nature* **606**, 902–908 (2022).

105. T. Liu, W. Shi, W. Tang, Z. Liu, B. C. Schroeder, O. Fenwick, M. J. Fuchter, High responsivity circular polarized light detectors based on quasi two-dimensional chiral perovskite films. *ACS Nano* **16**, 2682–2689 (2022).

106. C. Zhou, Y. Chu, L. Ma, Y. Zhong, C. Wang, Y. Liu, H. Zhang, B. Wang, X. Feng, X. Yu, X. Zhang, Y. Sun, X. Li, G. Zhao, Photoluminescence spectral broadening, chirality transfer and amplification of chiral perovskite materials (R-X-: P -

mBZA)2PbBr4(X = H, F, Cl, Br) regulated by van der Waals and halogen atoms interactions. *Physical Chemistry Chemical Physics* **22**, 17299–17305 (2020).

107. M. K. Jana, R. Song, H. Liu, D. R. Khanal, S. M. Janke, R. Zhao, C. Liu, Z. Valy Vardeny, V. Blum, D. B. Mitzi, Organic-to-inorganic structural chirality transfer in a 2D hybrid perovskite and impact on Rashba-Dresselhaus spin-orbit coupling. *Nat. Commun.* **11**, 4699 (2020).
108. H. Lu, C. Xiao, R. Song, T. Li, A. E. Maughan, A. Levin, R. Brunecky, J. J. Berry, D. B. Mitzi, V. Blum, M. C. Beard, Highly distorted chiral two-dimensional tin iodide perovskites for spin polarized charge transport. *J. Am. Chem. Soc.* **142**, 13030–13040 (2020).
109. F. E. Neumann, O. E. Meyer, *Vorlesungen Über Die Theorie Der Elasticität Der Festen Körper Und Des Lichtäthers, Gehalten an Der Universität Königsberg* (BG Teubner, 1885)vol. 4.
110. P. Curie, Sur la symétrie dans les phénomènes physiques, symétrie d'un champ électrique et d'un champ magnétique. *J. Phys. Theor. Appl.* **3**, 393–415 (1894).
111. K. Z. Du, Q. Tu, X. Zhang, Q. Han, J. Liu, S. Zauscher, D. B. Mitzi, Two-dimensional lead(II) halide-based hybrid perovskites templated by acene alkylamines: crystal structures, optical Properties, and piezoelectricity. *Inorg. Chem.* **56**, 9291–9302 (2017).
112. J. Even, L. Pedesseau, M. A. Dupertuis, J. M. Jancu, C. Katan, Electronic model for self-assembled hybrid organic/perovskite semiconductors: reverse band edge electronic states ordering and spin-orbit coupling. *Phys. Rev. B* **86**, 205301 (2012).
113. L. Pedesseau, D. Sapori, B. Traore, R. Robles, H. H. Fang, M. A. Loi, H. Tsai, W. Nie, J. C. Blancon, A. Neukirch, S. Tretiak, A. D. Mohite, C. Katan, J. Even, M. Kepenekian, Advances and promises of layered halide hybrid perovskite semiconductors. *ACS Nano* **10**, 9776–9786 (2016).
114. Y. A. Bychkov, E. I. Rashba, Properties of a 2D electron gas With lifted spectral degeneracy. *JETP Lett.* **39**, 78–81 (1948).
115. M. Kepenekian, J. Even, Rashba and Dresselhaus couplings in halide perovskites: accomplishments and opportunities for spintronics and spin-orbitronics. American Chemical Society [Preprint] (2017). https://doi.org/10.1021/acs.jpclett.7b01015.
116. M. K. Jana, R. Song, Y. Xie, R. Zhao, P. C. Sercel, V. Blum, D. B. Mitzi, Structural descriptor for enhanced spin-splitting in 2D hybrid perovskites. *Nat. Commun.* **12**, 4982 (2021).

117. L. Wan, Y. Liu, M. J. Fuchter, B. Yan, Anomalous circularly polarized light emission in organic light-emitting diodes caused by orbital–momentum locking. *Nat Photonics* **17**, 193–199 (2023).

118. D. Di Nuzzo, C. Kulkarni, B. Zhao, E. Smolinsky, F. Tassinari, S. C. J. Meskers, R. Naaman, E. W. Meijer, R. H. Friend, High circular polarization of electroluminescence achieved via self-assembly of a light-emitting chiral conjugated polymer into multidomain cholesteric films. *ACS Nano* **11**, 12713–12722 (2017).

119. D. M. Lee, J. W. Song, Y. J. Lee, C. J. Yu, J. H. Kim, Control of circularly polarized electroluminescence in induced twist structure of conjugate polymer. *Adv. Mater.* **29**, 1700907 (2017).

120. Y. Jiang, C. Sun, J. Xu, S. Li, M. Cui, X. Fu, Y. Liu, Y. Liu, H. Wan, K. Wei, T. Zhou, W. Zhang, Y. Yang, J. Yang, C. Qin, S. Gao, J. Pan, Y. Liu, S. Hoogland, E. H. Sargent, J. Chen, M. Yuan, Synthesis-on-substrate of quantum dot solids. *Nature* **612**, 679–684 (2022).

121. Y. Cao, N. Wang, H. Tian, J. Guo, Y. Wei, H. Chen, Y. Miao, W. Zou, K. Pan, Y. He, H. Cao, Y. Ke, M. Xu, Y. Wang, M. Yang, K. Du, Z. Fu, D. Kong, D. Dai, Y. Jin, G. Li, H. Li, Q. Peng, J. Wang, W. Huang, Perovskite light-emitting diodes based on spontaneously formed submicrometre-scale structures. *Nature* **562**, 249–253 (2018).

122. G. Jang, D. Y. Jo, S. Ma, J. Lee, J. Son, C. U. Lee, W. Jeong, S. Yang, J. H. Park, H. Yang, J. Moon, Core–shell perovskite quantum dots for highly selective room-temperature spin light-emitting diodes. *Adv. Mater.*, 2309335 (2023).

123. Q. Wang, H. Zhu, Y. Tan, J. Hao, T. Ye, H. Tang, Z. Wang, J. Ma, J. Sun, T. Zhang, F. Zheng, W. Zhang, A. H. W. Choi, W. C. H. Choy, D. Wu, X. W. Sun, K. Wang, Spin quantum dot light-emitting diodes enabled by two-dimensional chiral perovskite with spin-dependent carrier transport. *Adv. Mater.*, 2305604 (2023).

124. M. Li, Y. F. Wang, D. Zhang, L. Duan, C. F. Chen, Axially chiral TADF-active enantiomers designed for efficient blue circularly polarized electroluminescence. *Angew. Chem. Int. Ed.* **59**, 3500–3504 (2020).

125. Y. J. Zhang, T. Oka, R. Suzuki, J. T. Ye, Y. Iwasa, Electrically switchable chiral light-emitting transistor. *Science (1979)* **344**, 725–728 (2014).

126. Z. P. Yan, X. F. Luo, W. Q. Liu, Z. G. Wu, X. Liang, K. Liao, Y. Wang, Y. X. Zheng, L. Zhou, J. L. Zuo, Y. Pan, H. Zhang, Configurationally Stable Platinahelicene Enantiomers for Efficient Circularly Polarized Phosphorescent Organic Light-Emitting Diodes. *Chemistry - A European Journal* **25**, 5672–5676 (2019).

127. Y. Yang, R. C. Da Costa, D. M. Smilgies, A. J. Campbell, M. J. Fuchter, Induction of circularly polarized electroluminescence from an achiral light-emitting polymer via a chiral small-molecule dopant. *Adv. Mater.* **25**, 2624–2628 (2013).
128. F. Zinna, M. Pasini, F. Galeotti, C. Botta, L. Di Bari, U. Giovanella, Design of Lanthanide-Based OLEDs with Remarkable Circularly Polarized Electroluminescence. *Adv Funct Mater* **27** (2017).
129. S. Ma, Y. K. Jung, J. Ahn, J. Kyhm, J. Tan, H. Lee, G. Jang, C. U. Lee, A. Walsh, J. Moon, Elucidating the origin of chiroptical activity in chiral 2D perovskites through nano-confined growth. *Nat. Com.* **13**, 3259 (2022).
130. S. Jiang, N. A. Kotov, Circular polarized light emission in chiral inorganic nanomaterials. *Adv. Mater.* **35**, 2108431 (2023).
131. S. Feldmann, S. Macpherson, S. P. Senanayak, M. Abdi-Jalebi, J. P. H. Rivett, G. Nan, G. D. Tainter, T. A. S. Doherty, K. Frohna, E. Ringe, R. H. Friend, H. Sirringhaus, M. Saliba, D. Beljonne, S. D. Stranks, F. Deschler, Photodoping through local charge carrier accumulation in alloyed hybrid perovskites for highly efficient luminescence. *Nat Photonics* **14**, 123–128 (2020).
132. B. Guo, R. Lai, S. Jiang, L. Zhou, Z. Ren, Y. Lian, P. Li, X. Cao, S. Xing, Y. Wang, W. Li, C. Zou, M. Chen, Z. Hong, C. Li, B. Zhao, D. Di, Ultrastable near-infrared perovskite light-emitting diodes. *Nat Photonics* **16**, 637–643 (2022).
133. J. Wang, C. Zhang, H. Liu, R. McLaughlin, Y. Zhai, S. R. Vardeny, X. Liu, S. McGill, D. Semenov, H. Guo, R. Tsuchikawa, V. V. Deshpande, D. Sun, Z. V. Vardeny, Spin-optoelectronic devices based on hybrid organic-inorganic trihalide perovskites. *Nat Commun* **10** (2019).

List of publications

First author:

1. **S. Liu**, M. Kepenekian, S. Bodnar, S. Feldmann, M. W. Heindl, N. Fehn, J. Zerhoch, A. Shcherbakov, A. Pöthig, Y. Li, U. W. Paetzold, A. Kartouzian, I. D. Sharp, C. Katan, J. Even, F. Deschler. Bright Circularly Polarized Photoluminescence in Chiral Layered Hybrid Lead-Halide perovskites. *Science Advances*, **2023**, 9, eadh5083.
2. **S. Liu**, M. W. Heindl, N. Fehn, S. Caicedo-Dávila, L. Eyre, S. M. Kronawitter, J. Zerhoch, S. Bodnar, A. Shcherbakov, A. Stadlbauer, G. Kieslich, I. D. Sharp, D. A. Egger, A. Kartouzian, F. Deschler. Optically Induced Long-Lived Chirality Memory in the Color-Tunable Chiral Lead-Free Semiconductor (R)/(S)-$CHEA_4Bi_2Br_xI_{10-x}$ (x = 0–10). *J. Am. Chem. Soc.* **2022**, *144*, 14079–14089.
3. **S. Liu**, Q. Yu, C. Zhang, M. Zhang, N. Rowell, H. Fan, W. Huang, K. Yu, B. Liang. Transformation of ZnS Precursor Compounds to Magic-Size Clusters Exhibiting Optical Absorption Peaking at 269 nm. *J. Phys. Chem. Lett.* **2020**, *11*, 75−82.
4. **S. Liu**, Y. Li, S. Bodnar, J. Zerhoch, J. A. Gessner, P. Kollenz, A. Shcherbakov, G. May, N. Solhtalab, M. W. Heindl, U. W. Paetzold, F. Deschler. Bright Circularly Polarized Light-Emitting Diodes Using Chiral Lead-Halide Perovskite Heterostructure Emitters. (under review)
5. **S. Liu**, J. Zerhoch, M. W. Heindl, C. Zhang, T. Kodalle, K. Sun, A. Shcherbakov, S. Bodnar, C. Jandl, A. Pöthig, I. D. Sharp, P. Müller-Buschbaum, C. M. Sutter-Fella, F. Deschler. Chirality Funnels in Low-Dimensional Hybrid Perovskite Heterostructures for Circularly Polarized Photoluminescence. (to be submitted)
6. **S. Liu**, J. Zerhoch, S. Bodnar, J. A. Gessner, A. Shcherbakov, Frank Rominger, Rüdiger Klingeler, F. Deschler. Chirality Induced Long-Lived Intrinsic Spin Polarization in Ferromagnetic Hybrid Cobalt Halide Semiconductors. (to be submitted)

Co-author:

1. J. Zerhoch, S. Bodnar, J. E. Lerpinière, **S. Liu**, T. Neumann, B. Sergl, M. W. Heindl, A. Shcherbakov, A. Elghandour, R. Klingeler, A. B. Walker, F. Deschler. Motional Narrowing Effects in the Excited State Spin Populations of Mn-Doped Hybrid Perovskites. *J. Phys. Chem. Lett.* **2024**, 15, 10, 2851–2858.

2. A. Stadlbauer, L. Eyre, A. Biewald, F. Rauh, M. W. Heindl, **S. Liu**, J. Zerhoch, S. Feldmann, A. Hartschuh, F. Deschler. Photoexcitation Control of Excitation Relaxation in Mixed-Phase Ruddlesden-Popper Hybrid Organic-Inorganic Lead-Iodide Perovskites. *Adv. Opt. Mater.* **2024**, *12*, 2301331.
3. A. Shcherbakov, K. Synnatschke, S. Bodnar, J. Zerhoch, L. Eyre, F. Rauh, M. W. Heindl, **S. Liu**, J. Konecny, I. D. Sharp, Z. Sofer, C. Backes, F. Deschler. Solution-Processed $NiPS_3$ Thin Films from Liquid Exfoliated Inks with Long-Lived Spin-Entangled Excitons. *ACS Nano* **2023**, 17, 11, 10423–10430.
4. K. Sun, R. Guo, Y. Liang, J. E. Heger, **S. Liu**, S. Yin, M. A. Reus, L. V. Spanier, F. Deschler, S. Bernstorff, P. Müller-Buschbaum. Morphological Insights into the Degradation of Perovskite Solar Cells under Light and Humidity. *ACS Applied Materials & Interfaces* **2023**, *15*, 30342− 30349.
5. L. He, C. Luan, **S. Liu**, M. Chen, N. Rowell, Z. Wang, Y. Li, C. Zhang, J. Lu, M. Zhang, B. Liang, K. Yu. Transformations of magic-size clusters via precursor compound cation exchange at room temperature. *J. Am. Chem. Soc.* **2022**, 144, 41, 19060–19069.
6. M. W. Heindl, T. Kodalle, N. Fehn, L. K. Reb, **S. Liu**, C. Harder, M. Abdelsamie, L. Eyre, I. D. Sharp, S. V. Roth, P. Müller-Buschbaum, A. Kartouzian, C. M. Sutter-Fella, F. Deschler. Strong Induced Circular Dichroism in a Hybrid Lead-Halide Semiconductor Using Chiral Amino Acids for Crystallite Surface Functionalization. *Adv. Opt. Mater.* **2022**, *10*, 2200204.

Scientific Conferences:

- MATSUS Spring 2024, Barcelona, Oral talk.
- SPIE Optics + Photonics 2023, San Diego, Oral presentation.
- 2023 MRS Spring Meeting, San Francisco, Oral presentation.
- 2022 MRS Fall Meeting, Boston, Oral presentation.
- E-conversion Fall Meeting 2022 in Venice, Poster.
- DPG Fall Meeting 2022 in Regensburg, Oral presentation.
- MRS Fall Meeting 2021, Oral presentation.
- EMRS Fall Meeting 2021, Poster.

Acknowledgments

First and foremost, I would like to express my deepest gratitude to my supervisor, Dr. Felix Deschler, for his support, insightful guidance, and helpful feedback throughout the entire research process. I am truly grateful for the time you have dedicated to discussing data, reviewing drafts, and providing direction. Besides scientific guidance, Felix is more like a friend to us. I really enjoy the time I spent in Deschler group.

I also wish to extend my thanks to the colleagues in Deschler group, Andrii Shcherbakov, Stanislav Bodnar, Jonathan Zerhoch, Markus Heindl, Lissa Eyre, Anna Stadlbauer, Timo Neumann, Chaoran Zhang, Nasrin Solhtalab, Julia Gessner, Philipp Kollenz, Garrett May, Pavel Kolesnichenko, Danyellen Galindo, Ramesh Nandi and Lars Schneider, for their time, interest, and valuable suggestions. You are not only good scientific collaborators in the research, and also my best friends during my four-year life abroad. It is you who have brighten my life in Germany.

I am incredibly thankful to my collaborators at TUM, Univeristy Heidelberg, KIT, and Univ Rennes. Special thanks to Dr. Ian Sharp, Dr. David Egger, Dr. Mikaël Kepenekian, Dr. Alexander Pöthig, Dr. Claudine Katan, Dr. Jacky Even, Dr. Aras Kartouzian, Dr. Gregor Kieslich, Dr. Sebastián Caicedo-Dávila, Dr. Frank Rominger, Dr. Hans-Robert Volpp, Dr. Tiago Buckup, Silva Kronawitter, and Natalie Fehn for their support in experiments and calculations, and valuable discussions that have not only helped me to overcome research challenges but also made this journey enjoyable. The collaborative environment and shared experiences have made a significant difference in my academic and personal growth.

A special acknowledgment goes to our screatary at TUM and Univeristy Heidelberg, particularly Joana Figueiredo and Marina Sommer, for their contant and fast assistance with the logistical aspects of my research.

I would also like to acknowledge my friends outside of academia, especially Pan Ding, Menglong Liu, Guanda Zhou, and Jianian Chen. Your companionship has been a source of relaxation and joy, reminding me of the importance of enjoying my life.

I am profoundly grateful to my family, especially for my parents Xinghua and Shaofeng, and my girl friend Yimin Yang, for their unwavering love and support. It is my luck to meet you in this world. This thesis is dedicated to you.

Thank you to everyone who has been a part of this four-year journey. Your support, in its many forms, has been important parts in the completion of this thesis. Hope we can meet again in the future.